ALVEOLAR MACROPHAGE EXPRESSED NKR-P1B INTERACTS WITH CLR-G ON TYPE-II PNEUMOCYTES TO MODULATE ALVEOLAR MACROPHAGE LIPID METABOLISM AND SURVIVAL

By

Michal Scur

Submitted in partial fulfilment of the requirement
For the degree of Doctor of Philosophy

at

Dalhousie University
Halifax, Nova Scotia
November 2021

Dalhousie is located in the Mi'kma'ki, the
Ancestral and unceded territory of the Mi'kmaq.
We are all Treaty people

DEDICATION

I dedicate this thesis to my parents for the love and unconditional support throughout this journey and to Alexa Wilson, whose and love and support has become an inseparable part of my life.

TABLE OF CONTENTS

List of Tables

List of Figures

ABSTRACT

Alveolar macrophages (AMs) are specialized, tissue-resident macrophages at the frontline of pulmonary defense against inhaled pathogens, and surfactant homeostasis. To perform these roles, AMs undergo cellular programming in response to tissue- and cell-specific signals elicited by the pulmonary niche. However, the tissue-specific mechanisms that guide AMs metabolism have remained elusive. We show that the natural killer (NK) cell-associated receptor, NKR-P1B, expressed on AMs plays a critical role in inducing AM metabolic programming. *Nkrp1b*$^{-/-}$ mice exhibit significant vulnerability to pneumococcal infections due to an age-dependent collapse in their AMs population. AMs derived from *Nkrp1b*$^{-/-}$ mice show abnormal rates of surfactant lipid uptake and dysregulated surfactant metabolism. We also find that an interaction between AMs expressed NKR-P1B, and type-II pneumocyte expressed Clr-g, provides a critical link required to induce and fine tune AMs metabolic profile, thus outlining the first example of a tissue-specific, receptor-ligand interaction acting as a determinant of AMs metabolism.

List of Abbreviations Used

2-NBDG	(2-(*N*-(7-Nitrobenz-2-oxa-1,3-diazol-4-yl)Amino)-2-Deoxyglucose)
2D12	Anti-NKR-P1B antibody
ABCA1	ATP-binding cassette transporter 1
ABCG1	ATP-binding cassette sub-family G member 1
ACK	Ammonium-Chloride-Potassium
AGPAT	1-Acylglycerol-3-Phosphate O-Acyltransferase
AKT	Protein kinase B
AM	Alveolar macrophage
AMJ-P1B	AMJ-C11 cell line expressing NKR-P1B
AMJ-EV	AMJ-C11 cell line with empty vector insert
AKR1B10	Aldo-keto reductase family 1 member B10
ANOVA	Analysis of variance
APO-E	Apolipoprotein E
ATCC	American type culture collection
ATP	Adenosine triphosphate
BACH	Transcription regulator protein BACH
BCL	B-cell lymphoma/leukemia 10
BCIP	(5-Bromo-4-chloro-3-indolyl phosphate)
BDCA2	Blood Dendritic Cell Antigen-2
BHLH	Basic helix-loop-helix
BrdU	Bromodeoxyuridine
C-Maf	V-maf musculoaponeurotic fibrosarcoma oncogene homolog
Ca^{2+}	Calcium ion
CARD9	Caspase recruitment domain-containing protein-9
CBD	Carbohydrate binding domain
CCR2	C-C chemokine receptor type 2
CD	Cluster of differentiation

CDS1	CDP-diacylglycerol synthase 1
CE	Cholesterol ester
CEBP	CCAAT/enhancer-binding protein
CFU	Colony forming units
CHAPS	3-{Dimethyl[3-(3α,7α,12α-trihydroxy-5β-cholan-24-amido)propyl]azaniumyl}propane-1-sulfonate
CLEC	C-type lectin receptor
CNK	Connector-enhancer of KSR protein
CRIg	V-set and immunoglobulin domain containing 4
CTLR/Clr	C-type lectin like receptor
CTLD	C-type lectin like domain
CYP27A1	Sterol 27-hydroxylase
CYP27A6	Cholesterol Transporter (no known alias)
DAMP	Damage associated molecular patterns
DAPI	4′,6-diamidino-2-phenylindole
DAG	Diacylglycerol kinase
DC	Dendritic Cell
DC-SIGN	Dendritic Cell-Specific Intercellular adhesion molecule-3-Grabbing Non- Integrin
DCL-1	DEC-205vassociated C-type lectin-1
DIG	Deoxygenin
DGKG	Diacylglycerol kinase gamma
DLL4	Delta-like 4
DMEM	Dulbecco's modified eagle medium
DNA	Deoxyribonucleic acid
DNGR-1	Dendritic cell NK lectin group receptor-1
DOK-1	Docking protein 1
DPPC	Dipalmitolphsophatidylcholine
DRAQ5	1, 5-bis{[2-(di-methylamino)ethyl]amino}-4, 8-dihydroxyanthracene-9, 10-dione

EDTA	Ethylenediaminetetraacetic acid
FA	Fatty acids
FABP5	Fatty acid binding protein 5
FACS	Flow assisted cell sorting
FC	Free cholesterol
FcR	Fragment crystallizable-receptor
Fosb	FBJ murine osteosarcoma viral oncogene homolog B
FLT3	fms like tyrosine kinase 3
FLM	Foetal liver monocytes
FMMA	Fort moonmouth influenza A virus
FSC	Forward scatter
Fyn	Proto-oncogene tyrosine-protein kinase Fyn
GATA6	GATA-binding factor 6
G-CMSF	Granulocyte-monocyte colony stimulation factor
GFP	Green fluorescent protein
GO	Gene ontology
H/E	Hematoxylin/eosin
HDL	High-density lipoprotein
HILPDA	Hypoxia Inducible Lipid Droplet Associated
HMG-CoA	3-hydroxy-3-methyl-glutaryl-coenzyme A reductase
HRP	Horse-raddish peroxidase
Hsp	Heat-shock protein
HLA	Human leukocyte antigen
IAV	Influenza A virus
ICAM	Intercellular adhesion molecule
ID	DNA-binding protein inhibitor
IFN	Interferon
IKK	IκB kinase

IL	Interleukin
IRES	Internal ribosome entry site
ITAM	immunoreceptor tyrosine-based activation motif
ITIM	immunoreceptor tyrosine-based inhibition motif
JNK	c-Jun N-terminal kinases
Ki67	Antigen KI-67
KIR	Killer-cell immunoglobulin-like receptor
KO	knockout
KSR-1	Kinase suppressor of Ras 1
LAL	lysosomal acid lipase
LCK	lymphocyte-specific protein tyrosine kinase
LDL	Low-density lipoprotein
LDLR	Low-density lipoprotein receptor
LIPA	Lipase A, Lysosomal Acid Type
LOX-1	Lectin-type oxidized LDL receptor 1
LLT1	Lectin-like transcript 1
LPCAT 2	Lysophosphatidylcholine Acyltransferase 2
LPS	Lipopolysaccharide
LSP-1	Lymphocyte-specific protein 1
Lyn	Tyrosine-protein kinase Lyn
LXR	Liver-x-receptor
M-CSF	Macrophage colony stimulating factor
mAb	Monoclonal antibody
MAFb	V-maf musculoaponeurotic fibrosarcoma oncogene homolog B
MAPK	Mitogen associated protein kinase
MAVS	Mitochondrial antiviral-signalling protein
MALT1	Mucosa-associated lymphoid tissue lymphoma translocation protein 1
MCL	Mycobacterial receptor

MCMV	Murine cytomegalovirus
MDR	Macrophage disappearance reaction
MFI	Mean fluorescence intensity
MHC	Multi-histocompatibility complex
MIC-A	MHC class I polypeptide–related sequence A
MICL	Macrophage inhibitory lectin
MINCLE	Macrophage inducible Ca^{2+}-dependent lectin receptor
MR	Mannose receptor
mTORC	Mammalian target of rapamycin
Myd88	Myeloid differentiation primary response 88
NBT	nitro blue tetrazolium
NCEH	Neutral Cholesterol Ester Hydrolase 1
NCR1	Natural cytotoxicity triggering receptor 1
NFAT	Nuclear factor of activated T-cells
NFκB	Nuclear factor kappa-light-chain-enhancer of activated B cells
NK	Natural killer
NKG	Natural Killer Group
NKR	Natural killer cell receptor
NKT	Natural killer T-cell
NOD	Nucleotide-binding oligomerization domain
NPC	NPC Intracellular Cholesterol Transporter
NTM	Sodium-Tris-Magnesium
OCT	Optimal cutting temperature compound
ORO	Oil-Red-O
PA	Phosphatidic acid
PAF	Platelet aggregation factor
PAP	Pulmonary alveolar proteinosis
PAS	Periodic-Acid Schiff

PBS	Phosphate buffered saline
PC	Phosphatidylcholine
PD-1	Programmed cell death protein 1
PD-L1	Programmed cell death ligand 1
PE	Phosphatidylehanolamine
PFA	Paraformaldehyde
PFU	Plaque forming units
PG	Phosphatidylglyecrol
PGE	Prostanglandin-E
PI	Phosphatidylinositol
PIK3cb	Phosphatidylinositol-4,5-bisphosphate 3-kinase
PLC	Phospholipase C
PLCB2	Phospholipase C Beta 2
PLD4	Phospholipase D family member 4
PLIN2	Perilipin 2
PLPP3	Phospholipid Phosphatase 3
PMSF	Phenylmethylsulfonyl fluoride
PNPLA2	Patatin-like phospholipase domain containing 2
PPARγ	Peroxisome proliferator-activated receptor γ
PSAP	Prosaposin
PU.1	Hematopoietic transcription factor PU.1
PVDF	Polyvinylidene fluoride
qPCR	Quantitative polymerase chain reaction
Raf-1	RAF proto-oncogene serine/threonine-protein kinase
Rara	Retinoic acid receptor α
Rarg	Retinoic acid receptor γ
Rasgrp4	Ras guanine nucleotide releasing protein 4
RIG	Retinoic acid-inducible gene 1-like

RNA	Ribonucleic acid
RNA-seq	RNA sequencing
RPMI	Roswell Park Memorial Institute Medium
Rras 2	Ras-related protein R-Ras2
Sirp- α	Signal regulatory protein α
PAMP	Pathogen associated molecular pattern
pDC	Plasmacytoid dendritic cell
PRR	Pattern recognition receptor
SAP130	Histone deacetylase complex subunit SAP130
SD	Standard deviation
SEM	Standard error of means
SERPINB6	Serpin Family B Member 6
SIGLEC-F	Sialic acid-binding immunoglobulin-type lectin F
SMAD	Mothers against decapentaplegic homolog
SHP	Src homology region 2 domain-containing phosphatase
SOCS-1	Suppressor of cytokine signalling 1
SP	Surfactant protein
SPI-C	Transcription factor Spi-C
SR-A1	Macrophage scavenger receptor 1
SR-B1	Scavenger receptor class B type 1
SSC	Saline sodium citrate
SSO	Sulfo-N-succinimidyl Oleate
STAT	signal transducer and activator of transcription
TEM	Transmission electron microscopy
TG	Triglycerides
Th	T-helper
TLR	Toll-like receptor
TMRE	Tetramethylrhodamine methyl ester perchlorate

TGF- β	Transforming growth factor- β
TRIF	TIR-domain-containing adapter-inducing interferon-β
TRAF	TNF receptor associated factors
VHL	Von-Hippel Lindau protein
WT	Wild-type
ZEB2	Zinc finger E-box-binding homeobox 2

ACKNOWLEDGMENTS

Firstly, I would like to thank my supervisor Dr. Andrew Makrigiannis. Thank you for taking a chance on me even when I did not know much about NK cells and *in vivo* models, many others did not take that chance. I hope that I made you proud with the work that we have done here despite the complications and setbacks and frustrations. Thank you for letting me be a part of your lab and for letting me pursue science.

I would like to thank the lab crew in Ottawa, where I first started before making the transition to Halifax. Your help, input, attitude, endless Tim's breaks and sushi lunches made me feel welcome and laid down the scientific background for the rest of my PhD tenure. Special thanks to Dr. Andrew Wight who made a several months long stop over in Halifax before moving on to Boston to help analyze RNA-seq data of all things.

Special shoutout and thanks goes to Dr. Mir Munir Rahim and Dr. Brendon Parsons. Your skill in managing students and day-to-day operations of the lab went above and beyond and I assure that all of us appreciate your guidance, motivation and incredibly broad insight into all things science. One day I hope I will be able to write as effectively and concisely as you Brendon, but I wouldn't bet on it. You guys were (are) the lieutenants of the lab, and this place would not be able to function as efficiently as it does without you and I salute you.

Thank you to all the current members of the Makrigiannis lab, Dr. Haggag Zein, Gayani Gamage and Daniel Medina Luna. Your spirit of camaraderie and cooperation really elevated my experience working in this lab. Special thanks to Daniel for procuring the cakes and party favors for lab members birthdays. It is always highly appreciated.

Thank you to my committee members Dr. David Hoskin, Dr. Jeannette Boudreau and Dr. Jean Marshall. Your input and support throughout this project really helped shape the direction and bring it to a successful conclusion. I appreciate all your help and insight.

Thanks to $ummer $ports for all the fun we had over the summers. Shutout to Tupper Mixer for all the shenanigans and for keeping the graduate student body sane every Friday.

Lastly, special shutout to Dr. Patrick Slaine and Aaron Woblistin for the fun times throughout and to Alexa Wilson for your love and support.

CHAPTER 1: INTRODUCTION

1.1 General classes of pattern recognition receptors

1.1.1 Pattern recognition receptors

Pattern recognition receptors or PRRs, are a group of highly conserved receptors capable of detecting a wide variety of carbohydrate, lipid, protein, and glycoprotein ligands[1]. Many of the molecular patterns recognized by PRRs tend to be pathogen-associated and in some cases host-associated as they are released into the extracellular matrix due to damage and inflammation[2]. The majority of PRRs can be divided into 2 categories based on their cellular localization, being either bound to the surface membrane or on endosomal vesicles. These can be broken down further into a further 4 major PRR families: Toll-like receptors (TLRs), C-type lectin receptors (CLRs and the related family C-type lectin-like receptors CTLRs), retinoic acid-inducible gene 1-like receptors- (RIG-I), and nucleotide-binding oligomerization domain receptors (NOD)[3] as seen in Fig.1.1.

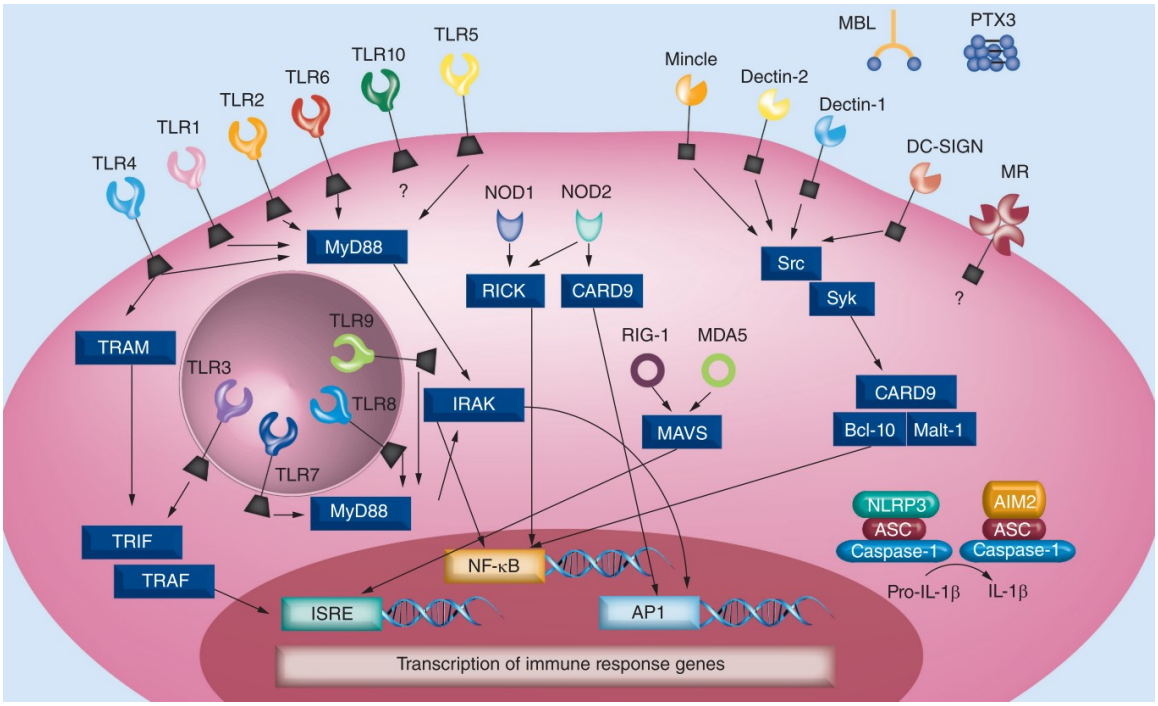

Figure 1.1: Known toll-like and rig-like receptors and their signalling pathways. The majority of toll-like receptors tend to be expressed on the cell surface where they can most easily interact with their classical bacterial/yeast-derived ligands. This is true for TLRs 1,2,4,5,6 and 11. These receptors signal primarily through Myd88 to achieve downstream NFκB activation and stimulation of immune cells. Intracellular TLRs, including TLRs 3,7,8, and 9 are found in endosomes where they are more likely to encounter their classical viral ligands. Intracellular TLRs signal primarily through Myd88. However, TLRs 3 and 4 have been experimentally shown to possess the ability to signal through a Myd88 independent signalling cascade which involves the activation of TRIF and/or TRAF to achieve immune activation. RIG and NOD-like receptors are found free in the cytoplasm of cells where they sample the intracellular environment for viral particles or damage-associated molecular patterns (DAMPs) respectively. Figure adapted from Jaeger et al, 2015[4]

There has been also widespread acceptance of another class of PRRs called absent in melanoma-2 (AIM2)-like receptors (ALRs). These receptors are present in most species, with bats being an interesting exception, and tend to be expressed primarily on macrophages and dendritic cells[5]. ALRs play a role in detecting cytosolic DNA through direct binding via their Hin domain and a protein-protein binding Pyrin domain. The end result being activation and modulation of cellular interferon responses[6].

Toll-like receptors were one of the first to be discovered with 10 functional receptors identified in humans including one pseudogene (TLR11)[7,8]. TLRs recognize a wide variety of pathogen-associated molecular patterns (PAMPs) with particular TLRs being specifically tailored to recognize one or two classes of PAMPs. Hence, TLR7/8 and TLR9, which are located in endosomal membranes are specific for single-stranded RNA and CpG DNA respectively, viral and bacterial components most likely encountered through viral entry into the cell or phagocytosis[7]. While TLR4, located on the cell surface is specific against lipopolysaccharide of Gram-negative bacteria which is where it is most likely to come into contact with bacterial cell membranes[7,9,10]. Upon activation of these receptors, signalling can proceed either through a Myd88-dependent or Myd88 independent mechanism to elicit an inflammatory response resulting in immune cell activation, cytokine secretion, and if possible activation of phagocytosis[11]. Conversely, RIG-I is a specialized receptor involved mainly in anti-viral defenses. It is especially proficient at binding double-stranded or single-stranded RNA, especially if no 5' cap is present, from many different viral families including rhabdoviruses and orthomyxoviruses among others[12]. The binding of RIG-I tends to result in the activation of anti-viral responses and secretion of antiviral proteins such as IFN-α in a MAVS-dependent manner[12]. Through this mechanism, RIG-I can behave like an early, viral detection protein and initiator of anti-viral responses that have managed to bypass the TLR-mediated system of viral nucleic acid detection, thus providing redundancy and a secondary viral detection mechanism for viruses that bypass or remain hidden within endosomes.

Similar to RIG-I receptors, NOD receptors and their close relatives NOD-like receptors (NLRs) are also specialized PRRs that intracellular pathogens including peptidoglycan motifs (N-acetylglucosamine) of Gram-positive bacteria and other ligands such as flagellin (NOD2) and viral single-stranded RNA (NLRB)[13]. Activating these receptors serves to engage anti-viral defenses and general cellular activation and cytokine secretion similar to RIG-I receptor and other PRRs[13]. However, some NLRs, specifically NALP3 which is a component of the inflammasome[14], can detect damage-associated molecular patterns (DAMPS) such as uric acid crystals found in gout sufferers[15] as well as silica dust and asbestos filaments[14] which irritate the lung epithelium and eventually results in epithelial destruction and DAMP release. All these receptors are evolutionarily well conserved and display a remarkable variety of different ligand-binding capacities which has resulted in a cellular repertoire of early detection systems that is large, varied, and usually accompanied by multiple redundancies. Nowhere is this more typified than in the last class of PRRs the C-type lectins and C-type lectin-like receptors, which demonstrate remarkable ligand binding capacity as well as signalling roles that go beyond simple immune activation.

1.1.2 C-type lectins (CLECs) function

The CLEC and CTLR families of receptors are the most evolutionarily diverse and numerous group of PRRs in the mammalian repertoire[16]. There have been several attempts to group this highly diverse receptor family into more manageable divisions with the most recent iteration resulting in the creation of 17 different sub-categories[17]. Owing to the family's large repertoire, covering them all is beyond the scope of this thesis, but certain categories warrant discussion and special attention: the various

collectins and selectins (which, respectively, bind to PAMPs to induce aggregation/opsonization and are responsible for cellular adhesion), the large variety of NK-cell related CLECs/CTLRs, and some unique proteins that nonetheless contain a CLEC domain, thus opening the door to some interesting protein-protein interactions and signalling possibilities. A non-exhaustive table of the 17 major families of CLECs as well as a representative member, its distribution and function can be found in table 1.1

#	Group name	Members	Distribution	Binding motifs and ligands
1	Lecitans/Hyalectins (Proteoglycans)	Aggrecan core protein (AGC1, CSPG1, Agc1)	Cartilage, ECM	carbohydrate recognition by CTLD
2	Type 2 receptors	Mincle Macrophage inducible C-type lectin (CLEC4E, CLECSF9)	cDC, monocytes, macrophages, B-cells, neutrophils, Kupffer cells	putative Ca2+-binding site 2 motif is present
3	Collectins	SP-D Pulmonary surfactant protein D (SFTPD, collectin-7, SFTP4, PSPD)	ECM, expressed by Clara, Type II, alveolar macrophages)	carbohydrate recognition by CTLD
4	Selectins	L-selectin (SELL, CD62L, LECAM-1, LAM-1, LYAM-1, Leu-8, TQ1, gp90-MEL, Ly22)	All leukocytes	CTLDs bind the carbohydrate
5	NK receptors	NKG2D Natural killer group receptor 2D (KLRK1, CD314)	NK cells, γδ, and CD8+ T cells	Non-Ca2+ binding
6	MMR family	MMR Macrophage mannose receptor (MRC1, CD206, CLEC13D, hMR)	MDDC, BMDC, M2 macrophages, iDC, mesangial cells, perivascular microglia, endothelial cells	No Ca2+ -binding site motif
7	Free CTLDs / Reg	REG2 Regenerating family member 1β (lithostathine-1-beta Reg1B, PSP-2, PTP, Reg2, Lithostathine-2, RegII,)	Secreted, β-cells	No Ca2+ -binding site motif
8	Type 1 receptors	Layilin (LAYN)	Epithelial cells, chondrocytes, synoviocytes	Ca2+-binding, although the motif is unusual (EPS)
9	Tetranectin family	Osteolectin Stem cell growth factor (CLEC11A, SCGF, LSLCL, p47, CLECSF3)	Secreted, osteoblasts, osteocytes, hypertrophic chondrocytes	Contain Ca2+ binding motif but not carbohydrate binding in CTLD
10	Polycystin family	Polycystin 1 Autosomal dominant polycystic kidney disease 1 protein (PC1, PKD1)	Renal cilia	Ca2+ and carbohydrate binding
11	Attractin family	Attractin (ATRN, DPPT-L, MGCA	T-cells, secreted	Unknown

		mahogany protein, Mg)		
12	CTLD/acidic neck	EMBP Eosinophil granule major basic protein (PRG2, BMPG, EMBP, MBP)	Eosinophils	Unknown
13	Type 1 CTLD /LDL containin protein	DiGeorge Syndrome Critical Region Gene 2 (DGCR2, IDD, Sez12)	Bone	No Ca2+ -binding site motif
14	Endosialin family	CD93 Complement component C1q receptor (C1QR1, MXRA4, Ly68, Aa4, C1aRp)	Endothelial cells, iDC, monocytes, macrophages plasma cells	Ca2+-binding, putative carbohydrate binding
15	Type I CTLD-containing protein	Bimlec (CD302)	fetal lung, liver, spleen and kidneys	Unknown
16	SEEC domain	Souble protein containing *SCP, EGF, E GF and CTLD domains (SEEC)*	Uncharacterized	CTLD has potential Ca-carbohydrate-binding motif (QPD)
17	Proteoglycans	FREM1 FRAS1-related extracellular matrix protein 1 (QBRICK)	ECM, expressed by epithelial and mesenchymal cells	No Ca2+ -binding site motif

Table 1.1 Non-exhaustive list of CLEC and CTLD members.

Table showing the 17 members of the CLEC and CTLR families with a representative member, its tissue distribution, ligands and binding motif(s). Table compiled from the works of both Brown, et al 2018[18] and Zelensky, et al 2005[17]

One of the main features distinguishing CLECs from the CTLRs is the requirement for calcium in ligand recognition. CLECs require a Ca^{2+} ion for efficient glycan-binding whereas CTLRs lack any type of ionic requirement for ligand recognition[19]. However, there exists significant overlap as to whether a receptor is a CLEC and CTLR as many of these receptors' binding domain structures have not been fully elucidated[20]. Therefore, receptors previously classified as CLECs or CTLRs continue to be reshuffled as more information is determined and this is shown in the literature where the same receptor may appear classified as both a CLEC and a CTLR depending on the time of publishing.

Due to CTLR's Ca^{2+} independence, they can recognize a large variety of ligands which includes lipids and protein on top of the canonical carbohydrate ligands via their unique carbohydrate-binding domains (CBD) which constitute the vast majority of CLEC

interactions[21]. The canonical, but not exclusive, role for both CLECs and CTLRs is to serve as PRRs on myeloid-derived immune cells to recognize various pathogen-associated molecular patterns (PAMPs) and initiate appropriate signalling cascades which can lead to immune activation[2]. Many of these receptors are classified as collectins and selectins but some fall outside of a specific classification scheme owing due either to the unique role they perform or their unique, cell-specific expression pattern.

Pertinent examples of CLECs, with TLRs as a reference PRR, listed in Fig1.2, include mannose receptor (CD206) which are present in most vertebrates and mainly, but not exclusively on macrophages. CD206 is mainly used to recognize mannose, fucose, and sulfate glycans residues present on bacterial membranes through multiple CTLDs to initiate immune responses[22]. Additionally, ovalbumin-antigen studies on mannose receptor-deficient mice have shown that lack of mannose receptor on DCs results in a lack of cross-presentation by DCs, while classical MHC-II presentation remains unimpaired[23]. The mechanism of mannose receptor influence on antigen presentation is not fully elucidated but these observations show that CLECs possess unique functional roles depending on cell type and context. DC-SIGN is a prototypical CLEC which enjoys wide distribution in mammals with several homologs identified[24]. It is expressed on macrophages and DCs, containing a single, calcium-containing CBD domain that functions primarily as a mannose receptor[25] that exclusively initiates phagocytosis. Demonstrating the variable function of CLECs depending on the context and ligand available, DC-SIGN has also been shown to act as an adhesion molecule through its binding of ICAM3[26]. MICL which is expressed primarily on monocytes, granulocytes and NK cells while enjoying wide mammalian distribution with orthologs in birds and

reptiles[27], is an interesting example. Since most CLECs have a role in binding pathogen-derived molecules MICL, appears to bind exclusively endogenous ligands[28], thus hinting at a potential immunomodulatory role for this receptor. Indeed, a later report has demonstrated that MICL plays a role in inhibiting innate immune responses and may also play a pivotal role in regulating runaway inflammation present during rheumatoid arthritis[29]. The fact this receptor plays such a prominent immunomodulatory role instead of the traditionally associated pro-inflammatory role of CLECs highlights the diversity not only of CLEC-ligand interactions but also of vastly different and complex roles CLECs play in immune homeostasis. Another intriguing example is the newly discovered receptor DCL-1 which was discovered within the DC-205 receptor locus as a perhaps alternate form of this receptor and is mostly expressed on myeloid cells with some NK expression[30]. The ligand for DCL-1 is unknown, yet it appears to play a role in endocytosis and cell-cell adhesion on macrophages[30], further demonstrating the varied

functions that CLECs can exhibit.

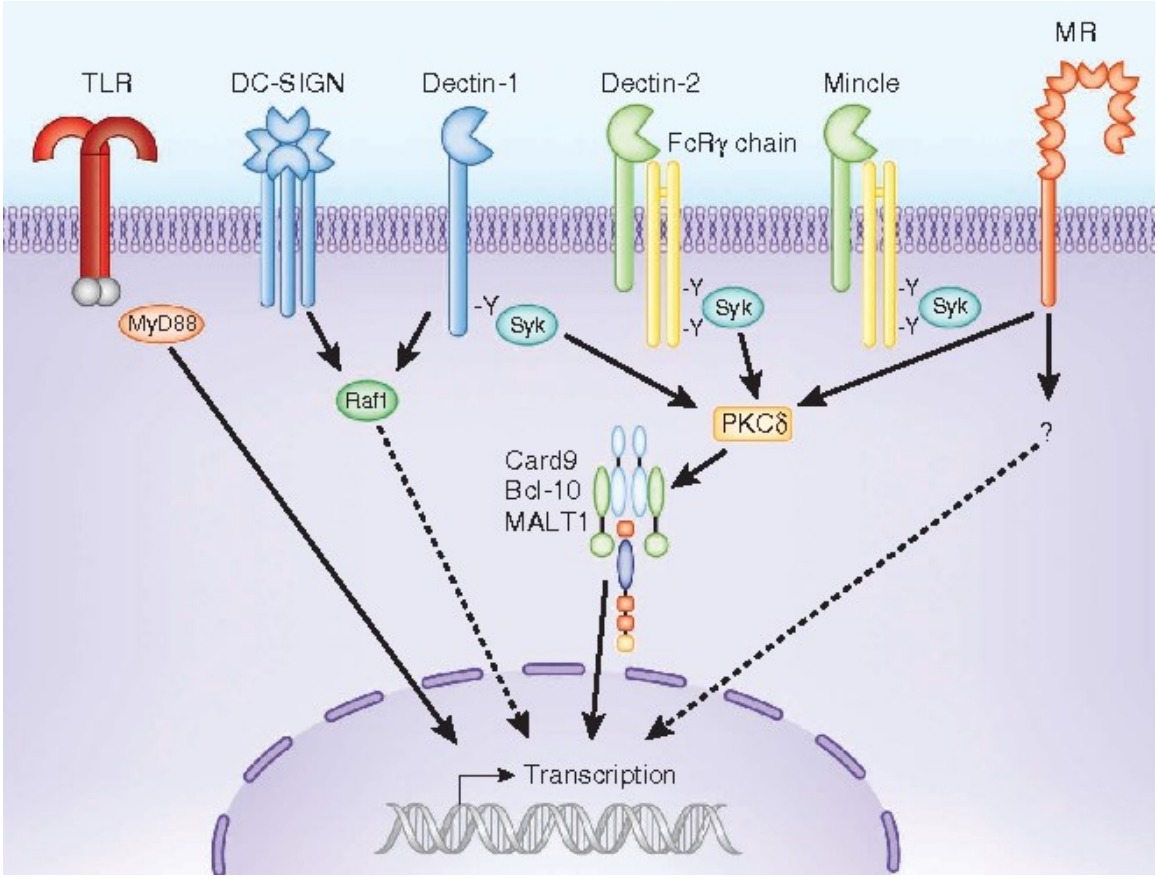

Figure 1.2: TLR and Well described CLECs and their signalling pathways. Extracellular TLRs which are PRRs and related to CLECs, work mainly through a MyD88 independent pathway and may act to synergize with other CLECs to promote cell activation. Dectin-1, Dectin-2, and MINCLE interact with Syk through ITAM (Y) motifs to induce activation of protein kinase Cδ which in turn activates the Card9, Bcl-10, and MALT1 complex which induces transcription of various pro-inflammatory mediators. It should be noted that while Dectin-1 possesses an ITAM, Dectin-2 and MINCLE require the use of the ITAM present on an FcRγ chain receptor, with which these two receptors dimerize to phosphorylate Syk. DC-Sign and Dectin-1 can also signal through the Raf1 pathway which modulates effects of TLR and other CLEC signalling, while the exact mechanism of mannose receptor (MR) signalling is not fully elucidated. Figure adapted from Hardison & Brown, 2012. [31]

1.1.3 CTLR function and non-canonical interactions

The CTLR family of receptors (Fig. 1.3), functionally Ca^{2+} independent, also comprises a wide array of signalling capable molecules with a large variety of ligand

specificities which can lead to a multitude of downstream effects based on the type of ligand and cell-type expression of receptors. Examples of some well-characterized CTLRs include DECTIN-1, expressed on myeloid cells and B-cells across higher order mammals and rodents, which responds to beta-glucans to mediate anti-fungal immunity[32]. DECTIN-1 in particular is a canonical CTLR example because it has a single CBD identical to DC-SIGN but contains no calcium ion and is more similar to NK-cell lectin receptors and other MHC-I binding proteins[33]. Other prototypical CTLRs include the LOX-1 receptor, expressed in most mammals and includes a human ortholog, is likewise present on macrophages and endothelial cells, serving mainly as a low-affinity receptor for oxidized-LDL and may play a role in atherosclerotic lesion formation[34]. The CTLR CLEC-2, a member of the DECTIN-1 superfamily conserved in most high order mammals, is mainly expressed on platelets and DCs whose only known ligand is podoplanin whose binding serves to activate platelets and promote aggregation[35]. Conversely, on DCs, CLEC-2 appears to work synergistically with LPS sensor TLR-4 to enhance the production of IL-10, suggesting a role in inflammation resolution towards the end stage of Gram-negative bacterial infection[36]. The above examples demonstrate the large variety in both ligand binding capacity and the consequences of such on the varied cell types expressing CTLRs. CLEC-1 has been confounding researchers for quite some time as it still has no known ligand and signalling remains poorly characterized despite being discovered more than a decade ago. It appears to be expressed on most myeloid cells and its expression is downregulated by inflammatory stimuli and upregulated by resolving cytokines, specifically TGF-β[37]. This receptor is also one of the few that is predominantly found intracellularly, adding further confusion as to its role and

ligand[38]. Although studies have shown that disruption of CLEC-1 appears to upregulate IL-12 secretion by DCs contributing to further exacerbation of Th1 responses[39,40].

Fig. 1.3 highlights some of the more well-characterized CTLRs and their respective ligands. It should also be noted that most CTLRs containing immunotyrosine activating motifs (ITAM) bearing domains or recruit adaptors which are able to then subsequently signal through their ITAM. Immunotyrosine inhibitory motifs (ITIM) containing CTLRs are in the minority and thus also fewer studies as noted by the lack of a defined ligand for DCIR and MICL. Most ITAMs contain a consensus sequence that is approximately defined as YXXL/I(X_{6-8})YXXL/I with X denoting any amino acid[41]. ITIMs, on the other hand, contain a consensus amino acid sequence that is usually denoted as (I/V/L/S)-X-Y-X-X-(L/V), with X representing any amino acid[42]. Usually dimerization[43] of signalling motif bearing receptors is required to achieve phosphorylation of the docking sites but that is not always the case. The mechanism of ITIM and ITAM signalling will be discussed, with examples, further below.

Outside of these classically defined ligands and functional roles, C-type lectin-like receptors have been known to bind several non-canonical ligands to produce cellular effects that go beyond simple immune activation. TLR-4 has been shown to induce the transition of macrophages into foam cells in an oxidized low-density lipoprotein mediated manner, thus showing its importance in atherosclerotic plaque formation and ability to influence macrophage metabolism[44]. Likewise, other studies have outlined the importance of the TLR-2, TLR-4 and CD36 axis in macrophage dysregulation leading to foam cells formation achieved by the binding of lipid species not normally associated with TLRs[44–46]. LOX-1, as discussed above, is expressed in significant amounts on

macrophages and tends to bind oxidized LDL in a low-affinity manner. However, DCs express low levels of LOX-1 as well, but in this context authors have found that it is also able to bind Hsp70 and promote antigenic cross-presentation on DCs[47], thus making it a potential target molecule for cancer therapies that rely on immunogenic cell death to spur anti-tumor responses. MINCLE (Clec4e), expressed on mammalian myeloid cells and possibly B-cells, presents a particularly interesting case because canonically associates with FcRγ to signal but it is also known to form heterodimers with MCL (Clec4d) to promote efficient phagocytosis and to synergistically increase ligand affinity of both receptors[48]. Likewise, MINCLE usually binds pathogen-derived glycolipids such as those present on the surface of mycobacterial membranes[49], but recent evidence has shown that it is able to bind a wide variety of other ligands including cholesterol sulfate[50] and products of cell death such as SAP130[51]. BDCA2 presents another puzzling case as it is present on human pDCs but lacks a mouse homolog[52]. The canonical ligands for BDCA2 include CpG DNA, similar to TLR-9, as well as galactose residues which happen to be preferentially expressed on many tumor cells[52,53]. However, a study has demonstrated that BDCA2 is able to bind glycan residues present on many immunoglobulin species, thus acting as an Fc receptor and a sink for antibodies in response to excess Ig presence in the bloodstream due to runaway inflammation.[54]

All of these factors demonstrate the flexible and highly complex nature of interactions between CLECs and CTLRs. The ability to bind ligands ranging from lipids, proteins, and glycoproteins plus the ability to form heterodimers provide these receptor families with a wide variety of cell type-dependent effects, which also translates into the

variable nature of CLEC and CTLR signalling.

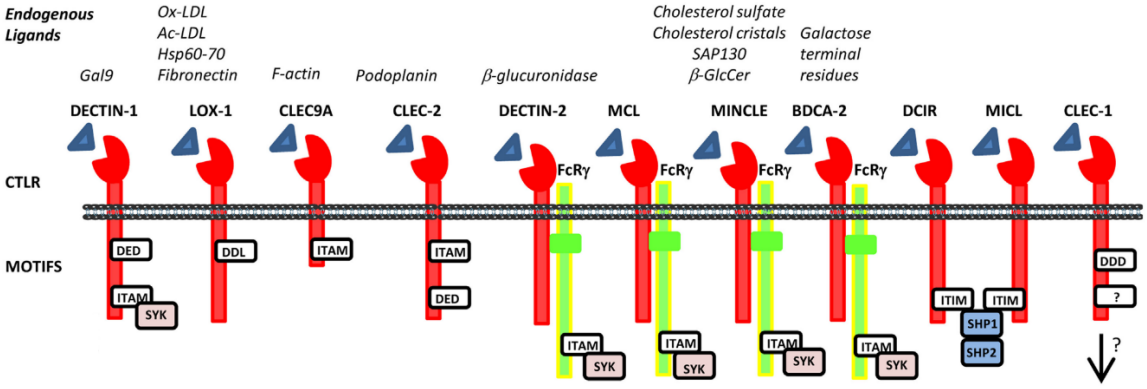

Figure 1.3: Various known C-type lectin-like receptors, their ligands, and known interacting partners.
Most CTLRs tend to be present on the surface of cells to interact with PAMPs such as carbohydrate residues unique to yeast and bacterial cells such as podoplanin, fibronectin and galactose. Some of them such as Dectin-1 and Clec-1 contain the tri-acidic domains DDD, DED respectively which are thought to play a role in phagocytosis and signal modulation of CTRLs and TLRs, specifically through Raf-1. For those receptors which contain an ITAM signalling is achieved through the recruitment of Syk kinase to allow for further NF-κB activation and signal transduction. Others such as MCL and Mincle, dimerize with FcRγ to take advantage of the ITAM present on the FcRγ receptor to initiate signalling cascades. This can be contrasted with MICL and DCIR, which bear ITIM domains on their cytoplasmic tails. These motifs have been known to recruit src-homology containing phosphatase ½ (SHP1/2). These phosphatases then play a role in signal modulation by dephosphorylating Syk or the further downstream activating factor NF-κB.. Figure adapted from Chiffoleau, 2018.[38]

1.1.4 CLEC and CTLR non-immune functions

On top of their immune function, CLECs and CTLRS have been observed to play a role in homeostasis and tissue maintenance. CLEC-2 has been implicated in the development of and maintenance of bone marrow hematopoietic stem cells[55]. The authors were able to positively link CLEC-2 expression on megakaryocytes to the secretion of thrombopoietin, thus providing an explanation for the gradual decline in hematopoietic stem cells observed in CLEC-2 deficient mice[55]. Surfactant proteins (SP-A, B, C and D),

a highly conserved group of 4 secreted CLEC proteins exclusive to the alveolar epithelium, possess critical roles not only in immune defense[56] but also in maintaining the coherence and other physical properties of pulmonary surfactant[57,58]. Without surfactant proteins maintaining the lipid/protein surfactant emulsion the respiration would not be possible. Another report has found that mannose receptor in tandem with asialoglycoprotein receptor are responsible for regulating circulating glycoprotein levels[59]. Mice double deficient for both of these CLECs showed elevated levels of thirty glycoproteins while females specifically showed retention of luteinizing hormone leading to complications with parturition[59]. Another good example of significant non-immune function among CLECs and CTLRs is CLEC-11a which is a secreted, calcium dependent glycoprotein conserved in primates and rodents[60]. CLEC-11a was found to promote osteogenesis both *in vitro* and *in vivo* and mice deficient in it suffered accelerated aging-related bone loss and reduced capacity to heal bone fractures[61].

Research on CLECs and CTLRs continues to show that these receptors can play much more subtle and intricate roles in an organism than simply immune function. Many of them appear to have a significant role in cell development, maintenance and homeostasis as well. This flexibility in function also coincides with their wide array and flexibility in signalling capabilities.

1.1.5 CLEC and CTLR signalling

As mentioned previously, CLECs and CTLRs possess ITAMs or ITIMs or are able to recruit effectors with signalling capabilities in order to exert their downstream functions. The vast majority of canonical CLEC signalling takes place via Syk recruitment to the ITAM, the ITAM being either incorporated into the receptor itself

(MINCLE) or borrowed from others such FcRγ,(Dectin-1) and producing a wide variety of downstream activating functions depending on ligand and cell type expressing the receptor[62]. This is in contrast to ITIM bearing CTLRs which tend to recruit SHP-1 and SHP-2 to their ITIM domains thus producing an inhibitory signal to suppress activation or cellular responses[63] (Fig 1.4). Outside of these canonical signalling pathways, CLECs and CTLRs display some unusual signal transduction mechanisms as well. DC-SIGN in particular offers a very intriguing case study as to the flexibility of CLEC/CTRL signalling since it does not possess any known signalling motifs; relying exclusively on a cascade of scaffolds and mediators to produce downstream effects. If DC-SIGN binds mannosylated ligands it will associate with the LSP1-KSR1-CNK signalling complex leading to Raf-1 activation and cellular activation and enhanced pro-inflammatory responses[64]. In contrast, the binding of fucosylated ligands causes the signal complex to fall apart leaving on LSP1 in association with DC-SIGN. This complex then recruits IKKε which causes repression of Bcl mediated TLR signalling and promotes secretion of anti-inflammatory cytokines and overall Th2 skewing of cell activation[65]. This mechanism of variable DC-SIGN signalling offers an insight into the flexibility and wide variety of signalling potential present in this receptor family class. Outside of these canonically defined signalling pathways, CLECs and CTLRs show remarkable variability in their signalling mechanisms (Fig 1.4), such as the ability of DECTIN-1 to preferentially recruit Raf-1 instead of Syk to order to drive non-canonical NF-κB signalling in helper T-cells[66], further demonstrating the flexible signalling characteristics of this receptor family.

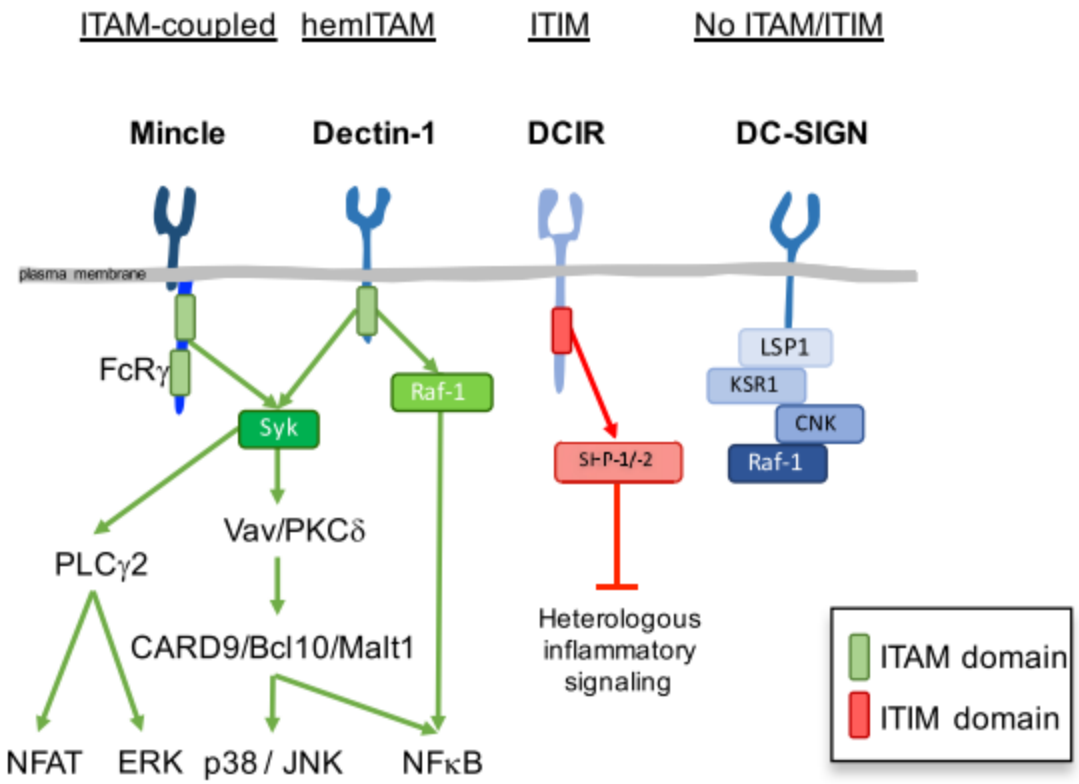

Figure 1.4: Canonical signalling pathways common to CLRs.
Most canonical CLEC/CTLR activating signalling involves dimerizing with FcRγ to utilize its tandem repeats for the recruitment of Syk. Activating CLECs/CTLRs rely on a hemi-ITAM on their cytoplasmic which, while shorter, is able to recruit Syk and initiate the downstream signalling cascade which culminates in activation of NFAT, NF-κB and P38/JNK signalling. ITIM bearing receptors such as DCIR recruit SHP-1/2 to inhibit and modulate activating signals and other pro-inflammatory cascades. Lastly, receptors such as DC-SIGN do not possess any intrinsic activating or inhibitory domains but through heterodimerizations with other receptors and interactions with differentially modified ligands, such as mannosylated versus fucosylated, can trigger downstream cascades that could be either activating or inhibitory. Figure adapted from del Fresno et al., 2018.[67]

As such, CLEC and CTLR signalling mechanics has been an active area of research and has shed light on the flexibility of these receptors to produce signalling events that appear to deviate from the norm and are in some cases even paradoxical (Fig 1.5). CLEC/CTLR signalling is influenced by not only the ligand but also whether homodimerization or heterodimerization occurs, which can have significant implications

for downstream signalling by potentially turning an ITAM bearing receptor responsible for an activating cascade into an inhibitory cascade. Such is the case of CLEC12A, where engagement with TLR-2 causes an inflammatory cascade[28] while engagement with CD40 causes an inhibitory cascade within dendritic cells[68]. Another good example would be the Dectin-2 and Dectin-3 heterodimer, the homodimers of which are known to associate with and recognize beta-glucans present in yeast cell walls[62]. Likewise, A recent report has demonstrated that the Dectin-2,3 heterodimer configuration is much more capable at recognizing and eliciting NF-kB mediated immune responses against *C. albicans* fungal infection than either homodimer alone[69].

Another intriguing example is the notion of the activating ITIM. Once again, CLEC12A (normally a suppressive receptor that controls sterile inflammation) has been found to enhance interferon responses controlled by RIG-I in response to viral infections[70]. The authors demonstrate that a bifurcation signalling event is responsible for this since the signalling effect was independent of SHP1/2 activation indicating the need for a different downstream kinase or phosphatase activation[70]. CLEC4A presents another intriguing example that contains an ITIM that functions in an activating manner by inducing type-I interferon secretion from DC cells upon binding of specific tuberculosis related ligands, hypothesizing that the ITIM may be acting as a molecular sink in this context, forcing SHP-1/2 to dock but not allowing them to exert downstream inhibitory functions.[71] Lastly, Ly49Q, an ITIM bearing receptor usually associated with natural killer cell inhibition, has been found to paradoxically induce IFNα secretion by pDCs[72,73]. The mechanism for this non-canonical signalling is currently unknown but is thought that

perhaps that it may act in an activating manner in the presence of TLR-7 and TLR-9 agonists or may be working in conjunction with DAP-12[72].

This flexibility can be further exemplified by a CLEC signalling phenomenon referred to as non-activating hemiITAM signalling, since it does not require dimerization and allows for the binding of only a single phosphor-kinase protein. This is best exemplified through the function of DNGR-1, whose hemiITAM can potentiate cross-presentation by $CD11^+$ DCs to T-cells[74] as well as priming $CD8^+$ T-cell memory responses[75] but it not involved in any classically defined inflammatory cascade that CLECs and CTLRs are known for (NFAT or NFκB activation). Other reports have shown that hemiITAM, Syk-mediated signalling of Dectin-1 in response to fungal pathogens can be modified through the specific cellular localization of Dectin-1 isoforms[76]. This represents another avenue for control of CLEC signalling depending on the location of the particular isoform of the receptor.

As the previously discussed phenomenon of an activating ITIM signalling pathway there have been reports published which highlighted the ability of an ITAM to act in a paradoxically inhibitory manner. A classic example of this notion is MINCLE which usually participates in activating immune signalling cascades through Syk upon stimulation. Yet, it has been found that under certain conditions of low-affinity ligand binding to *Leishmania* antigens, MINCLE can assume an inhibitory ITAM conformation which allows for transient Syk binding thus resulting in SHP-1 recruitment and a dampening of what would normally be an activating immune response[77]. A similar SHP-1-dependent response has been shown involving the mannose receptor. Upon binding of *m. tuberculosis* to MR couple to FcRγ, SHP-1 is recruited to the phagosome where it

inhibits degradation of the bacterium and thus allowing it to proliferate inside the macrophage[78].

Taken together, the C-type lectin-like family of receptors demonstrates that the varied expression of these receptors coincides with their significantly varied functionality. The ability of these receptors to promiscuously bind different ligands, form non-canonical hetero or homodimers, and to induce contradictory signalling such as activating cascades through ITIMs or inhibiting cascades through ITAMs, makes this family of receptors an important and particularly difficult area to investigate.

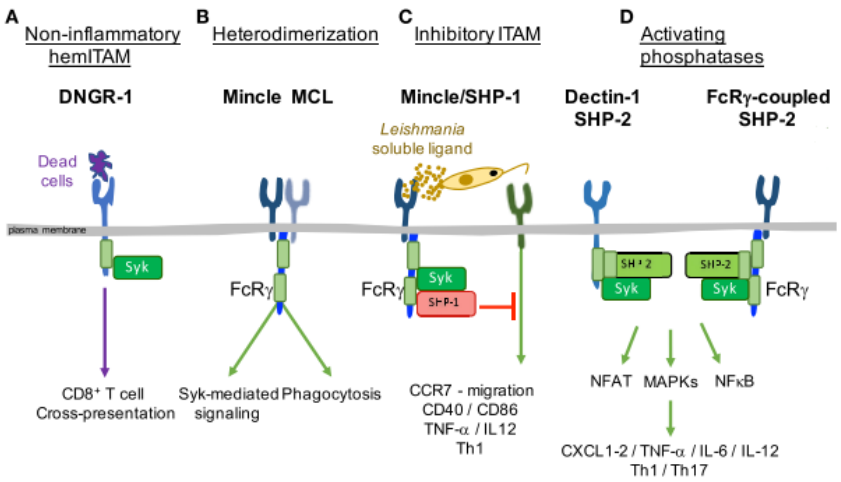

Figure 1.5: Non-canonical and alternative CLEC/CTLR signalling mechanisms. (A) DNGR-1, closely related to Dectin-1, has subtle mutations in the Syk binding domain which allow it to detect and internalize dead cells and potentiate cross-presentation but fail to upregulate inflammatory cytokine secretion. (B) Receptors such as MINCLE and MCL form heterodimers which increase the affinity for their shared fungal ligand and increase rates of internalization. (C) Binding of a soluble leishmania ligand in a low-affinity fashion produces a hypophosphorylated ITAM which preferentially recruits SHP1/2 and is used to modulate signalling from other receptors. Varying ligand avidity and affinity may play a role in immune homeostasis. (D) SHP-2 has been shown to act as a scaffold for the recruitment of kinases such as Syk which then enable downstream activation signalling, thus resulting in situation where a traditionally defined inhibitory phosphatase acts as a facilitator for activating signalling. Figure adapted from del Fresno et al., 2018 [67]

1.2 NK cell receptors

A very closely CLEC-related family are NK cell receptors. Unlike T-cells, NK cells do not undergo receptor recombination instead of having all of their receptors hard-coded into the genome in what has been termed the NK-gene locus[79]. Thus, to make up for the lack of recombination capacity, the NK cell receptor repertoire is large and composed of several different families of related receptors which all contribute to NK-cell functioning. NK cells operate on a balance of input signals received from their various surface receptors as they interact with the target cell. The net summary of these interactions determines whether an NK-cell will engage the target cell or whether it will move on to find a different target[80]. In mice, these receptors can be classified into families such as the Ly49s, NKG2s and NKR-P1s[81,82] (Fig 1.6). Many of these receptors, including the NKR-P1 and Clr family fall into the C-type lectin like receptor class, which along with the canonical CLECs discussed previously form a large and diverse family of receptors present mostly on immune cells and that carry out a wide array of immunological function as demonstrated in the preceding sections.

Some of the more notable receptors in the NK family of CLECs include the Ly49 family which serves as the mouse homolog for the well-known KIR family of proteins[83,84]. The Ly49 family of receptors performs a similar immunosurveillance function to KIRs[85], but also has a role to play in NK cell education[86] as well as NK cell memory formation[87]. Other well-known members of the NK gene cluster are the receptors of the NKG2 family. These receptors function by binding to stress ligands and other proteins expressed on the surface of target cells which may be undergoing

cancerous transformation or an active viral infection. The majority of these receptors tend to be activating, such as NKG2C and NKG2D[84]. NKG2D, for example, interacts with ligands like MIC-A and MIC-B, that are upregulated in stressed cells such as those undergoing transformation or viral infection[88]. NKG2A, is an example of an inhibitory NKG2 family receptor, and it tends to bind to HLA-E on humans and Qa-1^{b} on mice in what is thought to be analogous to other NK-cell inhibitory interactions[89]. Lastly, and most intriguingly, surfactant proteins A and D, part of the collectin family of CLECs and present in pulmonary surfactant, are also known to contain CLEC domains[90] and have well-characterized signalling and immunological functions.

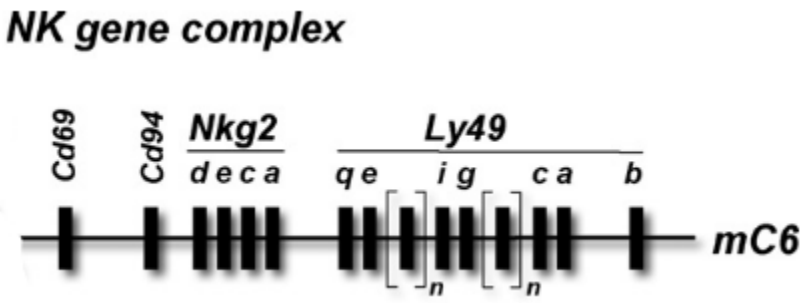

Figure 1.6: Partial Model of the NK gene complex.
Relative spaced model of the NK gene complex showing the major family member in centromeric order as seen on chromosome 6. Brackets indicate a gene product with known no known function and no assigned name. Figure adapted from Carlyle et al. 2008 [81]

1.2.1 NKRP1 and Clr receptor/ligand family

Turning now to the last major NK-cell receptor family, the NKR-P1s, this family of receptors and ligands possess some unique and interesting qualities. They are located in the NK gene complex along with the other NK-cell receptors discussed previously but the NKR-P1 receptors are inherited together with their ligands on one single locus[82] (Fig

1.7). These receptors tend to form homodimers and are classified officially as class II transmembrane C-type lectin-like receptors[91,92]. Another unique feature of the NKR-P1 family is that while the receptors are considered to be C-type lectin-like receptors their ligands (the Clr proteins) are C-type lectin related proteins[93] which opens up interesting possibilities regarding binding capability between CTLRs as well as to their potential function. Conservation of this family is evidenced in its presence among mice, rats, dogs, cattle, and humans, indicating that this gene family plays a significant role in immune functioning[83].

Among rodents, the locus itself is composed of the NKR-P1 receptors A, G, C, B/D, F, and the pseudogene E as well as the Clr ligands h, f, g, d, c, a, and b with Clr i, e, and j representing known pseudogenes which have now lost functionality.

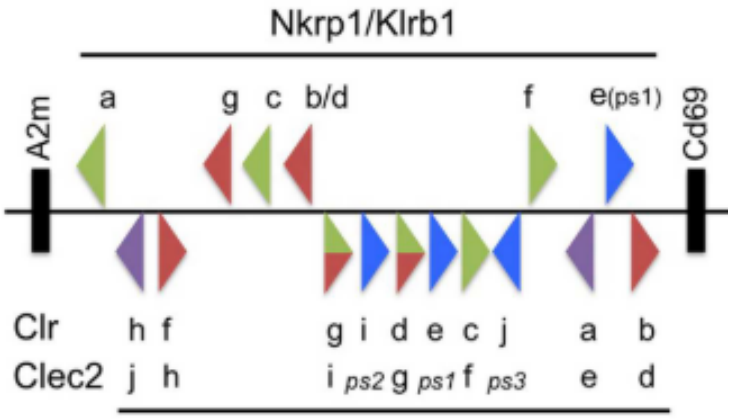

Figure 1.7: Graphical depiction of the NKRP1 gene locus.
All known NKR-P1 and Clr family members in centromeric sequence as seen on chromosome 6. Triangles depict the direction of orientation of the gene and color depicts their known function as follows: activating (green), inhibitory (red), half green/half red (bifunctional), pseudogene (blue), unknown function (purple). Figure adapted from Carlyle & Kirkham, 2014. [82]

While the receptor family shows good conservation among rodents, so far only one human homolog of the NKR-P1 family has been identified. Specifically, the interacting partners NKR-P1B/D and Clr-b, identified and described in mice, has been characterized in humans as well and given the name of NKR-P1A (CD161) [94]for the receptor and LLT1 for the ligand[83,95]. The receptor being expressed on almost all NK cells and a subset of $CD3^+$ T-cells, however this does not rule out the presence and function of other NKR-P1 receptors in humans[96].

Structurally, these molecules have been shown to interact with other proteins[82] but can also recognize high weight carbohydrates in a Ca^{2+} independent manner[97]. The NKR-P1 family is thought to exist primarily as homodimers as has been demonstrated with NKR-P1B and Clr-b, however, heterodimeric structures are theoretically possible as well[98]. Interestingly, the human NKR-P1A and CLEC9A, appears to be most structurally related to the mouse NKR-P1B, which may present an opportunity for direct translational research[99]. Significantly less is known about the mouse Clr and human LLT1 proteins in terms of structure and composition with some evidence pointing to a similarity between LLT1 and CD69[100]. However, a recent study analyzed the crystalized structure of NKR-P1B bound to Clr-b (Fig. 1.8). The study has determined that optimal binding affinity is achieved through an NKR-P1B dimer interacting with two Clr-b homodimers in order to achieve optimal avidity[101]. Likewise, uncovering these crystal structures provides additional evidence of the likeness between NKR-P1B and human NKR-P1A as well as the high homology and conservation between Clr-b and Clr-g[101] which could imply the possibility of potential alternative binding partners for NKR-P1B.

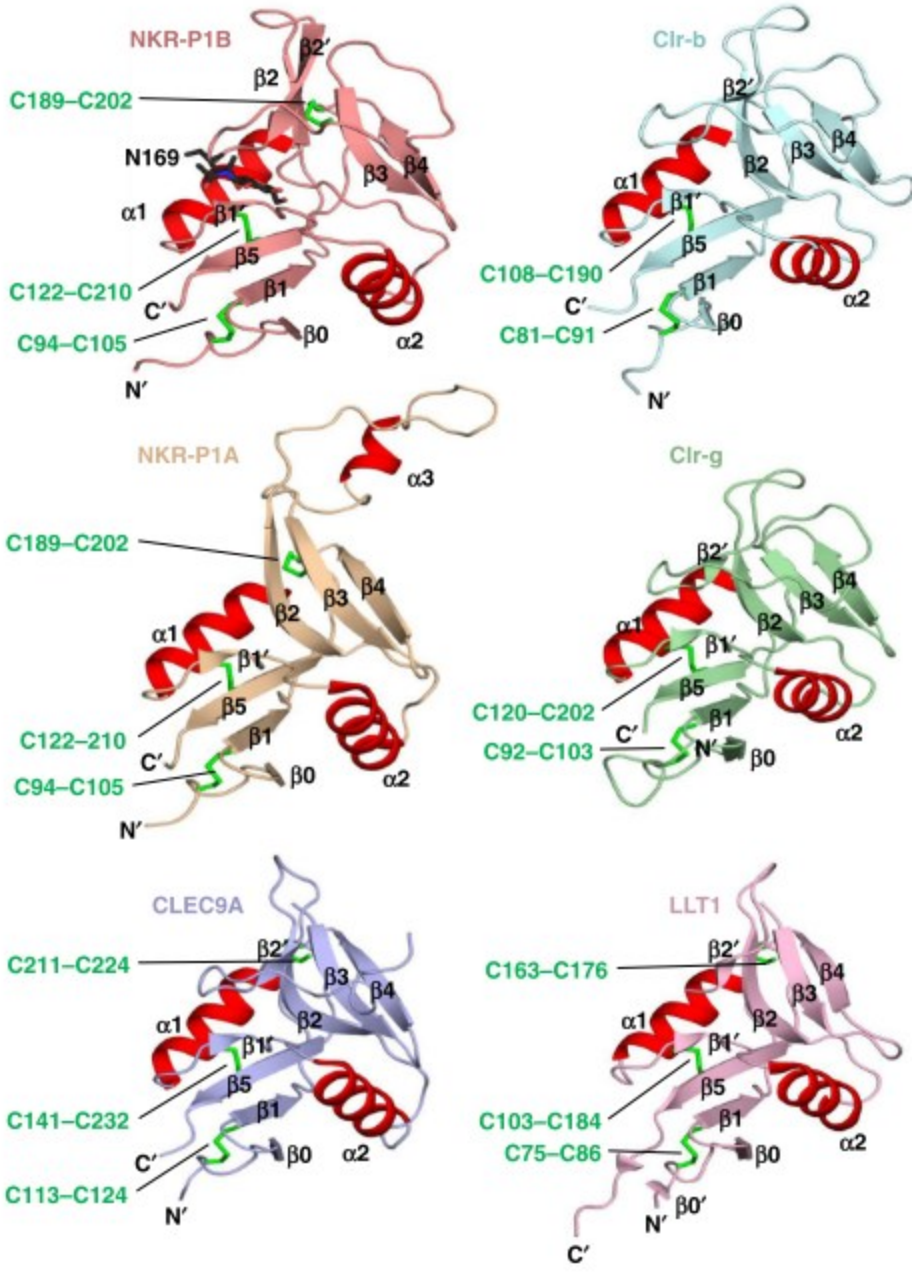

Figure 1.8: C-type lectin domain fold crystal (CTLD) structure of NKR-P1B/Clr-b. Comparisons between CTLDs of NKR-P1B:Clr-b and closely related molecules such as the human NKR-P1A and mouse Clr-g. α-helices are in red and disulfide bonds depicted as green sticks. Crystal structures show striking conservation of CTLD features between NKR-P1B:Clr-b and NKR-P1A and Clr-g [101].

1.2.2 NKRP1 and cell signalling and function

Similar to Ly49s and NKG2D, the NKR-P1 family contains receptors that can exhibit either an inhibitory or an activating effect upon the NK cell. As mentioned previously, the NKR-P1s are C-type lectin-like molecules that bind other proteins as well as long-chain carbohydrates[97]. Likewise, the structural similarities between the NKR-P1 family of receptors as well as their Clr ligands suggest that there is significant potential for cross-reactivity and promiscuity between receptor-ligand pairs. Based on experiments elucidating the roles of NKR-P1s and Clr binding upon NK-cell physiology, evidence has shown that there are several activating members of the NKR-P1s, including NKR-P1A, C, and F, which stimulate NK cell cytotoxic immune responses, and NKR-P1B/D, and G, which inhibit NK cell responses[81,98,102,103]. Further experimentation has revealed that NKR-P1F, as well as NKR-P1G, have several interacting partners, Clr-c, -d and -g for NKR-P1F and Clr-d, -g and -f for NKR-P1G[93,104] (Fig 1.9). However, the interacting partners of NKR-P1A, NKR-P1C as well as Clr-a and Clr-h are currently unknown.

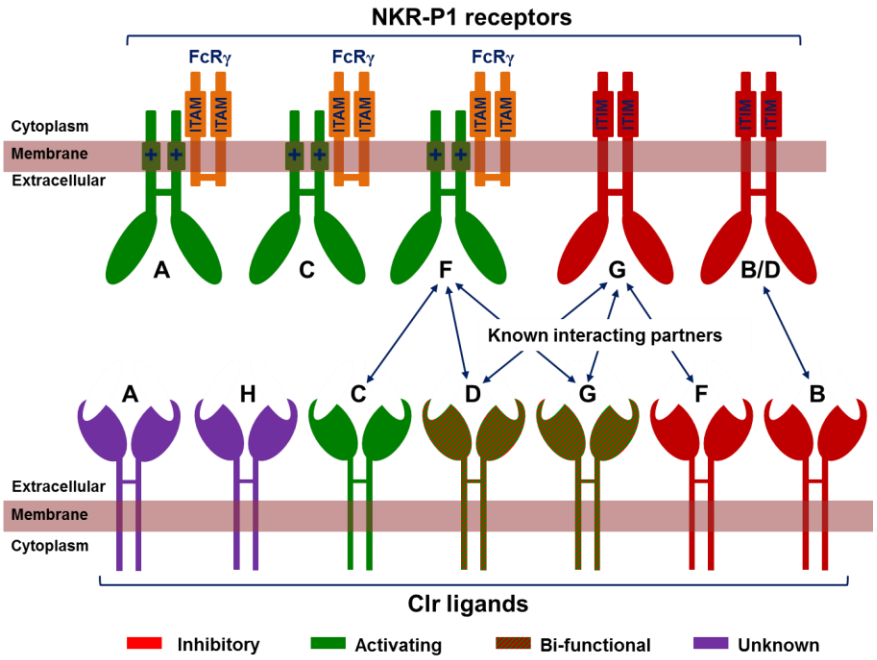

Figure 1.9: Schematic showing NKR-P1 receptors, Clr-ligands, their interaction and known signalling mechanisms.
Schematic showing known interactions between NKRP1 and Clr family members. NKR-P1F and G have several interacting partners (Clr c, d, and g and Clr d, g and f respectively), NKR-P1B has been shown to interact with only Clr-b. Whereas NKR-P1A and C have no described interactions. All known activating NKR-P1 members signal through dimerization with FcRγ to exert their activating effects, whereas the inhibitory NKR-P1G and B/D contain integrated ITIM domains in their cytoplasmic tail and likely exert their inhibitory effects through recruitment of SHP-1.

Mechanisms of signalling through the NKR-P1 receptors have been slowly elucidated over time. The activating receptors, appear to follow a canonical FcRγ receptor-mediated ITAM signalling path. For example, NKR-P1C was experimentally demonstrated to require FcRγ binding in order to promote the secretion of IFNγ in stimulated NK and NKT-cells[105,106]. All of the activating NKR-P1 receptors contain residues specifically required for FcRγ association as opposed to DAP12 association as well as the presence of an Lck and PLCγ recruitment motif designated (CxCPR/H) and

(YxxL) respectively[107] which is quite similar to the CD4 and CD8 T-cell co-receptor. NKR-P1C was experimentally verified through co-immunoprecipitation to recruit lck in a fashion similar to the T-cell co-receptor[108]. The NKR-P1F receptor, however, while retaining the sequences necessary to recruit the FcRγ receptor appears to be missing the canonical YxxL recruitment motif which may relegate it to a more co-stimulatory role as opposed to directly stimulating[93]. In general, FcRγ phosphorylation of activating NKR-P1s leads to downstream signalling through the recruitment of Syk and further signal transduction into the cell[109].

Conversely, both NKR-P1G and NKR-P1B both contain a consensus ITIM motif designated as ΦxYxxΦ[110,111]. In the context of NKR-P1B, this ITIM motif has been shown to recruit SHP-1 in NK cells when stimulated with pervanadate[92] to begin a downstream signalling cascade. NKR-P1G also appears to contain this canonical motif but lacks the recruitment sequence for lck[93], implying that perhaps it requires a costimulatory molecule or a co-receptor for optimal functioning.

This is in contrast to the human NKR-P1A which contains neither a canonical ITIM nor an lck recruitment motif but appears to have a non-canonical motif (AxYxxL) that has the theoretical potential to function as a weak ITIM[112]. CD161 has also been co-immuno-precipitated with complexes of lck, Fyn and Lyn, at least in the context of NK-cells[113]. Figure 1.10 illustrates the ITIMs and ITAMs, transmembrane domain, the CxCP Src kinase binding domain and the amino acid differences between inhibitory and activating NKR-P1 family members, highlighting their cellular signalling potential.

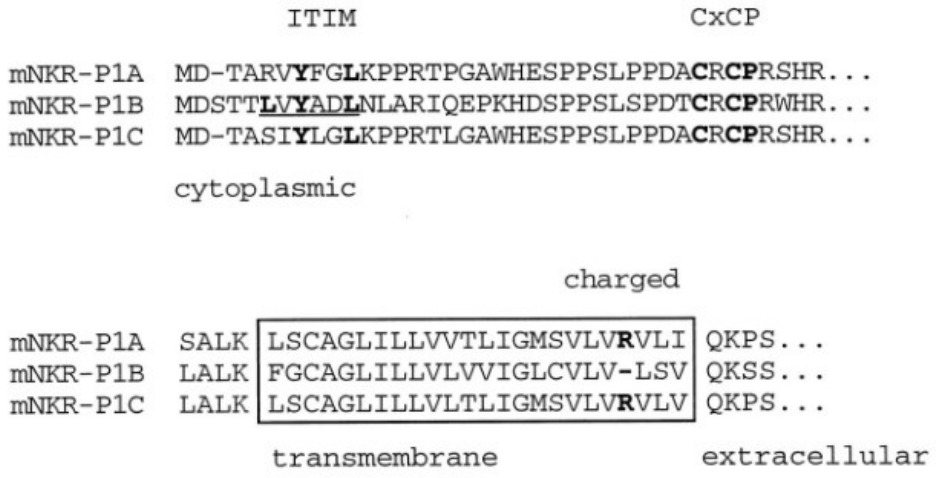

Figure 1.10: NKR-P1B locus amino acid sequence. Amino acid sequences of NKR-P1B, A and C highlighting the ITIM domain, CxCP Src binding domain as well as the charged transmembrane portion of the receptor. Adapted from Carlyle et al, 1999[92].

Progress on uncovering the detailed mechanism of action of these receptors as well as potential binding partners have been slow. This has been compounded by a lack of antibodies against the NKR-P1s or the Clrs, scarcity of mouse knockout models, and high potential for glycosylation[82,114], all of which make reaching definitive conclusions difficult. Nonetheless, some very interesting work has been done to reveal the function and binding interactions of both the NKR-P1 receptors as well as their Clr ligands.

1.2.3 NKR-P1 non-canonical function

The role of NKR-P1 receptors is for the most well defined in the context of NK-cells, since their presence was first detected on this cell type at the time of their initial discovery. Likewise, while we know that NKR-P1B sends an inhibitory signal into the NK-cell, the ubiquitous expression of its ligand Clr-b means that this receptor-ligand pair is part of a larger system. This system acts as an MHC-I independent recognition system that protects cells from NK cell-mediated cytotoxic responses as has been demonstrated

by our group and others when examining the interaction between Clr-b deficient target cells and NKR-P1B expressing NK cells[81,115,116]. A recent report has also demonstrated overexpression of LLT1 on human prostate cancer, likely a result of a mutation that serves to evade detection by NK cells by inhibiting NK activity through NKR-P1A[117]. This evidence serves to demonstrate the functional homology as a non-MHC-I method of immune surveillance, thus prompting the possibility of functional conservation between mice in humans in other aspects of the NKR-P1 and Clr family of interacting proteins.

However, the presence of some of NKR-P1 and Clr family of receptors and ligands has been documented on other cell types as well where they can possess significantly different functionality. For example, a study has shown that NKR-P1F signalling through DCs and B-cells plays a role in T-cell co-stimulation via Clr-g, resulting in T-cell expansion and IL-2 secretion[118]. Other reports have demonstrated the presence of NKR-P1G on $CD103^+$ DCs in the intestinal epithelium[119]. In this context, it is thought that the NKR-P1G receptor in tandem with its cognate ligand Clr-f, expressed almost exclusively on intestinal epithelial cells, acts as a method of immunosurveillance[119].

As obscure and unexplored as the NKR-P1 receptor family is, even less is known about the Clr family of ligands which in some circumstances can have unique distribution patterns and signalling functions of their own. For example, Clr-b and Clr-g expression are fairly ubiquitous, being present on most hematopoietic cells[100,120] to some extent and present at varying levels in many epithelial cells with the potential for induced expression under certain conditions such as MCMV infection and kidney reperfusion stress[100,120,121]. Several Clr-family members also have described roles in contexts other than NK cells. For example, the expression of Clr-a on the gut epithelium and its role in mediating

immune tolerance towards gut microbiota in conjunction with gut expressed Clr-f which is most likely also responsible for immune tolerance and gut immunosurveillance[119,122]. Other Clrs appear to have a more in-depth role in controlling cellular processes and differentiation, which sets up an important precedent for the discoveries being described in this work. For example, Clr-b has been to show inhibit osteoclast formation *in vitro* and *in vivo* Clr-b deficient mice appeared to exhibit an aberrant number of osteoclasts resulting in increased bone resorption and lack of bone formation leading to sub-average bone mass in these mice[123]. Further evidence of this is provided through genetic studies in human populations that contain a N19K substitution in the homologous LLT1 transcript. This LLT1 mutation was implicated in the increased loss of bone density in postmenopausal women compared to women expressing the normal LLT1 transcript[124]. Likewise, the mouse NKRP1:-Clr system has been described as a non-MHCI recognition system in mice and it appears to play a similar role in humans, but reports have also described some non-canonical functioning as well. Activation of NKR-P1A (CD161) in human in T-cells appears to inhibit T-cell cytotoxicity, in line with the potential of ITIM signalling, but also paradoxically induces proliferation[114].

Evidence has steadily been mounting which supports the notion of the NKRP1 and Clr family of receptor-ligands being expressed on other cell types and having potentially unique and varied cell-specific functions. This is of course not restricted to the NKRP1-Clr family. Previous sections have outlined the varied roles that NKG2 and Ly49 receptor family members can play on different cell types. The following study presented here continues with this trend and aims to examine the role NKR-P1B plays in steady-state functioning of immune cells to determine whether it exhibits any homeostatic or

developmental roles outside of its known role of inhibiting NK cell-mediated lysis. Since we report the presence and tissue-specific function of NKR-P1B on tissue-resident alveolar macrophages, this warrants a more in-depth discussion into the alveolar macrophages themselves.

1.3 Tissue-resident macrophages

1.3.1 Macrophage origins and tissue-resident functions

The innate component of the mammalian immune system is composed of several highly specialized subtypes of macrophages that perform unique tissue-specific roles. Over the past decade a great body of new innate immunity research has modified our understanding of the mononuclear phagocyte system to such a degree that significant revisions have been produced with respect to what monocytes, macrophages, and dendritic cells (DCs) are and the way their respective populations develop. New evidence has emerged which shows that macrophages are not simply terminally differentiated circulating monocytes but that they form unique populations which are distinct not only from monocytes but from other macrophages as well, all depending on their location[125,126]. This has given rise to a new concept termed tissue residency. Wherein macrophages residing in particular organs form unique, tissue-resident populations which are modified from the standard monocyte derived macrophage phenotype into a macrophage that possesses unique characteristics tailored specifically to their tissue of residence. Recent research has shown that many organs are seeded by fetal liver monocytes as is the case in the lungs[127], yolk sac macrophage precursors as is the case in the brain[128,129] or a combination of both as appears to be the case in the liver and the

heart[130,131] (Fig1.11).

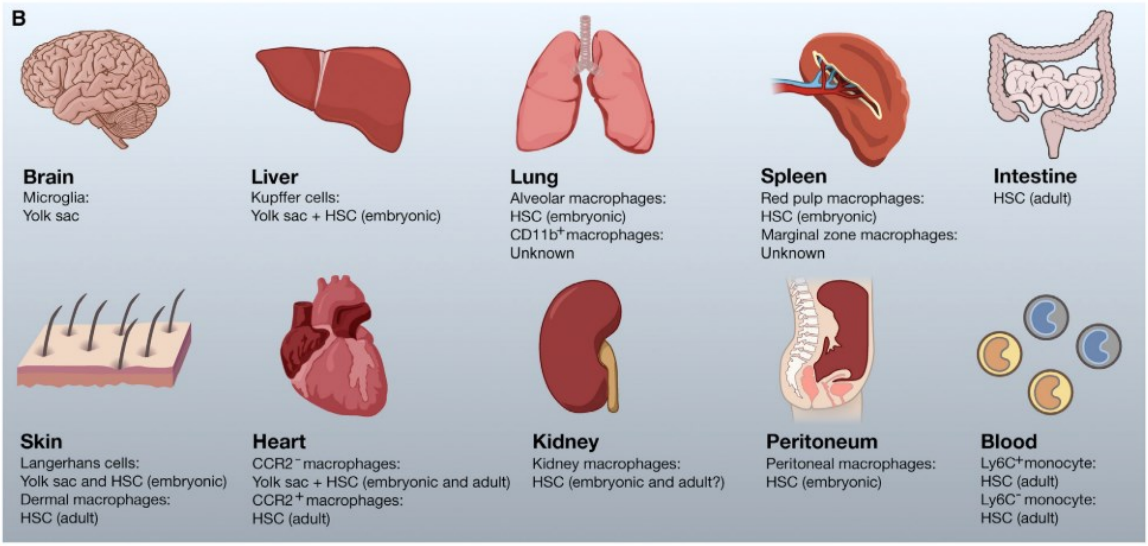

Figure 1.11: Resident macrophage ontogeny of various organs and tissues. Schematic highlighting the different ontogenies that make up the resident alveolar macrophage population for a particular tissue. In this sense, HSC populations have been split into two categories: (embryonic), which includes fetal liver monocytes and yolk sac macrophages but with no evidence implicating either directly, and (adult) which have passed through the $FLT3^+$ stage and are continuously replenished from the peripheral blood monocyte pool. Figure adapted from Epelman et al., 2014 [125]

Skin (Langerhans cells) and alveolar macrophages undergo an interesting transformation as the organism ages. While the embryonic cells do give rise to a persisting adult population of tissue-resident macrophages, over time peripheral blood monocytes to seem to play a more larger role in replenishing Langerhans and AM cell numbers, macrophages of peripheral blood monocyte origin have been found in these two populations as the organism ages, implying a time-dependent failure of resident macrophage replenishment possibly due to cell senescence[132,133]. This process of embryonic tissue seeding, and differentiation can best be explained as an intricate interplay between two pioneer populations of yolk-sac and fetal liver-derived macrophages which compete for niches to colonize. (Fig. 1.12).

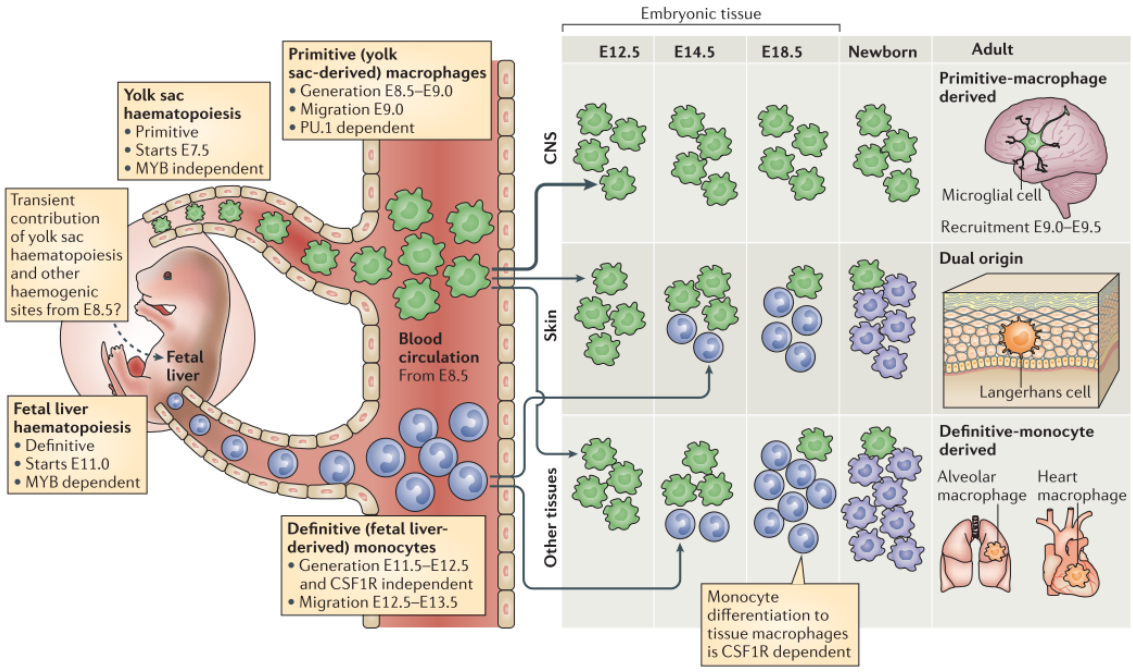

Figure 1.12: Development of tissue-resident macrophages from precursor populations.

The yolk sac and other early embryonic sites of hematopoesis give rise to primitive macrophages which in turn go on to colonize the entire embryo starting from ~E8 and ending this first wave of colonization at roughly E10. Simultaneously at roughly E10.5, HSCs produced aorta-gonads-mesonephros region develop which then go on to colonize the fetal liver. Fetal liver hematopoiesis into monocytes begins in earnest between E11.5-12.5 followed by migration and colonization of macrophage niches that were previously first colonized by yolk-sac precursors starts at around E13.5-14.5. The dashed line indicates the possibility of yolk-sac precursors colonizing the liver monocyte niche and contributing to their development but the evidence of this is still unclear. After the colonization of the various niches by fetal liver monocytes, they proceed to outcompete the yolk-sac precursor macrophages to varying degrees. Fetal liver monocytes make up the entirety of the lung and heart resident macrophage compartment. Langerhans cells, by contrast, can trace their lineage to fetal liver monocytes but retain a yolk-sac precursor derived minority into adulthood. Microglia, on the other hand, are completely derived from the yolk sac with no input from the liver monocytes whatsoever. These findings demonstrate the variety of origins of tissue-resident macrophages and the different population dynamics at a steady-state between the various organs and tissues. Figure adapted from Ginhoux & Sung, 2014. [134]

These fetal monocytes or yolk sac precursors then proceed to mature into fully-fledged tissue-resident macrophages with unique tissue-specific roles under the guidance of local issue specific factors which will be discussed later. The tissue-resident

macrophages that develop from these precursors, under the control of tissue-specific differentiation programming, are destined to perform unique tissue-specific tasks, thus cementing their status as truly specialized macrophage subpopulations (Table 1.2). Splenic red pulp macrophages have a unique transcriptomic and proteomic profile that allows them to process dead and senescent red blood cells, thus aiding in one of the main physiological functions of the spleen. Through the expression of specific factors such SPI-C and heme-oxygenase-1 gives splenic red pulp macrophages the ability to break-down and process hemoglobin[135,136] aiding in red blood cell recycling. Likewise, the liver with its lipid and organic molecule-rich environment is host to Kupffer cells. Kupffer cells are the specialized liver macrophage population whose transcriptomic profile includes fatty acid β-oxidation genes to process fats[137] and lipids in the liver as well as upregulation of CRIg which is responsible for degradation of complement coated pathogens and prevention of antibody-complex buildup during immune responses[138]. The peritoneal cavity is a host to two major macrophage species: the small and large peritoneal macrophages. While the small peritoneal macrophages are blood monocyte-derived and relatively short-lived, the large peritoneal macrophage population is fetal monocyte-derived with little input from the blood monocytes[139]. These large peritoneal macrophages are thought to play an anti-inflammatory, immune-suppressive role while under steady-state conditions, however, during inflammation these macrophages disappear[139,140], coined the macrophage disappearance reaction (MDR). While most MDR is likely due to a combination of cell migration and death, large peritoneal macrophages appear to migrate into the omentum during inflammation, where it is

thought that they serve as a reservoir of cells ready to resolve inflammation leading to improved immune homeostasis post-inflammation[139–141].

Microglia provide an interesting example of both ontogeny and tissue-dependent functionality. Firstly, they are the only tissue-resident macrophage population that is entirely derived from yolk sac macrophages[142,143]. This is presumed to be due to the closure of the central nervous system from the peripheral blood circuit during early embryogenesis, thus preventing any fetal monocytes from infiltrating[143]. The microglia play an important homeostatic role in the brain and are a major factor in neuronal development and a scavenger of dead neurons[144,145]. Another highly specialized form of tissue-resident macrophage is the osteoclast. These cells are larger than a standard macrophage and possess multiple nuclei with one of their main duties being the reabsorption of excess bone matter deposited by osteoblasts[146]. Osteoclasts are specifically equipped with cellular machinery to transport large amounts of protons across the membrane thereby contributing to acidification of the environment necessary for bone resorption[146,147]. This ability is also necessary to control and fine-tune the pH at the ruffled border, site of osteogenesis, during development and break healing[146,148]. The skin is also host to a specialized macrophage population called Langerhans cells. There has been some controversy as to whether they are specialized macrophages or a different variety of dendritic cells but recent fate-mapping studies have cemented their status of macrophages with mixed yolk sac and fetal liver monocyte origins[149,150]. Since the cell is located in the skin this means that it is usually the first immune element to encounter pathogens and is thus, highly migratory, being found in draining lymph nodes shortly

after a barrier breach and antigen uptake[151], which further confounds the picture as to the exact population dynamics of Langerhans cells.

Organ	Subset	Function
brain	microglia	neuronal development and homeostasis
bone	osteoclasts	ossification and osseous wound healing
gut	muscularis macrophages	gastro-intestinal motility
heart	cardiac macrophages	electrical conduction
liver	Kupffer cells	senescent red blood cell removal and iron recycling
spleen	red pulp macrophages	
lung	alveolar macrophages	surfactant degradation and alveolar homeostasis
peritoneal cavity	large peritoneal macrophages	coagulation factor production and microorganism capture

Table 1.2: Table showing the varied functions of different organ resident macrophage populations.
Table of major tissue resident macrophage populations. Adapted from Guilliams et al, 2020[126]

Finally, Alveolar macrophages (AMs) represent a particularly unique immune population since they are present in the exterior of the alveolar lumen and are therefore on the front line of immune defenses. In terms of ontogeny, yolk sac macrophages colonize the fetal lung, but they do eventually give way to a population of fetal liver monocytes. This fetal liver monocyte population eventually gives rise to a mature AM population shortly after birth[152,153].

1.3.2 Macrophage population dynamics

As mentioned previously, tissue-resident macrophages arise early in post-natal development, differentiating from an original colonizing population of fetal liver monocytes, yolk sac macrophages or in some cases a mixture of both. Subsequent experiments involving cell tracing and congenic bone marrow transplants have shown

that tissue-resident macrophages possess in some cases low cell turnover and a capacity to self-proliferate under steady-state conditions[154–156]. Studies have shown that almost all tissue-resident F4/80^{hi} macrophages possess the capacity to self-renew. Many tissue-resident populations possess certain specific secreted factors which are necessary for initiating and maintaining their self-replenishment capacity (Fig 1.13). For most tissue-resident macrophages, M-CSF is an indispensable secreted factor, whose presence is necessary for local, tissue-resident macrophage self-renewal programming. This includes Kupffer cells, Langerhans cells, splenic red pulp macrophages[127,157,158]. A major ontological exception to this rule appears to be intestinal macrophages which are not only derived exclusively from blood monocytes but are also actively replenished by the bone marrow-derived blood monocyte pool even under steady-state conditions[159]. This could be a requirement of immune tolerance due to the very close interaction between the immune system and the microbiome which may cause innate immune cell turnover and immune conditioning to facilitate homeostasis between immune responses and the presence of natural gut microbiota[157,159]. Another notable exception are microglia in the brain, which despite having an embryonic origin and even the capacity to self-renew[160], appear to be replenished at least partially from the blood monocyte pool in adulthood under steady-state conditions[161]. Monocytes have been demonstrated to cross the blood-brain barrier and be able to differentiate into full-fledged microglia with somewhat altered antigen presentation characteristics that may have implications on neuronal disease of immunological origin.

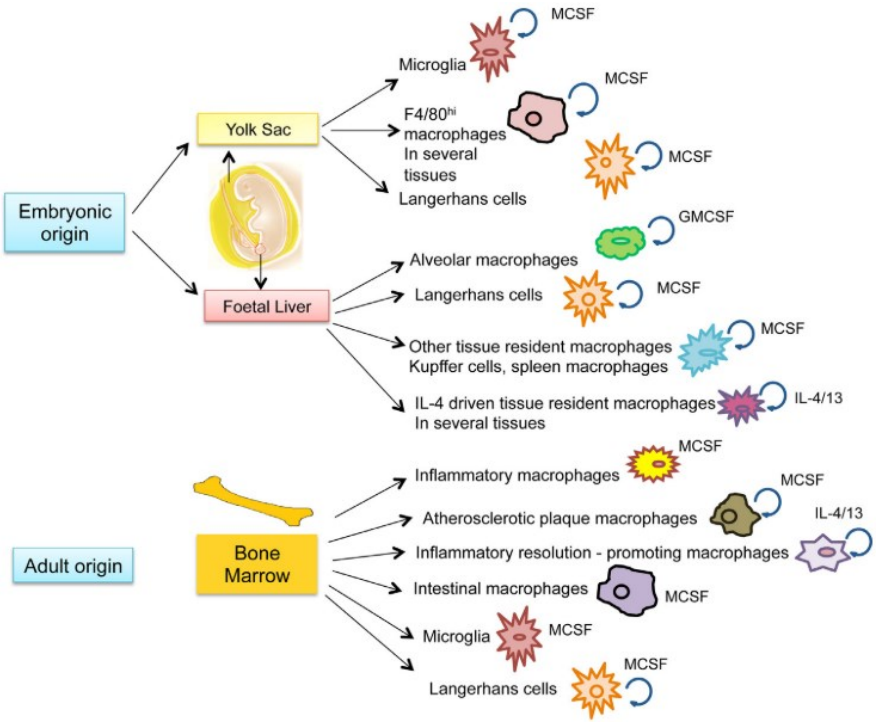

Figure 1.13: Origins and Self-renewal mechanisms of known tissue-resident macrophage populations.
Tissue-resident macrophages derived from either the yolk-sac or fetal liver monocytes show self-renewing capacity under steady-state conditions. The vast majority of this cellular self-renewal is driven primarily by M-CSF and GM-CSF. Notable exceptions being inflammatory macrophages of yolk sac origin which appear to renew via an IL-4/IL-13 mediated mechanism and intestinal macrophages which are continuously repopulated from the blood monocyte pool and differentiated into intestinal macrophages. Figure adapted from Gyory et al., 2015[155]

In the lungs, however, the population dynamics of AM turnover are also not quite as straightforward. AMs have been demonstrated to be surprisingly long-lived cells, on the order of months, and possess a definite capacity for self-renewal[162]. Recently, by using single-cell RNA sequencing, a potential "stem-like" subpopulation of self-renewing AMs has been identified based on their cell cycle and transcriptomic profile which may be responsible for resident AM replenishment[163]. Under, steady-state conditions, AMs are replenished with very little, if any, input from peripheral blood monocytes[127]. Over time,

the resident AM population does give way to a blood monocyte-derived one perhaps as a factor of cell senescence and constant exposure to airborne pathogen and pollutants[133]. During respiratory infections, AMs recruit monocytes which are also able to differentiate into full-fledged AMs through unique environmental cues such as the secretion of GM-CSF[164–166]. Indeed, AMs under certain can undergo MDR and be replaced almost fully by peripheral blood monocytes, before once again giving way to tissue-resident AMs which then aid recovery and epithelial healing post-infection[165,167]. *In vivo* bone marrow transplants and cell tracing experiments have demonstrated that fierce competition between AMs and peripheral monocytes occurs for colonization of the alveolar niche. AM resiliency has been demonstrated by showing that unless significant pressure is applied to permanently cripple resident AM's ability to self-renew, such as lethal irradiation, the AMs will outcompete blood monocytes for the alveolar niche every time[125,127] (Fig 1.14). Sub-lethal doses of radiation, clodronate liposomes and other temporary methods of AM depletion were not enough to tip the scales in favor of monocyte derived macrophages, demonstrating the ability of resident AMs to rapidly and efficiently colonize the alveolar airspace[125,127]. These findings are summarized in Fig

1.13 demonstrating the resiliency and efficiency of tissue-resident AM development.

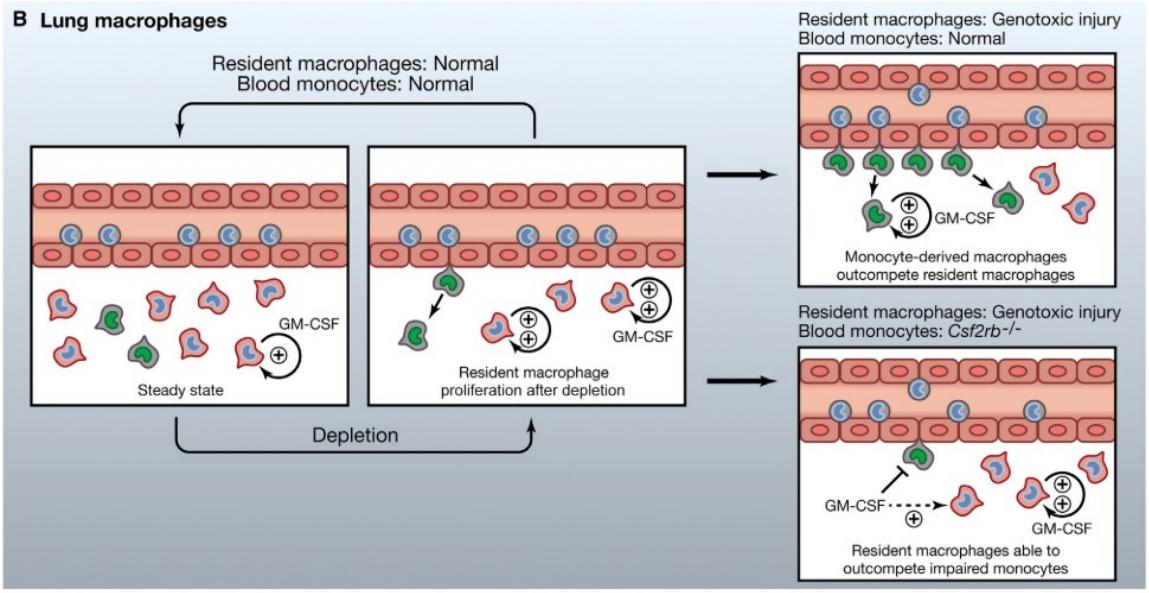

Figure 1.14: Repopulation strategy of the alveolar niche under different depletion methods.
Under normal steady-state conditions, AMs self-renew in a GM-CSF-dependent manner with little input from the blood monocyte pool. IF AMs are temporarily depleted using clodronate liposomes, AMs can outcompete infiltrating peripheral blood monocytes in colonizing the alveolar niche. As such, temporary depletion will always result in a predominantly tissue-resident AM population. However, when AMs undergo catastrophic genotoxic injury, such as that provided by lethal irradiation, the peripheral monocytes can outcompete resident AMs for the alveolar niche. A similar situation occurs in mice with ablated GM-CSF expression, whose lung spaces are devoid of tissue-resident AMs, having only a few foamy, monocyte-derived macrophages present. Figure adapted from Epelman et al., 2014. [125]

1.3.3 Determinants of macrophage fate and tissue differentiation

Over time it has become increasingly obvious that the tissue of residence must play a role in the differentiation of fetal liver monocytes, yolk sac precursors or even peripheral blood monocytes into the tissue-resident macrophage population unique to that specific organ. Much less is known about the extrinsic tissue-specific factors which govern macrophage differentiation into unique tissue-resident cells. Several studies have

attempted to address this issue. Certain secreted factors are necessary for all common macrophage development and a defect in one of them causes a variety of perturbations in all macrophages, be they adult peripheral monocyte-derived or tissue-resident (Fig 1.15). Studies have long ago established that CSF-1 is required for essentially all macrophage populations to develop[168]. However, a recent report has noted that a deletion of a CSF-1 specific enhancer (FIRE) appears to impact tissue-resident macrophages specifically while leaving adult-derived peripheral monocytes and macrophage populations unscathed[169]. These macrophages fail to express the CSF-1 receptor and while the exact impact of this enhancer is not known, authors speculate that it is activated at a specific time in neonatal development in the yolk sac and fetal liver monocytes[169]. Likewise, the transcription factor PU.1 plays a critical role in the development of most resident macrophage populations, the absence of which causes phenotypic dysregulation to varying degrees[153,170,171]. Other important interactions of transcription factors such as MAFB and c-MAF have been shown to affect most tissue-resident macrophages' capacity for self-renewal and post-natal development[172,173]. Finally, the transcription factor ZEB2 is critical for most tissue-resident macrophage development, but specifically, Kupffer cells, where its absence leads to a total loss of Kupffer cell identity[174]. On top of these general factors, there are a variety of tissue-specific factors that are used to imprint tissue-specific identity for the macrophages to perform their unique and specialized roles. Identifying these unique tissue-specific factors has proven to be quite challenging but recent reports have managed to elucidate the identity of some of these extrinsic factors. For example, peritoneal macrophages require the presence of retinoic acid, supplied by local stromal cells, to assume their final large peritoneal macrophage phenotype[141]. This

is followed by induction of GATA6 transcriptional programming which is required for terminal differentiation of FLMs into large peritoneal macrophages[141,175]. The theme of specialized organ cells delivering respective growth factors to tissue-resident monocyte tends to be a recurring one concerning tissue-resident cells. Kupffer cells rely on hepatic stellate cells as well as stromal cells to supply the required signalling. This involves the expression of DLL4 protein on the surface of hepatocytes to induce the LXR-α transcription factor and NOTCH pathway, while hepatocytes induce ID3 expression through a currently unknown mechanism[176]. Splenic red pulp macrophages require the induction of SPI-C to achieve terminal differentiation[177]. Later investigations revealed that SPI-C is strongly activated by heme, present in abundance in the splenic environment[135]. It has also been demonstrated that IL-33 secretion in the spleen during early post-natal development is necessary for priming early red-pulp macrophage precursor transcriptional programming[178]. The trend discussed continues and applies to microglial development as well. Neuronal secretion of IL-34 is critical for the development and function of Microglia by acting as an alternative ligand CSF-1 receptor[129]. TGF-β secreted by neurons and to a lesser extent by astrocytes and microglia themselves is another important endogenous differentiation factor that acts through SMAD2/3 signalling inside the microglia to initiate tissue-specific macrophage programming[179]. Interestingly, the same report found that Langerhans cells are severely affected by a lack of IL-34 signalling, even more so than microglial cells[129]. The source of this epidermally derived IL-34 is still not elucidated. Locally derived TGF-β was once again found to be critical for the development of Langerhans cells by inducing the transcription factor ID2[180], lack of which results in a failure of cell development[181,182].

The two preceding examples of microglia and Langerhans cells present an interesting and frustrating problem that is faced in determining tissue-specific identity factors. Both cell types require TGF-β and IL-34, but the secretion of these two cytokines leads to the development of two vastly different tissue-resident macrophage populations both at the transcriptional and physiological levels. Therefore, other unique tissue-level factors or interactions with tissue-specific cells must play a key determinant role in terminal macrophage differentiation since the variety of tissue-resident cells cannot be explained simply by alternative binding of the same secreted factors. Splenic macrophages provide a good example, where the abundant levels of heme in the spleen act as a major determinant in the fate of fetal liver monocytes colonizing the spleen. However, finding these unique tissue factors that produce the highly specialized tissue-resident macrophage phenotypes that have been observed has been frustrating and currently constitutes an area of active research.

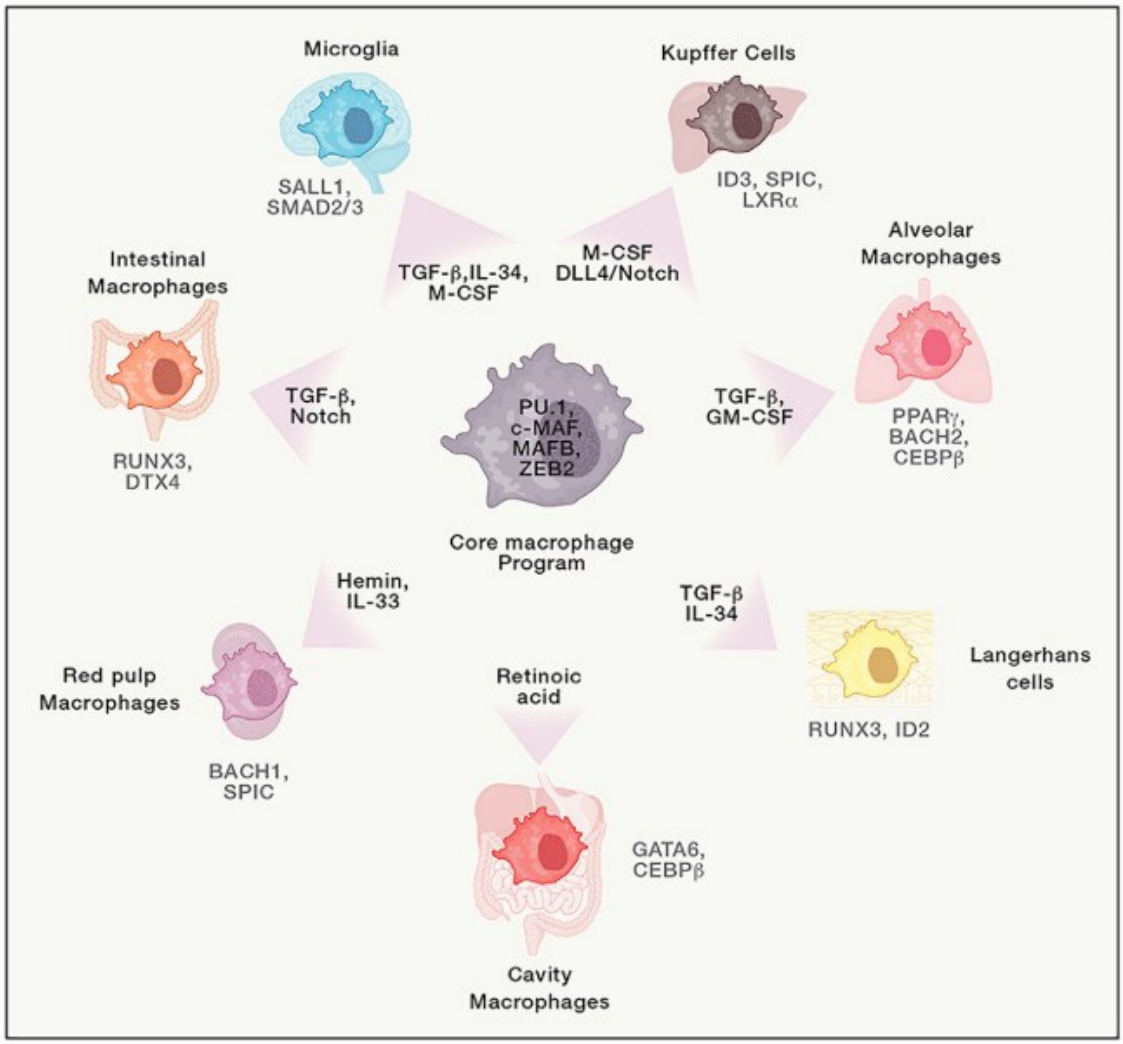

Figure 1.15: Tissue-specific factors governing tissue-resident macrophage identity. All macrophages appear to share a common genetic program that governs their overall macrophage identity. Some of the transcription factors discovered to govern this programming are PU.1, c-MAF, MAFB and ZEB2. However, less is known about the tissue-specific signals that govern the terminal differentiation and specialized transcriptomic profile which grant generic macrophage unique, tissue-specific functions and identities. Some of the unique tissue secreted factors that have been discovered are TGF-β and IL-34 which appear to be shared across several tissue-resident macrophage subsets. Likewise, the presence of CEBPβ and BACH2 as a necessary transcription factor in more than one subtype implies a degree of commonality with possible unique tissue signals and other transcription factors fine-tuning the macrophage programming to best suit the needs of the tissue of residency. Figure adapted from Chakarov et al., 2020[183]

1.4 Alveolar macrophages

1.4.1 AMs overview and development

AMs possess a unique almost DC-like phenotype ($CD11c^{+}$, $CD11b^{lo}$, $MHC\text{-}II^{lo}$, $SIGLEC\text{-}F^{+}$) which is significantly different among tissue-resident macrophages. With respect to ontogeny, the embryonic lung appears to undergo a complex and progressive series of precursor cell infiltrations starting with immature yolk-sac derived precursor macrophages up until about embryonic day 14[152]. These cells subsequently give way to an infiltration of fetal liver monocytes which colonize the developing alveolar niche[152]. Immediately after birth, these fetal liver monocytes rapidly develop into mature AMs post-partum through a burst of proliferation and differentiation that translates into a full complement of AMs being present in the lung as early as postnatal day 3 in mice[152,184]. It is not entirely known what triggers this rapid burst of cell cycling activity and differentiation, but it is possible that the commencement of gas exchange, surfactant secretion and cytokine secretion by the alveolar epithelium could be instructing fetal liver monocytes to begin the transition into fully developed AMs. As mentioned before, these tissue-resident AMs are self-renewing with very little input from peripheral blood monocytes under steady-state conditions and will remain with the individual throughout most of their natural life. However, these self-renewing tissue-resident AMs eventually give way to monocyte-derived AMs as they lose their ability to replenish their numbers due to cell senescence and constant exposure to airborne pollutants and pathogens[133].(Fig 1.16)

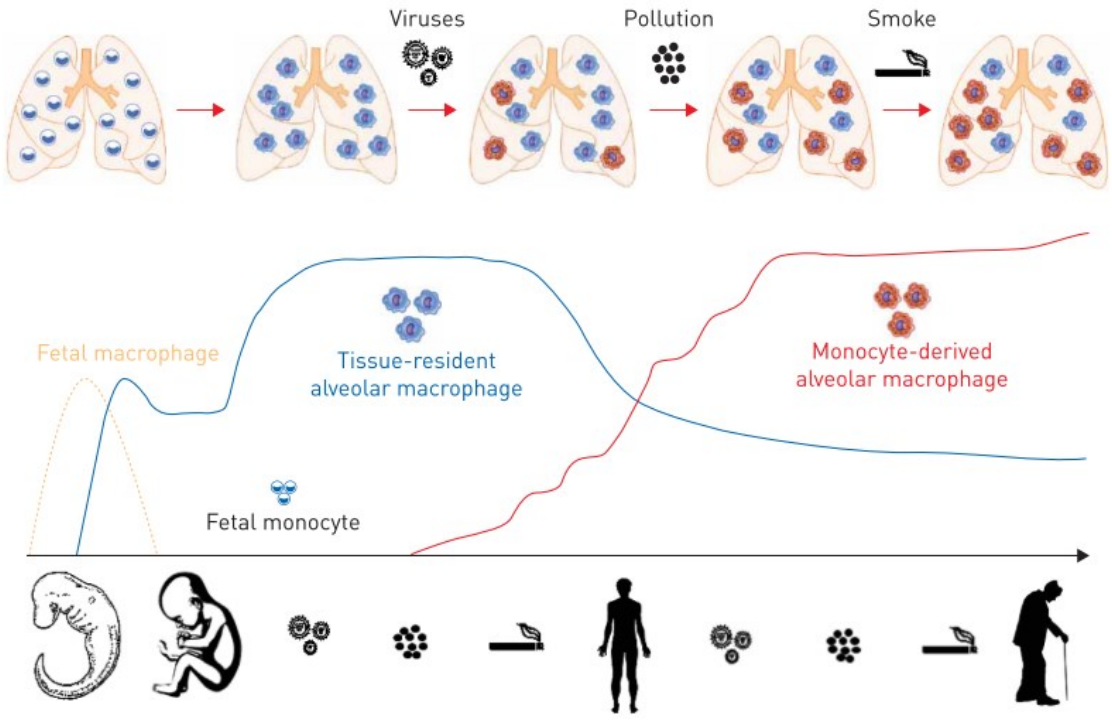

Figure 1.16: AM development and population composition throughout an individual's lifespan.
Fetal macrophage precursors colonize the early lung until they yield the niche to incoming fetal liver monocytes. Fetal liver monocytes populate the alveolar niche and experience a proliferative and differentiation burst early post-partum which gives rise to the full adult complement of mature tissue-resident AMs. Over time, due to aging, cellular senescence, exposure to pathogens and environmental irritants the fetal liver monocyte AMs are steadily replaced by monocyte-derived macrophages from circulation. Figure adapted from Morales-Nebreda et al. 2015[133].

1.4.2 AM pathogen interactions

Amongst all the tissue-resident macrophages, AMs are situated in the most unusual and arguably the most exposed location possible. AMs are positioned on the inside the alveolus of the alveolar epithelium where they play a role as front-line sentinel immune cells, aiding with foreign debris and pathogen clearance as depicted in Fig. 1.17

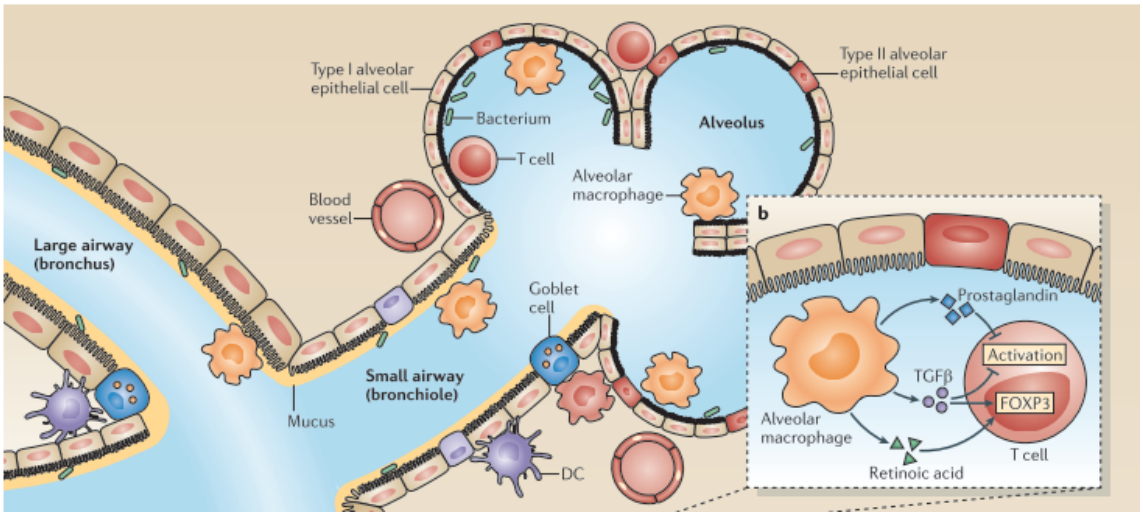

Figure 1.17: Lung cell physiology, *in situ,* under steady-state conditions. Major immune cell populations of the lung: AMs sit on the external wall of the alveolar lumen, $CD103^+$ DCs sit on the anterior wall with dendrites going through the epithelium into the lumen, constantly sampling the environment for pathogens that could be presented. Type-I pneumocytes make up most of the lung epithelial barrier and serve as structural cells while aiding gas exchange. Type-II pneumocytes are the minority epithelial population and serve mainly to secrete and recycle pulmonary surfactant. Goblet cells present in the lung secrete mucous which has immune and epithelial protective roles. Figure adapted from Hussel & Bell, 2014[185].

The critical role of AMs in pathogen clearance has been highlighted by studies showing their importance in helping clear pulmonary infections caused by numerous different pathogens ranging from bacterial such as pseudomonas, pneumococcus as well as viral such as influenza and respiratory syncytial virus[164,186,187]. They are also a key player in the pathogenesis of tuberculosis where they serve as hosts for the intracellular mycobacteria, allowing it to replicate and survive for many years[188]. AMs infected with mycobacteria secrete pro-inflammatory cytokines and recruit neutrophils and Th1 cells to the site of infection resulting in the production of a granuloma, the intent being to contain and mitigate the spread of mycobacteria due to the AMs inability to successfully clear the infection[189]. While AMs are mostly associated with phagocytosis and clearance of bacterial and fungal pathogens, they also play a prominent albeit more complex role in

pulmonary viral defenses. During influenza, AMs secrete pro-inflammatory cytokines and activate anti-viral defenses, but the extent and type of cytokines secreted can vary substantially depending on the particular strain of influenza[190]. It is also important to note that AMs themselves can be infected by influenza with varying degrees of success depending on the particular strain and this can result in AM apoptosis, possibly a mechanism of controlling viral spread by denying the initial virions a viable host to replicate in[191]. However, AMs play a much more significant role in protecting the lung from secondary bacterial infection during recovery from pulmonary viral insults, a time when the sensitive alveolar epithelium is especially vulnerable to bacterial superinfection[154,192]. Several studies have also demonstrated that sub-populations of AMs are created following challenges with pneumococcal bacteria leading to better and more efficient responses upon subsequent rechallenge[193]. Another report noted the existence of a phenomenon by which AMs are primed post-viral infection through Th1 cells and IFNγ. This results in a population of AMs characterized by a permanent steady-state alteration that includes increased chemokine production, reliance on glycolysis, and overall transcriptomic signature of a cell that is ready to initiate immune defense programming[194]. Sparking a little controversy, both studies have hinted at coining the phenomena they characterized as a new paradigm in immunological memory induction and maintenance[193,194].

Another well-defined role for AMs is to aid tissue repair and regeneration following pulmonary infections. Disposal of aged and excess neutrophils through AM phagocytic activity as well as apoptosis of AMs are critical to promote pulmonary tissue recovery post-inflammation, especially in low-dose infection models[195,196]. A recent

report has also highlighted through the use of *in vivo* imaging the efficient and methodical way that AMs rapidly patrol the alveoli in a rapid fashion upon inhalation of non-viral pathogens or debris[197]. The AMs then phagocytize any bacteria or debris they encounter without provoking an inflammatory response, thus in effect, concealing the pathogen from the rest of the immune system in order not to induce unnecessary inflamation[197]. Anti-inflammatory effects are also achieved through the secretion of cytokines such as TGF-β and other factors such as PGE, and PAF[198], especially following phagocytosis of apoptotic cells. Their ability to resolve and control inflammation combined with above-average levels of phagocytic activity serves to highlight that AMs act as front-line immunosuppressive cells which only trigger an inflammatory cascade if overwhelmed or themselves subject to infection.

1.4.3 Mouse models of pulmonary infection

This study as well as multitudes of others have made use of inbred mice as model organisms to mimic viral and bacterial infections of the upper and lower respiratory tract. Mice are of particular use due to their low maintenance, rapid breeding, wide availability of genetic mutants as well as being easily able to control for genetic variation. The choice of mouse strain is important since studies have shown that different mouse strains exhibit different levels of susceptibilities to bacterial infection[199]. A major factor in mouse strain selection is also its genetic characterization, as the cautionary tale of C57BL/6 CD45.1 congenic mice shows, where a mutation in the NCR1 gene conferred resistance to cytomegalovirus but a vulnerability to influenza[200]. When working with mouse genetic mutants it is advisable to confirm the integrity of the genome near the site of mutation to ensure that promoter regions are intact or have not been removed from adjacent genes as

well as to verify the presence or absence of epigenetic elements such as nearby micro-RNA sites that may cause transcriptional and translational level abnormalities.

The respective pathogen of choice, bacterial or viral, is-dependent on the experimental goals, but it is always optimal to select a pathogen with clinical or translational relevance. Since *Streptococcus pneumoniae*[201] and IAV[202] and the interplay between them in the form of superinfections (IAV followed by *S. pneumoniae* colonization)[203] are one of the major causative agents of pulmonary morbidity and mortality in humans, they are also the most widely studied and widely used models of pulmonary pathogenesis. There are of course differences in responses to pathogens between mice and humans that have already been outlined[204]. These need to be kept in mind when using bacterial pathogens, such as rodent's inherent resistance to bacterial infection exhibited by mice[205], breaking which entails using doses of pathogen that humans would not practically be exposed to in normal circumstances[206]. A similar problem arises with influenza A virus infection (IAV), perhaps even more so, since rodents are not normally infected with influenza at all[207]. IAV studies carried out in mice thus usually require the virus to be mouse-adapted either through serial passaging, direct genetic mutation or by using brute force methods of instilling high titer doses to invoke symptomatic infection[208].

The method of pathogen instillation is also non-trivial in mouse models of pulmonary infection. Intranasal instillation is easy to do and depending on the volume used can be utilized to mimic an upper or lower respiratory tract infection[209]. However, differences in volume, use of anesthesia, body position during instillation are all confounding factors that determine where the inoculum eventually ends up and how

much if it gets to into the lungs as opposed to the digestive tract[210]. Intratracheal instillation can be used as an alternative but this is a full surgical procedure requiring total anesthesia and includes post-surgical complications as well as practical difficulties of performing such a procedure on a small rodent as a mouse[209]. It is also prone to instilling pathogens into very specific areas of the lung itself which, especially in the case of viruses, is not representative of the diffuse nature of most pulmonary infection be they viral (which affect total lungs) or bacterial (which tend to be more lobar)[211].

Despite these considerations, a strength of mouse pulmonary infectious models permit multiple, simple readouts of immune function and infectious status available through simple lavage procedures combined with CFU/PFU counting, immune infiltrate isolation, and characterization as well as easy to interpret histological techniques (Fig. 1.18).

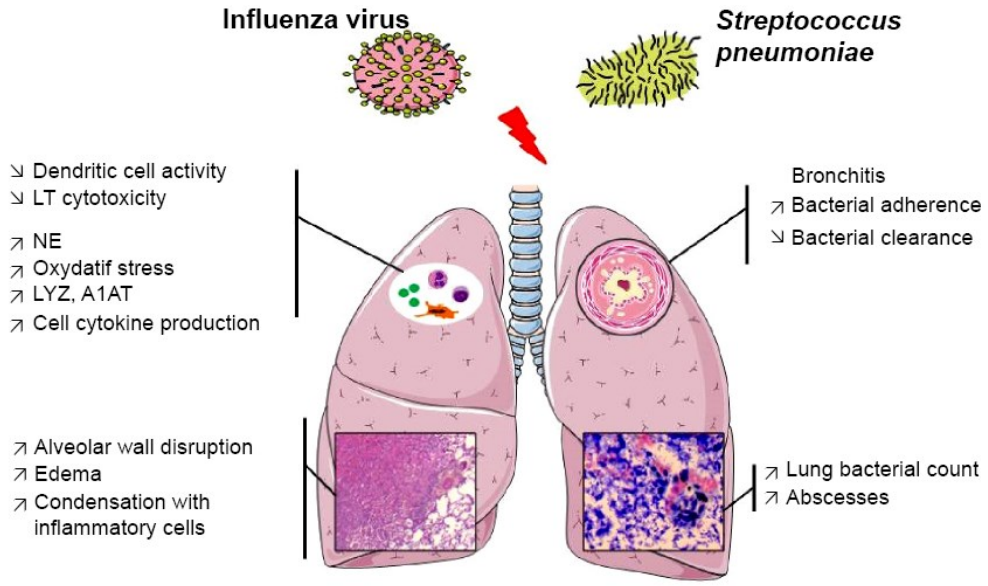

Figure 1.18: Common consequences of pulmonary infection in animal models and their use in quantifying severity and disease progression.

Pulmonary pathogens cause physiological changes as well as immune and secretory changes in the lungs which can be assessed using standard immunological, histological and physiological methods. Figure adapted from Hraiech et al, 2015[209]

Overall mouse pulmonary models offer certain advantages for the researcher in ease of data gathering, many genetic backgrounds to choose from based on experimental design and clinically relevant pathogen selection at the expense of relevance of outcomes to humans, reproducibility between experiments, and tricky pathogen instillation.

1.4.4 Homeostatic AM roles

As discussed above, AMs play a large role in maintaining barrier integrity and tissue homeostasis post-infection. This also translates to a naturally anti-inflammatory state (or M2 polarization) of AMs under homeostatic conditions. This phenomenon has been subtly demonstrated in studies showing that adoptive transfer of allergen-insensitive AMs into allergen sensitive hosts, where the transfer achieved a lowering of inflammation and decrease in lung tissue pathology upon stimulation with allergens[212]. Similar effects have been demonstrated in murine asthma models where tissue-resident AMs upon adoptive transfer can suppress airway hyper-responsiveness, while recruited peripheral blood monocytes are generally responsible for exacerbating it[167].

AMs have also been known to produce other powerful anti-inflammatory and resolving cytokines including the secretion of amphiregulin and hepatocyte growth factor, both of which serve to initiate tissue regeneration and regrowth of damaged epithelium[213]. This delicate homeostatic balancing act is maintained by crosstalk between AMs and the alveolar epithelium. AMs specifically secrete SOCS1 in exosomal vesicles which are taken up by the alveolar epithelium and proceed to inhibit cytokine signalling by interfering with STAT phosphorylation[214]. Conversely, the alveolar epithelium can request these exosomes through PGE2 secretion which stimulates AMs to produce SOCS1[215]. This crosstalk between AMs and epithelial cells is not limited to secreted

factors as contact between the two types of cells plays a direct role in the modulation of immune homeostasis. This is exemplified by the secretion of TGF-β and the expression of CD200 on the alveolar epithelium. AMs are known to express TGF-βR in abundance, stimulation of which induces an anti-inflammatory AM predisposition[185]. The CD200:CD200R interaction serves to suppress P38-MAPK and JNK activation in AMs in a DOK-dependent manner, thereby causing an overall inhibitory effect on the AM[216]. Likewise, loss of αvβ6 integrin leads to diminished TGF-β signalling and development of emphysema as well producing AMs which appear to be in a more phenotypically activated state[217].

Another major homeostatic role, and one which they are most uniquely adapted for from all other tissue-resident macrophages, is the phagocytosis and metabolism of pulmonary surfactant[218]. Surfactant is primarily composed of phosphatidylcholine (PC), dipalmitolphsophatydilcholine (DPPC), phosphatydilglycerol (PG), cholesterol, various other free fatty acids and surfactant proteins (SP-A,B,C,D), as seen in Fig. 1.19 and is produced constitutively by type II pneumocytes of the alveolar epithelium[219].

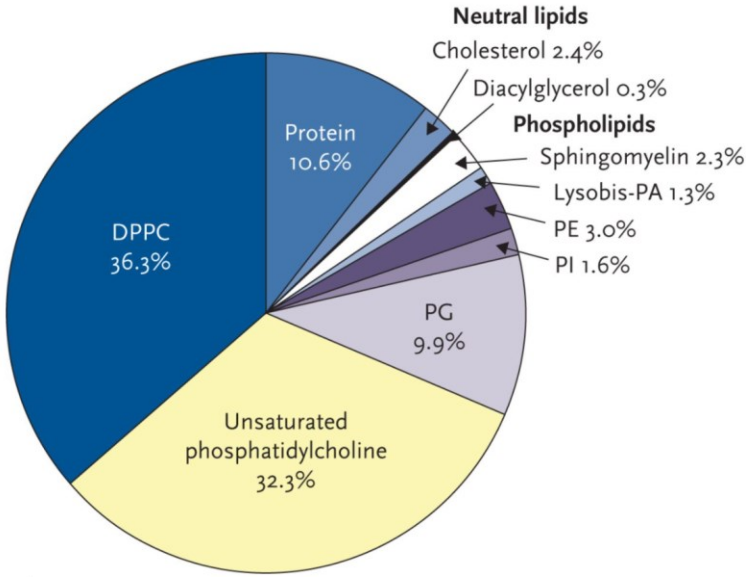

Figure 1.19: Standard surfactant composition.
Surfactant is complex mixture of several different lipid species and proteins. Percentages represent weight per volume of components. DPPC: Diphosphatidyl-choline, PG: phosphatidyl-glycerol. PE: phosphatidylethanolamine, PI: phosphatidylinositol. Protein portion made up of surfactant proteins SP-A, B, C and D. Figure adapted from Chakraborty & Kotecha, 2013[220].

This composition of pulmonary surfactant functions to ensure efficient gas exchange and lower surface tension to prevent atelectasis, or collapse of the lung, during expiration. Surfactant proteins present in this secretion have complex and varied roles ranging from acting as opsonins and helping in innate immune defense (such as SP-A and SP-D)[56,221], to ensuring proper lipid film formation and maintaining the biophysical properties of surfactant for optimal functioning (such as SP-B, SP-C and to a lesser extent SP-D)[57,222]. The fact that SP-D knockout mice are the only surfactant protein knockout mouse line that exhibits significant pulmonary dysfunction including excess macrophage and neutrophil infiltration as well as the presence of foamy lipid-laden macrophages is particularly striking but the mechanism behind this phenotype still remains to be fully elucidated[223]. All of the pulmonary surfactant in the lung is produced by type II pneumocytes at a fairly constant rate under steady-state conditions, with most of this

surfactant being taken up and recycled by the same type II pneumocytes that produced it[224]. However, about 20% of it is up-taken by AMs, metabolized and the by-products (mostly cholesterol) expelled back into the alveolar space[225].

A defect in this delicate balancing act between surfactant secretion, recycling, and catabolism can result in some significant dysregulation of the alveolar compartment that can potentially be lethal if not treated. Pulmonary alveolar proteinosis (PAP) is a surfactant clearance disorder identified in humans which is caused by an inability or lack of AMs to process surfactant resulting in surfactant accumulation in the alveolar space that will eventually lead to death due to gas exchange failure without regular intervention. The importance of AMs in PAP and in the processing of surfactant was highlighted in studies conducted with *gmcsfr1*$^{-/-}$ mice, which manifest classical PAP symptoms, due to a failure of AM development resulting in a very small and dysfunctional population of foam-like AM cells that are unable to metabolize pulmonary surfactant.

1.4.5 Surfactant secretion and AM lipid metabolism

The process of surfactant secretion is mediated by type-II pneumocytes and has been fairly well described in scientific literature. Type-II pneumocytes possess an unusually enriched endoplasmic reticulum which is necessary for the constant production and secretion of lipids and surfactant proteins[226]. The surfactant lipid transport is likely regulated by vesicular transport between the ER and into so-called multivesicular bodies which are then packaged into specialized storage molecules called lamellar bodies[227]. There they await to be secreted into the alveolar space, secretion of which is controlled by a multitude of mechanisms including ATP and Ca^{2+} release as well as mechanical expansion and compression of the lungs[226]. Once secreted these lamellar bodies complex

with tubular myelin and become part of the surfactant interfacial film[228]. The process is neatly summarized in Fig 1.20.

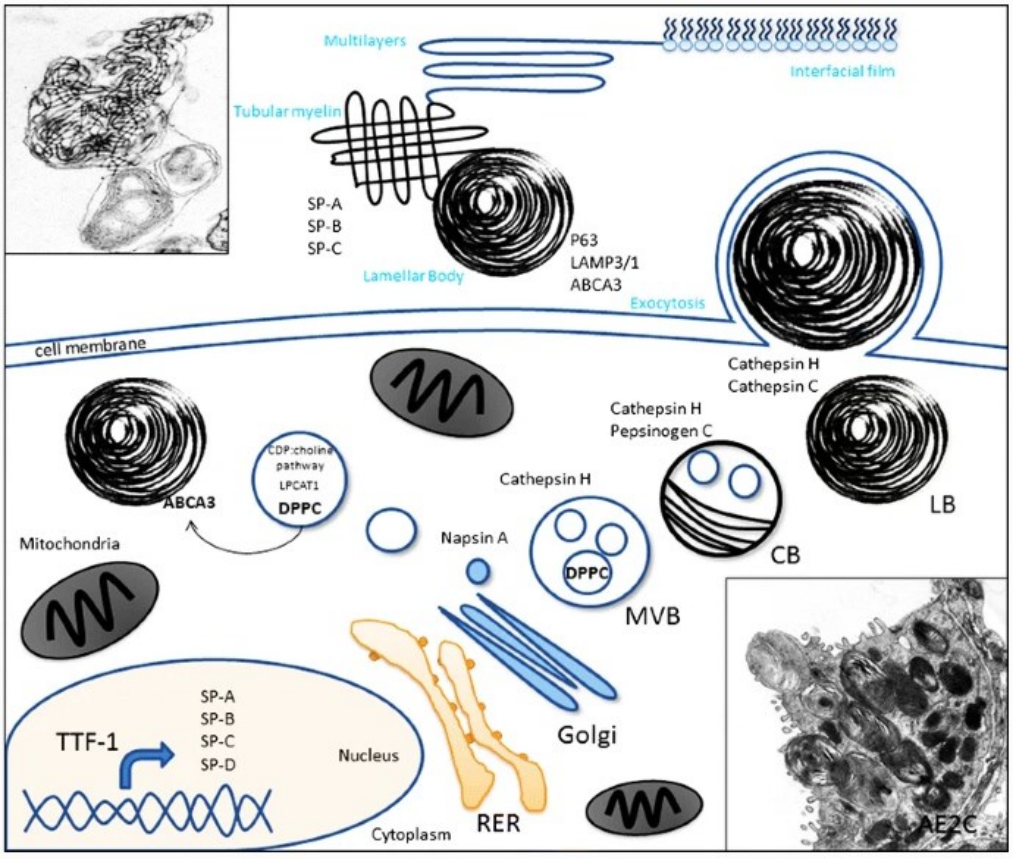

Figure 1.20: Surfactant assembly and secretion.
Surfactant components with proposed assembly and secretion pathway in type-II pneumocytes. Top left: electron micrograph of the lamellar body converting into tubular myelin. Bottom right: electron micrograph of the lamellar body being secreted from a type-II pneumocyte. Figure adapted from Lopez-Rodriguez et al, 2017[226].

While a good amount of information is known about the production, secretion, composition, and function of surfactant, significantly less is known about its lifecycle post-secretion, specifically the mechanism of recycling by type-II pneumocytes nor alveolar macrophage lipid metabolism. Previous sections discussed the importance of GM-CSF in this process and the following section will outline the battery of genes required for AM identity and phenotype acquisition, the majority of which are involved

in regulating the unique AM lipid metabolism. In this section, the focus is to outline the physiological knowns and unknowns of AM lipid catabolism.

The vast majority of lipid metabolism of macrophages comes from studies examining atherosclerotic plaques and the transition of circulating macrophages/monocytes into foam cells reflected in the terminology used in the literature where lipid-laden AMs are likewise frequently referred to as foam cells. Studies have shown that there are shared genes that influence the formation of foam cells in the lung and the heart the main ones being PPARγ and the genes under its control, as well as the cholesterol transport cassettes ABCA1 and ABCG1, the dysfunction of which leads to aberrant macrophage lipid metabolism and foam cell formation[229,230]. The cholesterol transport cassettes appear to play a particularly critical role in cholesterol efflux, both of HDL and LDL, which are governed mainly through induction of LXR and other nuclear receptors[231]. It appears, however, outside of this master regulator of lipid metabolism and cholesterol transporters, that this is where the similarities between atherosclerotic foam cells and pulmonary foam cells end, and while these have been shown to be important for AMs as well as macrophages in general, lipid metabolism in AMs takes on a much more prominent, complex and regulated role likely owing to the lipid-rich environment they are located in.

While phagocytosis of lamellar bodies has been observed in AMs (Fig 1.21), lipid scavenger receptors such as CD36, SR-A1, and SR-B1 play a large part in mediating the active transport required for uptake of surfactant components[231]. Lysosomal enzymes are particularly important for AMs with LAL, LIPA, CYP27A1, and CYP27A6, regulated by PPARγ have been correlated with the acquisition of PAP and formation of foamy

AMs[232,233]. NPC1 and NPC2 proteins, which act as esterified cholesterol transporters, have also been correlated with PAP development and AM dysfuction[234]. Similarly, APO-E, lipid transporters mainly expressed in the liver, are also found in the lungs and can result in foamy AMs and metabolic dysregulation[235].

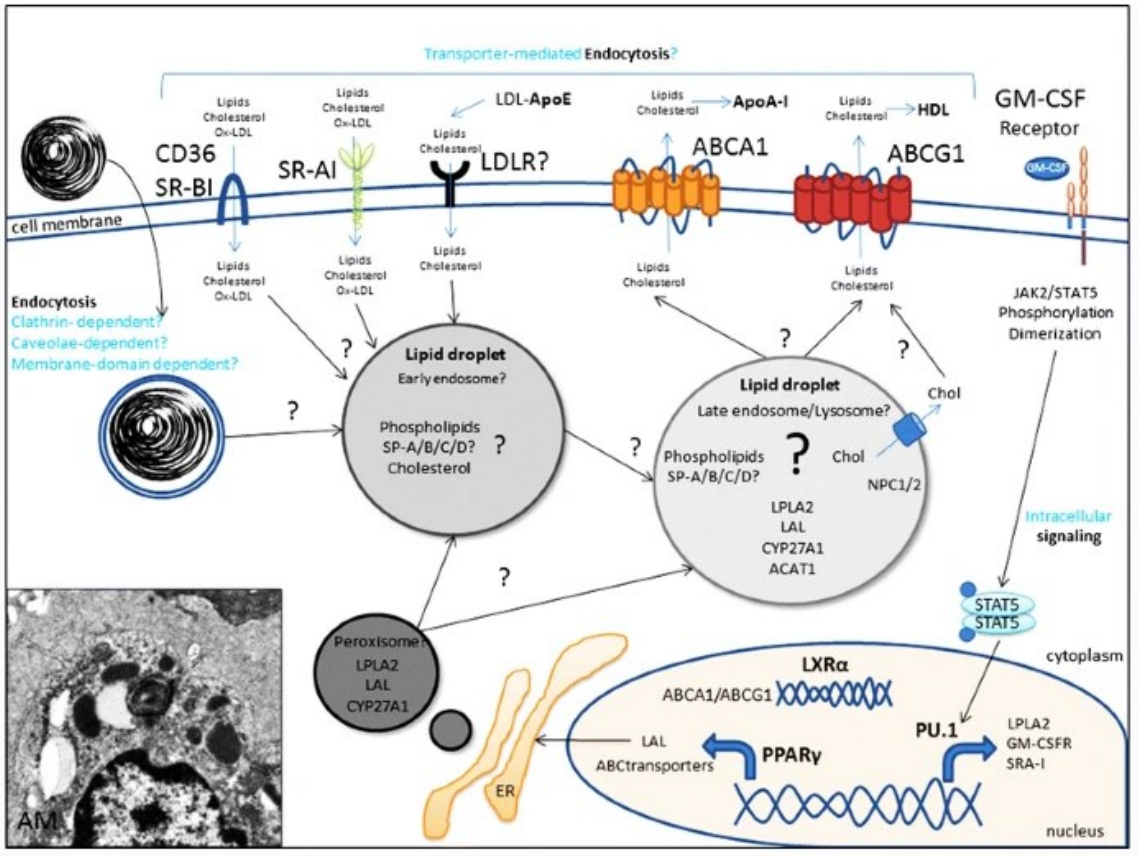

Figure 1.21: Surfactant uptake and degradation by AMs.
Theoretical scheme of surfactant uptake via various receptors and possible lysosome mediated degradation and temporary lipid droplet accumulation followed by the expulsion of cholesterol by-products through cholesterol pumps. Mediated through GM-CSF signalling and a unique transcriptomic signature involving PU.1, LXRα, and PPARγ. Figure adapted from Lopez-Rodriguez et al, 2017[226].

There already exists a body of work describing the nature of AM and alveolar epithelial crosstalk and its importance in the maintaining of AM homeostatic roles. Most of the connections involving receptor-ligand connection between AMs and the epithelium tend to be more of an immune regulatory nature such as the important connection between

CD200 and CD200r in suppressing AM activation and promoting inflammation resolution post-viral infection[236]. Other studies have highlighted the impact of PD-1 signalling on AM activity during tuberculosis infection[237] and the interaction between Sirp-α and CD47 which acts as a phagocytosis inhibitor to prevent the destruction of alveolar epithelium by AMs[238]. These physical interactions are summarized by Fig. 1.22

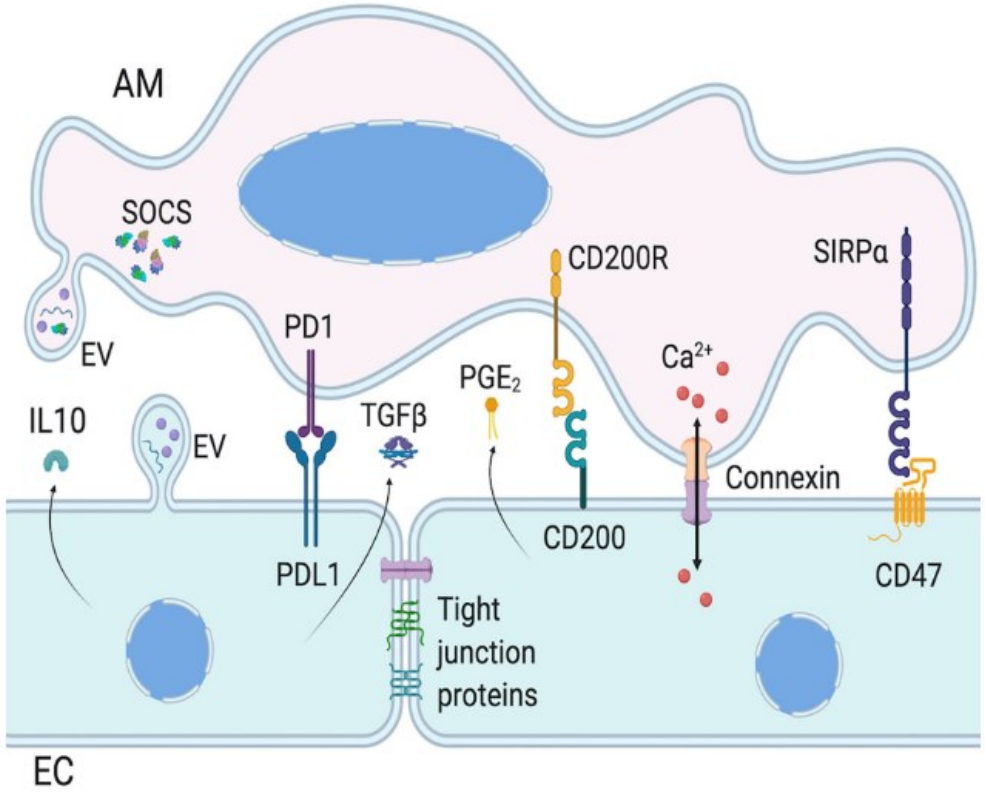

Figure 1.22: Communication between AMs and alveolar epithelial cells. Known interaction between AMs and epithelial cells. Receptor interactions include SIRPα-CD47, CD200R-CD200, PD1-PDL1 as well as secretory factors such as GM-CSF, TGFβ, IL-10, extracellular vesicles as well as calcium flux. Figure adapted from Bissonnette et al, 2020[239].

Many studies which attempt to elucidate the metabolic programming of AMs have been focused on a transcriptomic approach to identify the necessary transcription factors which give rise to AM metabolism or identity. Other explorations have narrowed

in on certain secreted factors which partially drive AM metabolism and identity and linked them to specific transcriptomic profiles. However, none of these secreted or transcriptomic factors are unique to the AM niche, which implies the existence of other tissue-specific interactions required to develop; this is a persistent problem that has been recognized explicitly in the field[240]. Studies that show the importance of physical AM and alveolar epithelial interaction in determining AM differentiation and especially metabolic programming are sorely lacking.

1.4.6 AM unique identity factors

As previously discussed, tissue-resident macrophages have been shown to possess a unique transcriptomic profile that grants them the ability to perform duties best suited for their tissue of residency. AMs, even among other tissue-resident macrophages, possess a very unique phenotype that is governed by the secretion of several cytokines and activation of a very specific set of transcription factors. One of the first factors identified that is important for AM development, besides M-CSF which is required for all macrophages, was GM-CSF[127,152,153]. Secretion of GM-CSF by the alveolar epithelium begins a cascade that results in the acquisition of a unique AM phenotype ($CD11c^{+}$ SIGLEC-F^{+}, $CD11b^{lo}$) and activation of PPARγ allowing the acquisition of a unique metabolic profile[152,232]. lack of GM-CSF receptor or production of anti-GM-CSF antibodies results in a lack of AM formation from birth with only a few foamy and undifferentiated AMs present in the lungs. This condition also results in PAP in mice and humans and ultimately leads to death if untreated[153,241]. Similarly, lack of PU.1 or lack of activation of PU.1 also results in PAP formation and similar phenotype as present in GM-CSF or PPARγ deficient mice[153]. Likewise, BACH1/2 double knockout mice produce a

lethal phenotype that is also characterized by foamy AMs and poor lipid homeostasis resulting in lethal PAP[242]. Interestingly, a recent report has found that paracrine secretion of TGF- β by AMs is critical for their survival and maintenance[184], with AMs completely absent in the lungs of 2-week-old TGF- β receptor-deficient mice, highlighting the need for yet another soluble factor required for proper AM development. Other reports underscored the need for mTORC signalling in AMs, lack of which resulted in a diminishment of the AM population and a slow-down in self-renewal capacity[243]. CEBp has also been shown to influence AM maintenance and homeostasis, lack of which results in poor AM numbers and dysregulation of peritoneal macrophage functional capacity[139]. Other reports have shown that a lack of VHL[244] signalling and BHLH40, BHLH41 transcription factors results in similar phenotypes of poor AM self-renewal and inability to process pulmonary surfactant[245]. All of this indicates that a complex interplay of transcription factors is necessary to regulate self-renewal and lipid metabolism in AMs. It should be pointed out, that only a couple of exclusive extrinsic signals have been identified that allow this transcriptional signature to occur, the main two being GM-CSF and TGF- β both of which are necessary and required for AM formation. Secretion of these two cytokines is not exclusive to the lungs and tissue-specific factors for AM development remain to be elucidated. Due to the high degree of documented crosstalk between the alveolar epithelium and AMs themselves, epithelial instruction through receptor-ligand expression may likely play a role in the imprinting of AMs unique phenotype and identity. However, the unique tissue-specific factors that are required for AM function are still not entirely elucidated.

In this study, we demonstrate that resident AMs express the usual NK cell-associated receptor NKR-P1B and using *nkrp1b*$^{-/-}$ mice we show that the loss of this receptor has functional consequences on AM development, function, and metabolism. NKR-P1B loss leads to increased susceptibility to *S. pneumoniae* infection due a gradual collapse of tissue-resident AMs followed by a period of peripheral blood monocyte mediated renewal. The collapse of the AM population is followed by an accumulation of foam-like AMs in the alveolar spaces of NKR-P1B deficient mice that can be resolved by removing them from the lipid rich alveolar environment and placing them into *in vitro* culture thus highlighting the importance of NKR-P1B signalling on the lipid processing ability of lung resident AMs. We also identify Clr-g expressed on lung epithelial cells as a potential new ligand for NKR-P1B, whose interaction with NKR-P1B could represent a novel tissue-specific interaction that imprints AMs with their unique metabolic signature and modulates AM metabolic signalling.

CHAPTER 2: MATERIALS AND METHODS

2.1 Experimental Model and Subject Details

C57BL/6 (Jackson Laboratories), *Nkrp1b*$^{-/-}$ (described previously in Rahim et al., 2015) , and *Clr-b*$^{-/-}$ (generous gift from Dr. Matthew T. Gillespie, Kartsogiannis et al., 2008) mice were bred in-house. CCR2-deficient mice were purchased from Jackson Laboratories and bred in-house. Generation of *Ccr2*$^{-/-}$*Nkrp1b*$^{-/-}$ double mutant mice entailed crossing CCR2-deficient mice and NKR-P1B deficient mice. Mice produced from the second generation of this pair were screened by PCR to determine their genetic status and used to establish the *Ccr2*$^{-/-}$*Nkrp1b*$^{-/-}$ mouse which was subsequently bred in-house. All mice were housed under specific pathogen-free conditions at Dalhousie University. Mice were fed autoclaved rodent feed and water *ad libitum*. Mice were age and sex matched for experiments with littermates used unless otherwise noted. All protocols used were in accordance with the guidelines drafted by Dalhousie University Animal Care Committee and the Canadian Council on the Use of Laboratory Animals

2.2 Tissue Processing and Flow Cytometry

Age and sex matched mice mice were euthanized, lungs excised, and minced by using a razor blade into approximately 1mm^3 pieces. The homogenate was incubated at 37ºC with 5% CO_2 in the presence of 5mg/mL collagenase D (Worthington Biochemical Corporation CAT# LS004188) for 1 hour with gentle agitation performed every 15 minutes. The resulting homogenate was then passed through a 70µm cell strainer (Falcon CAT# 352350) using the plunger of a 1mL syringe (BD CAT# 309659). The cell suspension was then subjected to a 20% Percoll (GE Healthcare CAT# 17-0891-01)

gradient and spun at 2000 x g for 30 minutes at room temperature. The supernatant was pipetted off and ACK (150mM ammonimum chloride, 10mM potassium carbonate, 0.1mM EDTA) lysis was performed for 5 minutes on ice after which the cells were spun down at 500g for 5 minutes. The final cell suspension was resuspended in PBS, cell counts were determined by a hemocytometer. Single-cell lung suspensions were stained with anti-CD45-APC (BioLegend CAT# 103112), anti-MHCII-BV510 (BioLegend CAT# 107635), anti-SIGLEC-F-eFluor 710 (Invitrogen CAT# 46-1702-82) and in some experiments with anti-CD11c-FITC (eBioscience CAT# 11-0114-85), anti-NKR-P1B (a generous gift from Dr. Carlyle) and anti-Clr-b antibodies (generous gift from Dr. Koho Iizuka), refer to table 2.1 for antibody details. After gating out doublets and dead cells, AMs were identified as $CD45^{+}MHCII^{mid}SIGLEC\text{-}F^{+}CD11c^{+}$ cells with high forward and side scatter characteristics. In lavage experiments, mice were euthanized by CO_2 asphyxiation, the trachea exposed and then cannulated using a 20-gauge syringe wrapped in surgical tubing. Up to 1mL of cold PBS was then flushed into lung, withdrawn and the lavage fluid placed into a sterile 15mL tube. This was repeated 3 more times. The lavaged AMs were then used for downstream experiments. Mouse spleens were used in some experiments, and these were prepared by euthanizing the mouse using cervical dislocation, excising the organ and crushing it between a pair of glass microscope slides. The resulting cell suspension was then the subjected to ACK lysis culminating in a final resuspension of the cell suspension in 8mL of PBS.

Antigen	Clone	Conjugate	Titration	Manufacturer
CD45	30-F11	APC	1:200	BioLegend
MHCII	M5/114.15.2	BV510	1:200	BioLegend
SIGLEC-F	1RNM44N	eFluor 710	1:200	Invitrogen
CD11c	N418	FITC	1:200	eBioscience
NKR-P1B	2D12	Biotin	1:200	N/A
Clr-b	4A6	N/A	1:200	N/A
Rat IgG H+L	Polyclonal	488	1:750	Abcam

Table 2.1: List of Antibodies Used for Flow Cytometry.

2.3 Histology and Confocal Microscopy

For PAS staining formalin-fixed paraffin-embedded tissues were prepared by excising the lungs, placing them in sample cassette and immersing them in a container with neutral buffered formalin for 24 hours. After 24 hours the samples were washed twice with 70% ethanol and then embedded in paraffin wax. formalin-fixed paraffin-embedded tissues were cut at 5μm using a microtome, deparaffinated and stained with a PAS kit as per manufacturer's instructions (Abcam CAT# ab150680). Slides were deparaffinized by taking them through a series of graded xylene and alcohol washes, and then rehydrated in distilled water. Slides were covered with periodic acid solution for 10 minutes followed by 4 rinses in distilled water. Slides were then covered with Schiff reagent for 30 minutes and rinsed quickly in hot tap water to aid in colour development. Slides were counterstained with Mayer's hematoxylin for 1 minute and 15 seconds, rinsed in distilled water and then counterstained with light green solution for 1 minute. Slides were quickly rinsed in distilled water then dehydrated through a series of graded alcohols and mounted

in using a synthetic mounting medium. For ORO staining, stock solution was purchased from Sigma-Aldrich (CAT# 01391). For some experiments, lungs were inflated with OCT and 20% sucrose and snap frozen in liquid nitrogen followed by long term storage at -80ºC. Frozen sections were cut at 10µm using a cryostat then air dried for 30 minutes. ORO working solution was prepared by diluting 3 parts of stock ORO solution into 2 parts of distilled water. The solutions were mixed and left to sit at room temperature for 10 minutes. Afterwards the solution was passed through a Wattman filter paper. This working solution is stable for about 60 minutes. ORO staining was performed by fixing the sections with 3 washes of 60% isopropanol, the incubating them with working concentration of ORO solution for 15 minutes. Slides were then washed quickly with 60% isopropanol, counter-stained with Mayer's hematoxylin to highlight nuclei and then mounted using aqueous mounting media (Vectorlabs CAT# H-5501). Confocal microscopy was conducted on 10µm frozen lung sections. After cutting frozen blocks on a cryo-microtome, sections were fixed in acetone for 13 minutes and left to dry overnight. Sections were blocked with normal horse serum for 1 hour and then incubated with anti-SIGLEC-F antibody (Invitrogen CAT# 14-1702-82) overnight. Nuclei were highlighted using DraQ5 (Abcam CAT# ab108410) by incubating the sections with 1:1000 dilution of DraQ5 in PBS. In some experiments, fluorescent mounting media containing DAPI was used to highlight nuclei instead of DRAQ5. The sections were then mounted and visualized on a Zeiss LSM 550 confocal microscope or the Leica SP8 confocal microscope for some experiments. Mouse spleen frozen blocks were prepared by immersing the excised organ in OCT freezing media for 20 minutes and then snap freezing in liquid nitrogen. Frozen sections of spleens were prepared as described above.

2.4 Electron Microscopy

2, 6, and 12-week-old mice were lavaged as described above. Four mice were pooled together to obtain enough cells for one biological replicate. The cell pellet was fixed in 2.5% glutaraldehyde solution diluted with 0.1M sodium cacodylate buffer for 1 hour. The pellet was washed 3 times for 10 minutes with 0.1M sodium cacodylate buffer. Samples were then fixed with 1% osmium tetroxide for 2 hours. After a quick rinse with water samples were placed in 0.25% uranyl acetate and incubated overnight at 4^{o}C. Samples were dehydrated through a series of graded acetone baths (50%, 70%, 95% and 100% acetone) for 10 minutes each. Samples were infiltrated with epon araldite resin, first with a 3:1 ratio of acetone to resin for 3 hours, then with a 1:3 acetone to resin ration overnight and finally with 100% resin for 3 hours. Samples were imbedded into molds and placed into a 60^{o}C oven for 48 hours to cure. Samples were cut using a Reichert-Jung ultracut E ultramicrotome with a diamond knife and placed on 300 grade mesh copper grids and stained as follows: 2% aqueous uranyl acetate for 10 minutes, 2 rinses of distilled water for 5 minutes, lead citrate for 4 minutes, 1 rinse of distilled water and then left to air dry. Samples were then viewed on a JEOL JEM 1230 transmission electron microscope and images captured using a Hamamatsu ORCA-HR digital camera.

2.5 TMRE Assay

AMs from 2-week-old WT and *Nkrp1b*$^{-/-}$ mice were obtained by lavage. The AMs were pelleted, resuspended in RPMI and placed into separate wells of a 96-well plate. TMRE dye was added at a ratio of 1:1000 directly from stock solution. The wells were mixed, and cells incubated with TMRE for 20 minutes at 37^{o}C and 5% CO_2. AMs were then stained with fixable viability dye and other markers and used for flow cytometry.

2.6 2-NBDG Assay

AMs from 2-week-old WT and *Nkrp1b*$^{-/-}$ mice were obtained by lavage. The AMs were pelleted, resuspended in RPMI and placed into separate wells of a 96-well plate. 2-NBDG or vehicle was added to a final concentration of 25μM and left to incubate with the AMs for 20, 40 and 60 minutes. The cells were then pelleted, washed once with FACS buffer, stained for viability and other markers and subjected to flow cytometry.

2.7 Lipid Uptake Assays and NKR-P1B Cross-linking

NBD-labelled dipalmitol-phosphatidylcholine and phosphatidylglycerol were purchased from Avanti BioLipids (CAT# 810131, 801064 respectively) in powdered form. The lipid was then resuspended in 90% ethanol at a concentration of 4 mg/mL. For the assay a final lipid concentration of 20μg was applied to AMs obtained via lung lavage as described above and resuspended in 100μL of DMEM with no supplements and then allowed to incubate for 10, 20 and 40 minutes. Cells were then washed once with FACS buffer, stained for viability and immediately acquired on a flow cytometer without fixation. MFIs were used to analyze lipid uptake. In some experiments, lavaged AMs were first blocked using normal mouse serum, stained with biotinylated anti NKR-P1B (0.05mg/mL) antibody and then cross linked in suspension with streptavidin (0.02 mg/mL) for 1, 3, 6, or 16 hours and then analyzed for lipid uptake as described above. In some experiments, AKT inhibitor MK2206 (Sigma-Aldrich CAT# A6730) was added to the cells for 20, 40 or 60 minutes prior to lipid uptake analysis at a final concentration of 5μM. For some experiments GM-CSF was added to media prior to incubation with

fluorescent lipid. For these experiments, GM-CSF was added at 20U/mL for 6 hours prior to addition of fluorescent lipid.

2.8 *In situ* Hybridization

In situ hybridization was performed using the Roche DIG RNA labelling kit SP6/T7 (CAT# 11 175 025 910) with some modifications. Slides were deparaffinized, cut to a thickness of 3μm and treated with 30μg/mL of proteinase K for 5 minutes, fixed for 4% PFA for 10min and incubated with acetic 0.25% acetic anhydride solution In 0.1M triethanolamine solution for 10 minutes. Slides were prepared for hybridization using hybridization solution (50% v/v formamide and 5x SSC pH 4.5 with 2% w/v of blocking powder, 0.05% w/v CHAPS, 5mM EDTA, 50 μg/mL of heparin and 1 μg/mL of yeast RNA) in an oven set to 58ºC for 1 hour. Slides were the incubated with hybridization solution containing 500ng/mL DIG-labelled probes overnight at 56ºC. following hybridization, washes were performed using 2x SSC pH 7.5 and followed by a wash of 50% formamide/2x SSC pH4.5 at 55ºC three times at 10 minutes each. Slides were then stained with sheep anti-DIG, AP-conjugated antibody at a ratio of 1/1000 diluted in blocking solution at 4ºC overnight. Slides were washed 3 times for 5 minutes each Tris/NaCl buffer, equilibrated in NTM buffer (0.1M Tris-Cl pH9.5, 0.1M NaCl, 0.05 M $MgCl_2$). Color development was performed using NBT/BCIP substrates while in the dark at room temperature for a minimum of 20 minutes. Slides were counterstained eosin and scanned on a Leica Aperio slide scanner and visualized using the Leica Aperio-ImageScope software.

2.9 *In situ* Tetramer Staining

NKR-P1B Tetramer assembly was conducted from monomers (a generous gift from Dr. James Carlyle) by addition of PE-labelled streptavidin at a molecular ratio of 4:1 biotin monomer:streptavidin. 1/10th of the PE-labelled streptavidin was added at 15 minute intervals at 4^{o}C[102]. Frozen lung sections were cut at 10μm and left to air-dry for at least 3 hours. Native biotin was blocked using the BioLegend avidin-biotin blocking system (CAT# 927301) as per manufacturer's instructions. Sections were subsequently blocked using rodent M block (ThermoFisher CAT# 5083262) for 2 hours. Primary antibodies against CD45 (1:100) (BioLegend CAT# 103101) and PSPTC (1:500) (Abcam CAT# ab90716) and 1.1μg of NKR-P1B tetramers were applied to the sections and incubated overnight at 4^{o}C. Next day, sections were washed once in PBS and fixed using 4% PFA for 12 minutes and washed 3 times in PBS. The sections were then incubated for 2 hours with 1:100 anti-PE antibody (BioLegend CAT# 408101). The sections were washed and incubated with anti-rat IgG-AlexaFluor 488 (Invitrogen CAT# A-11001), anti-mouse IgG-AlexaFluor 555 (BioLegend CAT# 405324) and anti-goat IgG-Cy5 (Invitrogen CAT# A-10523) secondary antibodies for 1 hour at room temperature. Sections were then washed 3 times in PBS and mounted using Vectashield (Vector Labs CAT# H-1200-10), DAPI containing fluorescent mounting medium. Sections were imaged on a Leica SP8 confocal microscope.

2.10 *S. pneumoniae* and IAV (FMMA) infections

2, 6 and 12-week-old mice age and sex-matched mice were infected intranasally with 730 CFU/g bodyweight of *S. pneumoniae* encapsulated serotype III (ATCC 6303). Mice were

monitored for up to 7 days and sacrificed when reached appropriate endpoints. For CFU counts, mice were sacrificed at day 3 post-infection and lavaged as described previously. The lavage fluid was then plated onto fresh sheep blood agar plates and the alpha-hemolytic colonies, indicating *S. pneumoniae*, were counted and CFUs determined. In some experiments, mice were infected with 60 PFU of influenza-A virus (variant A/FM/1/47 H1N1 aka FMMA). At day 3 post-infection, mice were sacrificed and had their lungs processed in order to prepare frozen sections as described above.

2.11 *In vivo* BrdU Assay

2-week-old mice were injected with 1mg of BrdU intraperitoneally. 24 hours later mice were sacrificed and lavaged as described previously to obtain the alveolar macrophages. The cells were then processed using the BioLegend Phase-Flow kit (CAT# 370704) as per manufacturers instruction. The samples were then run on a BD-Fortessa flow cytometer and analyzed for cell cycle status.

2.12 *In vitro* Proliferation Assay

AMs were isolated from the lungs of 2 or 6-week-old WT and *Nkrp1b*$^{-/-}$ mice by lavage. Cells were counted and equal amounts were plated on standard 6-well tissue culture plates. Cells were allowed to adhere for 1 hour after which pictures were taken which represented the day 0 measure (baseline). After this GM-CSF or vehicle was added to the medium at a concentration of 75 U/mL to induce proliferation and pictures were taken on days 3 and days 6. Medium was changed every second day to ensure a steady supply of fresh GM-CSF.

2.13 *In vivo* Drug Treatment

Three-week-old *Ccr2*$^{-/-}$*Nkrp1b*$^{+/+}$ and *Ccr2*$^{-/-}$*Nkrp1b*$^{-/-}$ mice were given either regular water or water supplemented with pravastatin calculated to deliver 10 μg/g body weight of the drug each day. The mice were treated for two weeks after which the lungs were frozen and processed for ORO staining as described above. For SB203580, *Ccr2*$^{-/-}$ *Nkrp1b*$^{+/+}$ and *Ccr2*$^{-/-}$*Nkrp1b*$^{-/-}$ at 4 weeks of age were given the drug at a concentration of 1nM/g body weight intraperitoneally every second day for two weeks after which the mice were sacrificed, and lungs stained with ORO as described above. For MK2206, *Ccr2*$^{-/-}$*Nkrp1b*$^{+/+}$ and *Ccr2*$^{-/-}$*Nkrp1b*$^{-/-}$ of 4 weeks of age were given MK2206 via oral gavage at a concentration of 100 mg/kg body weight every second da For SSO, *Ccr2*$^{-/-}$ *Nkrp1b*$^{+/+}$ and *Ccr2*$^{-/-}$*Nkrp1b*$^{-/-}$ at 4 weeks of age were injected intraperitoneally with 50mg/kg of SSO every day for four days followed by a 3-day break from dosing.

2.14 NK Cell Depletion

NK cell depletion was achieved by intraperitoneally injecting anti-NK1.1 antibody, derived from the PK136 hybridoma, by injecting 200μg of anti-NK1.1 mAb. Depletion was maintained through injection of 100μg of anti-NK1.1 mAb every 48 hours.

2.15 Transfections

The full coding sequence for NKR-P1B and Clr-g was isolated from mouse cDNA and inserted into the pLJM1 vector (Addgene) and PcDH vector (Addgene) respectively. Lentiviral assembly was conducted in HEK293T cells by PEI transfection with the pLJM1 vector containing the NKR-P1B sequence or an empty pLJM1 vector, psPAX2 viral packaging vector and the pMD2G viral envelope vector in a ratio of 3:2:1 μg of

DNA. Cell supernatants were harvested 48 hours post transfection and lentiviral stocks were kept at -80ºC until further use. AMJ-C11 cell line was obtained from ATCC (CRL-2455). AMJ-C11 cells were transfected with supernatants containing the packaged lentiviruses containing either pLJM1 with NKRP1B or PLJM1 with no insert and selected using puromycin selection (8µg/mL as determined by a kill curve performed previously). Thus, we were able to generate stable cell lines from AMJ-C11 cells transfected with lentiviral vector containing NKR-P1B (AMJ-P1B) and a control stable cell line containing an empty lentiviral vector (AMJ-EV). NKR-P1B expression was confirmed by flow cytometry. For Clr-g experiments, MLE-12 cells were obtained from ATCC (CRL-2110). Cells were cultured in DMEM-F12 ITES defined media as per ATCC instructions. Transient transfections were conducted using FuGene (ProMega E2691) as per manufacturers instruction using PcDH vector containing the Clr-g coding sequence and empty PcDH vector which served as a control. Cells were then selected for transfectants using puromycin at an initial concentration of 4µg/mL for 48 hours and then reduced to 2µg/mL for the next 4 days. Cells were detached from the plate using a 10mM EDTA in PBS solution and stained with fixable viability dye and NKR-P1B tetramer at a concentration of 0.9µg per sample for 20 minutes. The samples were then acquired on a BD-Fortessa flow cytometer.

2.16 Immunoprecipitations

One day before starting the assay, anti-SHP1 antibody (generous gift from Dr. Andre Viellete) or biotinylated anti-NKR-P1B antibody were incubated with pre-washed protein-G agarose beads (ProteinMods) or neutravidin beads (Thermo Scientific CAT# 29202) respectively overnight at 4ºC in a rotating platform. Cells from AMJ-P1B and

AMJ-EV were cultured in AMJ growth medium as per ATCC specifications and subjected to 30μM stimulation for 20 minutes with pervanadate to inhibit phosphatase activity. After which the cells were spun down and lysed with protein lysis buffer (150mM NaCl, 50mM Tris-HCL pH 7.5, 1% NP-40, 1mM PMSF, 5mM EDTA and Roche protease inhibitor and phospho-stop cocktail (CAT#05 892 791 001, 04 906 845 001 respectively). Cells were lysed for 30 minutes with occasional agitation, then spun down at max speed for 15 minutes to remove cell debris. The lysates were pre-cleared with protein G-beads or neutravidin beads for 1 hour at 4ºC in a rotating platform. The lysates were then added to the beads with pre-attached antibodies as described above and incubated at 4ºC overnight in a rotating platform. The next day the bead-antibody-protein complexes were spun down and resuspend in 25μL of sample loading buffer with 20% mercapto-ethanol added and boiled for 15 minutes to ensure complete dissociation of the protein-antibody-bead complex. The samples were loaded onto an SDS-PAGE gel, transferred onto PVDF membranes and blocked overnight. Following blocking, the membrane was stained with 1º antibodies against SHP1 or against NKR-P1B and incubated overnight at 4ºC with agitation. The membranes were then washed and incubated with either anti-rabbit IgG-HRP (Cell Signalling CAT# 7074) or anti-mouse IgG-HRP (GE Healthcare CAT# NXA931) 2º antibodies for 2 hours at room temperature. Immunoprecipitations were visualized using BioRad (CAT#) ECL system and imaged on a BioRad image dock.

2.17 RNA Sequencing

Alveolar macrophages (approximately 100 000 cells per mouse) were extracted from 2-week-old mice mouse lungs by lavage as described above and sorted on a BD-FACS

ARIA-II cell sorter achieving an average 98% purity. RNA from the sorted AMs was extracted using Ribozol (VWR CAT# 97064-952) in conjunction with ZymoReserach RNA clean-up and concentrator kit (CAT# R1016) to achieve the required purity and quantity of RNA for sequencing (20ng/μL in a total of 15μL). 5 mice were pooled together to represent one biological replicate. The RNA sequencing was performed by Genome Quebec (McGill university) by creating a cDNA libraries using tagmentation which were then run on a HiSeq 4000 PE100 to a read depth of 30 million reads/sample. FASTQ files were uploaded to the Galaxy web platform and analyzed using the public usegalaxy.org server. Analysis was performed by trimming off Illumina primer sequences using Trimmomatic software, sequences were then aligned to a reference genome using Bowtie2, read number and length was aligned to the reference genome using the CuffLinks package and significant differential expression of genes was performed using the CuffDiff software package. Differential pathway overrepresentation tests were conducted by using GENEONTOLOGY Panther software for biological processes using Fisher's exact test and false discovery rate for multiple correction test. Genes present in significantly overrepresented pathways were then analyzed for variable gene expression profiling using Morpheus web-based tool. Top 30 genes from selected overrepresented categories were displayed on heatmaps as Log2 Z-score values with a rows being clustered using one minus Pearson correlation index with average linkages.

2.18 qPCR Analysis

AMs from WT and *Nkrp1b*$^{-/-}$ mice were lavaged as described above, pelleted and resuspended in Ribozol to lyse AMs for RNA extraction. An RNA Isolation Kit (Zymo Research; cat # R1016) was used to additionally purify the extracted RNA, which was

then used in a reverse-transcription reaction primed by random hexamer polynucleotides to make cDNA using RevertAid First Strand cDNA Synthesis kit (Thermo Scientific; cat # K1622). SYBR green-based quantitative PCR (qPCR) was performed on 0.1-0.5μg of cDNA using NEB Luna Universal qPCR Master Mix (NEB; cat # M3003S/L/X/E). During data analysis, *5S rRNA* was used as the internal control, and changes in the quantity of gene transcripts in *Nkrp1b-/-* AMs were normalised to those in WT AMs. The fold changes in the transcript levels were transformed using the binary logarithm to produce the log2 fold change in transcripts in *Nkrp1b-/-* AMs relative to the WT. Target genes were chosen by assessing the results from RNA sequencing previously performed on *Nkrp1b-/-* and WT AMs. The candidate genes include *CD36*, *CD63*, *Ldlr*, *Nceh*, *ABCA1*, *ABCG1*, *Ppar-γ*, *HMGCoA*, *Serpinb6*, *Rara*, *Fabp5*, *ApoE* and *Psap*. Refer to Table 2.2 for detailed primer list

2.19 Lipidomics Analysis

AMs were collected by lavage from 6-week-old mice as described above yielding on average 100 000 cell from WT mice and 20 000 cells from *Nkrp1b*$^{-/-}$ mice. 4 mice were pooled to represent one biological replicate. The lavage fluid was spun at 500g for 5 minutes, supernatant removed, and cell pellet frozen at -80ºC for analysis. Analysis was performed at the Laboratory of Genetic Metabolic Diseases, University of Amsterdam. The HPLC system consisted of an Ultimate 3000 binary HPLC pump, a vacuum degasser, a column temperature controller, and an auto sampler (Thermo Scientific, Waltham, MA, USA). The column temperature was maintained at 25 ◦C. The lipid extract was injected onto a “normal phase column” LiChrospher 2x250-mm silica-60 column, 5 μm particle diameter (Merck, Darmstadt, Germany) and a “reverse phase

column" Acquity UPLC HSS T3, 1.8 μm particle diameter (Waters, Milford Massachusetts, USA). A Q-Exactive Plus Orbitrap (Thermo Scientific) mass spectrometer was used in the negative and positive electrospray ionization mode. In both ionization modes, mass spectra of the lipid species were obtained by continuous scanning from m/z 150 to m/z 2000 with a resolution of 280,000 full width at half maximum (FWHM).

2.20 Statistical Analysis

Statistical significance was determined by Student *t* test where applicable, with a cut-off *P* value of 0.05. Other experiments, where appropriate utilized a two-way ANOVA analysis with Sidak's correction for multiple comparisons. Significance in survival experiments was determined using the log-rank test with a cut-off *P* value of 0.05.

PRIMERS USED FOR QPCR	
Target Gene	**Sequence (Forward, Reverse)**
ABCA1	5'-ATGGAGCAGGGAAGACCAC-3' 5'-GTAGGCCGTGCCAGAAGTT-3'
ABCG1	5'-GGCCTGTCTGATGGCCGCTT-3' 3'-AGAGTAGCTGCTGGCATTC-3'
ApoE	5'-GAGTGGCAAAGCAACCAAC-3' 5'-TTCCGTCATAGTGTCCTCCA-3'
CD36	5'-GAACCACTGCTTTCAAAAACTGG-3' 5'-TGCTGTTCTTTCGCCACGTCA-3'
CD63	5'-CGGTGGAAGGAGGAATGAAG-3' 5'-CTACATTACTTCATAGCCACTTCG-3'
Fabp5	5'-CGACCGTGTTCTCTTGTAACC-3' 5'-TCCCATCCTTCAGTTTCCTTG-3'
HMGCoA	5'-CTTGTGGAATGCCTTGTGATTG-3' 5'-AGCCGAAGCAGCACATGT-3'
Ldlr	5'-AGGCTGTGGGCTCCATAGG-3' 5'-TGCGGTCCAGGGTCATCT-3'
Nceh	5'-CAGCTGTGCACAACAATGG-3' 5'-GACCTGTGGGACTAGCTTGT-3'
Pparg	5'-CTGTGGACCTCTCCGTGATG-3' 5'-CCATTGGGTCAGCTCTTGTG-3'
Psap	5'-CCTGTCCAAGACCCGAAGAC-3' 5′-CAAGGAAGGGATTTCGCTGTG-3′
Rara	5'-CTGGACTGCTCAGTGCCATCT-3' 5'-TGCAGCATGTCCACCTTGTC-3'
Serpinb6	5'-ATGACGGTGAGGTGCATGAG-3' 5'-TTAACATGGTGAATGAAGAAAAGGAA-3'
5S rRNA	5'-GCCCGATCTCGTCTGATCT-3' 5'-AGCCTACAGCACCCGGTAT-3'
PRIMERS USED FOR GENOTYPING	
Target Gene	**Sequence (Forward, Reverse)**
Nkrp1b	(R WT) 5'-GAACATCTTCCTCATCGGTC-3' (R KO) 5'-GCTGCTTAAGGGATTCCATG-3' (F common) 5'-GAGCAAAGCTGCTATTGGCC-3'
Clrb	5'-TTTCAATCCTGTAGTGGAAA-3' 5'-CAGCTCATCCTGGTTGTC-3'
Ccr2	(R WT) 5'-CACAGCATGAACAATAGCCAAG-3' (R KO) 5'-CCTTCTATCGCCTTCTTGACG-3' (F common) 5'-CCACAGAATCAAAGGAAATGG-3'
PRIMERS USED TO MAKE RNA PROBES	
Clrg	5'-AGATTGCTTGGAGACAGGAG-3' 5'-GAAGAGTCTCTTGGTTAAGTG-3'

Table 2.2: Table of Primers Used in This Work.

Chapter 3: NKR-P1B Deficiency Characterization

3.1 *Nkrp1b*$^{-/-}$ Mice Exhibit Greater Mortality and Morbidity Upon Infection with *S. Pneumoniae.*

3.1.1 6-Week-Old *Nkrp1b*$^{-/-}$ And 12-Week-Old *Nkrp1b*$^{+/-}$ Mice Have a Drastic Decrease on Survival Rates.

Several studies demonstrated the importance of C-type lectin receptors in the maintenance of immune function and homeostasis[119,122]. Our previous research shows the importance of Ly49 in pulmonary immunity against virus infection[247] and the importance of NKR-P1B in maintaining gut homeostasis[248]. Likewise, as previously described, NKR-P1B exhibits broad distribution among leukocytes and is involved in anti-bacterial responses in the intestine and potentially anti-viral responses in the lungs as well. Based on these observations we investigated whether NKR-P1B plays a role in respiratory immune responses as well. To this end, we infected healthy, 6-week-old WT and *Nkrp1b*$^{-/-}$ littermates with *Streptococcus pneumoniae*. While around 75% of WT mice were able to clear and survive *S. pneumoniae* infection, *Nkrp1b*$^{-/-}$ mice showed 100% lethality by day 4 of the experiment as determined by mice reaching humane endpoints (Fig. 3.1a). An inability to clear the pneumococcal infection was also observed in older, 12-week-old *Nkrp1b*$^{-/-}$ mice infected with *S. pneumoniae*, with only a 24-hour delay until the onset of mortality (Fig. 3.1b), demonstrating the significant vulnerability of *Nkrp1b*$^{-/-}$ mice to pneumococcal infection.

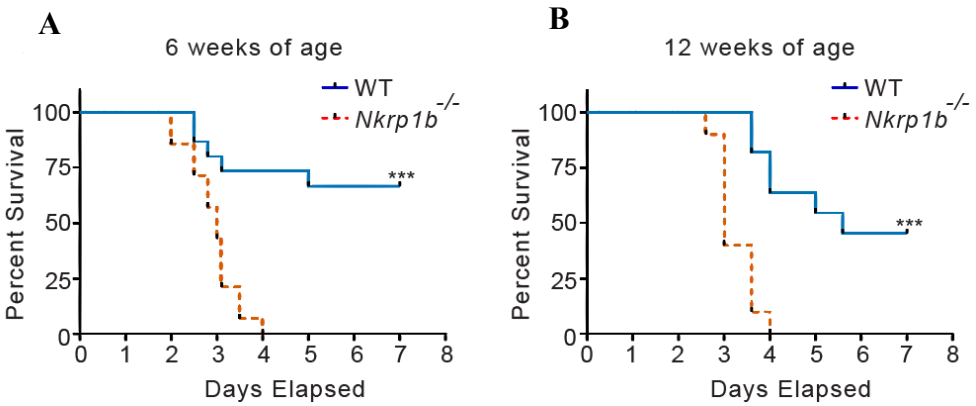

Figure 3.1: Pneumococcal challenge in *Nkrp1b*$^{-/-}$ mice.
(A and B) Kaplan-Meyer curves of WT versus *Nkrp1b*$^{-/-}$ mice susceptibility to *S. pneumoniae* at 6- and 12-weeks of age respectively. WT N = 16 and 13, respectively, *Nkrp1b*$^{-/-}$ N = 15 and 12, respectively.

To determine the extent of NKR-P1B contribution to the clearance of *S. pneumoniae*, we infected 6 and 12-week-old NKR-P1B heterozygotes with the same dose of *S. pneumoniae* and assayed survival. At 6-weeks of age both WT and *Nkrp1*$^{+/-}$ mouse survival was similar upon *S. pneumoniae* infection, while 12-week-old *Nkrp1*$^{+/-}$ mice succumbed by day 3.5 of the experiment, highlighting a potential haploinsufficiency (Fig. 3.2) which is most evident at 12-weeks of age.

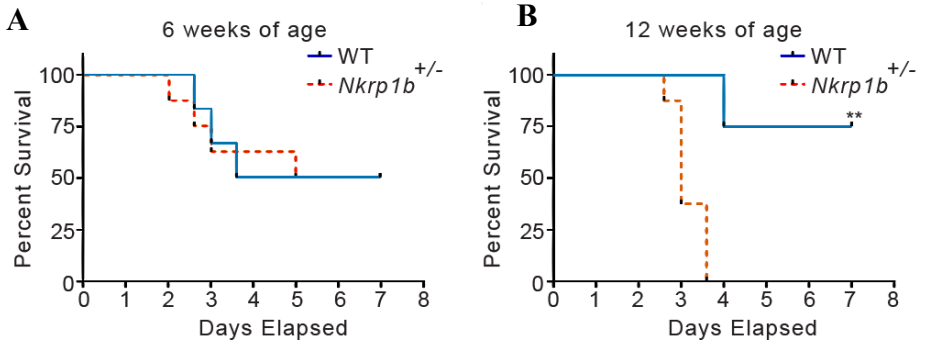

Figure 3.2: Pneumococcal challenge in *Nkrp1b*$^{+/-}$ mice.
(A and B) Kaplan-Meyer curves of WT versus *Nkrp1*$^{+/-}$ mice susceptibility to *S. pneumoniae* at 6- and 12-weeks of age respectively. WT N = 6 and 3, respectively, *Nkrp1b*$^{-/-}$ N = 8 and 9, respectively.

These results show that not only are *Nkrp1b*$^{-/-}$ mice highly susceptible to pneumococcal infection but that the possibility of a haploinsufficiency exists as well due to the increased vulnerability of 12-week-old *Nkrp1b*$^{+/-}$ mice to pneumococcal infection.

3.1.2 *Nkrp1b*$^{-/-}$ Mice Experience Greater Bacterial Burnden and Increased Pulmonary Pathology Post Pneumococcal Infection.

To assess the cause of this enhanced mortality, we examined gross lung pathology of *Nkrp1b*$^{-/-}$ mice 3 days post-infection, before the onset of mortality, using H/E staining of the total lung. *Nkrp1b*$^{-/-}$ mice showed significant alveolar epithelial damage as seen in Fig 3.3 compared to WT. Regions of increased inflammation, alveolar leakage and obstructive changes have been highlighted with arrows.

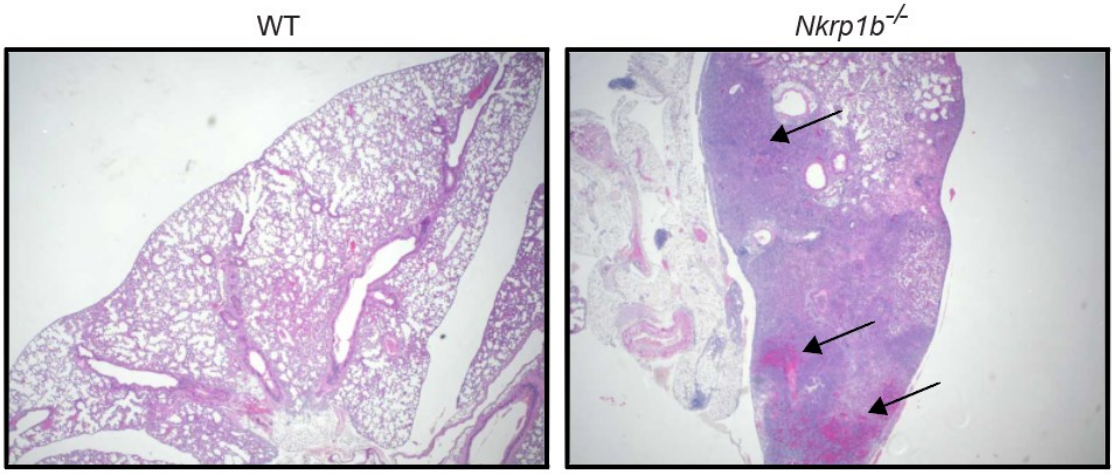

Figure 3.3: H/E staining of WT and *Nkrp1b*$^{-/-}$ mouse lungs post pneumococcal challenge.
Images of mouse lungs stained with H/E, 3 days post-*S. pneumoniae* infection at 5x magnification. Images are representative of 3 separate experiments. Arrows indicate areas of severe alveolar inflammation, bronchopneumonia and obstructive changes compounded with the destruction of local vasculature causing bleeding into the alveolar space.

Pathological scoring and analysis of lung sections from infected 6 and 12-week-old WT and *Nkrp1b*$^{-/-}$ littermates show an increase in peri-bronchial and alveolar inflammation as well as a general increase in the amount of inflamed tissue present in *Nkrp1b*$^{-/-}$ mice (Fig. 3.4a-c). Likewise, there is an increase in obstructive changes present in the alveolar epithelium which is a likely contributor to increased *Nkrp1b*$^{-/-}$ mouse mortality by reducing the surface area that is available for gas exchange (Fig. 3.4d). These results also highlight the vulnerability of *Nkrp1b*$^{-/-}$ mice to pneumococcal infection at both 6 and 12 weeks of age, with only minor differences in pathological inflammation and obstructive changes present in the pulmonary space. Death in *Nkrp1b*$^{-/-}$ mice is likely due to runaway inflammation in response to pneumococcal insult and the resulting failure of the lungs to maintain efficient gas exchange.

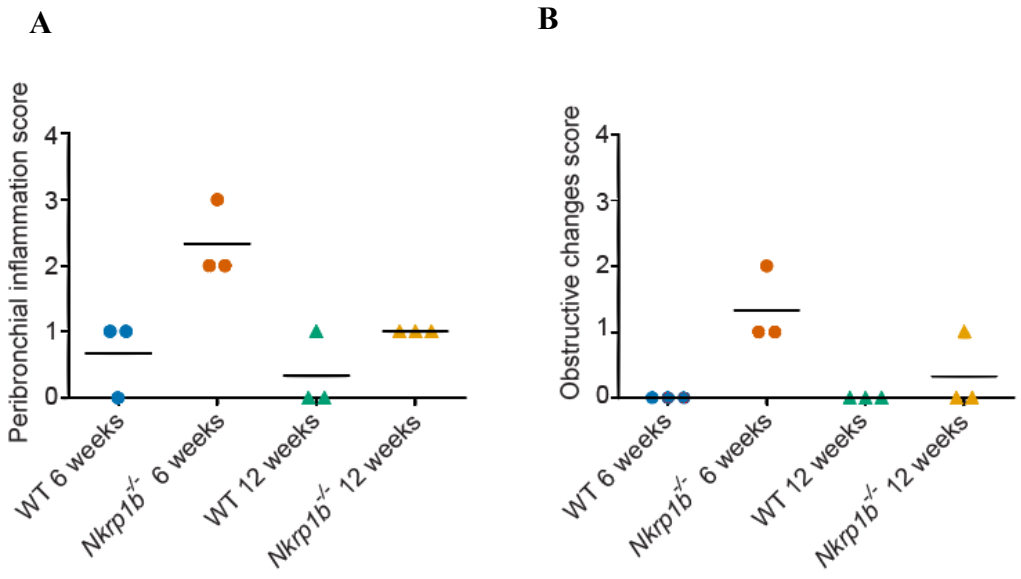

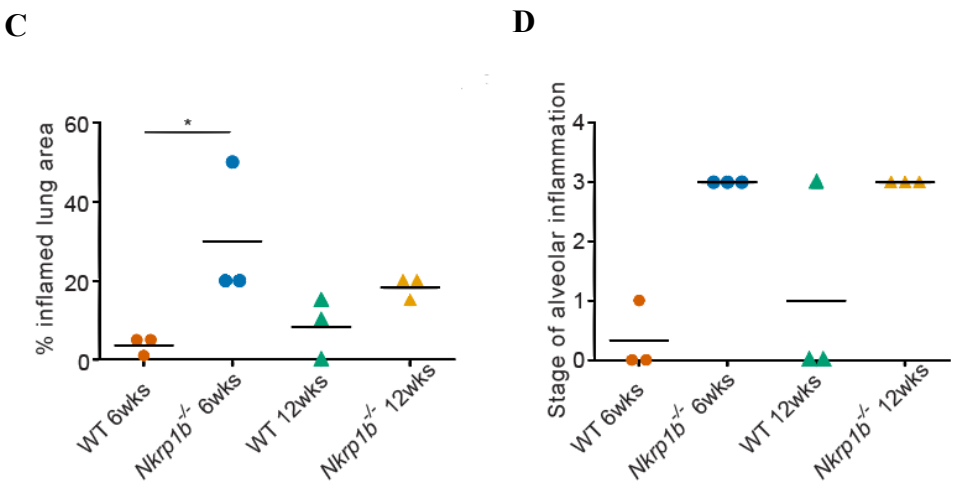

Figure 3.4: Pathological analysis of lungs from WT and *Nkrp1b*$^{-/-}$ mice post pneumococcal infection.
(A-D) Pathological interpretations of H/E-stained mouse lung sections extracted from 6- and 12-week-old WT and *Nkrp1b*$^{-/-}$ mice 3 days post-infection with *S. pneumoniae*. The analysis involved scoring peribronchial and alveolar inflammation, percent inflamed area and obstructive changes. N=3 for each genotype at every time point analyzed. Statistics determined by Student's t-test where * is $P = <0.05$.

To characterize this pneumococcal vulnerability further we decided to analyze the lavage fluid of WT and *Nkrp1b*$^{-/-}$ mice for bacterial burden 3 days post-infection. As can be seen in Fig. 3.5, bacterial burden, as determined by CFU counts on blood agar from plated lavage fluid, appeared to be 3 times higher in *Nkrp1b*$^{-/-}$ mice compared to WT mice. No hemolytic bacteria were present in the lungs of mock-infected mice at all since hemolytic bacteria are not part of natural lung flora and would therefore not be detected as such on blood agar. These results suggest a profound inability to clear pathogenic bacteria which is a fundamental function of pulmonary immunity.

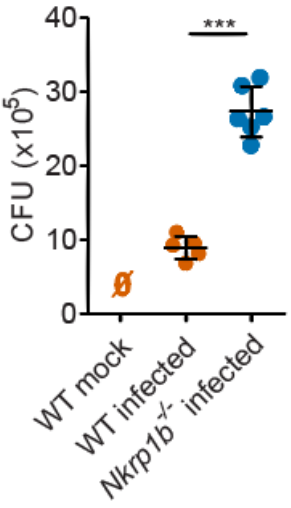

Figure 3.5: CFU analysis of lavage fluid from WT and *Nkrp1b*$^{-/-}$ mice post pneumococcal challenge.
CFU counts of WT and *Nkrp1b*$^{-/-}$ mice 3 days post pneumococcal infections as determined by plating lavage fluid on blood agar plates. Error bars represent the standard error of means (SEM). Statistical significance determined by Students t-test where *** is p = <0.0005. N = 5 for WT and N = 6 for *Nkrp1b*$^{-/-}$ mice.

3.1.3 NK Cell Depletion or Absence of Clr-b Have No Effect on Survival Rates Following Pneumococcal Challenge.

Since NKR-P1B is traditionally an NK-cell-associated receptor, we wanted to determine whether the observed pneumococcal susceptibility observed in *Nkrb1p*$^{-/-}$ mice was due to NK cell dysfunction. Using antibody-mediated NK cell depletion, which was begun prior to infection and continued throughout the treatment, allowed us to determine NK cell contribution to the observed phenotype. As seen in Fig. 3.6, mortality rates were not significantly different between WT mice and WT mice which have undergone NK cell depletion, thus concluding that NK cells do not appear to contribute to the increased mortality observed in *Nkrb1p*$^{-/-}$ mice.

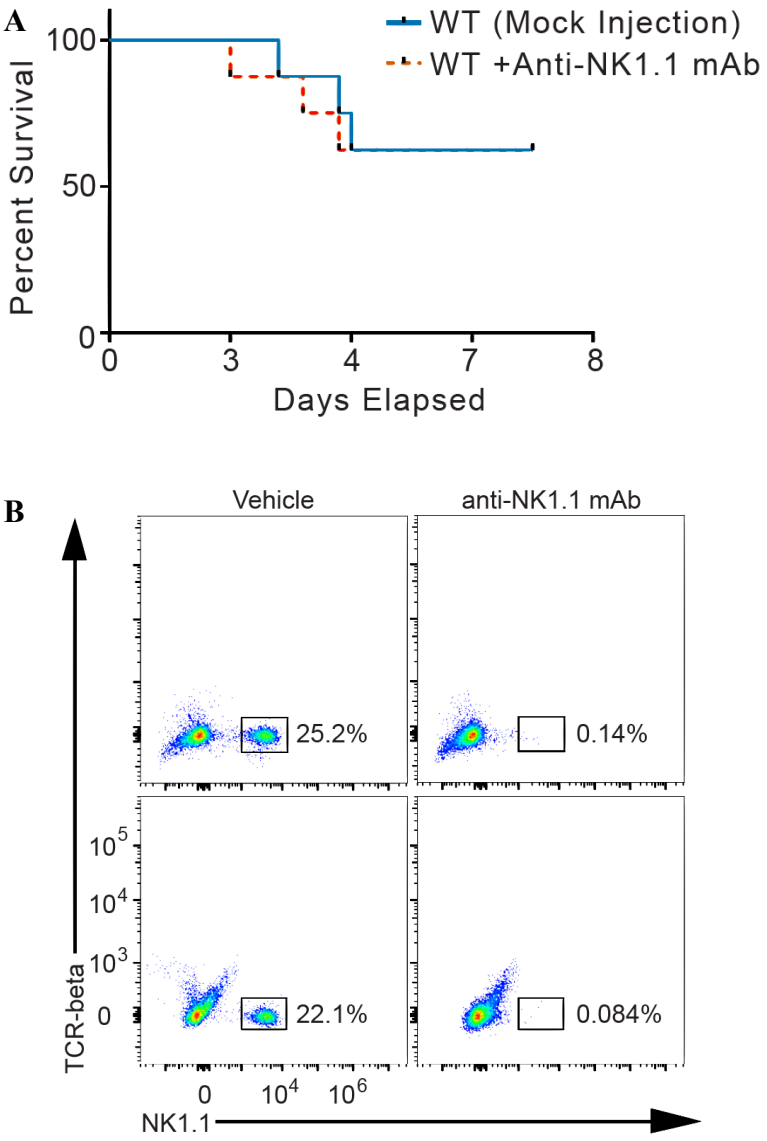

Figure 3.6: Pneumococcal challenge in WT mice post-NK-cell depletion.
(A) Kaplan-Meyer curves of WT mice susceptibility to *S. pneumoniae* after depletion of NK cells via anti-NK.1.1 mAb or a mock injection. N = 8. (B) Flow cytometry dot plots showing percent depletion of NK in WT mice using either a vehicle injection or anti-NK1.1 mAb. Top panel shows NK cell depletion in the lungs, bottom panel shows NK cell depletion in the spleen. Dot plots representative of 3 independent experiments.

NKR-P1B expressed on NK cells is known to interact with Clr-b expressed on target cells. By utilizing *Clr-b*$^{-/-}$ mice we are able to assess this interaction in the absence of NKR-P1B's ligand as well. Since we noticed the dramatic vulnerability to pneumococcal

infection in *Nkrp1b*$^{-/-}$ mice, we were interested in determining whether a similar vulnerability exists in mice deficient in Clr-b as well. As seen in Fig. 3.7, *Clr-b*$^{-/-}$ mice were found to not be significantly more susceptible than WT mice, unlike their *Nkrp1b*$^{-/-}$ counterparts. This lack of phenocopying between *Nkrp1b*$^{-/-}$ and *Clr-b*$^{-/-}$ mice in the context of pneumococcal infection heavily implies that the known interaction between NKR-P1B and Clr-b appears to be decoupled in the context of pulmonary immunity.

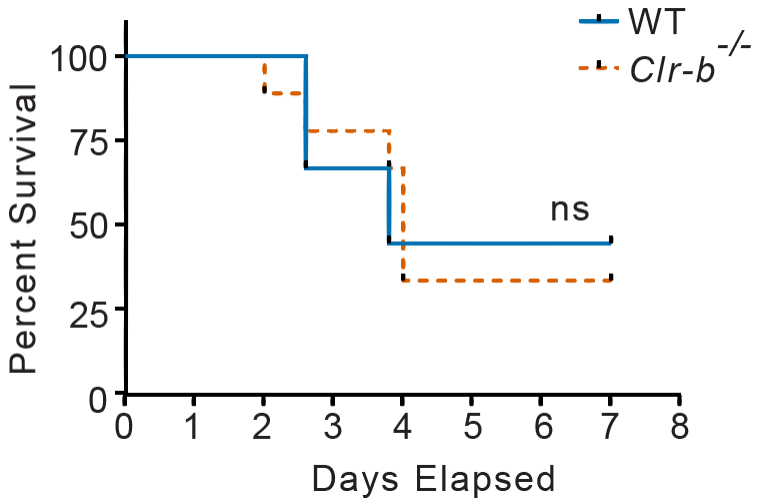

Figure 3.7: Comparison of vulnerability to pneumococcal infection of WT and *Clrb*$^{-/-}$ mice.
Kaplan-Meyer curves comparing susceptibility to pneumococcal infection of WT and *Clrb*$^{-/-}$ mice at 6 weeks of age. N = 9 for both groups.

The above data indicate that mice deficient in NKR-P1B exhibit dramatic loss of ability to resist pneumococcal infection and increased bacterial burden resulting in significantly elevated mortality, independent of classical NK and NKT cells. This mortality is likely due to a combination of increased bacterial burden as well as increased inflammation which then inhibits gas exchange causing death due to respiratory failure. It also appears that the Clr-b deficient mouse do not phenocopy the NKR-P1B deficient mouse upon

pneumococcal challenge, potentially implying that in the context of pulmonary immunity against pneumococci the classical NKR-P1B:Clr-b receptor-ligand relationship is not a relevant factor.

3.2 AMs Express NKR-P1B And *Nkrp1b*$^{-/-}$ Mice Show a Time-Dependent Collapse of The AM Population Followed By a CCR2 Mediated Recovery at Steady State.

3.2.1 NKR-P1B Is Expressed on AMs And *Nkrp1b*$^{-/-}$ Mice Exhibit a Slow Age-Dependent Collapse of The AM Niche

The NKR-P1B requirement for clearance of *S. pneumonia* led us to explore whether any constituents of the lung immune milieu were detectably altered in *Nkrp1b*$^{-/-}$ mice at steady-state. Utilizing flow cytometry, we proceeded to characterize the major immune populations in the lungs of adult 6-week-old *Nkrp1b*$^{-/-}$ mice compared to WT mice. This analysis revealed a surprising and significant decrease in the number of alveolar macrophages (AMØ) in *Nkrp1b*$^{-/-}$ mice, while levels of other major immune cells remained unchanged (Fig. 3.8).

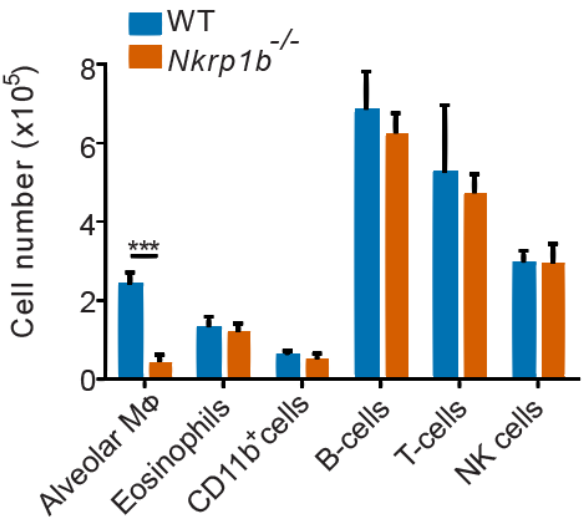

Figure 3.8: Immune cell numbers in the lungs of WT and *Nkrp1b*$^{-/-}$ mice at steady-state.
The number of various immune cells present in the lungs of WT and *Nkrp1b*$^{-/-}$ mice at 6 weeks of age as determined by flow cytometric phenotyping. Error bars represent SEM. Significance determined by Students t-test where *** is P = <0.0005

Resident AMs are at the frontline of pulmonary defense against bacterial pathogens, and therefore develop very early in mice, becoming terminally differentiated and present in large numbers by 2 weeks-of-age. Since we have shown a deficiency in AMs at the 6-week time point, we next determined how NKR-P1B loss affects AMs population kinetics relative to the age of the mice. As seen in Fig. 3.9a, AMs (gated on live CD45^{+}, SIGLEC-F^{+}, MHC-II^{lo}) in *Nkrp1b*$^{-/-}$ mice show a dramatic reduction at 6 weeks of age. Quantifications of flow cytometry results show approximately 400,000 AMØ in the lungs at 2 weeks of age, which then stabilizes to around 250,000 cells/lung up until 21 weeks in WT mice. Conversely, the number of AMs in *Nkrp1b*$^{-/-}$ mouse lungs at 2 weeks of age are similar to WT numbers, but decline significantly with age, with the lowest number of AMs detected at 6 weeks of age before the lung is re-populated at 12 weeks (Fig. 3.9b).

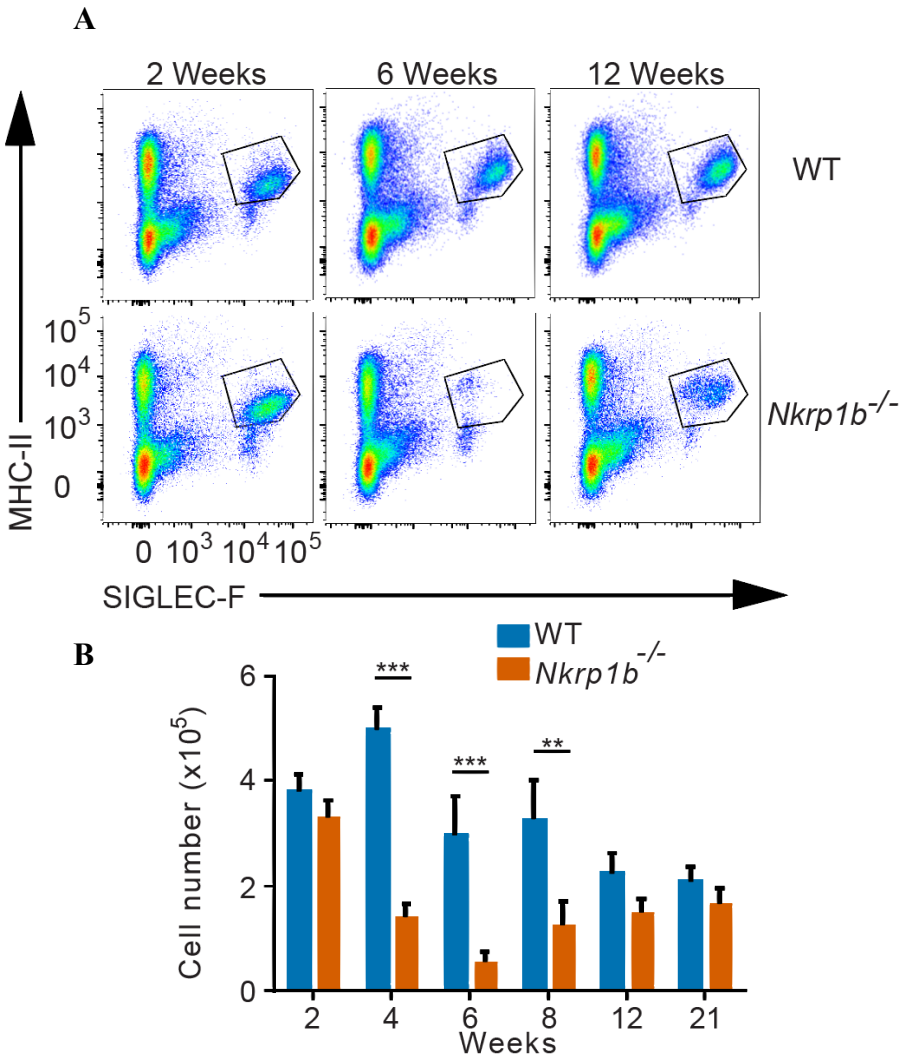

Figure 3.9: Cytometric analysis of AMs in WT and *Nkrp1b*$^{-/-}$ mice from ages 2-12 weeks.
(A) Representative flow cytometry dot plots of AMs found in the lungs of WT and *Nkrp1b*$^{-/-}$ mice at 2, 6 and 12 weeks of age. Images are representative of 7 different experiments.
(B) Quantifications of AMs obtained by flow cytometric analysis from WT and *Nkrp1b*$^{-/-}$ mice at 2, 4, 6, 8, 12 and 21 weeks of age. Statistical significance was determined by two-way ANOVA with Tukey's correction where ** is P = <0.005 and *** P = <0.0005. N = 7

In agreement with these observations, anti-SIGLEC-F immunofluorescent staining of mouse lungs showed AMs (large, SIGLEC-F^{+} cells) distributed throughout the lungs of WT mice at all ages, while *Nkrp1b*$^{-/-}$ mouse lungs showed a significant decrease in detectable AMs at 6 weeks of age followed by subsequent reconstitution (Fig. 3.10a and

Fig. 3.10b). These corroborating results indicate a clear age-dependent collapse and reconstitution of AMs in mice lacking NKR-P1B expression.

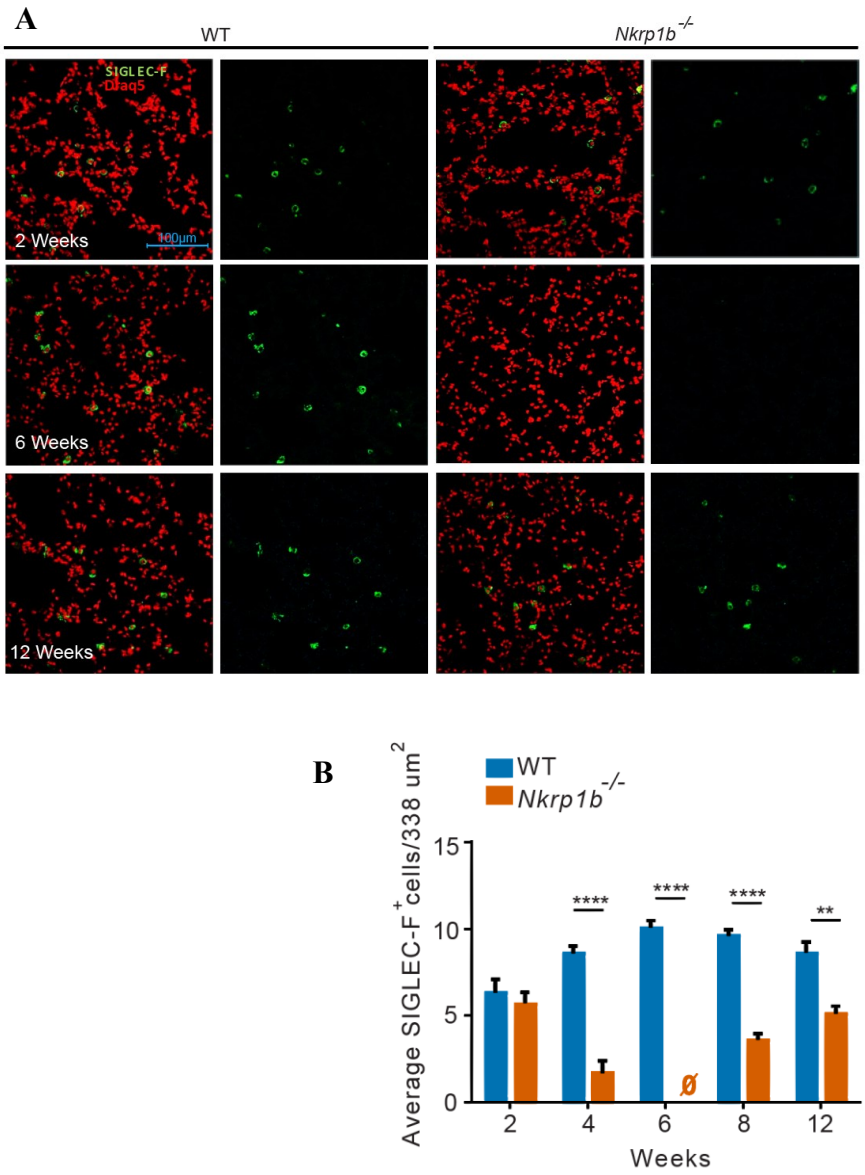

Figure 3.10: Microscopic analysis of AMs in WT and *Nkrp1b*$^{-/-}$ mice from ages 2-12 weeks.
(A) Representative compiled stack images of frozen WT and *Nkrp1b*$^{-/-}$ lungs stained with anti-SIGLEC-F antibody (green) and the nuclear stain DRAQ5 (Red). Images are representative of 6 experiments.
(B) Quantifications of AMs present in the lungs of WT and *Nkrp1b*$^{-/-}$ mice as determined by confocal staining in (E). Data presented as number of SIGLEC-F positive cells/338um^2. N = 6

AMs also possess a unique phenotype compared to other tissue-resident macrophages that is characterized by low CD11b expression and slightly lower levels of F4/80[185]. To follow up on our observations of AM population dynamics we were interested to see if AM differentiation was also affected. We also performed a cytometric analysis of certain surface AM surface markers and noticed that the levels of F4/80 and specifically CD11b were dysregulated compared to WT AMs (Fig. 3.11). Suggesting potential dysregulation in terminal AM differentiation.

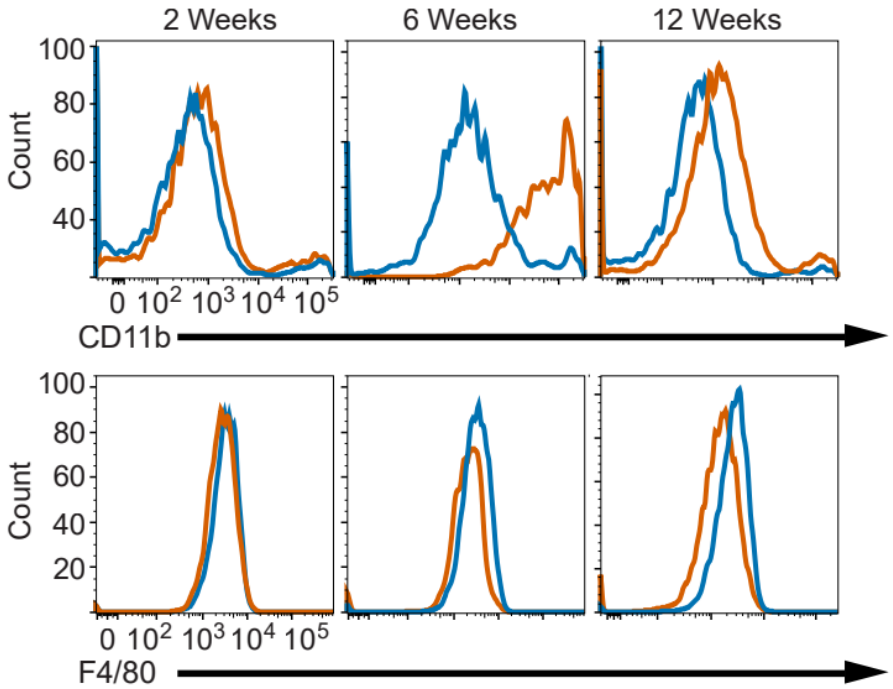

Figure 3.11: Expression profile of AM cell surface markers.
Expression profile of CD11b and F4/80 on AMs obtained from 2, 6 and 12-week-old WT and *Nkrp1b*$^{-/-}$ mice. The histogram is representative of 3 independent experiments.

Following through on these observations we wanted to determine whether AMs express NKR-P1B. This was performed by flow cytometric analysis using anti-NKR-P1B antibody (2D12 from here on out), to look for the presence of NKR-P1B on the cell surface. AMs from 2-week-old mice, prior to the collapse of the population but

sufficiently post-partum so that the AM population is fully developed, were stained with 2D12 and the presence of NKR-P1B was detected as seen in Fig. 3.12a. Interestingly, experiments conducted on neonatal littermates detected the trace presence of NKR-P1B on AMs as early as 3 days post-partum, when AMs reach the peak of their proliferative and differentiation burst (Fig. 3.12b). Analyzing NKR-P1B expression on *Nkrp1b*$^{+/-}$ mice revealed an interesting observation regarding NKR-P1B expression. Whereas NK cells either do or do not express NKR-P1B in a binary manner, with *Nkrp1b*$^{+/-}$ NK cells showing a 50/50 split between cells with and without NKR-P1B in context of AMs it appears that every *Nkrp1b*$^{+/-}$ AM has half as much NKR-P1B on the surface (Fig. 3.12c), which could be the causative factor behind the apparent haplo-insufficiency observed in the previous section.

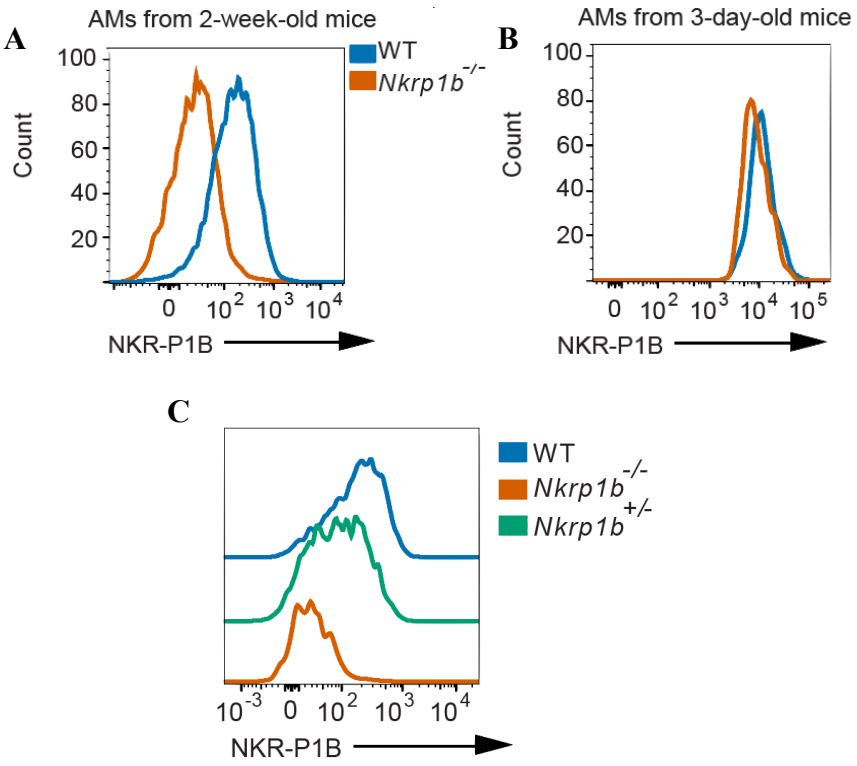

Figure 3.12: Expression of NKR-P1B on the surface of AMs.
(A) Expression profile of NKR-P1B on AMs obtained from 2-week-old WT and *Nkrp1b*$^{-/-}$ mice. The histogram is representative of 3 independent experiments.
(B) Expression profile of NKR-P1B on AMs obtained from 3-day-old WT and *Nkrp1b*$^{-/-}$ neonates. The histogram is representative of 2 independent experiments.
(C) Expression profile of NKR-P1B on AMs obtained from 2-week-old WT, *Nkrp1b*$^{+/-}$ and *Nkrp1b*$^{-/-}$ mice. Histogram is representative of 3 independent experiments.

To further characterize the potential haploinsufficiency present in *Nkrp1b*$^{+/-}$ mice we performed flow cytometric analysis of AMs in these mice to determine how the population changes compared to *Nkrp1b*$^{-/-}$ mice. As seen in Fig. 3.13a and Fig. 3.13b, *Nkrp1b*$^{+/-}$ mice appear to have a full complement of AMs until about 12 weeks-of-age, at which point the AM population is dramatically decreased compared to WT. Note that *Nkrp1b*$^{-/-}$ mice have begun reconstituting their AMs at the 12-week time point after reaching a low at 6-weeks-of age. These results are indicative of a haploinsufficiency in which AMs from *Nkrp1b*$^{+/-}$ mice appear to be on a 6-week delay in terms of collapse.

These results suggest that half as much NKR-P1B on the surface of AMs is able to temporarily compensate in the absence of a full NKR-P1B surface complement for about 6 extra weeks before AMs undergo a collapse.

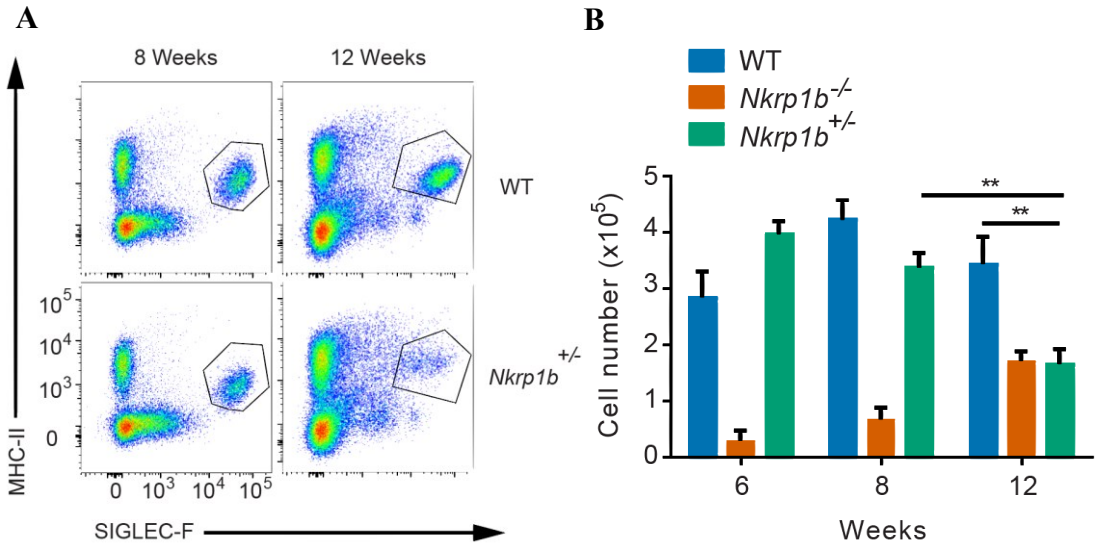

Figure 3.13: Cytometric analysis of AMs in WT, *Nkrp1b*$^{-/-}$ and *Nkrp1b*$^{+/-}$ mice at 6, 8 and 12 weeks of age.
(A) Representative flow cytometry plots of AMs found in the lungs of WT, *Nkrp1b*$^{+/-}$ mice at 8 and 12 weeks of age. Images are representative of 6 experiments.
(B) Quantification of AMs found in the lungs of WT, *Nkrp1b*$^{-/-}$, and *Nkrp1b*$^{+/-}$ mice at 8 and 12 weeks of age. N = 6-7 Statistical significance was determined by two-way ANOVA with Tukey's correction where ** is P = <0.005

3.2.2 Reconstitution of AMs in *Nkrp1b*$^{-/-}$ mice is CCR2-dependent.

Under certain circumstances, such as lower respiratory tract infections, blood monocytes infiltrate the alveolar niche, through a CCR2-mediated mechanism and differentiate into fully functioning AMs [249,250]. To assess the origin of the reconstituted macrophage population, we generated CCR2/NKR-P1B double knockout mice (*Nkrp1b*$^{-/-}$*Ccr2*$^{-/-}$). Tissue-resident AMs have previously been shown to not express CCR2 and do not depend on it for migration, however, peripheral blood monocytes do [251], therefore the tissue-resident AM population dynamics of *Nkrp1b*$^{-/-}$*Ccr2*$^{-/-}$ should be similar to WT

mice, especially in juveniles and mice reaching middle age. The lungs of WT, *Nkrp1b*$^{-/-}$ *Ccr2*$^{+/+}$and *Nkrp1b*$^{-/-}$*Ccr2*$^{-/-}$ littermates of various ages were analyzed by flow cytometry to determine the origin of reconstituted AMs. As seen in Fig. 3.14a and Fig. 3.14b, *Nkrp1b*$^{-/-}$*Ccr2*$^{-/-}$ mice fail to reconstitute AMs at adequate numbers by 12-weeks-of-age. Only a marginal increase in AMs was observed in the lungs of *Nkrp1b*$^{-/-}$*Ccr2*$^{-/-}$ by 21 weeks-of-age, at which point the alveolar niche in *Nkrp1b*$^{-/-}$*Ccr2*$^{+/+}$ mice is essentially fully repopulated. These results show that AM replenishment in *Nkrp1b*$^{-/-}$ mice is driven by peripheral blood monocytes in a primarily CCR2-dependent mechanism, with some marginal infiltration occurring through other alternate pathways.

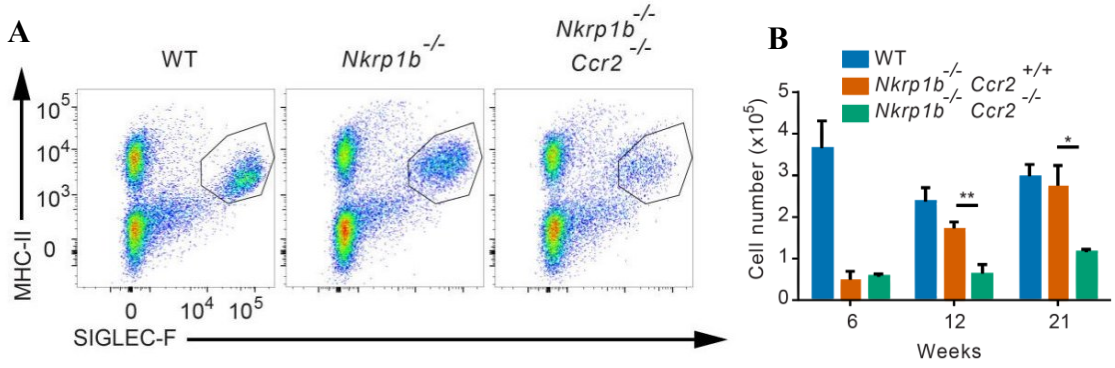

Figure 3.14: Cytometric analysis of AMs in WT, *Nkrp1b*$^{-/-}$ and *Nkrp1b*$^{-/-}$*Ccr2*$^{-/-}$ mice at 6, 8 and 12 weeks of age.
(A) Flow cytometry plots of AMs found in the lungs of WT, *Nkrp1b*$^{-/-}$ and *Nkrp1b*$^{-/-}$*Ccr2*$^{-/-}$ mice at 6, 8 and 12 weeks of age. Images are representative of 5 experiments.
(B) Quantification of AMs numbers found in the lungs of WT, *Nkrp1b*$^{-/-}$ and *Nkrp1b*$^{-/-}$ *Ccr2*$^{-/-}$ mice at 6, 8 and 12 weeks of age. Error bars represent SEM. Statistical significance was determined by two-way ANOVA with Tukey's correction where * is P=<0.05 and ** is P = <0.005 N = 5-7

3.2.3 Other Major Tissue-Resident Macrophages Appear to Have Normal Numbers in *Nkrp1b*$^{-/-}$ Mice and Do Not Express NKR-P1B.

To examine whether NKR-P1B expression on other tissue -resident macrophages was directly associated with the observed changes in *Nkrp1b*$^{-/-}$ lung macrophage numbers, and to determine if other macrophage subtypes may be affected by NKR-P1B loss, we assessed expression of NKR-P1B on several major tissue macrophages (using 2D12 mAb). As shown previously, we detected NKR-P1B on resident AMs, but not on Kupffer cells, splenic red pulp macrophages, or on either large or small peritoneal macrophages, which also did not show any change in numbers in *Nkrp1b*$^{-/-}$ mice at 6 weeks of age (Fig. 3.15a-Fig. 3.15d). These findings demonstrate that NKR-P1B is expressed exclusively on lung AMs and plays a crucial role in their homeostasis**.**

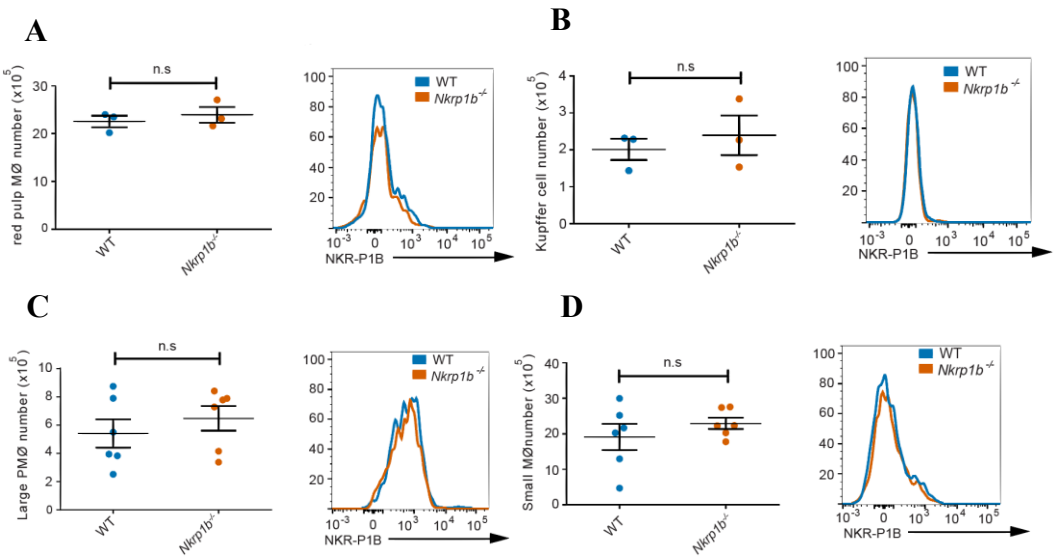

Figure 3.15: Numbers of tissue-resident macrophages specific to the liver, spleen, and peritoneal cavity.
(A) Number of red pulp macrophages present in the spleen of WT and *Nkrp1b*$^{-/-}$ mice at 6 weeks of age as determined by flow cytometric phenotyping. Error bars represent SEM. N=3. Significance determined by Students t-test.
(B) Number of Kupffer cells present in the liver of WT and *Nkrp1b*$^{-/-}$ mice at 6 weeks of age as determined by flow cytometric phenotyping. Error bars represent SEM. N=3. Significance determined by Students t-test.
(C) Number of large peritoneal macrophages present in the peritoneal cavity of WT and *Nkrp1b*$^{-/-}$ mice at 6 weeks of age as determined by flow cytometric phenotyping. Error bars represent SEM. N=6. Significance determined by Students t-test.
(D) Number of small peritoneal macrophages present in the peritoneal cavity of WT and *Nkrp1b*$^{-/-}$ mice at 6 weeks of age as determined by flow cytometric phenotyping. Error bars represent SEM. N=6. Significance determined by Students t-test.

3.2.4 Cd103^{+} DC Numbers Follow an Inverse Relationship Relative to AMs in *Nkrp1b*$^{-/-}$ Mice.

While performing flow cytometric analysis on various lung immune subsets in *Nkrp1b*$^{-/-}$ mice we noticed an anomaly in the numbers of CD103^{+} DCs which led us into exploring their population dynamics further. To this end, we analyzed the CD103^{+} DC numbers in *Nkrp1b*$^{-/-}$ mice aged 2, 6 and 12 weeks and found that they follow an inverse relationship as compared to AMs from *Nkrp1b*$^{-/-}$ mice. Specifically, as the number of AMs decreased

the number of CD103^{+} DCs increased and as AM numbers normalized at around 12 weeks-of-age so do the numbers of CD103^{+} DCs (Fig. 3.16a and Fig. 31.6b). There is some evidence to suggest that CD103^{+} DCs preferentially engulf apoptotic bodies and cell debris[252] and as the AMs population is collapsing, likely leaving behind cell debris, CD103^{+} DCs may be temporarily recruited to clean up the alveolar spaces in the *Nkrp1b*$^{-/-}$ mouse. It is also possible that they function as a temporary compensatory mechanism during the absence and subsequent reconstitution of AMs to ensure adequate immune surveillance in the alveolar space.

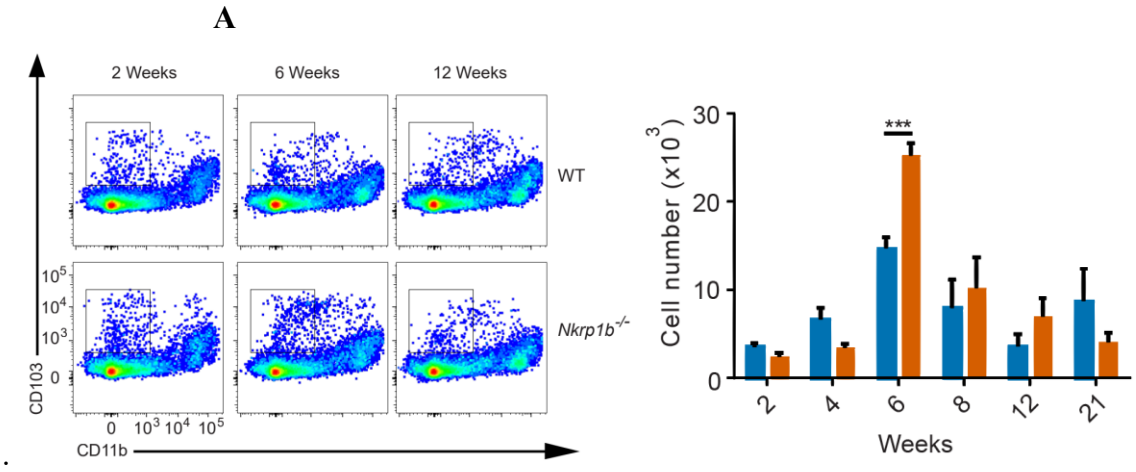

Figure 3.16: Numbers of CD103^{+} DCs in the lungs of WT and *Nkrp1b*$^{-/-}$ mice.
(A) flow cytometry dot plots of CD103^{+} DCs found in the lungs of WT and *Nkrp1b*$^{-/-}$ mice at 2,4, 6, 8, and 21 weeks of age. Images are representative of 6 different experiments.
(B) Quantifications of CD103^{+} DCs obtained by flow cytometric analysis from WT and *Nkrp1b*$^{-/-}$ mice at 2, 4, 6, 8, 12 and 21 weeks of age. Statistical significance was determined by two-way ANOVA with Tukey's correction where ** is P = <0.005 and *** P = <0.0005. N = 3-8

3.2.5 AM Defect inn *Nkrp1b*$^{-/-}$ Mice is Independent of GM-CSF Regulation and *Clr-B*$^{-/-}$ AMs Do Not Phenocopy *Nkrp1b*$^{-/-}$ AMs and Do Not Express Aberrant Levels of NKR-P1B.

Resident AMs are known to be self-renewing under steady-state conditions, with little input from blood monocytes [152,153,253]. This mechanism is driven primarily by GM-CSF and subsequent activation of classical AM associated transcription factors such as PU.1 and PPARγ. Thus, we examined the GM-CSF content in alveolar lavage fluid from 2- and 6-week-old *Nkrp1b*$^{-/-}$ mice, as well as the levels of GM-CSF receptor on *Nkrp1b*$^{-/-}$ AMØ. There were no significant differences observed in lavage fluid GM-CSF content nor GM-CSF receptor expression between WT and *Nkrp1b*$^{-/-}$ mice (Fig. 3.17a and Fig. 3.17b). This data suggests that the phenotype *Nkrp11b*$^{-/-}$ AMs experience is not due to the canonical lack of GM-CSF signalling that is associated with pulmonary foam cell formation, raising the interesting possibility that NKR-P1B signalling is working independently of the GM-CSF, PU.1, PPARγ axis yet produces a similar phenotype.

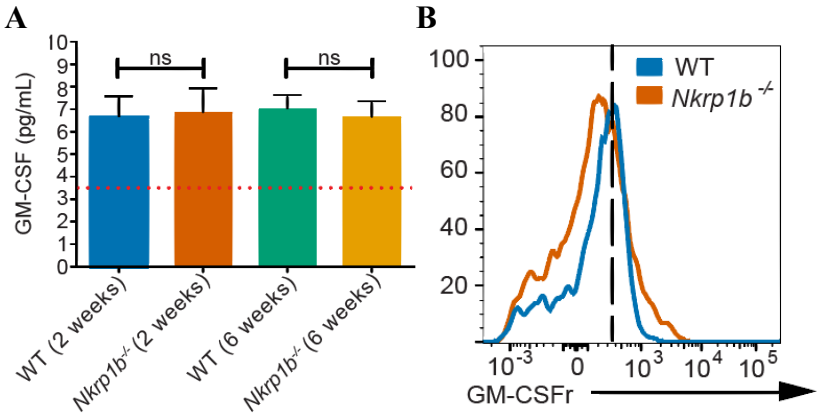

Figure 3.17: Evaluation of lung GM-CSF secretion and AM GM-CSFr expression.
(A) GM-CSF ELISA assay performed on lavage fluid of 2- and 6-week-old WT and *Nkrp1b*$^{-/-}$ mice. Error bars represent SEM. N=3 and N=6 respectively. Experiments were performed in duplicate. Significance determined by Student's t-test. Dashed red line indicated limit of detection.
(B) Expression profile of GM-CSFr on AMs obtained from 2-week-old *Nkrp1b*$^{-/-}$ mice. Histogram is representative of 3 independent experiments.

Following up on the observations presented in the preceding section, we wanted to determine whether *Clr-b*$^{-/-}$ mice experience an AM defect similar to what was observed in *Nkrp1b*$^{-/-}$ mice. Flow cytometric analysis was conducted on the lungs of *Clr-b*$^{-/-}$ mice of

various ages, and we discovered that Clr-b deficient AMs do not undergo any sort of population collapse, with their numbers remaining comparable to WT mice throughout all the timepoints examined (Fig 3.18a and Fig. 3.18b). This data set strongly suggests that the classically defined NKR-P1B:Clr-b relationship is not applicable to AMs and their relation to the alveolar niche in general.

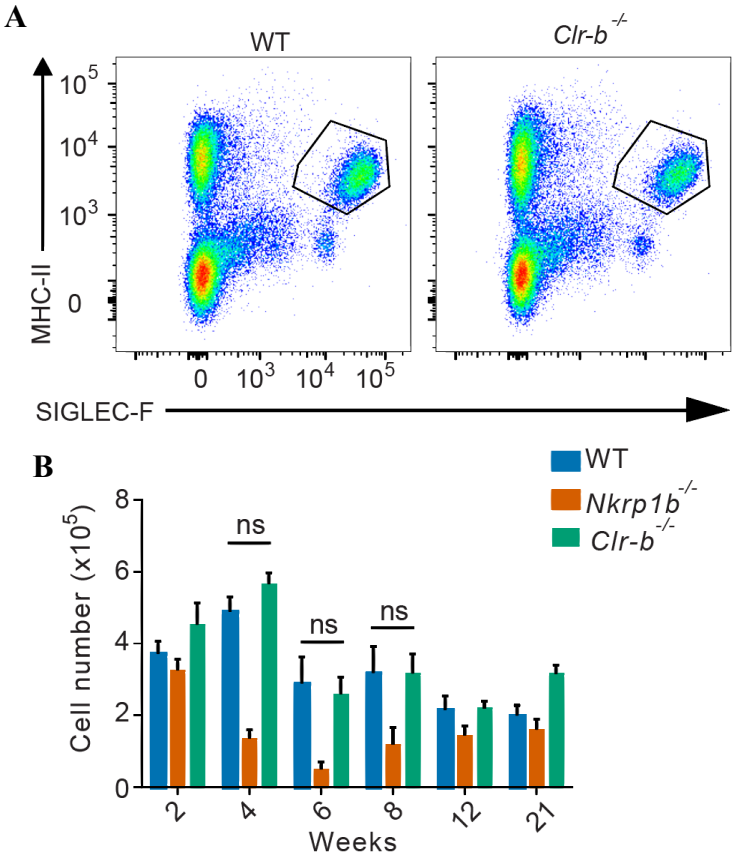

Figure 3.18: Numbers of AMs in the lungs of WT, *Nkrp1b*$^{-/-}$ and *Clrb*$^{-/-}$ mice at steady-state.
(A) Representative flow cytometry dot plots of AMs found in the lungs of WT and *Clr-b*$^{-/-}$ mice at 6 weeks of age. Images are representative of 5 different experiments.
(B) Quantifications of AMs obtained by flow cytometric analysis from WT and *Clrb*$^{-/-}$ mice at 2, 4, 6, 8, 12 and 21 weeks of age. Error bars represent SEM. Statistical significance was determined by two-way ANOVA with Tukey's correction.

With respect to NKR-P1B dynamics in *Clr-b*$^{-/-}$ mice, it is known that NK cells tend to upregulate NKR-P1B in response to loss of Clr-b[116], however, cytometric analysis of Clr-b deficient AMs determined that this is not the case for AMs, whose levels of NKR-P1B remained steady despite Clr-b loss (Fig. 3.19). This result further cements the notion of a de-coupling between Clr-b and NKR-P1B in the context of AMs.

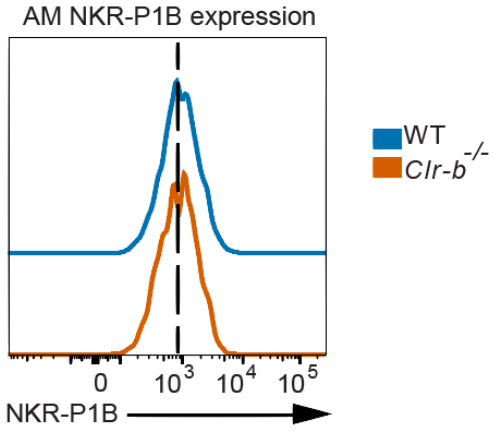

Figure 3.19: Expression of NKR-P1B on the surface of AMs in WT and *Clrb*$^{-/-}$ mice. Histogram of NKR-P1B surface protein expression on WT and *Clr-b*$^{-/-}$ AMØ, representative of 3 independent experiments.

Together, these data show that AMs not only express NKR-P1B, but that loss of NKR-P1B leads to a progressive collapse of the resident AMØ population beginning at approximately 4 weeks of age, followed by a CCR2-dependent reconstitution of the alveolar niche by blood monocytes beginning at 8 weeks of age. This mechanism appears to not be driven by a lack of GM-CSF cytokine or signalling through the receptor as is the case for classically defined AM lipid dysregulation. Finally, Clr-b deficient mice appear not to phenocopy NKR-P1B deficient mice in at all with respect to AM population collapse providing further evidence that another, so far undescribed NKR-P1B ligand is responsible for the collapse of AMs in *Nkrp1b*$^{-/-}$ mice.

3.3 *Nkrp1b*$^{-/-}$ AMs Exhibit Altered Cell Morphology Compared to WT AMs.

3.3.1 NKR-P1B Deficiency Leads to Altered AM Physical Characteristics.

As mentioned previously, mice which exhibit AM deficiencies tend to have a residual population of AMs with dramatically altered cell characteristics. As part of the flow cytometric analysis on primary AMs from WT and *Nkrp1b*$^{-/-}$ mice, we assessed AM forward scatter (FSC) and side scatter (SSC) characteristics. These measurements reveal a trend of increasing cell size and complexity in AMØ, peaking in 6-week-old *Nkrp1b*$^{-/-}$ mice relative to their WT counterparts (Fig. 3.20). These cell morphology alterations in NKR-P1B deficient AMs are highly indicative of a potential metabolic defect resulting in an excess of cytoplasmic inclusions.

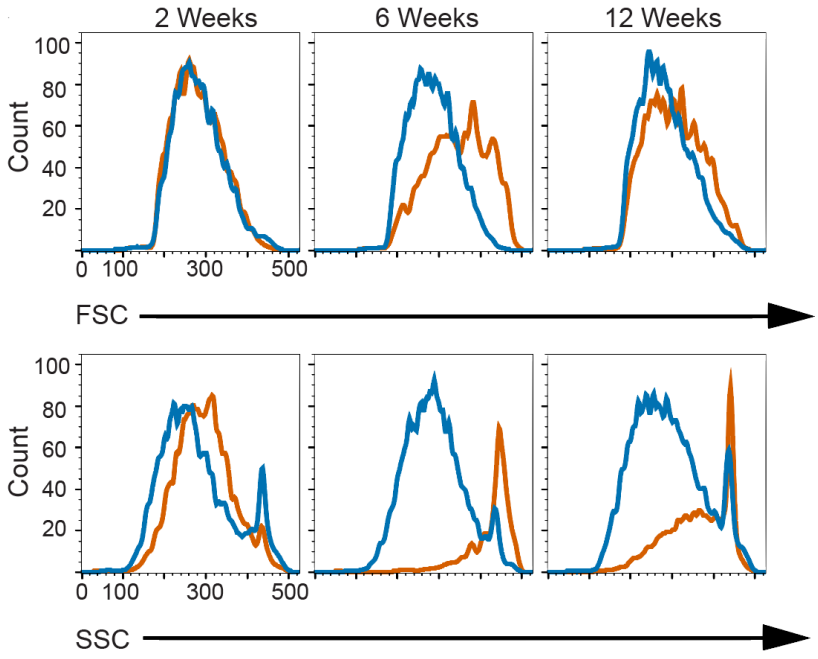

Figure 3.20: Cell morphology characteristics of WT and *Nkrp1b*$^{-/-}$ AMs as determined by flow cytometry.
Histograms showing the FSC and SSC profiles of AMs at the 2-, 6- and 12-week timepoints. Histogram representative of 3 independent experiments.

3.3.2 *Nkrp1b*$^{-/-}$ AMs are Larger and Have Many Electron-Poor Inclusions Most Prominent at 6 Weeks of Age and Which Resolve at 12 Weeks of Age.

To better examine these changes observed in *Nkrp1b*$^{-/-}$ AM morphology, we performed transmission electron microscopy (TEM) analysis of lavaged AMs. TEM images show that *Nkrp1b*$^{-/-}$ AM contain many electron-poor inclusions in the cytoplasm at 6 weeks compared to WT AM, with some inclusions also present at both 2- and 12-week time points (Fig. 3.21a). Quantification of AM inclusions and cell size shows that AM are on average significantly larger and more complex in *Nkrp1b*$^{-/-}$ mice at all ages compared to WT mice (Fig. 3.21b and Fig 3.21c), corroborating our cursory FSC/SSC data from Fig. 3.20. We also evaluated the number of mitochondria present in each cell (Fig. 3.21d). While this measure is imperfect, it does provide circumstantial evidence of potential metabolic dysregulation in *Nkrp1b*$^{-/-}$ AMs. These data indicate a departure from a normal AM phenotype in *Nkrp1b*$^{-/-}$ mice with microscopy and cytometry showing increases in cell size and complexity compounded by the addition of electron poor intracellular inclusions and potential mitochondrial dysregulation.

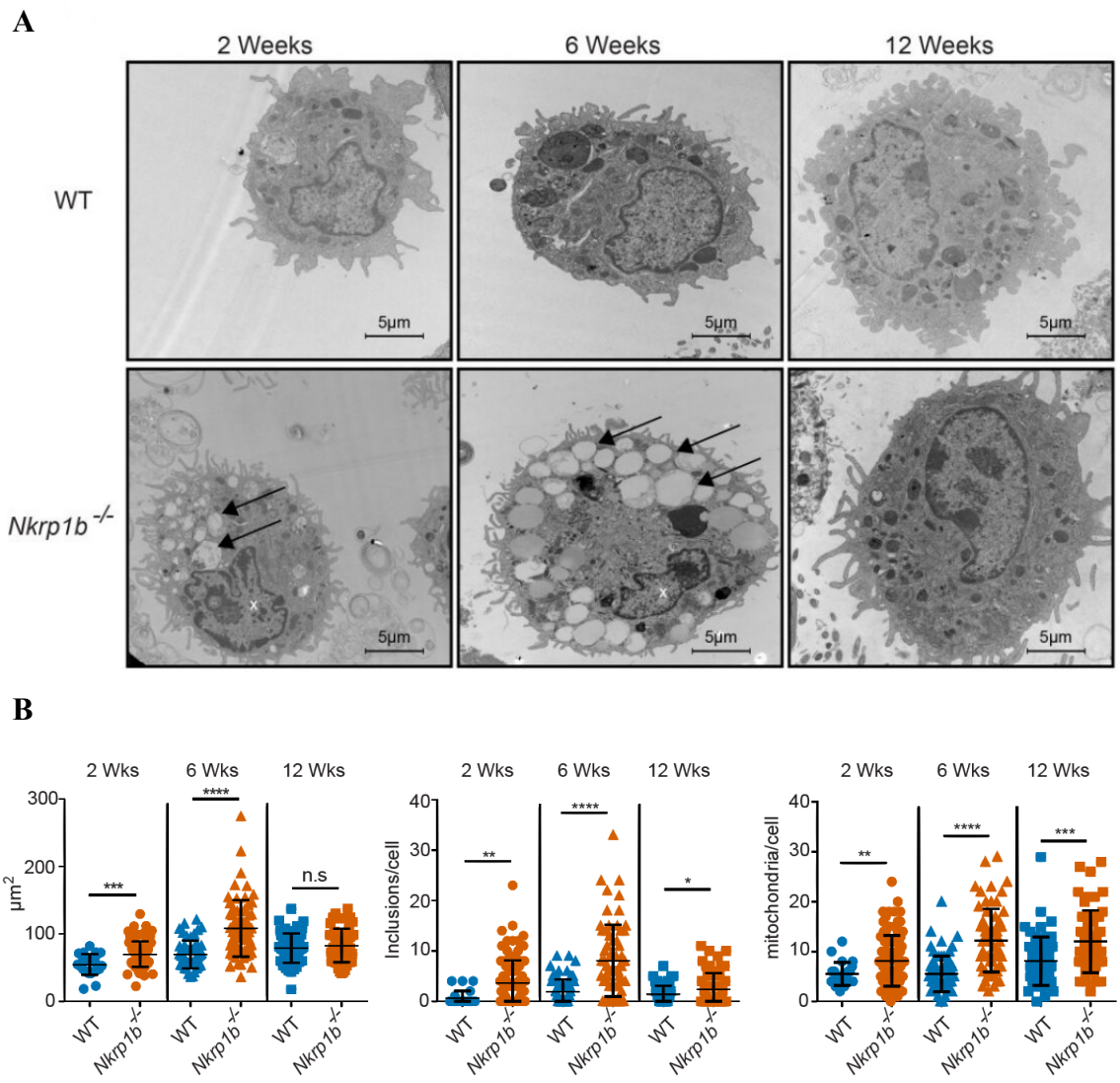

Figure 3.21: TEM analysis of AMs from WT and *Nkrp1b*$^{-/-}$ mice at steady-state.
(A) Images of AMs as seen by TEM isolated from WT and *Nkrp1b*$^{-/-}$ mice at 2, 6 and 12 weeks of age. Images are representative of 3 independent experiments. Inclusions highlighted by arrows; nucleus highlighted with a white "x".
(B) Quantifications of AMs surface area, number of electron poor inclusions and mitochondria respectively as seen by TEM. AMs isolated from mice aged 2, 6 and 12 weeks. Error bars represent SEM Statistics determined by Students t-test where * is P = <0.05, ** is P = <0.005, *** is P = <0.0005 and **** is P = <0.00005. N = 3 with 55 AMs examined per experiment.

CHAPTER 4: Functional Consequences of NKR-P1B Loss

4.1 *Nkrp1b*$^{-/-}$ AMs Exhibit Altered Lipid Metabolism

4.1.1 *Nkrp1b*$^{-/-}$ AMs are ORO and PAS Positive, Mostly Present at 6 Weeks of Age and Resolve at 12 Weeks of Age.

Reduced AM numbers and AM dysfunction has been positively correlated with mucous accumulation in alveolar spaces which can result in a condition present in both mice and humans known as pulmonary alveolar proteinosis (PAP)[127,153,241,254]. This condition is characterized by low AM numbers, foam cell formation and eventual accumulation of surfactant and mucous which can cause death to interrupted gas exchange. To determine if *Nkrp1b*$^{-/-}$ mice accumulated mucous and protein in their lung, we performed PAS staining on frozen WT and *Nkrp1b*$^{-/-}$ mouse lung sections; PAS staining has been used as the gold standard test for PAP diagnosis. While neither WT nor *Nkrp1b*$^{-/-}$ mice showed any accumulation of mucin or glycoprotein in alveolar spaces, we noticed intracellular accumulations in lungs of 6-week-old *Nkrp1b*$^{-/-}$ mice, which were not present in WT mice as seen in Fig 4.1a. We found that *Nkrp1b*$^{-/-}$ mice exhibited quantifiable intracellular accumulations of PAS positivity in cells confined strictly to the alveolar space beginning at 4 weeks of age, followed by a peak at 6 weeks and a decline at 12 weeks of age (Fig 4.1b).

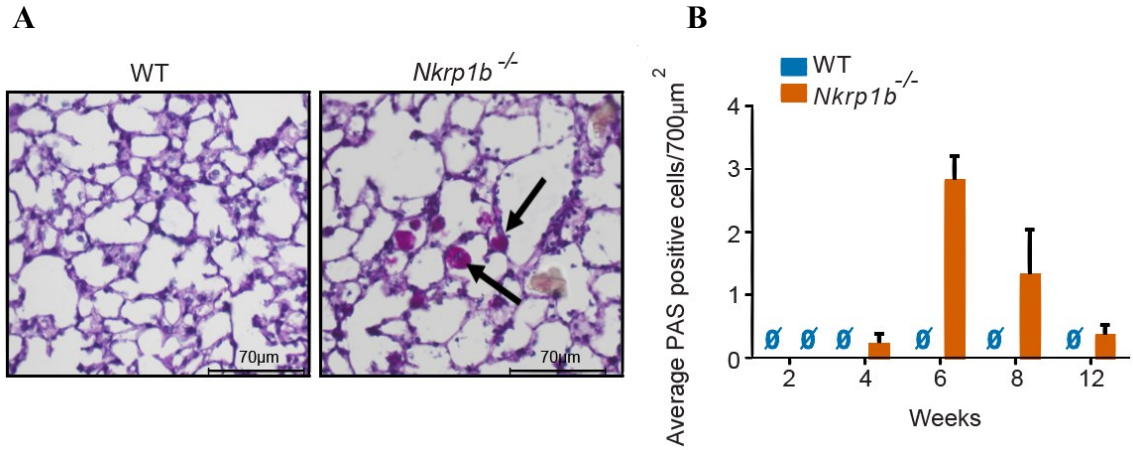

Fig 4.1: PAS staining of lungs from WT and *Nkrp1b*$^{-/-}$ mice.
(A) Representative images of PAS staining of frozen lung sections of WT and *Nkrp1b*$^{-/-}$ mice at 6 weeks of age showing positive intracellular inclusions. Images are representative of 3 independent experiments.
(B) Quantification of PAS positive staining cells as seen on PAS-stained frozen lung sections obtained from WT and *Nkrp1b*$^{-/-}$ mice 2, 4, 6 ,8 and 12 weeks of age. N = 3

PAS staining is commonly known to detect glycol-lipids as well as mucin and other glycoproteins. TEM data presented in the previous section combined with PAS positivity present in *Nkrp1b*$^{-/-}$ lungs is highly suggestive of lung foam cell formation. A well-known secondary role of AMs is processing pulmonary surfactant [223,255], which has been described previously through the use of mutant mice which disrupt AM metabolic development. Considering the electron-poor nature of their inclusions, we postulated that *Nkrp1b*$^{-/-}$ AMs were accumulating lipids in their cytoplasmic inclusions. To this end, we stained frozen lung sections of WT and *Nkrp1b*$^{-/-}$ mice with the neutral lipid stain, oil-red-O (ORO). AMs from *Nkrp1b*$^{-/-}$ mice exhibited many ORO-positive intracellular accumulations compared to WT mice (Fig 4.2a), which appear at around 4 weeks of age, peak in number at 6 weeks of age, and decline at 12 weeks of age (Fig 4.2b).

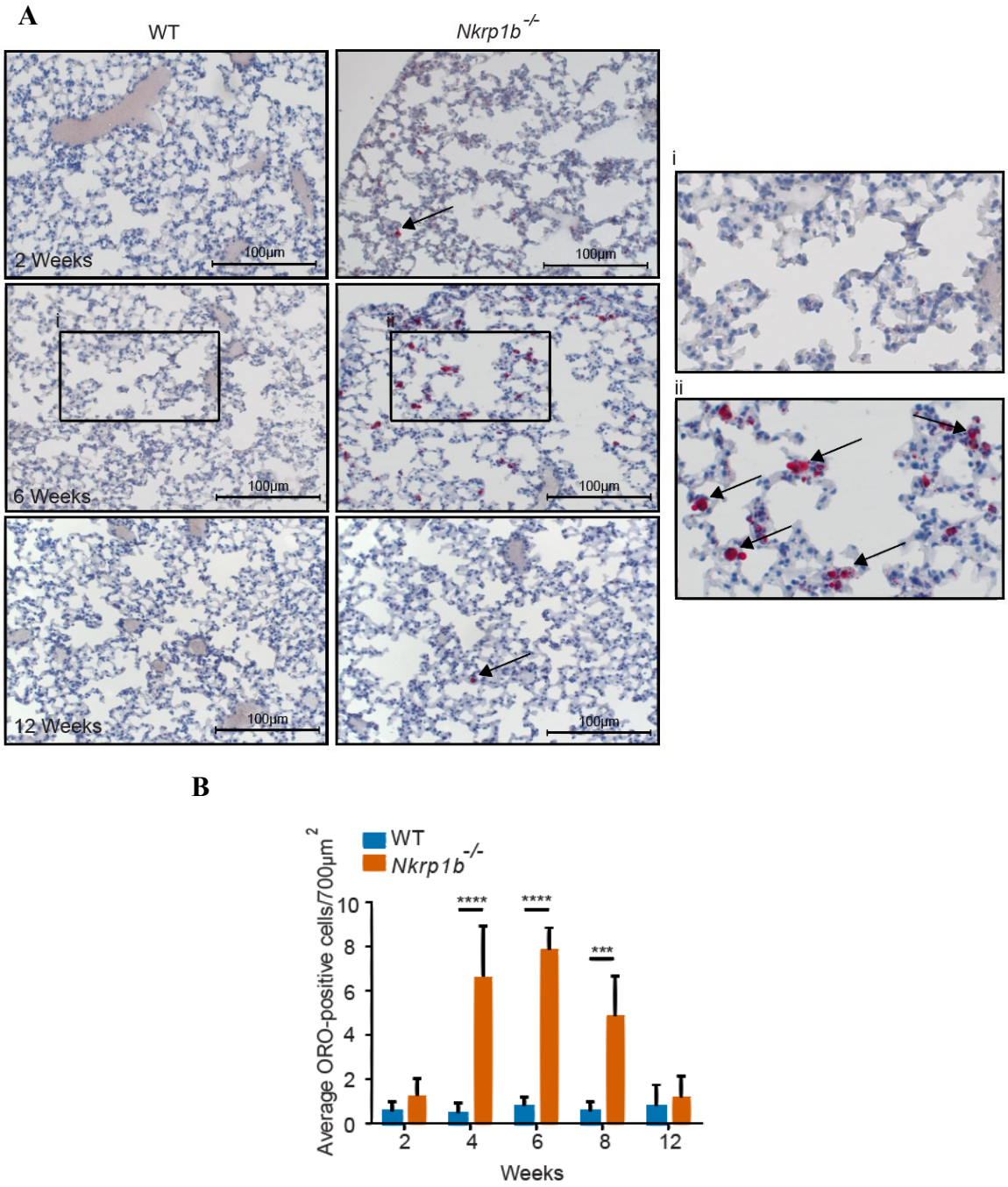

Fig 4.2: ORO staining of lungs from WT and *Nkrp1b*$^{-/-}$ mice.
(A) Frozen lung sections stained with ORO obtained from WT and *Nkrp1b*$^{-/-}$ mice 2, 6 and 12 weeks of age. Cutouts (i) and (ii) highlighting intracellular ORO positivity. Images are representative of 3 independent experiments.
(B) Quantifications of ORO positive cells/µm^2 in frozen lung sections stained with ORO obtained from WT and *Nkrp1b*$^{-/-}$ mice at 2, 4, 6, 8, and 12 weeks of age. Statistical significance was determined by two-way ANOVA with Tukey's correction where *** is P = <0.0005 and **** P = <0.00005. N = 3

ORO is a histological stain that is highly specific for neutral lipids and triglycerides[256]. To further characterized the nature of the accumulated intracellular lipids present in *Nrkp1b*$^{-/-}$ AMs we decided to perform amplex-red staining, a quantitative technique used to measure free cholesterol. Lipid extracts obtained from AMs lavaged from WT and *Nkrp1b*$^{-/-}$ mice at 6 weeks of age were stained with amplex-red and we found that *Nkrp1b*$^{-/-}$ mouse AMs exhibited a significant increase in the level of intracellular free cholesterol compared to WT AMs (Fig. 4.3). This result is potentially indicative of a breakdown in the pathways responsible for cholesterol homeostasis in AMs, cholesterol being the major neutral lipid present in pulmonary surfactant.

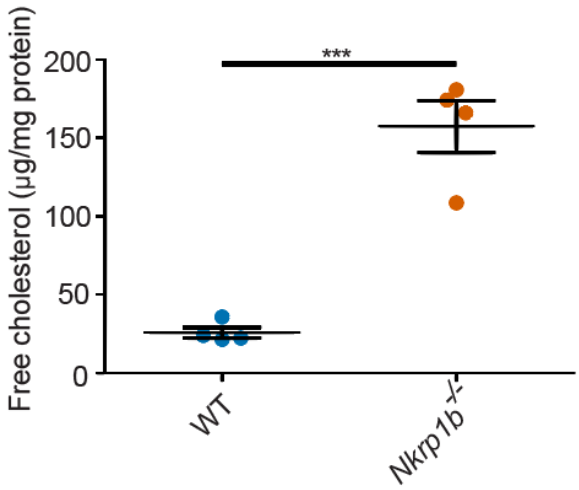

Fig 4.3: Amplex-red assay conducted on AMs isolated from 6-week-old WT and *Nkrp1b*$^{-/-}$ AMs.
Free cholesterol content of WT and *Nkrp1b*$^{-/-}$ lavaged AMs as determined by amplex-red assays. N = 4

Lipid dysregulation in AMs can occur either through a breakdown of specific metabolic pathways or through an increase in uptake overwhelming them. CD36 is expressed by AMs and is known to be a lipid scavenging receptor and a major determinant in AM lipid

uptake kinetics[257,258]. Thus, we examined the level of CD36 on *Nkrp1b*$^{-/-}$ AMs and found a slight increase in CD36 expression compared to WT AMs (Fig. 4.3a and Fig. 4.3b), suggesting a possible mechanism for the increased AM lipid content.

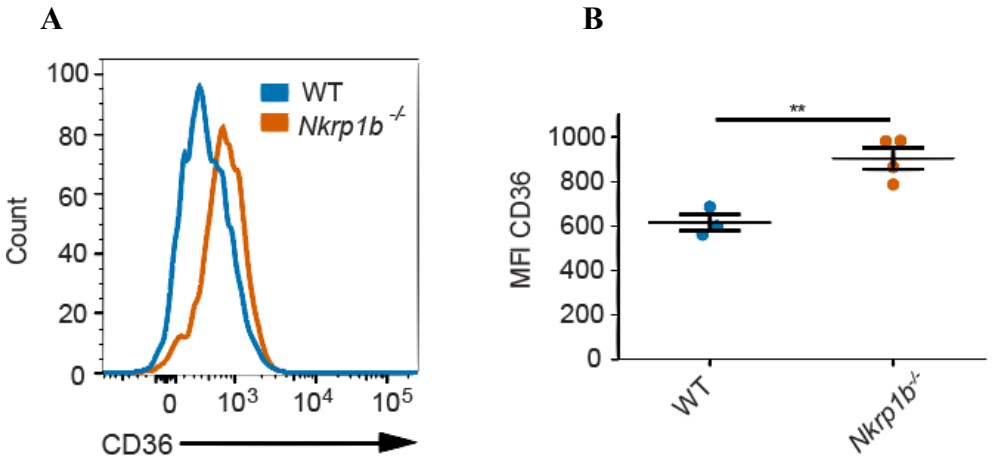

Fig 4.4: CD36 expression on WT and *Nkrp1b*$^{-/-}$ AMs.
(A) Expression profile of CD36 on AMØ obtained from 2-week-old WT and *Nkrp1b*$^{-/-}$ mice. Histogram is representative of 3 independent experiments.
(B) MFI quantifications of CD36 expressions on AMs obtained from 2-week-old WT and *Nkrp1b*$^{-/-}$ mice. Error bars represent SEM. N=3 and 4 respectively. Significance determined by Student's T-test where * is P = <0.05 and ** is P = <0.005

To follow up on this data we also decided to investigate basic AM metabolic function using a pair of flow cytometric assays. Since altered metabolism is closely related to alteration in energy requirements, as a first step, we wanted to determine the extent of the potential mitochondrial activity. To determine the extent of any mitochondrial dysregulation we opted to stain AMs isolated from WT and *Nkrp1b*$^{-/-}$ mice with tetramethylrhodamine-ester (TMRE) which is readily sequestered by mitochondria. As can be seen from Fig 4.5 the difference in mitochondrial membrane potential between WT and *Nkrb1p*$^{-/-}$ mice was marginal. A caveat of TMRE analysis being that two factors can influence the read-out those being the number of healthy/active mitochondria as well as the state of mitochondrial membrane polarization. Without more detailed analysis, on

an instrument such as a SeaHorse FX analyzer, drawing conclusions becomes difficult and we decided not to pursue this line of inquiry further.

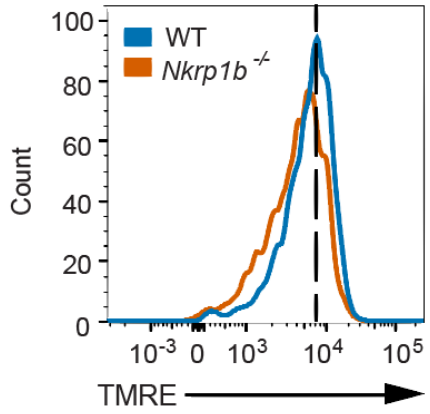

Fig 4.5: TMRE staining of AMs shows no obvious signs of mitochondrial dysfunction.
Histograms showing absorption of TMRE dye by WT and *Nkrp1b*$^{-/-}$ AMs derived from 2-week-old mice. The histogram is representative of 3 independent experiments.

However, we did analyze AM glucose uptake, another energy requirement peripherally related to mitochondrial activity. The relation between glucose uptake and metabolic status means that cells that exhibit higher metabolic activity import more glucose to meet their energy demand**.** To determine glucose kinetics, we used the fluorescent glucose analog 2-NBDG, the uptake of which causes cells to acquire green fluorescence. Using 2-NBDG we were able to show that *Nkrp1b*$^{-/-}$ AMs uptake glucose at a faster rate compared to WT AMs (Fig. 4.6a and Fig. 4.6b), suggesting a potentially increased metabolic rate or more metabolic activity happening inside of *Nkrp1b*$^{-/-}$ AMs. This increase in energy demand may be related to the increase in lipid burden observed in *Nkrp1b*$^{-/-}$ AMs or it could be a consequence of general metabolic dysregulation present in these AMs.

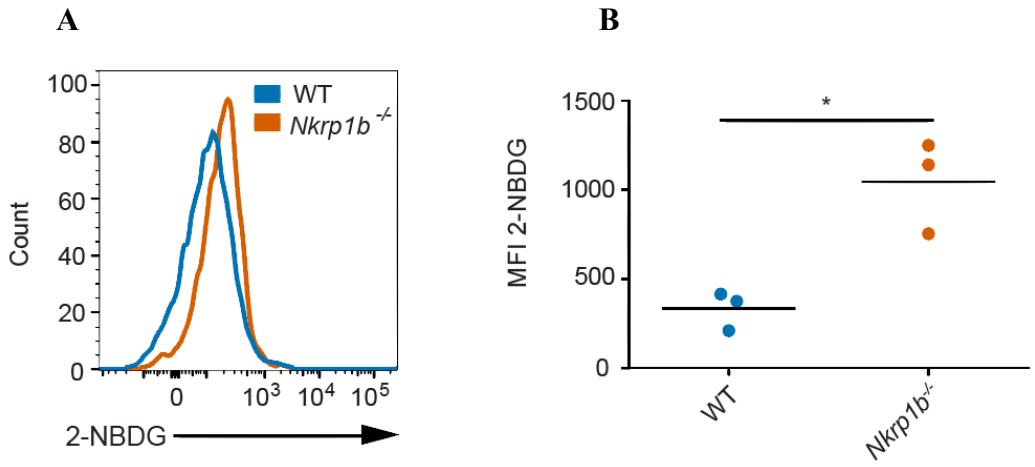

Fig 4.6: *Nkrp1b*$^{-/-}$ derived AMs uptake glucose faster compared to WT AMs.
(A) Histograms showing uptake of 2-NBDG by WT and *Nkrp1b*$^{-/-}$ AMs derived from 2-week-old mice. Image is representative of 3 independent experiments.
(B) MFI quantifications of 2-NBDG uptake on AMs obtained from 2-week-old WT and *Nkrp1b*$^{-/-}$ mice. Error bars represent SEM. N=3. Significance determined by Student's T-test where * is $P = <0.05$.

4.2 *In Vitro* Resolution of *Nkrp1b*$^{-/-}$ AM Foam Cell Phenotype

4.2.1 Foam Cell Phenotype Appears to Auto-Resolve After *In Vitro* Culture of 6-Week-Old *Nkrp1b*$^{-/-}$ AMs.

Having established that NKR-P1B deficiency leads to a foam cell phenotype and potential metabolic dysfunction observed *in vivo*, we next determined if removing AMs from the lipid rich alveolar environment and culturing them *in vitro* would be sufficient to rescue them from lipid accumulation. As discussed previously, the alveolar environment contains lipid-based surfactant and we postulated that removal AMs from this lipid rich environment might be sufficient to alleviate their lipid accumulation. After 6 days of *in vitro* culture on cover slips, AMs from 6-week-old WT and *Nkrp1b*$^{-/-}$ mice were stained with ORO and analyzed by microscopy side by side with freshly-lavaged *Nkrp1b*$^{-/-}$ AMs as a positive ORO control. As can be seen in images in Fig 4.7a, WT AMs have little to no ORO positivity either when freshly lavaged or after 6 days *in vitro*.

Conversely *Nkrp1b*$^{-/-}$ AMs show a dramatic decrease in ORO positive cells after 6 days *in* vitro compared to freshly lavaged AMs from *Nkrp1b*$^{-/-}$ mice. Quantifying these observations confirmed a clear significant reduction in ORO positive *Nkrp1b*$^{-/-}$ AMs following 6 days of *in vitro* culture (Fig 4.7b).

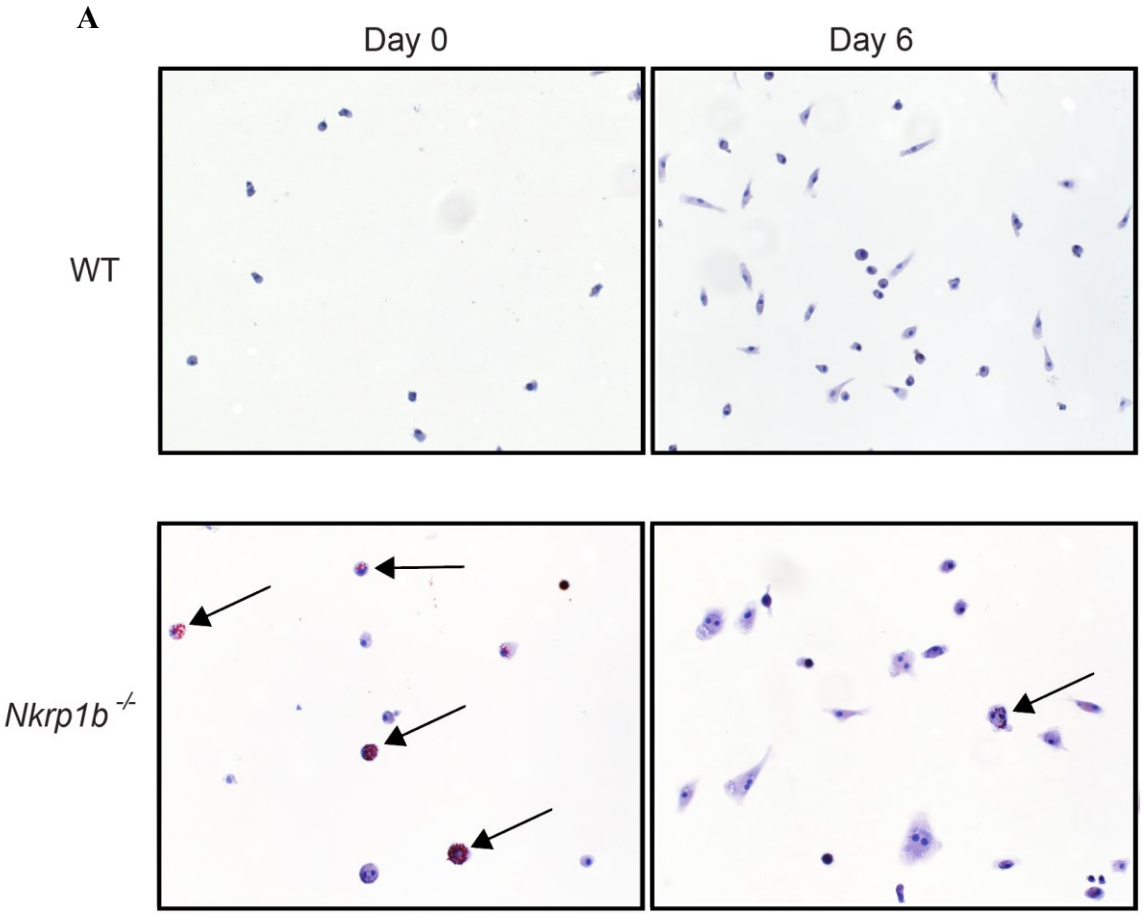

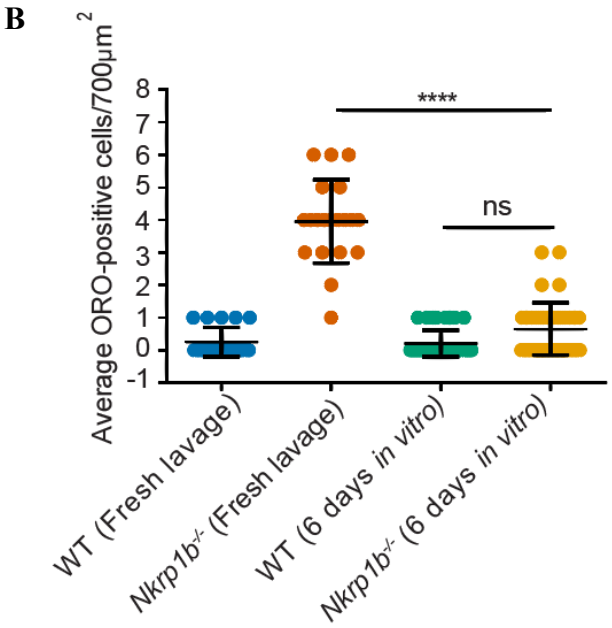

Fig 4.7: *In vitro* culture of WT and *Nkrp1b*$^{-/-}$ AMs results in loss of ORO positivity. (A) Representative images of WT and *Nkrp1b*$^{-/-}$ AMØ at either day 0 or day 6 of *in vitro* culture after staining with ORO at 20x magnification. ORO positive lipid accumulations are highlighted (arrows). Images are representative of 3 independent experiments. (B) Quantification of ORO positive AMØ/µm^2 derived from WT and *Nkrp1b*$^{-/-}$ mice at day 0 or day 6 of *in vitro* culture. Error bars represent SEM. N = 3. Statistics determined by Students t-test where * is P = <0.05, ** is P = <0.005, *** is P = <0.0005 and **** is P = <0.00005

Taken together, the data so far indicates that resident *Nkrp1b*$^{-/-}$ AMs exhibit metabolic dysfunction causing them to accumulate free cholesterol and perhaps other lipids that are present in, or derived from, pulmonary surfactant. As a result, AMs of *Nkrp1b*$^{-/-}$ mice acquire a foam cell phenotype, and the observed increase in AM size and lipid accumulation aligns with the decline in AM population numbers, a characteristic resemblant of cell death caused by lipo-toxicity. Additionally, while *Nkrp1b*$^{-/-}$ AMs appear to not experience significant mitochondrial dysfunction they do express higher levels of critical lipid scavenger CD36 while exhibiting increased metabolic rate as measured by 2-NBDG uptake, suggesting a role for NKR-P1B in affecting lipid uptake kinetics in AMs. We have also shown that *Nkrp1b*$^{-/-}$ AMs lose their ORO positivity *in*

vitro, strongly implicating the lipid-rich alveolar environment as the causative agent of this dysfunction.

4.2.2 Adding Surfactant to Media of Either WT or *Nkrp1b*$^{-/-}$ AMs Fails to Recapitulate the ORO Positive Phenotype *In Vitro*.

Following the previous finding of ORO resolution post-*in vitro* culture of *Nkrp1b*$^{-/-}$ AMs, we decided to examine whether the ORO positive phenotype could be recapitulated *in vitro* while also determining whether incubating lipid-laden AMs in media with surfactant could lead to an exacerbation of lipid accumulation. To this end we decided to incubate WT and *Nkrp1b*$^{-/-}$ AMs in regular culture with varying concentrations of pulmonary surfactant (Infasurf/Calfactant generously donated for research purposes by Onybiotech), a bovine-derived phospholipid emulsion used as a surfactant substitute for treatment of prematurely delivered infants[259]. Lung surfactant composition is remarkably well conserved amongst vertebrates to the point of reaching functional interchangeability in mammals[260], with bovine, porcine and synthetic surfactant compositions being used routinely in clinical and research settings[261,262]. Using Infasurf (a bovine derived surfactant) to supplement the culture medium with surfactant we then cultured WT and *Nkrp1b*$^{-/-}$ AMs for a period of 3 and 6 days but were unable to observe any increased in ORO positivity at either timepoint nor at a high or low concentration of surfactant in the medium (Fig 4.8a and Fig 4.8b)

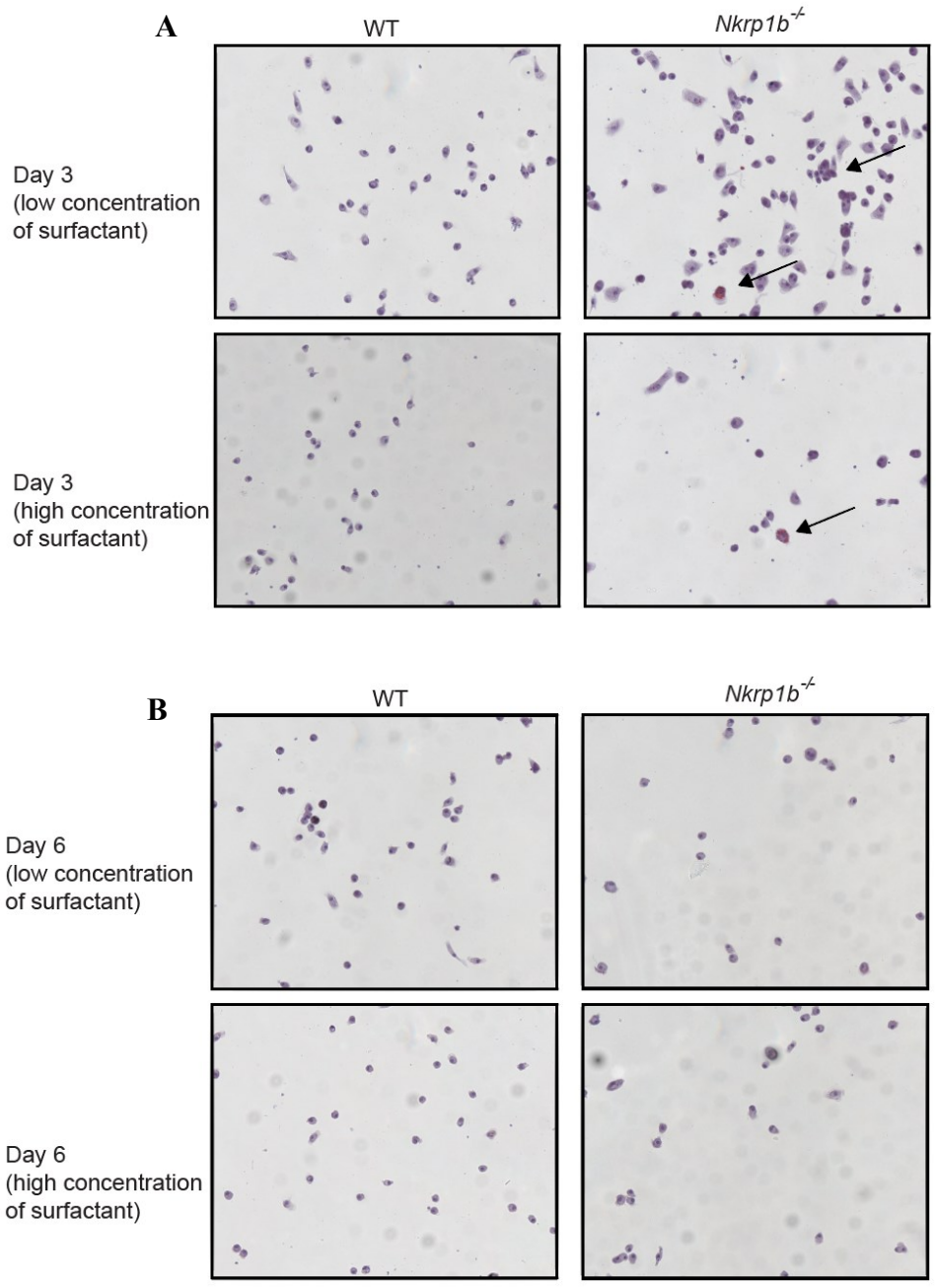

Fig 4.8: Incubation of WT and *Nkrp1b*$^{-/-}$ AMs in surfactant enriched media does not result in an increase in ORO positivity.
AMs from 6-week-old WT and *Nkrp1b*$^{-/-}$ incubated in media with Infasurf bovine surfactant formula at either high (50µg/mL) or low (25µg/mL) concentration. Cells were stained with ORO and imaged at 3 (A) and 6 days (B) post-incubation with lipid-rich media. Images are representative of 2 independent experiments.

We were able to notice some lingering ORO positivity in *Nkrp1b*$^{-/-}$ AMs at day 3 (black arrow) of the experiment but this was mostly abolished by day 6 of the experiment in accordance with our previous experiments involving culture of *Nkrp1b*$^{-/-}$ AMs *in vitro*. The failure to recapitulate the lipid-laden AM phenotype *in vitro* could be due to several factors concerning inadequate replication of the alveolar environment *in vitro*.

4.3 *Nkrp1b*$^{-/-}$ AMs Experience Cell Cycle Disruption That Impairs Their Ability to Self-Renew *In Vivo* While Showing Normal Proliferative Capacity *In Vitro*.

4.3.1 *Nkrp1b*$^{-/-}$ AMs Show Signs of Cell Cycle Deficiency and S-Phase Arrest.

The previous sections discussed the manifestation of metabolic dysfunction in *Nkrp1b*$^{-/-}$ AMs. As well as processing surfactant another hallmark of tissue-resident AMs is the ability to proliferate *in vivo* without input from blood monocytes, as discussed previously. Seeing as our NKR-P1B deficient mice experience tissue-resident AM collapse followed by CCR2 mediated blood monocyte replenishment, we decided to explore how NKR-P1B loss impacts the capacity of resident AMs to proliferate and self-renew. We began by examining the levels of Ki67, a well characterized marker of cell proliferation, on resident AMs from 2-week-old WT and *Nkrp1b*$^{-/-}$ mice. The two-week timepoint was chosen in order to see if there are any inherent defects present due to NKR-P1B loss before the AM population collapses due to its excess lipid burden. Compared to WT AMs, *Nkrp1b*$^{-/-}$ AMs exhibit lower levels of Ki67 as determined by intracellular flow cytometric analysis (Fig 4.9a and Fig 4.9b), suggesting a possible dysregulation of cell proliferation.

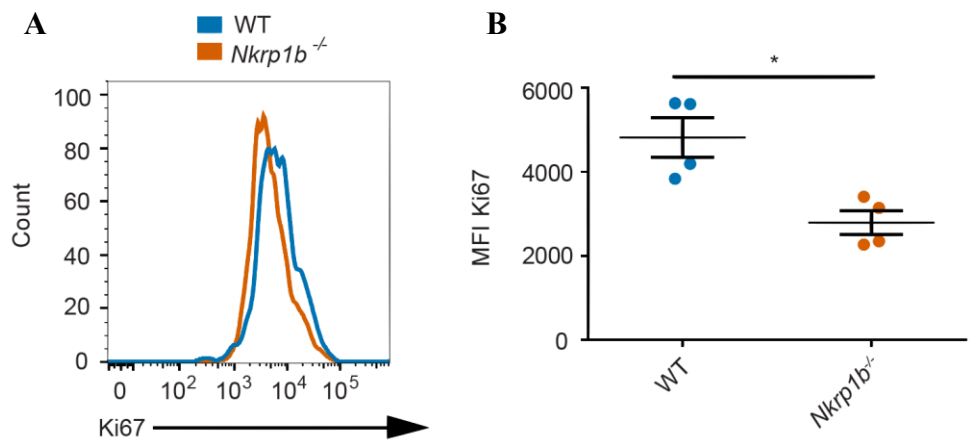

Fig 4.9: Ki67 expression profile of WT and *Nkrp1b*$^{-/-}$ AMs.
(A) Expression profile of Ki67 on AMØ obtained from 2-week-old WT and *Nkrp1b*$^{-/-}$ mice. The histogram is representative of 3 independent experiments.
(B) MFI quantifications of Ki67 expressions on AMØ obtained from 2-week-old WT and *Nkrp1b*$^{-/-}$ mice. Error bars represent SEM. N=4 respectively. Significance determined by Student's T-test where * is $P = <0.05$.

Since we have already established that AM replenishment in *Nkrp1b*$^{-/-}$ mice is mostly CCR2-dependent, we proceeded to assess proliferative capacity using *Nkrp1b*$^{-/-}$*Ccr2*$^{-/-}$ mice to exclude any possible monocyte infiltration into the lung alveolar niche that might potentially skew data relating to cell cycle analysis. Tissue-resident AMs do not express CCR2 nor do they utilize it for migration[251], meaning that the original tissue-resident AM population seeded by fetal liver monocytes at birth will be unaffected and left intact. To assess the extent of AM proliferative defect, we performed an *in vivo* BrdU assay, with the rate of BrdU incorporation being analogous to proliferative activity. Flow cytometry analysis of lavaged AMs from *Nkrp1b*$^{-/-}$*Ccr2*$^{-/-}$ mice shows an accumulation of AMs in S-phase of cell division (Fig 4.10a), with *Nkrp1b*$^{-/-}$*Ccr2*$^{-/-}$ having almost 20% of cells lingering in S-phase compared to less than 10% for *Nkrp1*$^{+/+}$*Ccr2*$^{-/-}$ AMs (Fig 4.10b), suggesting a possible S-phase cell cycle arrest. The number of AMs in G2-phase was found to be normal in both WT and *Nkrp1b*$^{-/-}$ AMs (Fig 4.10c). The assays performed

above indicate that a possible cell cycle dysfunction is present in *Nkrp1b*$^{-/-}$ AMs before the onset of the foamy AM phenotype, which could be contributing to their lack of self-renewal.

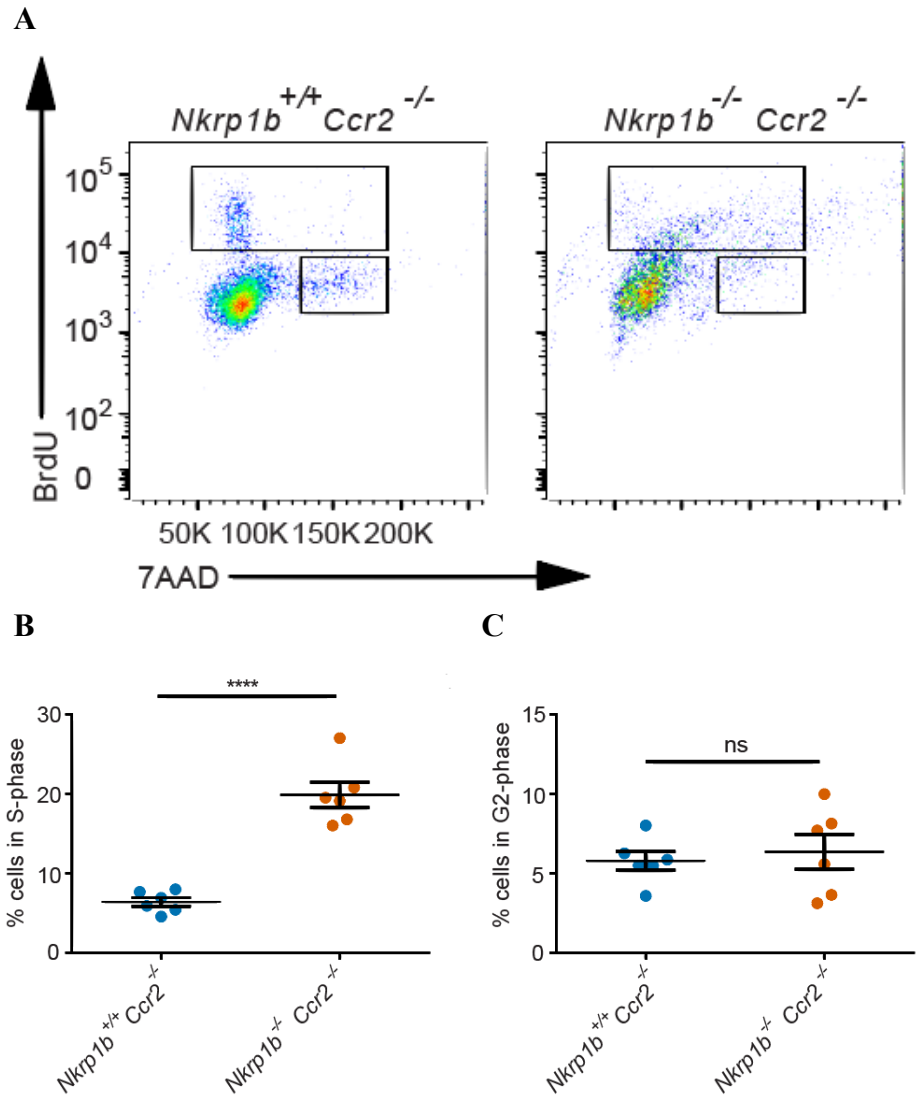

Fig 4.10: *In vivo* BrdU analysis of AM proliferation in WT and *Nkrp1b*$^{-/-}$ mice.
(A) Flow cytometry plots of AMs isolated from 2-week-old WT and *Nkrp1b*$^{-/-}$*Ccr2*$^{-/-}$ mice 24 hours post-BrdU injection. The top gate represented S-phase; the bottom gate represents G2 phase. Plots representative of 3 independent experiments.
(B) Quantifications of AMs in S-phase and G2-phase respectively at time of harvest as seen in (A). N = 6. Error bars represent SEM. N = 3. Statistics determined by Students t-test where * is P = <0.05, ** is P = <0.005, *** is P = <0.0005 and **** is P = <0.00005

4.3.2 Both WT and *Nkrp1b*$^{-/-}$ AMs Proliferate *In Vitro* Upon GM-CSF Stimulation

We demonstrated previously that *Nkrp1b*$^{-/-}$ AMs accumulate surfactant, which has the potential to cause lipo-toxicity, which makes it likely that the lipid rich alveolar environment is a causative agent in the phenotype observed in *Nkrp1b*$^{-/-}$ AMs. To understand the confounding effects of a lipid-rich environments, we decided to investigate whether AMs isolated from the lungs could be induced to proliferate *in vitro*. Visual quantification of lavaged AM numbers as seen in Fig 4.11a revealed no proliferation *in vitro* when GM-CSF was absent from the growth medium, but upon addition of GM-CSF to AMs of 2-week-old *Nkrp1b*$^{+/+}$*Ccr2*$^{-/-}$ and *Nkrp1b*$^{-/-}$*Ccr2*$^{-/-}$ mice showed a similar proliferation rate over the entire 6-day period (Fig 4.11b). This was also true for AMs extracted from 6-week-old mice (Fig 4.11c). The ability of AMs from both 2-week-old and 6-week-old (lipid-laden) mice to proliferate and survive *in vitro* was surprising but these results further implicate the presence of surfactant in the medium as the main driver of dysfunctional AM lipid metabolism in the absence of NKR-P1B. Interestingly, it appears that lavaged AMs do not proliferate uniformly upon GM-CSF exposure. Instead there are very clear, localized centers of cell division visible (Fig. 4.11a). These results provide peripheral evidence of a possible sub-population of AMs that exhibits increased proliferative capacity and is responsible for AM self-renewal.

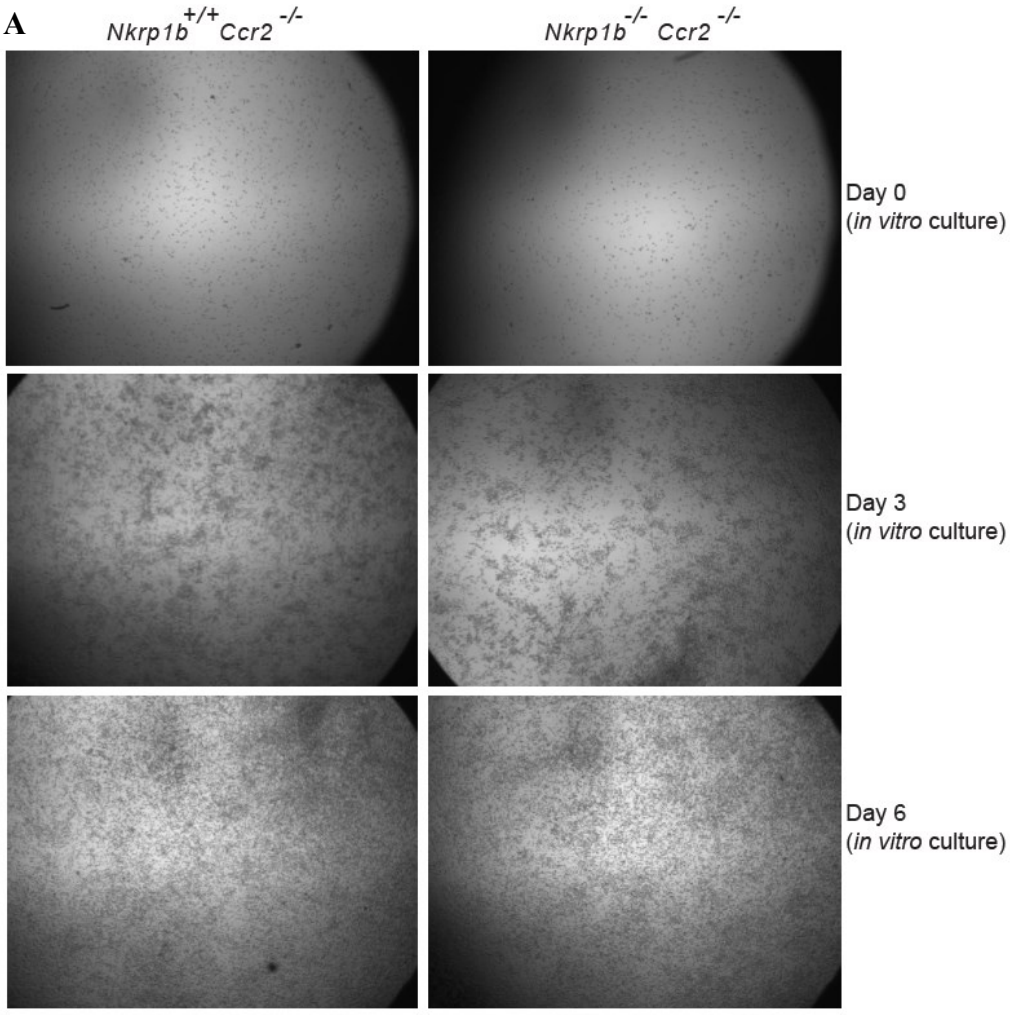
A
Nkrp1b+/+ Ccr2-/-
Nkrp1b-/- Ccr2-/-
Day 0
(in vitro culture)
Day 3
(in vitro culture)
Day 6
(in vitro culture)

B

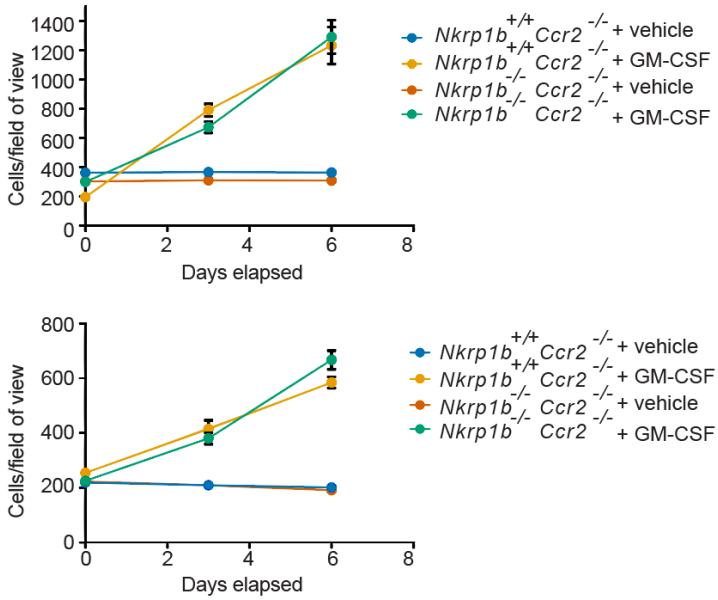
Cells/field of view
Days elapsed
Nkrp1b+/+ Ccr2-/- + vehicle
Nkrp1b+/+ Ccr2-/- + GM-CSF
Nkrp1b-/- Ccr2-/- + vehicle
Nkrp1b-/- Ccr2-/- + GM-CSF

Fig 4.11: Analysis of proliferative capacity of WT and *Nkrp1b*$^{-/-}$ AMs *in vitro*.
(A) Image captures of lavaged AMØ isolated from 2-week-old *Nkrp1b*$^{+/+}$*Ccr2*$^{-/-}$ and *Nkrp1b*$^{-/-}$*Ccr2*$^{-/-}$ mice at 10x magnification. AMØ were cultured *in vitro* in presence of GM-CSF. Images are representative of 3 independent experiments.
(B) Quantification of number of visible cells per field of view taken from WT and *Nkrp1b*$^{-/-}$*Ccr2*$^{-/-}$ mice at 2 and 6 weeks of age, respectively. Cell numbers were quantified on day 0, 3 and 6 post plating. Error bars represent SEM.

Previously, we have described an experiment that aimed to determine if the lipid rich alveolar environment is a contributing factor in the reduced survival and altered morphology of NKR-P1B deficient AMs (Fig. 4.7). In this experiment we cultured WT and *Nkrp1b*$^{-/-}$ AMs *in vitro*, stained them with ORO hematoxylin and analyzed their cell physiology. While both *Nkrp1b*$^{+/+}$*Ccr2*$^{-/-}$ and *Nkrp1b*$^{-/-}$*Ccr2*$^{-/-}$ lavaged AMs were able to survive *ex vivo* (Fig 4.12a), *Nkrp1b*$^{-/-}$*Ccr2*$^{-/-}$ AMs, we noticed another peculiar observation that further reinforces the possibility of a cell cycle defect in NKR-P1B AMs. In the same experiment we noticed the presence of double nucleated cells at a frequency that was not observed in WT AMs. Quantifying these results (Fig 4.12b) shows that while only a few WT AMs attain a double nucleated phenotype, a significant portion of *Nkrp1b*$^{-/-}$ *Ccr2*$^{-/-}$ AMs display double nuclei after 6 days in culture without any GM-CSF, suggesting the possibility of an inherent cell cycling defect in *Nkrp1b*$^{-/-}$*Ccr2*$^{-/-}$ AMs.

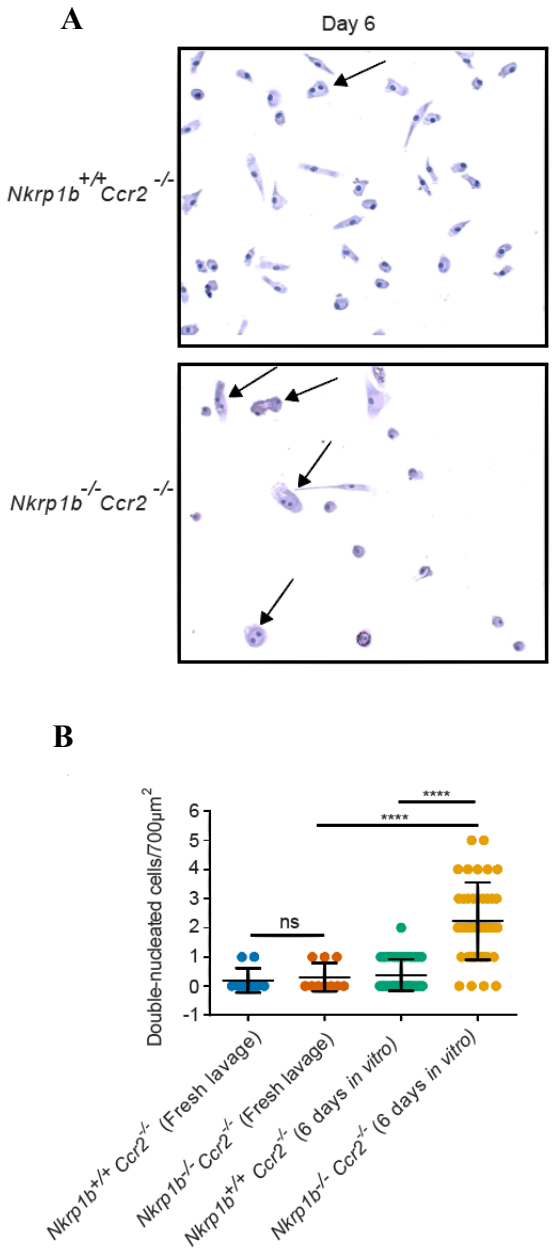

Fig 4.12: Double nucleated phenotype of *Nkrp1b*$^{-/-}$ AMs post *in vitro* culture.
(A) Images of AMs isolated from WT and *Nkrp1b*$^{-/-}$*Ccr2*$^{-/-}$ mice after being kept *in vitro* for 6 days and stained with ORO followed by a counterstain with Mayer's hematoxylin. *Nkrp1b*$^{-/-}$*Ccr2*$^{-/-}$ frame highlighting double nucleated cells (arrows). Images are representative of 3 independent experiments.
(B) Quantifications of double nucleated cells as seen in (A). Freshly-lavaged AMs from WT and *Nkrp1b*$^{-/-}$*Ccr2*$^{-/-}$ were compared to WT and *Nkrp1b*$^{-/-}$*Ccr2*$^{-/-}$ AMØ kept *in vitro* for 6 days. Error bars represented SEM Statistical significance was determined by two-way ANOVA with Tukey's correction where *** is P = <0.0005 and **** P = <0.00005. N = 3

Collectively, these data show that *Nkrp1b*$^{-/-}$ AMs functional impairment manifests both through a dysregulated lipid metabolism but also through an abnormal cell cycle phenotype *in vivo* while retaining their metabolic and proliferative capacities *in vitro*. The ability of *Nkrp1b*$^{-/-}$ AMs to survive, proliferate and metabolize their ORO burdens *in vitro* heavily implicates the lipid-rich alveolar environment as a determinant in the manifestation of the phenotype observed *in vivo*. Interestingly, *Nkrp1b*$^{-/-}$ AMs are able to overcome their respective proliferation defect *in vivo* despite the appearance of double-nucleated cells, suggesting that loss of NKR-P1B plays a more fundamental role in AM cell cycle and self-renewal that extends beyond simple cell process breakdown due to increased lipid burden.

4.4: RNA-Seq and Lipidomic Analysis Indicates NKR-P1B Signalling Regulates Critical Metabolic Genes Preventing the Formation of Lipid Droplets Containing Toxic Lipid Species.

4.4.1 Cell Cycling, Metabolic/Immune Profile and Serine/Threonine Kinase Activity is Affected by Loss Of NKR-P1B

Two obvious defects in *Nkrp1b*$^{-/-}$ AMs are apparent: lipid processing and cell cycle. To identify the cellular programs that underlie the observed defects of *Nkrp1b*$^{-/-}$ AMs, we performed RNA-seq analysis on AMs sorted from 2-week-old WT and *Nkrp1b*$^{-/-}$ mouse lungs. The two-week timepoint was chosen because *Nkrp1b*$^{-/-}$ mice at 2 weeks of age still contain a normal number of AMs, thereby allowing us to capture dysregulated transcriptional programs of the *Nkrp1b*$^{-/-}$ AM population that may contribute to the eventual collapse. Altogether we found that 590 genes were significantly dysregulated.

Gene ontology analysis on this data set, revealed a pattern of dysregulated lipid metabolism characterized by excessive lipid storage and upregulation of various lipid metabolic pathways (Fig 4.13a and Fig 4.13b). Our previous results have demonstrated, *in vivo,* the accumulation of lipids and subsequent ORO positivity in *Nkrp1b*$^{-/-}$ AMs which corresponds to the transcript level dysregulation determined by RNA-seq. As well, kinase activity was found to be abnormal, as indicated by an apparent increase in factors regulating positive P38-MAPK loops, and a decrease in the ERK cascade due to a decrease in factors regulating it (Fig 4.13c and Fig 4.13d). This data set is useful because it presents several potential candidates for pharmacological intervention. Other areas of dysregulation that emerged out of this analysis include a drastic reduction in cell cycle and mitotic pathways as seen in Fig 4.13e and Fig 4.13f, in agreement with our BrdU analysis as well as other cell cycle observations demonstrated previously in NKR-P1B deficient AMs. Finally, there was a tendency for *Nkrp1b*$^{-/-}$ AMs to display a more immune-activated phenotype (Fig 4.13g), which is diametrically opposed to their usual homeostatic/immunosuppressive phenotype present under steady-state conditions. This loss of immune suppression and a skew towards activation may be an important factor as to why 12-week-old *Nkrp1b*$^{-/-}$ mice with monocyte-derived AMs fail to provide adequate protection against *S. pneumoniae* infection.

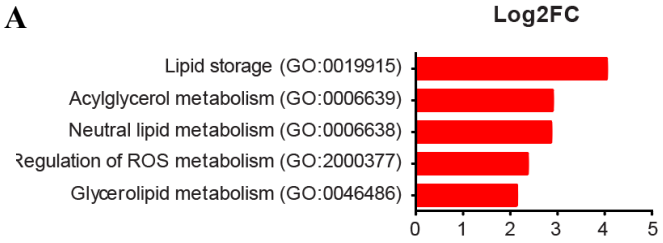

B

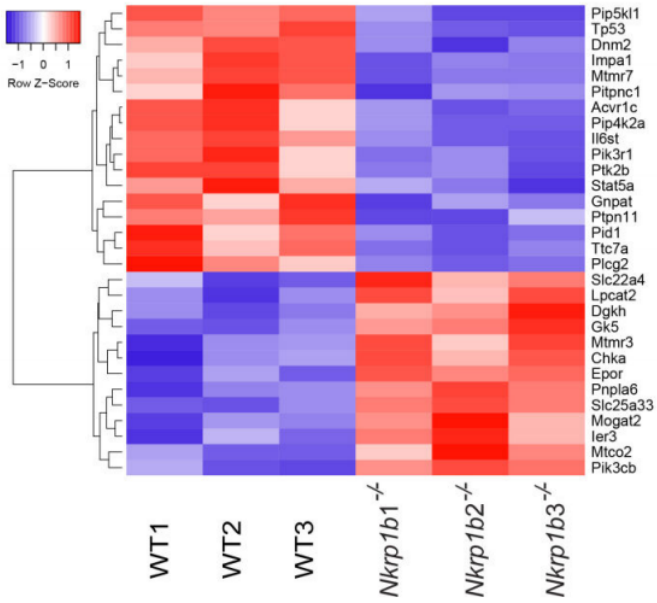
−1 0 1
Row Z-Score
Pip5kl1
Tp53
Dnm2
Impa1
Mtmr7
Pitpnc1
Acvr1c
Pip4k2a
Il6st
Pik3r1
Ptk2b
Stat5a
Gnpat
Ptpn11
Pid1
Ttc7a
Plcg2
Slc22a4
Lpcat2
Dgkh
Gk5
Mtmr3
Chka
Epor
Pnpla6
Slc25a33
Mogat2
Ier3
Mtco2
Pik3cb
WT1
WT2
WT3
Nkrp1b1−/−
Nkrp1b2−/−
Nkrp1b3−/−

C

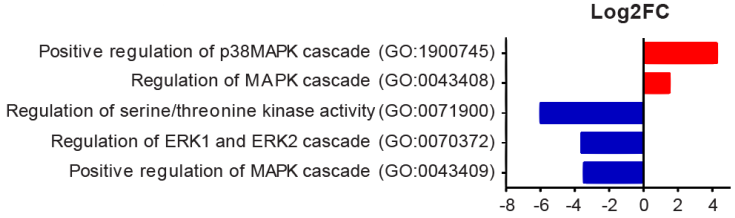
Log2FC
Positive regulation of p38MAPK cascade (GO:1900745)
Regulation of MAPK cascade (GO:0043408)
Regulation of serine/threonine kinase activity (GO:0071900)
Regulation of ERK1 and ERK2 cascade (GO:0070372)
Positive regulation of MAPK cascade (GO:0043409)
-8 -6 -4 -2 0 2 4

D

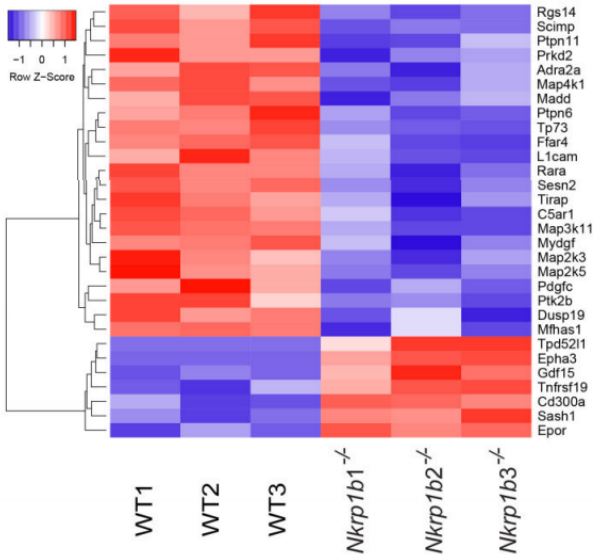
−1 0 1
Row Z-Score
Rgs14
Scimp
Ptpn11
Prkd2
Adra2a
Map4k1
Madd
Ptpn6
Tp73
Ffar4
L1cam
Rara
Sesn2
Tirap
C5ar1
Map3k11
Mydgf
Map2k3
Map2k5
Pdgfc
Ptk2b
Dusp19
Mfhas1
Tpd52l1
Epha3
Gdf15
Tnfrsf19
Cd300a
Sash1
Epor
WT1
WT2
WT3
Nkrp1b1−/−
Nkrp1b2−/−
Nkrp1b3−/−

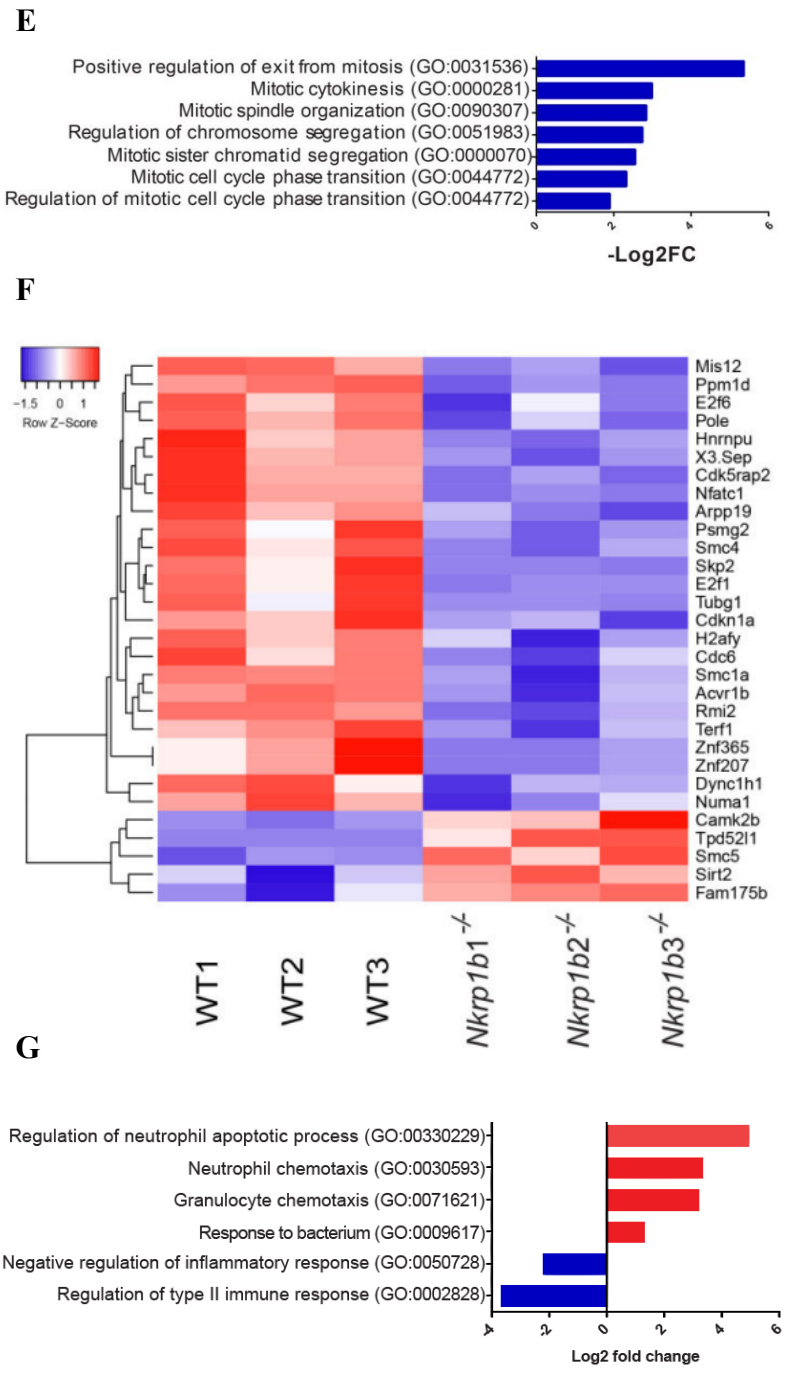

Fig 4.13: Major areas of genetic dysregulation in NKR-P1B deficient AMs.
(A) Gene ontology pathways related to lipid metabolism and processing (Log2 fold change) in AMs obtained from *Nkrp1b*$^{-/-}$ mice at 2 weeks of age as determined by RNA-seq analysis.
(B) Top 30 dysregulated genes related to lipid metabolism and processing as determined by RNA-seq analysis. Data presented as Z-scores of Log2 fold change.
(C) Gene ontology pathways related to ERK and P38-MAPK (Log2 fold change) in AMs obtained from *Nkrp1b*$^{-/-}$ mice at 2 weeks of age as determined by RNA-seq analysis.

(D) Top 30 dysregulated genes related to ERK and P38-MAPK kinase activity as determined by RNA-seq analysis. Data presented as Z-scores of Log2 fold change.
(E) Gene ontology pathways related to cell cycle enriched (-Log2 fold change) in AMs obtained from *Nkrp1b*$^{-/-}$ mice at 2 weeks of age as determined by RNA-seq analysis.
(F) Top 30 dysregulated genes related cell cycle as determined by RNA-seq analysis. Data presented as Z-scores of Log2 fold change.
(G) Gene ontology pathways related to immune function (-Log2 and Log2 fold change) in AMs obtained from *Nkrp1b*$^{-/-}$ mice at 2 weeks of age as determined by RNA-seq analysis.

The transcriptional profile of *Nkrp1b*$^{-/-}$ AMs showed altered expression of genes that encode well-characterized components of lipid processing and efflux such as ABCA1, ABCG1 and DAG-kinases, as well as lipases such as LPCAT2 and PNPLA2. Other dysregulated genes such as *Cd36, Lpcat2 and Cds1* have roles in uptake and conversion of lipids from one species into another (Fig 4.14a). Likewise, the expression of genes which encode mediators of AM and general macrophage signalling such as PIK3cb, Fosb, Rras2, Rara and Rasgrp4, were significantly dysregulated in *Nkrp1b*$^{-/-}$ AMs (Fig 4.14b). We also noted a significant upregulation of *pparg,* as well as the downregulation of *Stat5a*, *Rara*, *Rarg*, *Il4ra*, which can have significant consequences on AM metabolic programming and differentiation[232,242,263] (Fig 4.14b). We also identified an upregulation in the expression of mediators of AM lipid metabolism. In particular, *Akrb10, Hilpda, Plin2, Fabp5* and *Serpinb6*, were upregulated in *Nkrp1b*$^{-/-}$ AMs, all of which are involved and have functional consequences related to lipid transition and metabolism as well as lipid droplet formation. From this transcriptomic data emerges a pattern of progressive multi-faceted metabolic breakdown in *Nkrp1b*$^{-/-}$ AMs which appears to involve pathways relating lipid uptake, conversion, and expulsion.

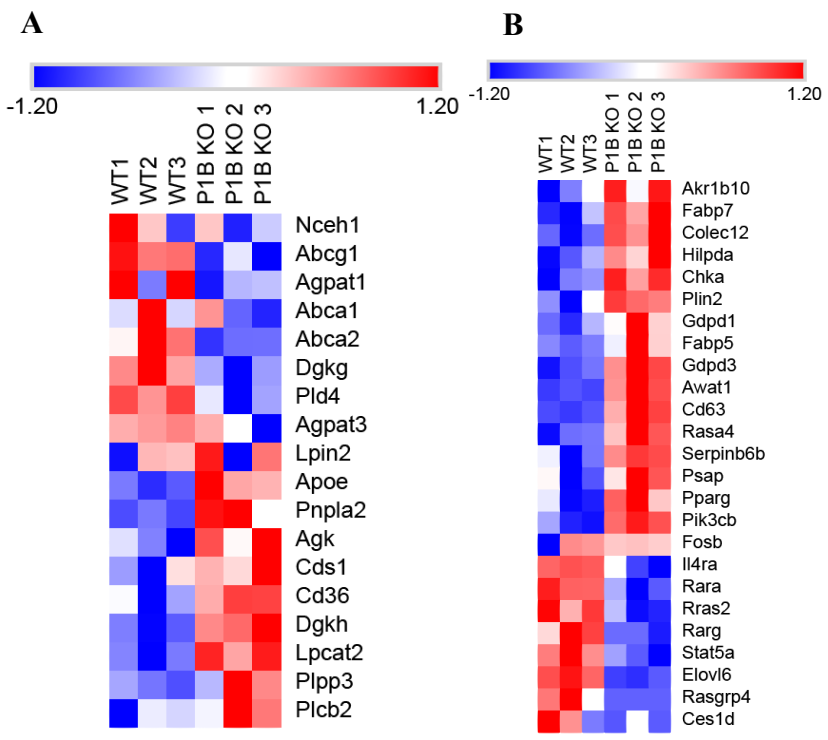

Fig 4.14: Genes related to lipid metabolism and general metabolic activity are dysregulated in *Nkrp1b*$^{-/-}$ AMs.
Heatmaps of relevant (A) lipid-specific metabolism genes and (B) genes related to general AMØ metabolic activity. Log2 fold change enrichment presented as Z-scores. N = 3 for WT and *Nkrp1b*$^{-/-}$ mice with every N consisting of AMs pooled from 5 different mice.

4.4.2 Lipidomic Analysis Indicates Severe Dysfunction of Surfactant Components, Diacylglyceride and Cholesterol in *Nkrp1b*$^{-/-}$ AMs.

We have previously described the metabolic dysregulation of *Nkrp1b*$^{-/-}$ AMs utilizing RNA sequencing. However, to produce a clearer picture of the actual dynamics of lipid processing, a genomic screen insufficient, nor does it provide information on the exact points at which AM metabolism begins to break down. To resolve this problem, we performed lipidomic analysis on AMs to elucidate the nature of the lipid droplets in AMs and to gain insight into the *Nkrp1b*$^{-/-}$ AM metabolic defect. AMs from WT and *Nkrp1b*$^{-/-}$ mice that were 6 weeks of age, when the most lipid-laden cells are present and thus

contain the most lipid available for analysis. The lipidomic analysis revealed dysregulation in several critical lipid classes. Mainly low levels of phosphatidic (PA), lysophosphatidic acid (LPA) and overall low levels of triglycerides (TG). Conversely, levels of PC, PG, lyso-PC, and lyso-PC were considerably higher (Fig. 4.15). Likewise, there appears to be significant accumulation of diacylglycerols (DAG) as well as cholesterol esters (CE). These lipid dysregulations are indicative of an accumulation of surfactant components as well as cholesterol and a dysregulation in intermediary, conversion lipid species.

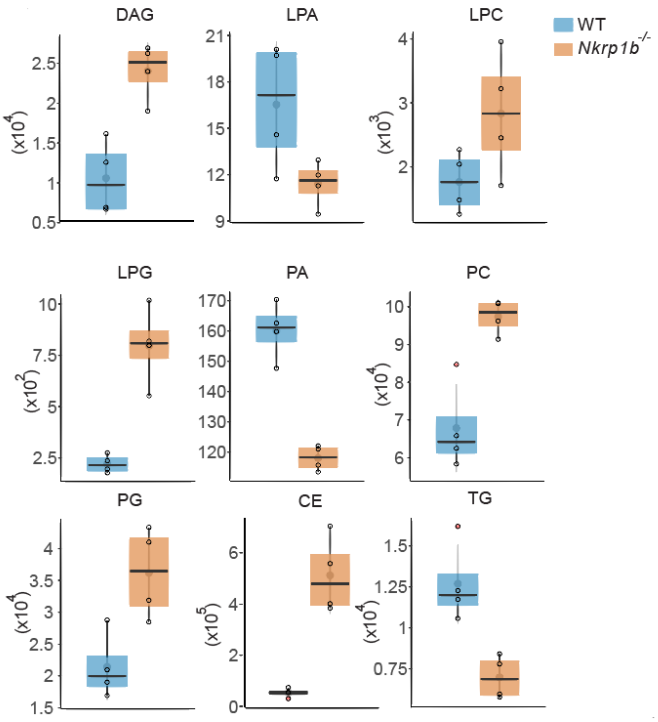

Fig 4.15: Lipidomic analysis shows significant differences in lipid species present in WT and *Nkrp1b*$^{-/-}$ AMs.
Lipidomic analysis comparing various lipid species found in AMØ isolated from WT and *Nkrp1b*$^{-/-}$ mice at 6 weeks of age. DAG (Diacylglyceride), LPA (Lysophosphatidic acid), LPC (Lysophosphatidylcholine), LPG (Lysophosphatidylglycerol), TG (Triglyceride), PA (Phosphatidic acid), PC (Phosphatidyl choline), PG (Phosphatidyl glycerol), CE (Cholesterol ester). Boxes and bars represent the interquartile range with standard deviation (SD).

4.4.3 Combining RNA-seq And Lipidomics Allows Us to Build an Integrated Genomic/Lipidomic Model to Highlight the Accumulation of Lethal Lipid Droplets in *Nkrp1b*$^{-/-}$ AMs

Combining the sequencing data with lipidomics allows us to re-construct and examine changes in relevant metabolic networks that define AM function. As illustrated in Fig 4.16, upregulation of CD36 and perhaps the activity of other receptors as well, may account for the increased uptake of PC, PG, cholesterol and perhaps LPC and LPG, which together comprise the bulk of surfactant lipids. Also, our findings indicate the dysregulation of lipid metabolic processes in *Nkrp1b*$^{-/-}$ AMs, which is supported by the upregulation of enzymes such as PLCB2, PNPLA2, PLPP3, which catalyze the breakdown of TGs, PA, and LPA by converting them into DAG and various fatty acids, lipid classes which are respectively diminished and increased in our analysis. This shunt towards DAG accumulation in *Nkrp1b*$^{-/-}$ AMs, combined with a deficiency of DGKG, serves to create an excess of DAG species which are shuttled into lipid droplets along with the canonical lipid storage species of CE, which is also found in excess in *Nkrp1b*$^{-/-}$ AMs. However, the low TG lipid pool, considered to be a safe storage lipid, is indicative that lipid droplets in *Nkrp1b*$^{-/-}$ AMs contain species of DAG, FC and various fatty acids in excess, all of which have been shown to induce lipo-toxicity[264,265]. Additionally, downregulation of the cholesterol transport cassettes Abca1, Abcg1 and converting enzyme Nceh results in the accumulation of the accumulatio of CE and FC. The failure to convert CE to FC in a timely manner combined with slow expulsion of FC is a source of

additional lipid species that can contribute to *Nkrp1b*$^{-/-}$ AM lipo-toxicity.

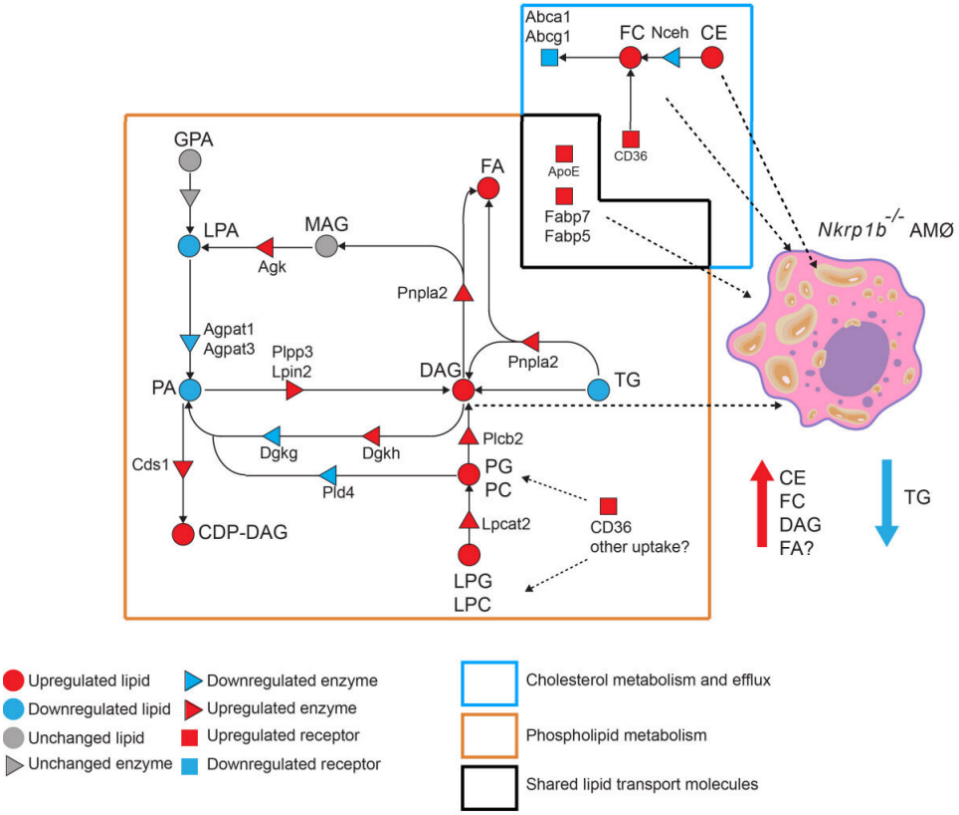

Fig 4.16: Dysregulation of AM lipid metabolism through NKR-P1B ablation leads to accumulation of toxic lipid species inside the AM.
Model combining RNA-seq data from (3.33) and lipidomic data from (3.34) showing the accumulation of toxic lipid species in *Nkrp1b*$^{-/-}$ AMØ. Dashed arrows indicate shuttling of lipid into droplets.

The above data demonstrates that loss of NKR-P1B AMs causes them to undergo profound changes in their lipid metabolism and ability to proliferate, demonstrated by both transcriptional and experimental data. Interestingly, both of these defects can be resolved by simply removing the AMs from the lipid-rich alveolar environment. Synthesis of lipidomic and transcriptional data has allowed us to create a model of *Nkrp1b*$^{-/-}$ AM collapse due to an accumulation of toxic lipid species caused likely by a combined effect of both excessive lipid uptake and internal metabolic dysfunction.

CHAPTER 5: Mechanism of NKR-P1B Signalling in AMs

5.1 Lipid Uptake Dynamics of AMs as a Factor of NKR-P1B Stimulation

5.1.1 Cross-Linking of WT AMs Results in Differential Regulation of Certain Key Metabolic Genes as Analyzed by qPCR.

To follow up on the results presented in previous chapters, we decided to begin performing assays verifying the casual influence of NKR-P1B on the phenotypes that we have observed *in vitro* and *in vivo.* To verify the transcriptional dysregulation of specific lipid uptake and metabolic mediators revealed in the RNA-seq screen, we performed qPCR analysis on AMs of 2-week-old WT and *Nkrp1b*$^{-/-}$ mice for the lipid uptake receptor, *Cd36*, the cholesterol efflux cassettes, *Abca1*, *Abcg1*, and the transcription factor, *Rara*, all of which have been highlighted by RNA-seq as being dysregulated. The differential expression results for all the genes selected for qPCR analysis, except for *Ldlr*, corresponded with the observed changes identified by RNA-seq (Fig 5.1a). We postulated that if a lack of NKR-P1B results in dysregulation in the genes examined in Fig 5.1a, cross-linking the NKR-P1B receptor using an anti-NKR-P1B antibody (clone 2D12), thereby forcing signalling through its ITIM, should produce the opposite effect in WT AMØ. Indeed, cross-linking of NKR-P1B on WT AMs resulted in increases of *Nceh* and *Abcg1,* as well as decreases in *Serpinb6b, Fabp5, ApoE*, *and Psap*, compared to unstimulated WT AMs (Fig 5.1b), all of which showed the opposite effect in qPCRs and RNA-seq performed on *Nkrp1b*$^{-/-}$ AMs, thus indicating a potential direct modulatory role of NKR-P1B signalling in these genes. Levels of *Cd36, Cd63, Ldlr, Abca1* and *Rara* were similar to that of NKR-P1B deficient AMs indicating a secondary effect of NKR-

P1B loss. These results provide the first evidence of NKR-P1B signalling exerting control over the AM transcriptomic profile.

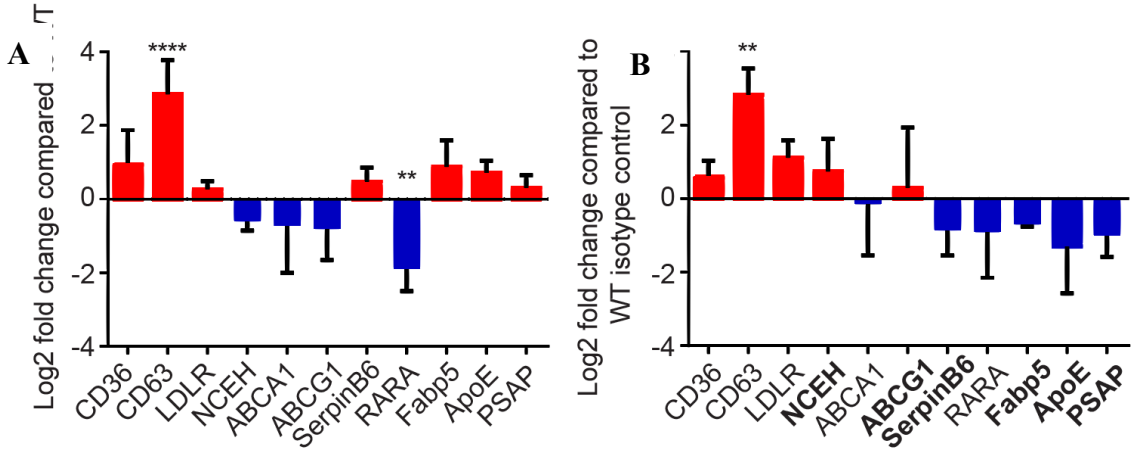

Fig 5.1: qPCR analysis of WT AMs, *Nkrp1b*$^{-/-}$ AMs and WT AMs subjected to 2D12 mediated cross-linking.
(A) qPCR analysis of select metabolic genes performed on AMØ isolated from WT and *Nkrp1b*$^{-/-}$ mice at 2 weeks of age. Data is normalized to WT levels. N = 4
(B) qPCR analysis performed on WT AMØ that have been crosslinked with 2D12 or isotype antibody. Data normalized to isotype control. N = 3. Statistics determined by Students t-test where * is P = <0.05, ** is P = <0.005, *** is P = <0.0005 and **** is P = <0.00005

5.1.2 Increased Rates of PC and PG in *Nkrp1b*$^{-/-}$ AMs

While previous data points to an apparent defect in lipid metabolism and storage, surfactant components must also be actively transported into the macrophage through scavenger receptors. Therefore, we set out to determine if NKR-P1B plays a direct role in modulating lipid uptake kinetics in AMs. Surfactant lipid is mainly composed of two major lipid species PC and PG, with cholesterol and other lipids forming a minor surfactant fraction[219]. Rate of surfactant uptake can be analyzed using fluorescently labelled surfactant components (NBD-PC or NBD-PG)[153,266]. Lavaged *Nkrp1b*$^{-/-}$ AMØ showed an increase in both PC and PG uptake *in vitro* compared to their WT counterparts

(Fig 5.2a and Fig 5.2c) when incubated with NBD-labelled PC or PG for 20,40 and 60 minutes. Quantifications shown in Fig 5.2b and Fig 5.2d reveal a trend of increased PC and PG uptake in *Nkrp1b*$^{-/-}$ AMs, which is primarily evident at 40- and 60-minute time points and 20- and 60- minute time points respectively.

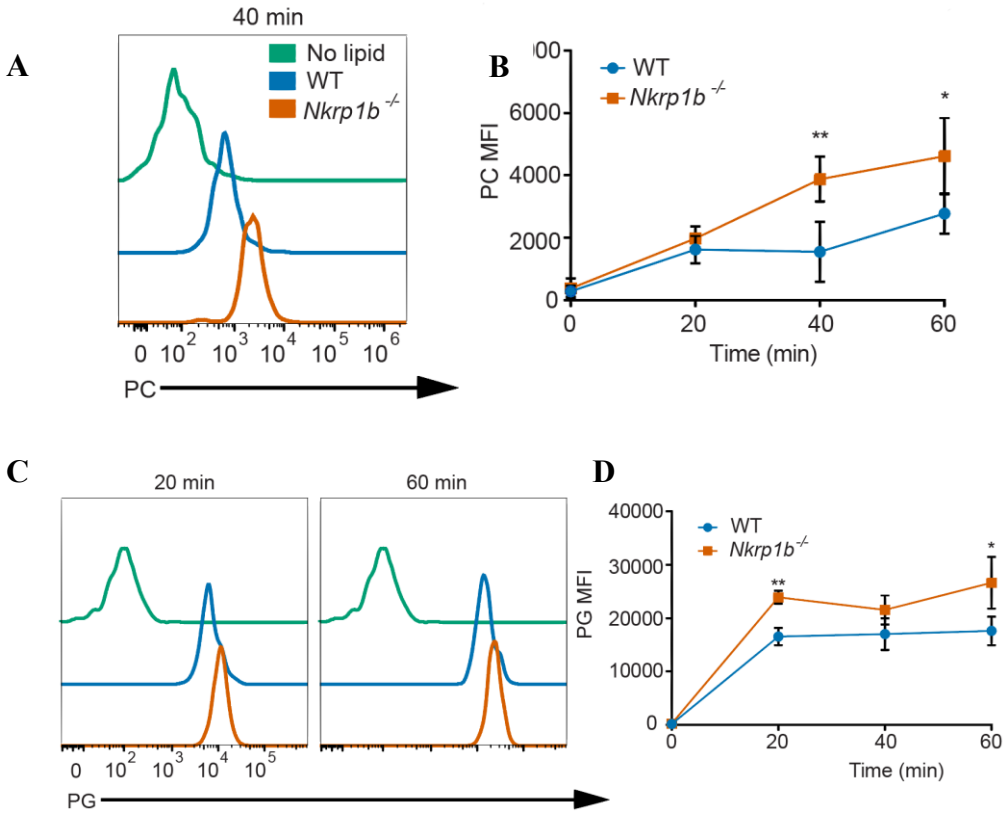

Fig 5.2: Differential lipid uptake in *Nkrp1b*$^{-/-}$ AMs.
(A) Histogram of fluorescent lipid content in AMs isolated from WT and *Nkrp1b*$^{-/-}$ mice and cultured with NBD-PC at the 40-minute timepoint. Plot representative of 6 independent experiments.
(B) Difference in MFI of NBD-PC uptake between WT and *Nkrp1b*$^{-/-}$ AMs over time as measured at 0-, 20-, 40- and 60-min time points. Error bars represent SEM. N = 6
(C) Histograms of fluorescent lipid content in AMs isolated from WT and *Nkrp1b*$^{-/-}$ mice and cultured with NBD-PG at 20-and 60-minute timepoints. Plot representative of 5 different experiments. Statistical significance was determined by two-way ANOVA with Tukey's correction where * is P = <0.05 and ** P = <0.005.
(D) Difference in MFI of NBD-PG uptake between WT and *Nkrp1b*$^{-/-}$ AMs over time as measured at 0-, 20-, 40- and 60-min time points. Error bars represent SEM. N =5

In the previous section, set we have been able to verify certain transcripts uncovered through RNA-seq by qPCR as well as assign NKR-P1B a role in mediating the expression of some of these genes. We were curious to see if NKR-P1B plays a direct role in AM lipid uptake dynamics as well. We therefore hypothesized that cross-linking of the NKR-P1B receptor on WT AMs should produce the opposite effect. Indeed, cross-linking of NKR-P1B on AMs derived from WT mice prior to a 40-minute incubation with PC, results in significantly decreased PC uptake (Fig 5.3a and Fig 5.3b). Decreases in lipid uptake were not observed when cross-linking AMs with an isotype antibody, nor when cross-linking was attempted on AMs derived from *Nkrp1b*$^{-/-}$ mice. Likewise, cross-linking of WT AMs with 2D12 prior to a 20-minute incubation with PG also resulted in decreased lipid uptake (Fig 5.3c and Fig 5.3d). Similarly, to our data showing transcriptome level changes when WT AMs were subjected to NKR-P1B cross-linking, we have been able to show that NKR-P1B cross-linking appears to actively affect the rate of AM lipid uptake, acting as a potential negative regulator.

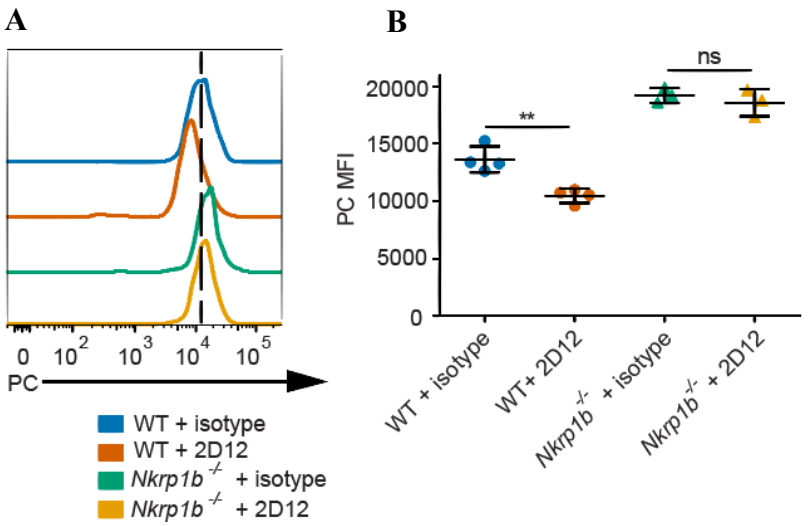

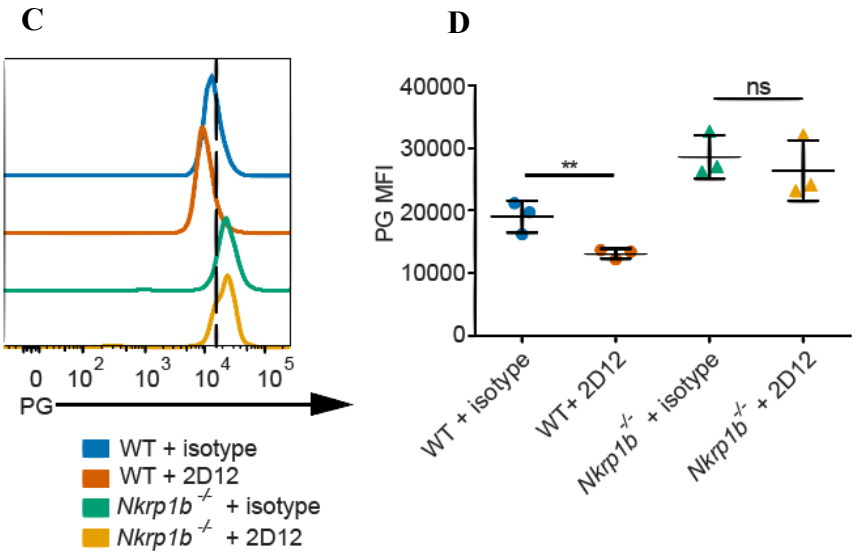

Fig 5.3: Differential lipid uptake observed in WT AMs crosslinked with 2D12.
(A) Histogram showing NBD-PC uptake in WT AMs crosslinked with 2D12 or isotype control, AMs from *Nkrp1b*$^{-/-}$ AMØ serve as an additional control. Plot representative of 3 independent experiments.
(B) MFI quantifications of NBD-PC uptake in WT AMs crosslinked with 2D12 or isotype control. AMs from *Nkrp1b*$^{-/-}$ mice serve as an additional control. Error bars represent SEM. Data analyzed by two-way ANOVA with Tukey's correction where ** is $P = <0.005$
(C) Histogram showing NBD-PG uptake in WT AMs crosslinked with 2D12 or isotype control, AMs from *Nkrp1b*$^{-/-}$ AMØ serve as an additional control. Plot representative of 3 independent experiments.
(D) MFI quantifications of NBD-PG uptake in WT AMs crosslinked with 2D12 or isotype control. AMs from *Nkrp1b*$^{-/-}$ mice serve as an additional control. Error bars represent SEM. Data analyzed by two-way ANOVA with Tukey's correction where ** is $P = <0.005$

5.1.3 GM-CSF Appears to Have no Effect on AM Rates of Lipid Uptake.

We have so far demonstrated the effects of NKR-P1B on the uptake of lipids by AMs in an *in vitro* system. Those experiments however does not account for the cytokine milieu that is constantly present in the alveolar space and which has been shown to heavily influence AM metabolism and differentiation as described above. To assess the contribution of GM-CSF in our system we performed lipid uptake assays on WT macrophages crosslinked with either isotype antibody or with 2D12 in the presence of

absence of GM-CSF. After which the AMs were exposed to NBD-PC for 40 minutes and analyzed by flow cytometry. As seen in Fig 5.4a and Fig 5.4b, the addition of GM-CSF appeared to show a trend in basal lipid uptake in both isotype and 2D12 cross-linked group, but this was found to be non-significant, while the expected reduction in NBD-PC uptake occurred as previously demonstrated in the groups without GM-CSF addition.

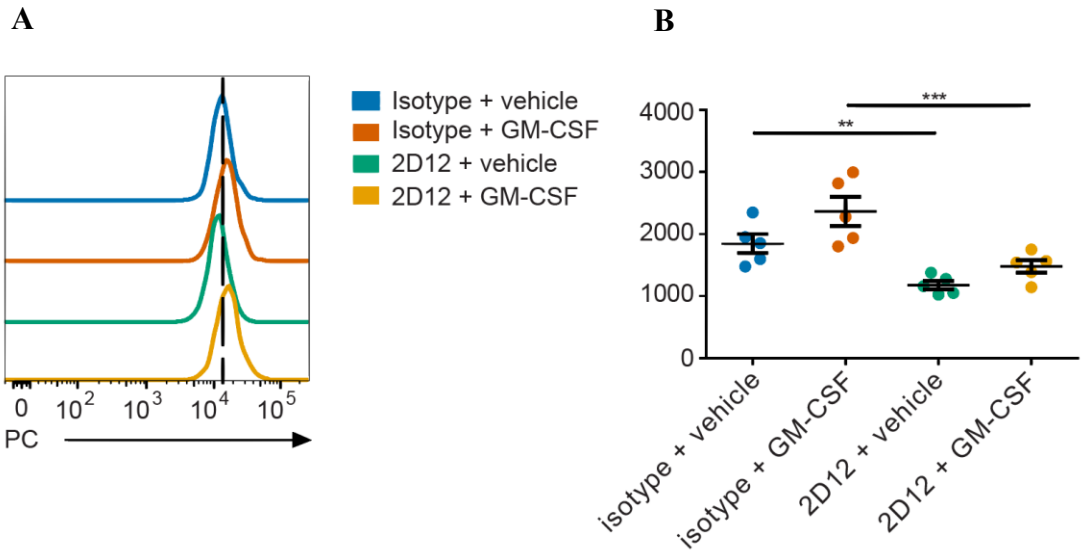

Fig 5.4: Differences in lipid uptake in WT AMs subjected to 2D12 mediated cross-linking with or without the presence of GM-CSF.
(A) Histogram of fluorescent lipid content in AMs isolated from WT mice and cultured with NBD-PC at the 40-minute timepoint with or without the presence of GM-CSF. Plot representative of 5 independent experiments.
(B) Difference in MFI of NBD-PC uptake at the 40-minute timepoint between WT AMs subjected to cross-linking with or without the presence of GM-CSF =. Error bars represent SEM. N = 5. Statistical significance was determined by two-way ANOVA with Tukey's correction where ** is P = <0.005 and *** P = <0.0005

These experiments and our previous work showing GM-CSF secretion and signalling is unperturbed implies that the effect NKR-P1B is having is likely independent of direct GM-CSF signalling or the NKR-P1B mediated effect is exerted significantly downstream of GM-CSF signalling.

5.1.4 AM Phagocytosis Appears to be Unaffected

The preceding sections have highlighted the impact of NKR-P1B loss on the uptake of surfactant lipid and overall lipid metabolism of AMs. To compliment this data, we decided to analyze the AM phagocytosis, which is a hallmark macrophage ability and one in which C-type lectin and lectin like receptors play a critical role. Internalization of foreign particles by macrophages can occur through a multitude of different pathways including antibody dependent-phagocytosis, a well-known and characterized mechanism of phagocytosis crucial for bacterial and viral pathogen clearance[267,268]. To this end isolated AMs were incubated with fluorescently labelled, antibody coated beads for 20,40,60 minutes after which they were analyzed by flow cytometry for fluorescence, in effect stimulating antibody dependent phagocytosis in AMs. As can be seen from Fig 5.5a and Fig 5.5b, WT AMs show a tendency towards rapid phagocytosis which then slowly decreases through 40 and 60 minutes while *Nkrp1b*$^{-/-}$ deficient AMs start off slowly but proceed to have a higher proportion of AMs with phagocytic activity the longer the incubation lasts. However, the results proved to be inconclusive with only a non-significant trend towards slightly lower bead uptake among *Nkrp1b*$^{-/-}$ AMs at the earlier timepoints of the experiment.

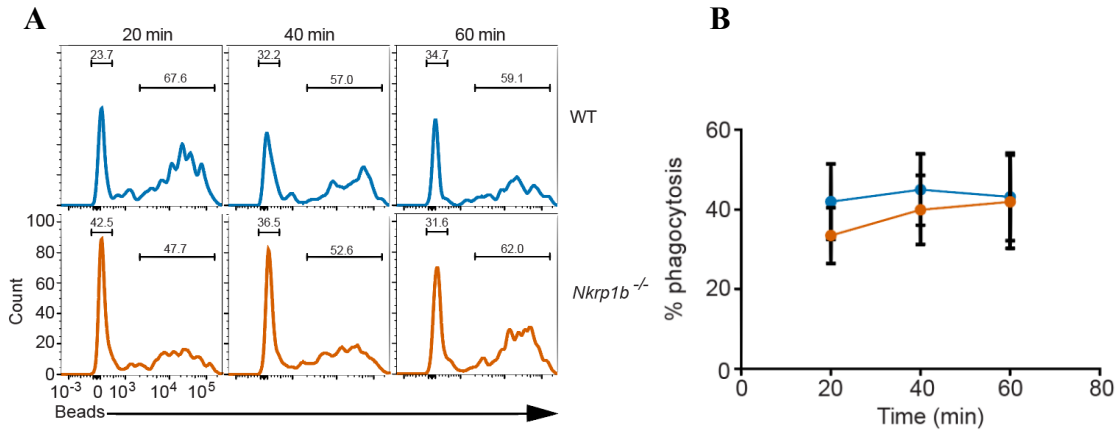

Fig 5.5: Analysis of phagocytosis in WT and *Nkrp1b*$^{-/-}$ AMs as analyzed by fluorscent bead uptake.
(A) Histograms of phagocytosis of fluorescent beads by WT and *Nkrp1b*$^{-/-}$ AMs at 20-, 40- and 60-minute timempoints harvested from 2-week-old mice. Right gate denotes percetage of AMs which have taken up beads while left gate denotes AMs which have not yet taken up any beads. The histograms are representative of 3 independent experiments. (B) Quantifications of percetage of AMs which have phagocytized fluorscent beads at 20, 40 and 60 minute timepoints as shown in (A). N=3

Antibody mediated phagocytosis is not the only mechanism through which AMs are able to engulf cells and other foreign matter. Active phagocytosis of cancer cells is a well characterized method of macrophage phagocytosis[269,270] which involves many different receptor and ligand interactions between effector and target, such as the interaction between CD47 on target cells and SIRP-α on the surface of macrophages[271]. For this purpose we incubated AMs with HeLa cells constitutively expressing GFP for 20 minutes and analyzed them by flow cytometry. As can ben seen from Fig 5.6a and Fig 5.6b, there was little difference between WT and *Nkrp1b*$^{-/-}$ AMs in terms of HeLa cell phagocytosis with only a slight tendency towards an increase phagocytic capability in *Nkrp1b*$^{-/-}$ AMs.

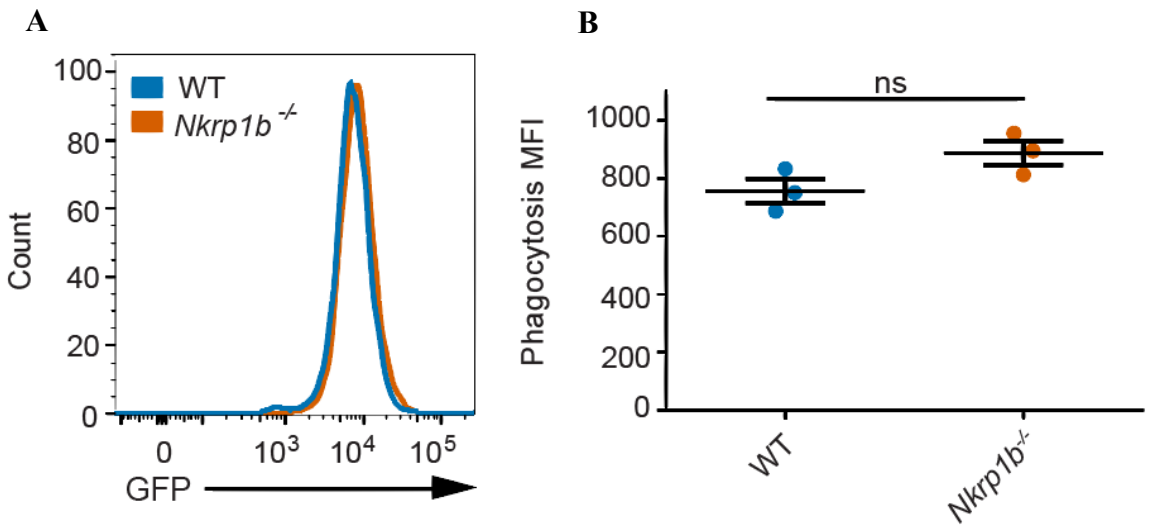

Fig 5.6: Analysis of the phagocytic ability of WT and *Nkrp1b*$^{-/-}$ AMs through engulfment of fluorescent cancer cells
(A) Histograms of phagocytosis of fluorescent beads by WT and *Nkrp1b*$^{-/-}$ AMs at 40-minute timepoint harvested from 2-week-old mice. Histograms are representative of 3 independent experiments
(B) Quantifications of AMs which have phagocytized fluorescent cells at 40-minute time point as shown in (A). N=3. Significance is determined by Student's t-test.

The above data demonstrate that NKR-P1B loss appears to affect primarily lipid uptake pathways while leaving two major macrophage phagocytic pathways (antibody mediated, and cancer cell surface receptor mediated phagocytosis) unimpaired, thus we decided not to proceed with experiments characterizing NKR-P1B cross-linking and its effect on overall phagocytic ability. These further cements the role of NKR-P1B as a specific regulator of AM lipid metabolism and the rate of lipid uptake.

5.1.5 AMJ-C11 Transfected With NKR-P1B Show Similar Lipid Uptake Kinetics as Primary AMs When Subjected to NKR-P1B Cross-linking.

For the next phase of our study, we wanted to create an *in vitro* AM system that could overcome the low AM numbers and high mouse burden that are limiting factors when working with primary AMs derived from 2-week-old mice. As such we used the AMJ-

C11 cell line, a J2 murine retrovirus-immortalized AM line of the C57BL/6 background. We generated stable NKR-P1B-expressing AMJ-C11 cells (AMJ-P1B henceforth) by lentiviral transduction and AMJ-C11 control cells transduced with an empty lentiviral vector (AMJ-EV henceforth) (Fig 5.7). Using 2D12 antibody we were able to verify stable expression of NKR-P1B compared to the empty vector and parental strain.

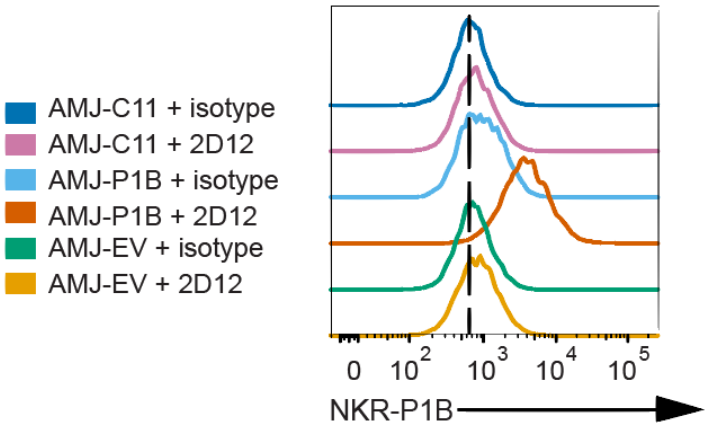

Fig 5.7: Expression of NKR-P1B on AMJ-C11 cells stably transfected with PLJM-1 lentiviral vector.
AMJ-C11 cells transfected with NKR-P1B carrying lentiviral vector express the receptor stably on their surface as determined by 2D12 staining.

To confirm that our AMJ-P1B model was representative of primary AMs, we performed a 2D12-crosslinking assay followed by incubation with PC as demonstrated previously in cross-linking experiments involving primary AMs. As seen in Fig 5.8a and b, AMJ-EV cells showed no change in lipid uptake when crosslinked with either 2D12 or isotype controls while AMJ-P1B cells demonstrated a small but consistent and significant decrease in lipid uptake after 20- and 40-minute incubations with NBD-labelled PC.

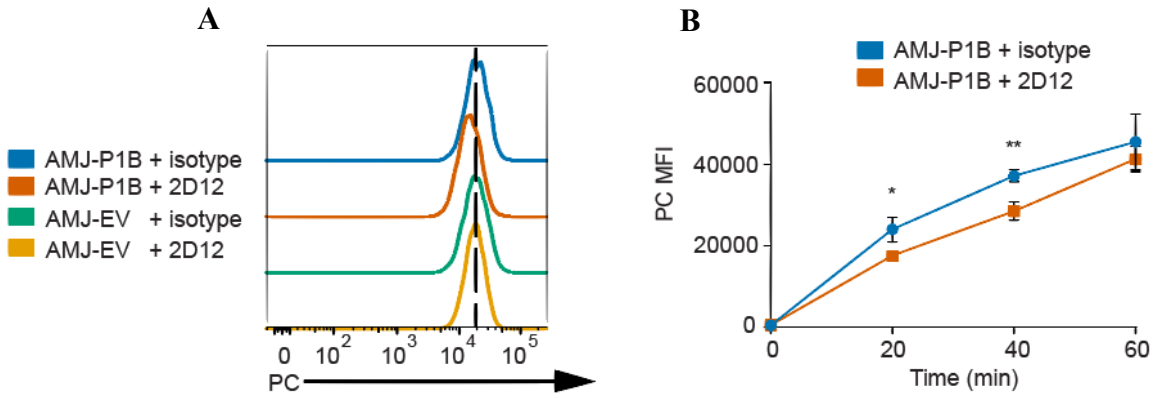

Fig 5.8: Cross-linking of AMJ-C11 cells results decrease in lipid uptake
(A) Histogram showing NBD-PC uptake in AMJ-C11 cells crosslinked with 2D12 or isotype control, parental AMJ-C11 stably transfected with empty lentiviral vector serve as an additional control. Plot representative of 3 independent experiments.
(B) MFI quantifications of NBD-PC uptake in AMJ-C11 cells crosslinked with 2D12 or isotype control. Data analyzed by two-way ANOVA with Tukey's correction where * is $P = <0.05$ and ** is $P = <0.005$

The NKR-P1B AMJ-C11 cell line has shown that it can faithfully replicate the phenomenon of NKR-P1B-driven lipid uptake and will prove a useful tool for subsequent experiments. We have also demonstrated the effect of NKR-P1B cross-linking in a reductionist assay through the transfection of AMJ-C11 cells via lentiviral vector. This experiment solidifies our previous data from primary cells which demonstrates the effect of NKR-P1B cross-linking on primary AMs. Taken all together, the above data shows that NKR-P1B modulation, be it by its absence or through stimulation, drives AM lipid uptake kinetics while having negligible effect on a couple of major AM phagocytic pathways.

5.2 Excess Lipid Uptake by *Nkrp1b*$^{-/-}$ AMs can be Partially Inhibited *In Vitro* and *In Vivo*

5.2.1 AKT Inhibition Abrogated Aberrant Lipid Uptake in *Nkrp1b*$^{-/-}$ AMs *In Vitro*

With the established relationship between NKR-P1B and lipid uptake combined with several promising hits from RNA-seq analyses we next determined if modulating some of these signalling pathways *in vitro* and *in vivo* could rescue AM numbers in *Nkrp1b*$^{-/-}$ mice or alleviate some of the lipid accumulations present. AKT plays a crucial role in downstream GM-CSF signalling and AM metabolic activation, which made it a potential target for a pharmacological intervention. By applying MK2206 *in vitro*, a known AKT inhibitor, we were able to normalize the uptake of both PC and PG in *Nkrp1b*$^{-/-}$ AMs (Fig 5.9a-d).

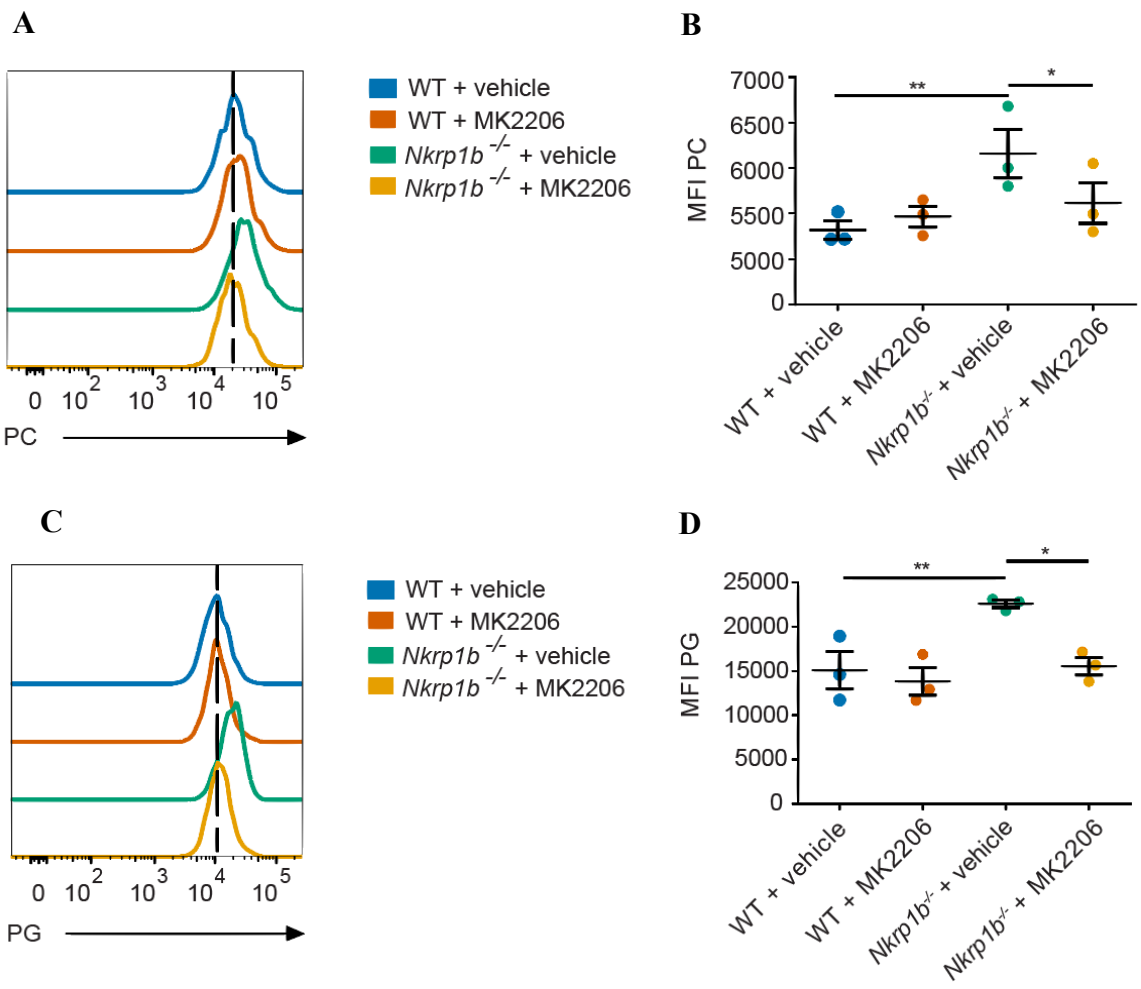

Fig 5.9: MK2206 mediated inhibition of AKT results in decreased lipid uptake in *Nkrp1b*$^{-/-}$ AMs.
(A) Histogram of fluorescent lipid content in AMs isolated from WT and *Nkrp1b*$^{-/-}$ mice and cultured with NBD-PC at the 40-minute timepoint in the presence or absence of MK2206. Plot representative of 3 independent experiments.
(B) Difference in MFI of NBD-PC uptake between WT and *Nkrp1b*$^{-/-}$ AMs as measured at the 40 min timepoint. N = 3. Error bars represent SEM. Data analyzed by two-way ANOVA with Tukey's correction where * is $P = <0.05$ and ** is $P = <0.005$.
(C) Histogram of fluorescent lipid content in AMs isolated from WT and *Nkrp1b*$^{-/-}$ mice and cultured with NBD-PG at the 40-minute timepoint in the presence or absence of MK2206. Plot representative of 3 independent experiments.
(D) Difference in MFI of NBD-PG uptake between WT and *Nkrp1b*$^{-/-}$ AMs as measured at the 40 min timepoint. N = 3. Error bars represent SEM. Data analyzed by two-way ANOVA with Tukey's correction where * is $P = <0.05$ and ** is $P = <0.005$.

The success in normalizing lipid uptake of *Nkrp1b*$^{-/-}$ AMs *in vitro* however did not translate when applied *in vivo*. Systemic AKT inhibition using MK2206 actually

appeared to reduce the *Nkrp1b*$^{-/-}$ AM population even further compared to WT AMs in two pilot experiments with both a high and low dose of the compound and was thus not pursued any further. Systemic administration of MK2206 is likely a confounding factor in this system and could be compensated for with a more targeted delivery.

5.2.2 P38 MAPK Inhibition Restored Ki67 Levels in AMs *In Vivo*

After the limited success that we saw with AKT inhibition as demonstrated in the previous figure we decided to move on to P38-MAPK as a potential intervention target. Dysregulation of P38-MAPK signalling featured prominently in our RNA-seq analysis and is known to be involved in AM cell cycle and some metabolic programming. Thus, we decided that this would be a logical lead to pursue as well. Analysis of P38-MAPK phosphorylation status in WT and *Nkrp1b*$^{-/-}$ AMs revealed a trend of higher P38-MAPK phosphorylation in *Nrkp1p*$^{-/-}$ AMs (Fig 5.10a and Fig 5.10b).

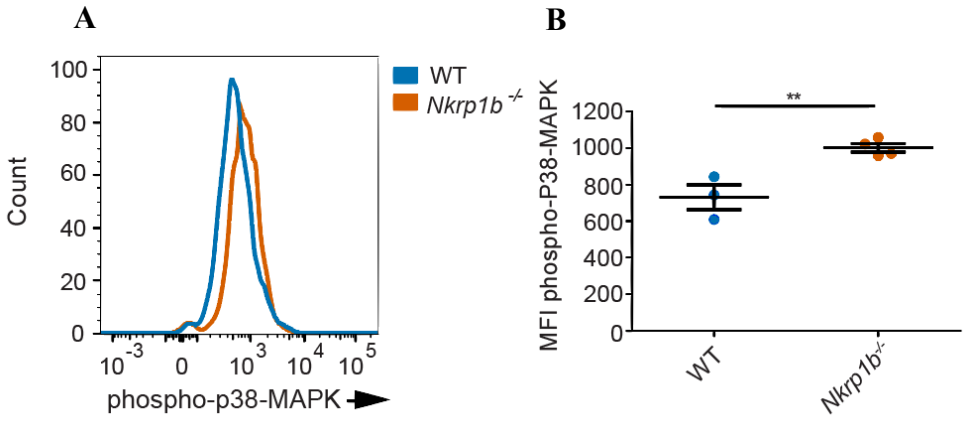

Fig 5.10: Levels of phosphorylated P38-MAPK in WT and *Nkrp1b*$^{-/-}$ AMs
(A) Expression profile of phosphorylated P38-MAPK on AMs obtained from 2-week-old WT and *Nkrp1b*$^{-/-}$ mice. Histogram is representative of 3 independent experiments.
(B) MFI quantifications of phosphorylated P38-MAPK expressions on AMs obtained from 2-week-old WT and *Nkrp1b*$^{-/-}$ mice. Error bars represent SEM. N=3 and 4 respectively. Significance determined by Student's t-test where * is $P = <0.05$ and ** is $P = <0.005$

This gave us the confidence to move forward into *in vitro* and *in vivo* rescue attempts. For the majority of our *in vivo* rescue experiments, WT and *Nkrp1b*$^{-/-}$*Ccr2*$^{-/-}$ mice were used unless otherwise noted to once again focus on the original liver monocyte-derived population. Likewise, mice of 3 weeks of age were used. This is the earliest possible weaning age for mice and was chosen to avoid confounding factors of a maternal milk diet and fast neonatal development which can have unforeseen consequences regarding systemic administration of pharmaceuticals that inhibit vital cellular processes. To this end we utilized SB203580, a known pharmacological inhibitor of P38-MAPK. *In vitro* studies using this compound failed to rescue aberrant lipid uptake in *Nkrp1b*$^{-/-}$*Ccr2*$^{-/-}$ AMs in a couple of pilot experiments with varying concentrations and was not pursued further (data not shown). *In vivo* administration of SB203580 did however produce a partial rescue of aberrant levels of Ki67 present in *Nkrp1b*$^{-/-}$*Ccr2*$^{-/-}$ AMs as described earlier. As observed in Fig. 5.11a and 5.11b, *in vivo* administration of SB203580 not only restored but, on average, induced Ki67 expression in *Nkrp1b*$^{-/}$*Ccr2*$^{-/--}$ AMs even beyond WT levels.

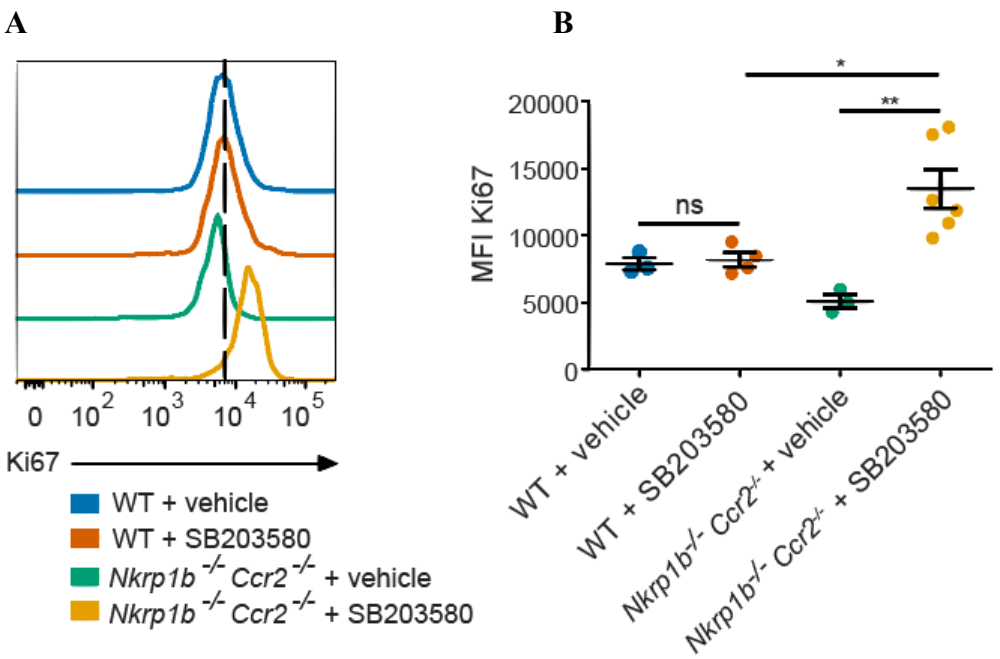

Fig 5.11: SB203580 administered *in vivo* appears to rescue Ki67 expression in *Nkrp1b*$^{-/-}$ AMs
(A) Histograms showing expression profile in WT and *Nkrp1b*$^{-/-}$*Ccr2*$^{-/-}$ AMs isolated from 5-week-old mice after a 2-week treatment with either vehicle or SB203580. Histogram is representative of 3 independent experiments.
(B) MFI quantifications of Ki67 expressions on AMs obtained from 5-week-old WT and *Nkrp1b*$^{-/-}$*Ccr2*$^{-/-}$ mice. Error bars represent SEM. N=6. Significance determined by two-wat ANOVA with Tukey's correction where * is $P = <0.05$ and ** is $P = <0.005$

This restoration of Ki67 expression in AMs did not translate to an increase in AM numbers, however, suggesting that induction of cell cycling through P38-MAPK modulation is simply insufficient to make any noticeable difference in restoring *Nkrp1b*$^{-/-}$ *Ccr2*$^{-/-}$ AM population kinetics to those of WT mice. Likewise, we did not observe any change in lipid uptake kinetics upon SB203580 administration *in vitro* highlighting the multi-faceted aspect of NKR-P1B on AMs and the multiple likely pathways that are disrupted due to lack of NKR-P1B signalling.

5.2.3 SSO Administration *In Vivo* Allows for a Slight Increase in *Nkrp1b*$^{-/-}$ AM Numbers

We have already shown previously through RNA-seq and flow cytometry that CD36 is slightly upregulated on AMs and its importance as a major scavenger receptor for lipid has been characterized previously as well. Sulfosuccinimidyl oleate (SSO) is a well-known irreversible inhibitor of CD36 which has been frequently used *in vivo* to block its function. Using SSO administered *in vivo* to *Nkrp1b*$^{-/-}$*Ccr2*$^{-/-}$ mice we noticed a slight trend towards an increase in AM cell numbers in *Nkrp1b*$^{-/-}$*Ccr2*$^{-/-}$ treated with SSO compared with vehicle treated mice (Fig A1a and Fig A1b). The SSO intervention is the first one trialled in this work which produced a noticeable increase in AM numbers when administered to *Nkrp1b*$^{-/-}$*Ccr2*$^{-/-}$ mice and thus represents a preliminary data set. While the number of AMs appears to modestly recover their differentiation status does not, nor is their lipid burden resolved when analyzed through ORO analysis and due to time constraints, expense and difficulty obtaining SSO during the pandemic no further follow up was conducted. Further experiments may elucidate the functional relation between NKR-P1B and CD36 in further detail.

5.2.4 Inhibition of HMG-CoA Pathway Via Pravastatin Moderately Improves AM Numbers in 5 Week Old *Nkrp1b*$^{-/-}$*;Ccr2*$^{-/-}$

Finally, due to a recent publication showing the potential of statin therapy to improve AM metabolism in mice with severe PAP[272], we decided to apply the same treatment to *Nkrp1b*$^{-/-}$*Ccr2*$^{-/-}$ mice. After 2 weeks of pravastatin administration, we collected the lungs of WT and *Nkrp1b*$^{-/-}$*Ccr2*$^{-/-}$ mice and stained them with ORO. A significant reduction in

ORO positive AMs of statin-treated compared to vehicle-treated *Nkrp1b*$^{-/-}$*Ccr2*$^{-/-}$ mice was observed (Fig 5.12a and Fig 5.12b).

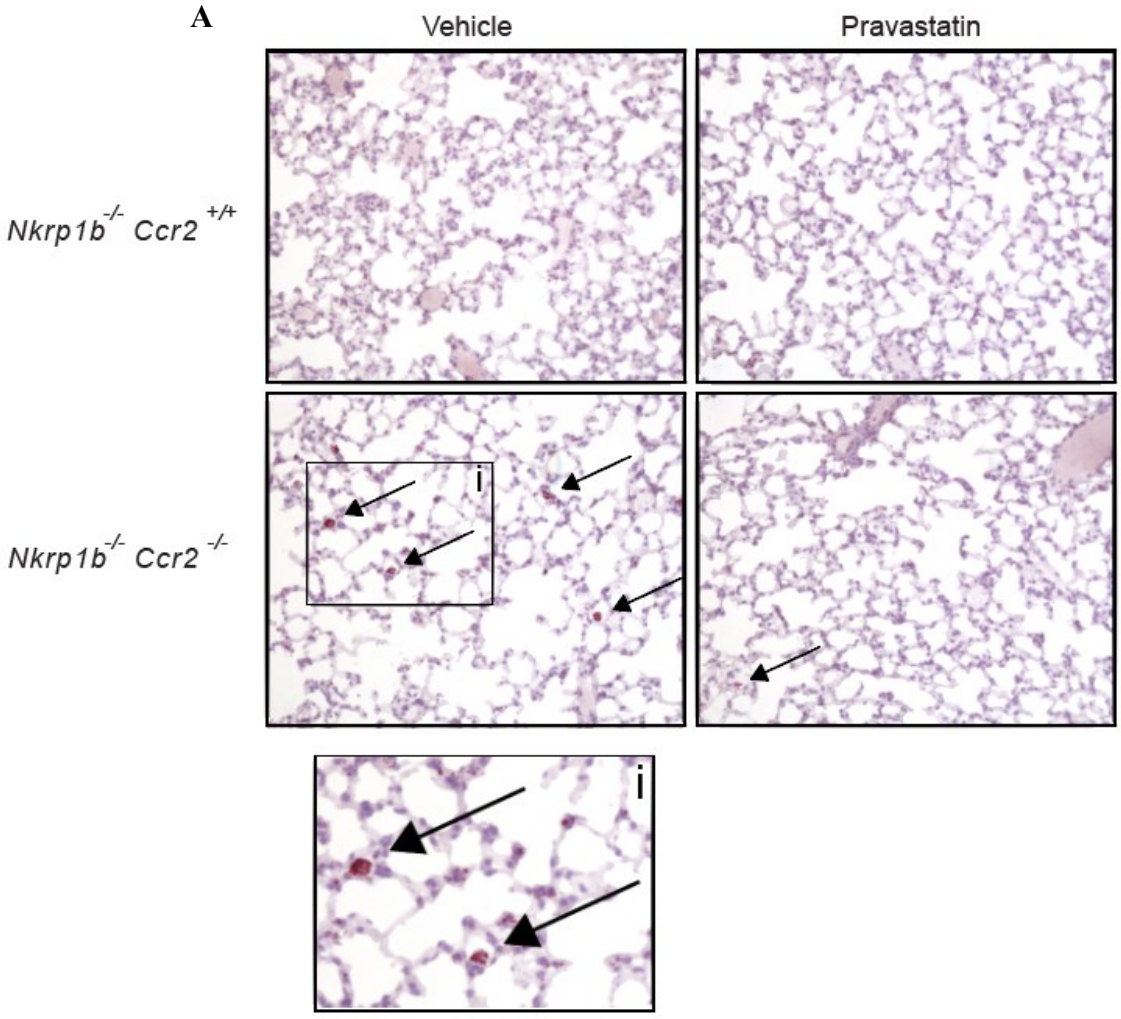

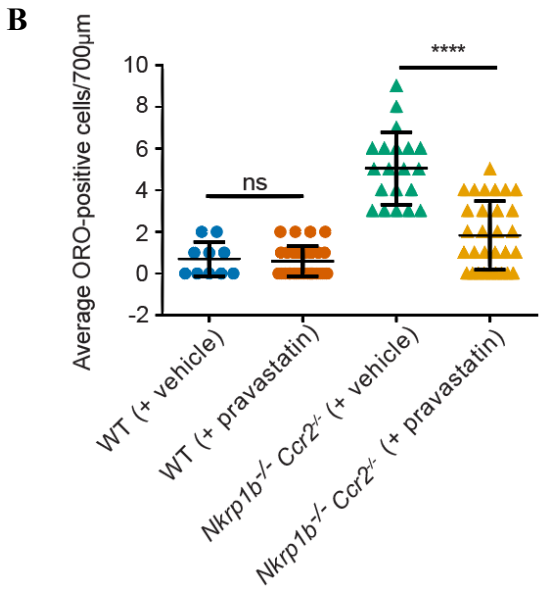

Fig 5.12: *In vivo* statin administration resolves *Nkrp1b*$^{-/-}$ AM lipid accumulation phenotype
(A) ORO-stained frozen lung section of 5-week-old *Nkrp1b*$^{+/+}$*Ccr2*$^{-/-}$ and WT mice after a 2-week treatment with water supplemented with vehicle or pravastatin. Images are representative of 2 independent experiments. Arrows indicate ORO positive cells. Panel (i) corresponds to a magnified image of area highlighted by a black bracket
(B) Quantifications of ORO positive cells/µm^2 in frozen lung sections stained with ORO as seen in Fig.S6a from mice after a 2-week treatment with water supplemented with vehicle or pravastatin. Error bars represent SEM. Significance was determined by ordinary one-way ANOVA analysis with Sidak's correction for multiple comparisons where **** is $P = <0.00005$

However, statin treatment failed to improve the number of AMs present in the lungs of *Nkrp1b*$^{-/-}$ mice. Altogether the above data demonstrates that using *in vitro* AKT inhibition we are able to rescue the aberrant lipid uptake phenotype present in AMs. Likewise, by using specific interventions *in vivo*, P38-MAPK and CD36 inhibition, we are able to partially recover some aspects of cell cycling and induce *Nkrp1b*$^{-/-}$ AM proliferation to a small extent. The biggest success we met was by using pravastatin *in vivo*. *Nkrp1b*$^{-/-}$ AMs lipid burden appeared to be significantly reversed by *in vivo* statin administration. Due to the inability of a single intervention to rescue the aberrant cell cycling and lipid

metabolism in *Nkrp1b*$^{-/-}$ AMs is indicative that NKR-P1B loss in AMs is a complex, multi-faceted phenotype.

5.3 Analysis of NKR-P1B Signalling in The Context of AMs

5.3.1 SHP-1 Appears to be Recruited to NKR-P1B to Facilitate Downstream Signalling.

As described previously, NKR-P1B contains a canonical ITIM site and previous work has shown that NKR-P1B expressed on NK-cells recruits SHP-1 to exert an inhibitory signal inside the NK-cell upon binding of its respective ligand. We set out to elucidate whether this was true for NKR-P1B expressed on AMs as well by using a pull-down assay. To avoid the problem of low cell numbers we utilized our NKR-P1B expressing AMJ-C11 cell line as a model system, which we have already shown previously to faithfully replicate the lipid uptake decrease upon NKR-P1B cross-linking, similarly to primary AMs. Using pervanadate stimulation and 2D12 as the pulling antibody we were able to detect the presence of SHP-1 in both input and output of NKR-P1B and empty vector expressing AMJ-C11 cells (Fig 5.13a and b)

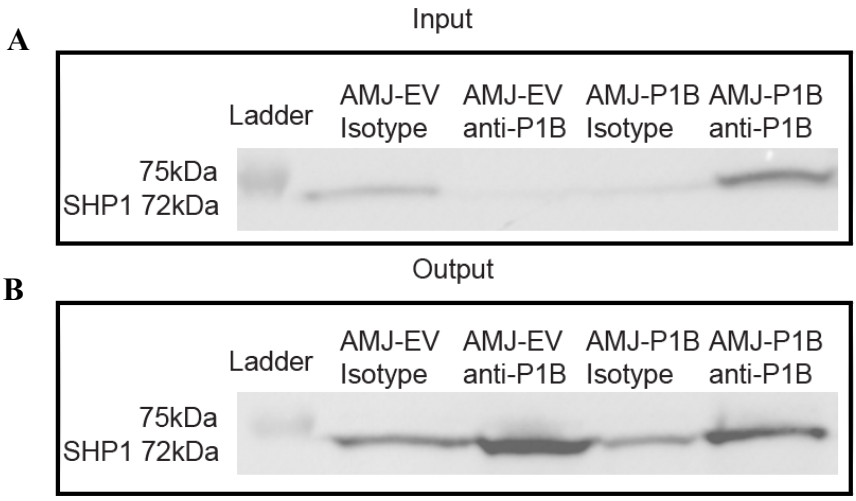

Fig 5.13: Co-immunoprecipitation of SHP-1 with NKR-P1B
Western blot of SHP-1 showing the (A) input before Co-IP and (B) output post-elution from a co-immunoprecipitation of NKR-P1B using 2D12 as the precipitating antibody or an isotype as the precipitating antibody. AMJ-C11 cells expressing NKR-P1B are denoted AMJ-P1B or empty vector, denoted as AMJ-EV were stimulated with pervanadate prior to protein extraction. Image representative of 3 independent experiments.

We have verified previously no endogenous expression of NKR-P1B by RT-PCR and flow cytometry on the surface of AMJ-C11 cells, but different splice variants or simple non-specificity may be responsible for the presence of SHP-1 in the outputs of both empty vector and NKR-P1B expressing AMJ-C11 cells. As such we decided to reverse the experiment and to use the SHP-1 antibody as the pulling antibody and to blot for the presence of NKR-P1B in pervanadate stimulated AMJ-C11 cells stably transfected with either empty vector or NKR-P1B carrying lentiviral vector. Using this method, we were able to show that NKR-P1B does bind to SHP-1 upon pervandate stimulation in AMJ-C11 cells (Fig 5.14a and b)

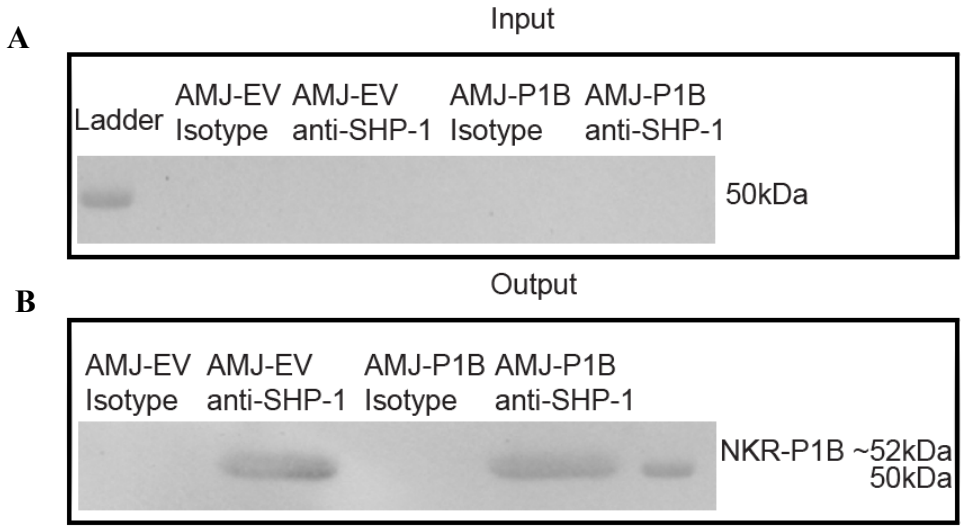

Fig 5.14: Co-immunoprecipitation of NKR-P1B with SHP-1
Western blot of NKR-P1B showing the (A) input before Co-IP and (B) output post-elution from a co-immunoprecipitation of SHP-2 using anti-SHP-1 antibody as the precipitating antibody or an isotype as the precipitating antibody. AMJ-C11 cells expressing NKR-P1B are denoted AMJ-P1B or empty vector, denoted as AMJ-EV were stimulated with pervanadate prior to protein extraction. Image representative of 3 independent experiments

The above experiments have shown that NKR-P1B appears to bind to SHP-1 when expressed on the surface of an alveolar macrophage derived cell line (AMJ-C11). The presence of NKR-P1B in the AMJ-EV cells after precipitation of SHP-2 implies that there is endogenous expression of NKR-P1B on these cells despite us not being able to detect any by RT-PCR. A qPCR screen on these cells may be useful to determine whether NKR-P1B expression is induced under these conditions. More experiments, such as pulldown assay combined with mass spectrometry, and verification is required to fully confirm this finding but due to a very limited supply of antibody any further work in this area was halted.

5.4 Clr-g as an Alternate Ligand for NKR-P1b

5.4.1 *In Situ* Hybridization Indicates Presence of Clr-g in the Lung Epithelium.

As described previously, the only known ligand for NKR-P1B is Clr-b. However, our data very has demonstrated that the *Clrb*$^{-/-}$ mouse does not phenocopy the *Nkrp1b*$^{-/-}$ conditions with respect to pneumococcal vulnerability, foam cell accumulation and AM population decline followed by reconstitution. This is strongly suggestive that there must be an alternate Clr family ligand binding to NKR-P1B in the context of the lung, or an insofar undescribed interaction between NKR-P1B and a completely novel ligand. Our previous discussion has shown that C-type lectins and lectin like receptors can display remarkable ligand binding flexibility, and this has been experimentally demonstrated in the NKR:Clr family as well, with some receptors binding to multiple Clr ligands. As such, we decided to elucidate the identity of this new interacting partner for NKR-P1B in the context of AMs and macrophage metabolism. Our previous study found high levels of *Clr-g* mRNA in the lungs[120] of WT mice and we confirmed this here by *in situ* hybridization of DIG-labelled *Clr-g* probes in mouse lung tissue, showing high expression of *Clr-g* mRNA throughout the alveolar space (Fig 5.15).

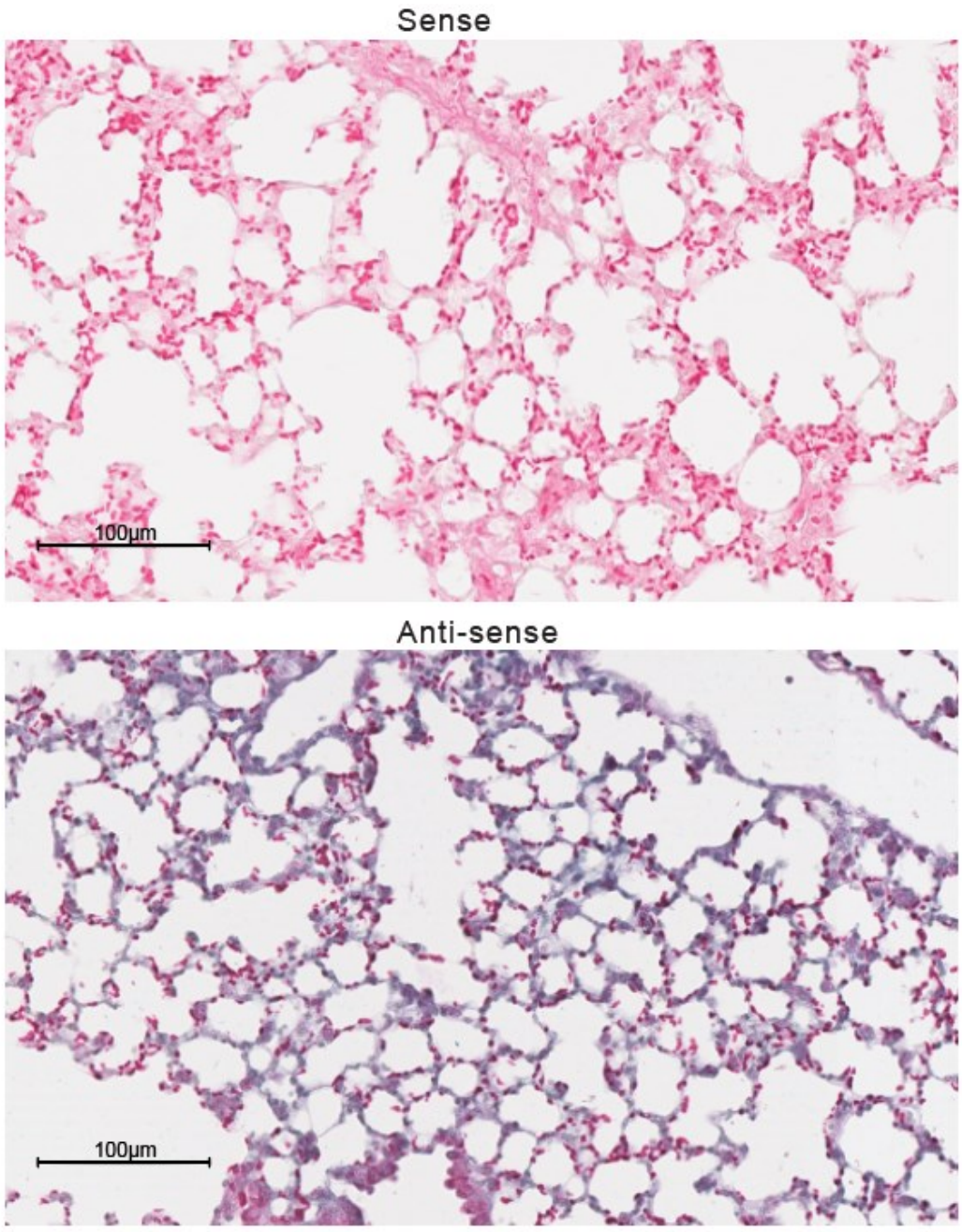

Fig 5.15: *In situ* hybridization of Clr-g probes to WT mouse lungs indicates presence of Clr-g

in situ hybridization of Clr-g probes on mouse formalin-fixed paraffin-embedded tissue sections. DIG positive staining indicated by purple/black colour development. Images are representative of 3 independent experiments.

The epithelial nature of the DIG staining pattern is highly suggestive of possible Clr-g

protein expression on the alveolar epithelium, providing us with the foundation for

subsequent exploration into the nature of the NKR-P1B and Clr-g relationship in the lung.

5.4.2 Confocal Microscopy Indicates Binding of NKR-P1B Tetramers to Type II Pneumocytes in *Clrb*$^{-/-}$ Mice.

In situ hybridization shows binding of Clr-g probes to what appears to be alveolar epithelial cells but there remains a degree of non-specificity, likely due to the high level of homology between Clr proteins. The alveolar epithelium is made up of type-I and type-II pneumocytes and given the intimate relationship between the surfactant secreting type-II pneumocytes and AMs[273–275] we hypothesized the alveolar epithelium to be the source of the new NKR-P1B ligand. To get around the background observed in the *in-situ* hybridization experiments we decided to probe the lungs of WT and Clr-b deficient mice with NKR-P1B tetramer to assess whether there is common binding to alveolar epithelial structures present in both control and Clr-b deficient mice. These NKR-P1B tetramers have been used previously by flow cytometry to detect the presence of Clr-b on lymphoid cells. We have recapitulated these results cytometrically (Fig 5.16a) and demonstrated that we are able to achieve the same positive outcome using histological methods (Fig. 5.16b). Demonstrating that NKR-P1B tetramers are able to faithfully bind to their canonical ligand using both techniques.

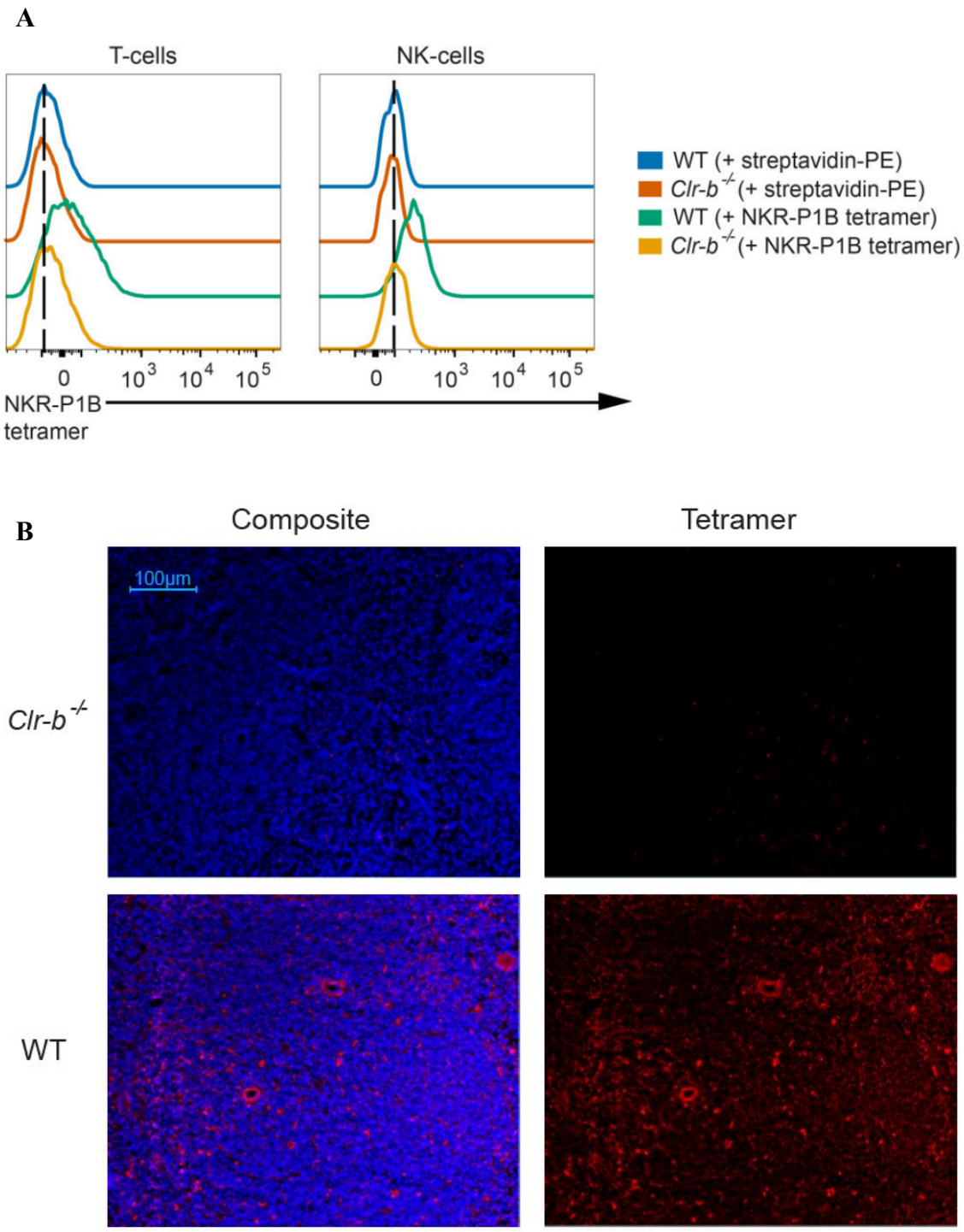

Fig 5.16: Validation of NKR-P1B tetramer staining by cytometry and confocal imaging.
(A) Histogram of NKR-P1B surface protein expression on WT and *Clr-b*$^{-/-}$ AMØ, representative of 3 independent experiments.
(B) Expression of Clr-b on T-cells and NK cells obtained from spleens of WT and *Clrb*$^{-/-}$ mice as determined by NKR-P1B tetramer binding. Histograms are representative of 3 independent experiments.

After verifying the tetramer staining by microscopy and flow cytometry, we proceeded to stain lung tissue sections of WT and *Clr-b*$^{-/-}$ mice with pro-surfactant protein C (P-SPC) antibody (a marker exclusive for type-II pneumocytes) and biotinylated NKR-P1B tetramers. Through these experiments we were able to show co-localization of P-SPC and NKR-P1B tetramer in both WT and *Clr-b*$^{-/-}$ mice (Fig 5.17)

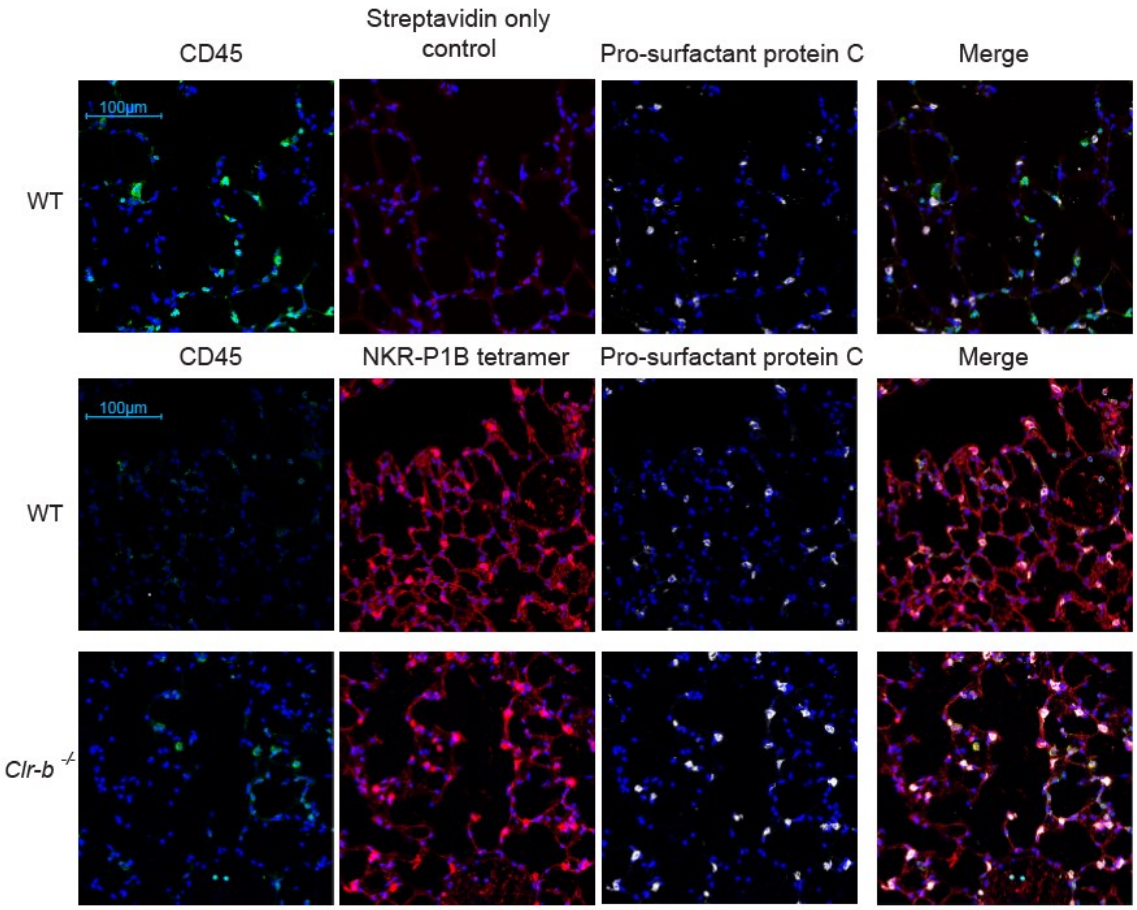

Fig 5.17: NKR-P1B tetramer staining overlaps with P-SPC staining in both WT and Clr-b deficient mouse lung sections.
Confocal image stacks of WT and *Clr-b*$^{-/-}$ frozen lung sections stained with CD45 (Green), NKR-P1B tetramer (Red), DAPI (Blue) and pro-surfactant protein C (White). Images show overlapping staining of P-SPC and NKR-P1B tetramers in both WT and Clr-b deficient mouse lungs.

The co-localization of NKR-P1B tetramers and P-SPC in both WT and *Clrb*$^{-/-}$ mice is highly indicative of the presence of a potentially new ligand for NKR-P1B present on exclusively type-II pneumocytes. We have also been able to show co-localization of NKR-P1B tetramers on CD45^{+} cells in WT but not in *Clrb*$^{-/-}$ mice (Fig 5.18) indicating that the tetramers are binding to their canonical ligand on top of binding to a novel ligand shared between both WT and *Clrb*$^{-/-}$ mice.

5.4.3 Potential Alternate Ligand is Downregulated Upon *S. Pneumoniae* and IVA Infection.

AMs respond to infection with their immune and metabolic programming controlled in part through interactions with pathogens and the alveolar epithelium[276,277]. As such, we wanted to explore whether this potential new ligand responds to infection with potential consequences on AM behavior during infection. Confocal imaging of *S. pneumoniae* or IAV-infected WT and *Clr-b*$^{-/-}$ mouse lung sections showing a reduction in NKR-P1B tetramer staining when compared to vehicle controls, thus showing that type-II pneumocytes respond by downregulating Clr-g from the surface of type-II pneumocytes (Fig 5.18).

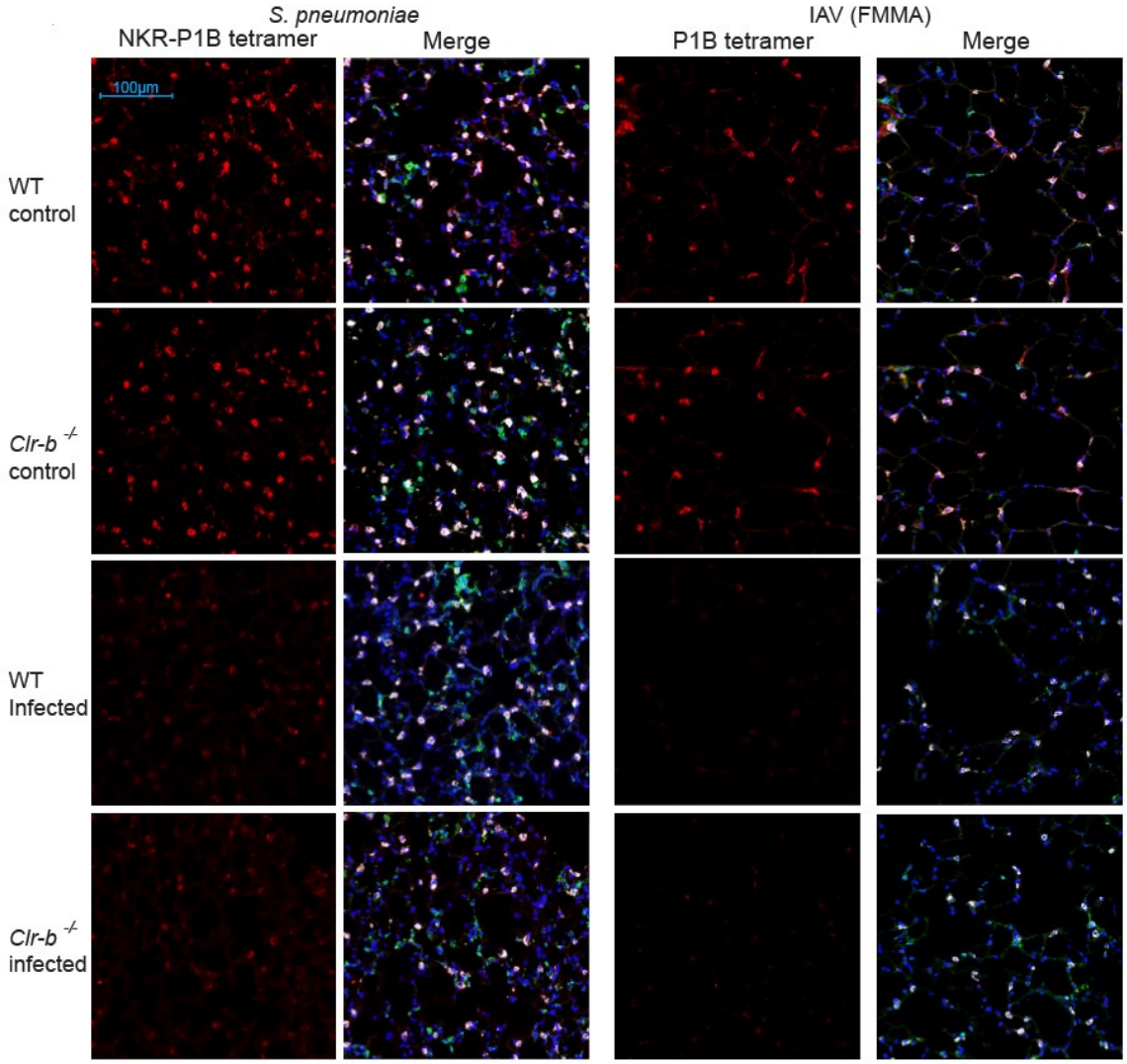

Fig 5.18: Potential new ligand responds to infections as seen through NKR-P1B staining of WT and Clr-b deficient mice infected with *S. pneumoniae* or IAV.
Confocal image stacks of WT and *Clr-b*$^{-/-}$ frozen lung sections post infection with *S. pneumoniae* or IAV (FMMA) harvested 3- and 6-days post-infection respectively. Sections are stained with CD45 (Green), NKR-P1B tetramer (Red), DAPI (Blue) and pro-surfactant protein C (White).

The above data shows that the alveolar epithelium responds actively responds to infection by downregulating the potential new ligand as seen through the poor binding ability of tetramers on type-II pneumocytes. This alveolar epithelial "ligand denial" to NKR-P1B AMs may have important consequences in changing AM metabolism and orchestrating their response to pulmonary infections.

5.4.4 NKR-P1B Tetramers Bind to MLE-12 Cells Transfected with Clr-g Confirming Tissue-Specific Expression and Binding Capability of Alternative Ligand.

To confirm this new interaction in a more reductionist setting, we decided to replicate the interaction observed between NKR-P1B tetramers and type-II pneumocytes *in vitro*. To this end we obtained MLE-12 cells which is a C57BL/6 mouse, type-II pneumocyte derived cell line, grew them on coverslips and transfected it transiently with either an empty vector or a Clr-g expressing vector. Transient transfection was chosen due to our inability to establish a stably expressing cell line despite repeated attempts. The vector contains an IRES-GFP which acts as a positive control for transfection. Indeed, 48 hours after transfection we were able to observe co-localization between GFP^+ cells and NKR-P1B tetramer which was not seen in the empty vector control (Fig 5.19), thus suggesting that NKR-P1B tetramers are able to bind to Clr-g that is expressed on mouse derived type-II pneumocytes.

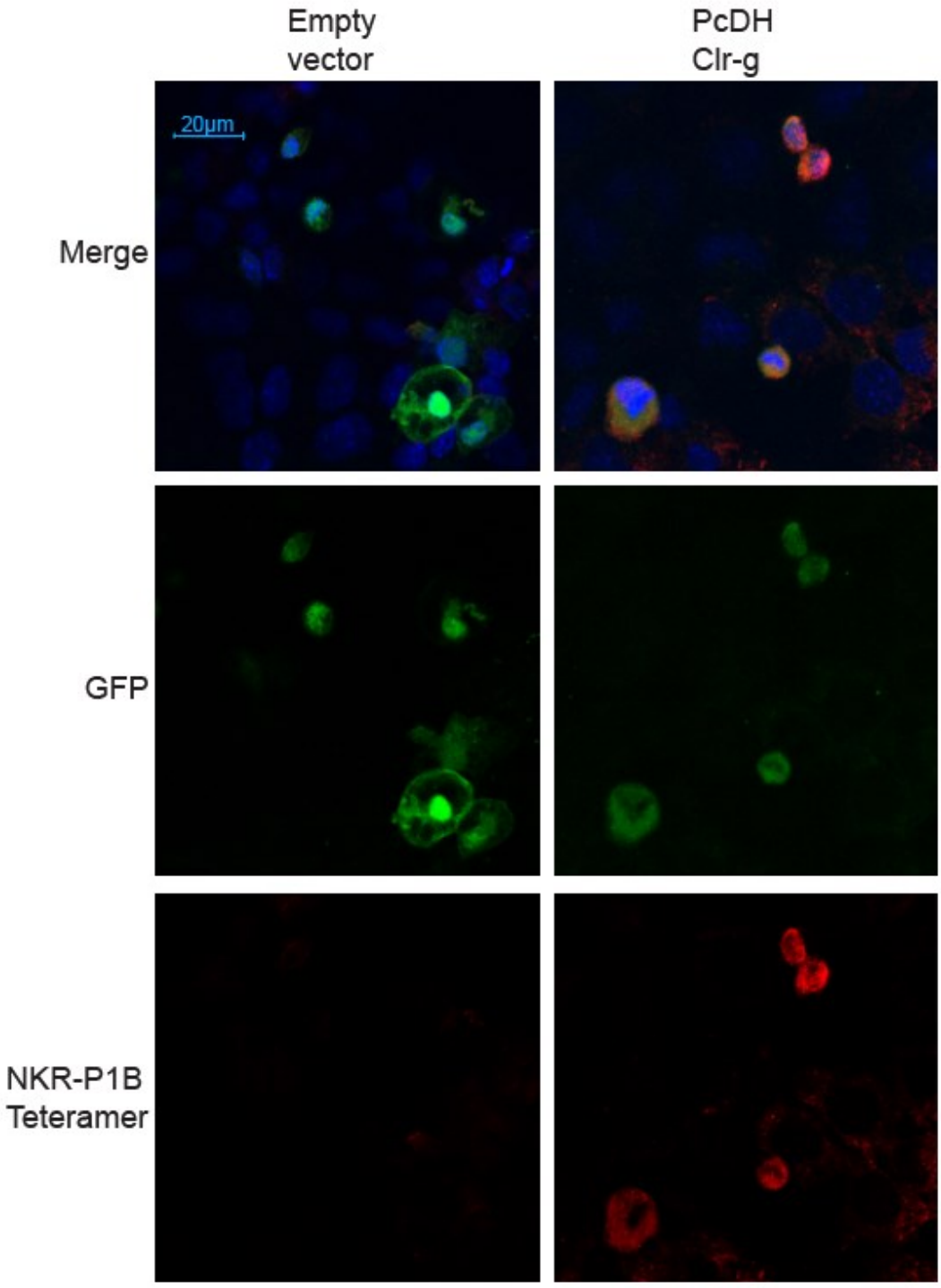

Fig 5.19: NKR-P1B tetramers bind to Clr-g expressed on MLE-12 cells.
MLE-12 cells transiently transfected with either empty or *Clr-g* carrying PcDH. The vector contains a separate GFP message for verification of transfection. Cells were grown on coverslips and stained 48 hours post-transfection. Images representative of 3 independent experiments.

This result points to the possible differential post-translational modifications unique to type-II pneumocytes which allow the binding of NKR-P1B tetramers, and thus the ability of NKR-P1B expressed on AMs to bind to Clr-g expressed specifically on type-II pneumocytes.

5.4.5 Human AMs Appear to Show Some Expression of the Only Currently Identified NKR-P1 Homolog (NKR-P1A)

As described previously, currently the only known human homolog of NKR-P1B is the human gene NKR-P1A. Expression patterns of NKR-P1A show that it is predominantly expressed on NK cells, certain subsets of T-cells and peripheral monocytes. The status of NKR-P1A expression on human AMs is currently unknown. Therefore, we decided to conduct, at the time of writing, the first analysis of NKR-P1A on human AMs with the potential of elaborating some of our mouse data regarding NKR-P1B into human data. For this analysis we obtained human samples from Dr. Xu; these patients were undergoing lung biopsies and we were able to obtain some healthy tissue from the area surrounding the actual pathogenic biopsy sample. The first analysis was based on flow cytometry. AMs were identified as $CD206^{+}$, $CD86^{+}$, $CD15^{-}$, $CD169^{+}$ while blood monocytes were identified as $CD206^{+}$,$CD86^{+}$, $CD15^{-}$, $CD169^{-}$, which were used as a positive control for CD161 (human NKR-P1A) staining (see Fig. A2 for gating strategy). As can be seen from Fig 5.20a Samples 1 and 3 correlate with each other by showing only slight expression of CD161 compared to isotype controls while. Sample 2 however shows a dramatic difference between CD161 staining on AMs compared to isotype. As per previous reports, good CD161 staining was observed on monocytes in all 3 samples

compares to isotype control. Quantification of the MFIs of sample 1 and sample 3 (Fig 5.20b) show a slight increase in CD161 compared to isotype control. Sample 2 was excluded in this analysis since the difference between sample 2 and the others is substantial and likely related to patient specific factors which could not be accounted for in this analysis.

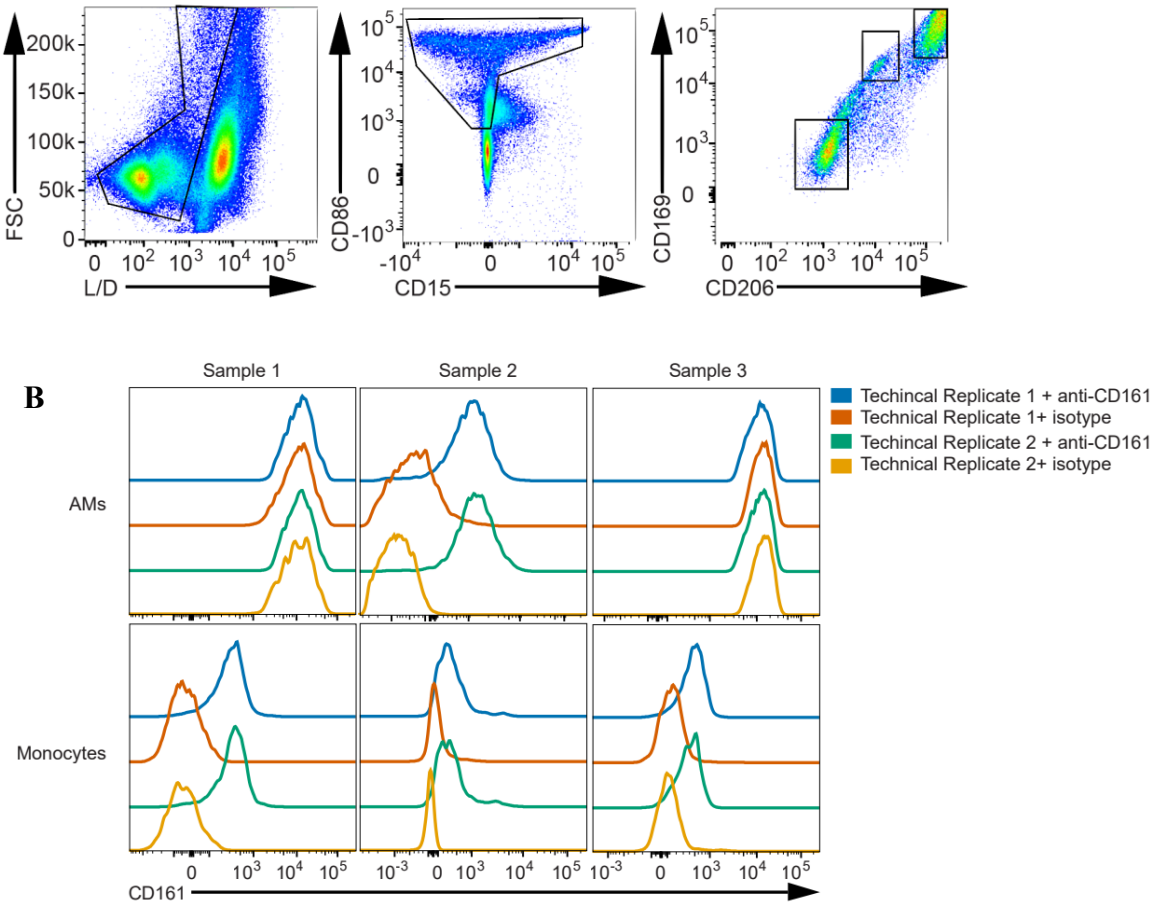

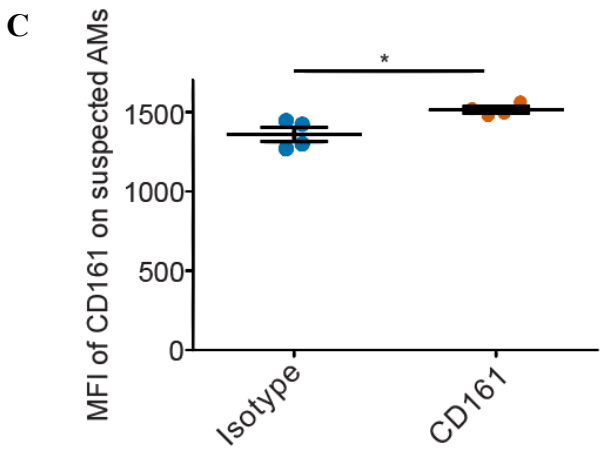

Fig 5.20: Analysis of CD161 expression on human AMs and monocytes
(A) Gating strategy for human AMs. After live dead exclusion cells were gated on $CD86^{+}$ and $CD15^{+/-}$. Afterwards cells were sub-gated according to CD169 and CD206. $CD169^{hi}CD206^{hi}$ cells are AMs, $CD169^{mid}CD206^{mid}$ are interstitial macrophages and $CD169^{lo}CD206^{lo}$ cells are monocytes.
(B) Histograms showing expression of CD161 on human AMs and monocytes. Each biological replicate contains 2 technical replicates. Histograms are representative of 3 independent experiments.
(C) MFI quantifications of CD161 expression on human AMs. Only biological samples 1 and 3 were included in this analysis, each biological sample contains 2 technical replicates. Statistics performed using Student's t-test where * is $p = <0.05$.

To complement the cytometry analysis, we decided to perform immunofluorescent microscopy on frozen human lung tissue sections to determine AM expression of CD161. However, due to mouse anti-human antibodies being largely mouse-derived and needing at minimum three markers to definitively identify human AMs, we were forced to use cell morphology and anatomical, *in situ,* position compounded with CD169 staining as a method of identifying AMs. As seen in Fig 5.21, in both samples we can identify a multitude of large, high cytoplasmic content cells located outside of the alveolar epithelium co-staining with both CD169 and CD161. This is indicative of positive CD161 expression in what is thought to be AMs as determined by our parameters.

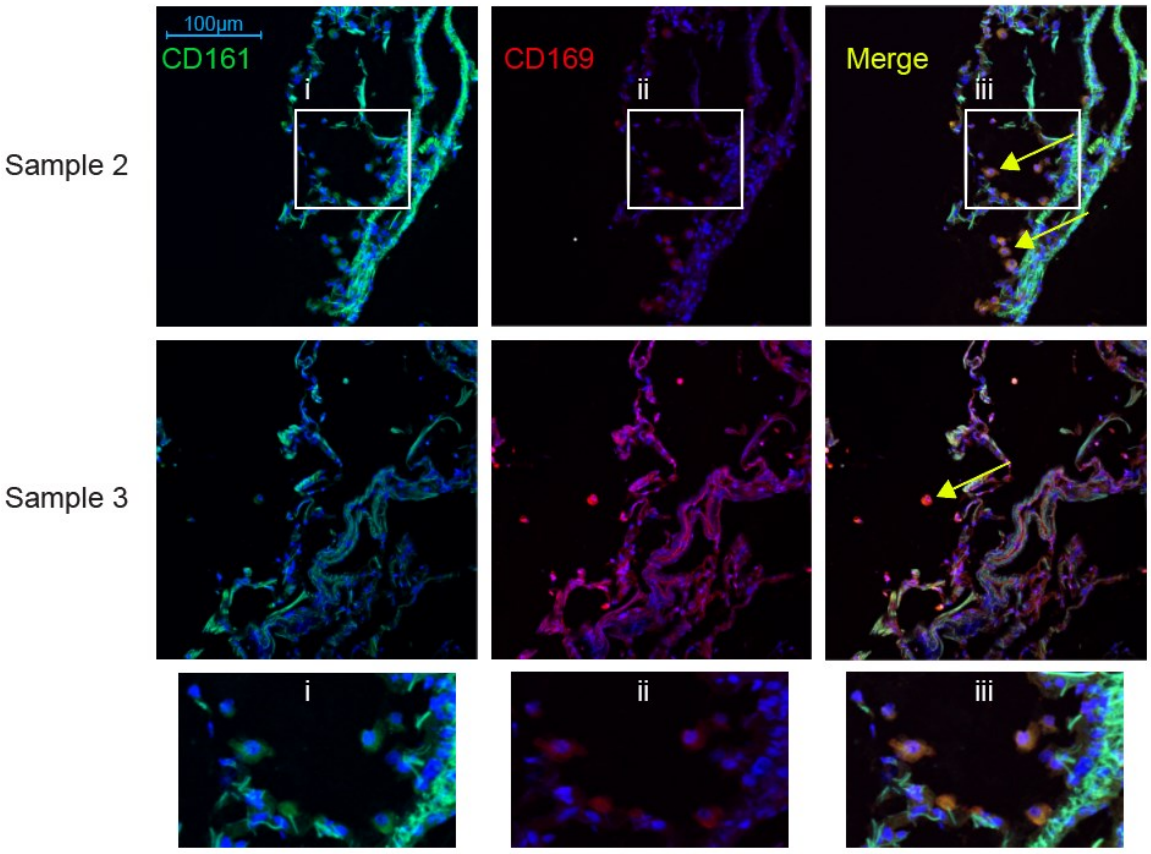

Fig 5.21: Confocal analysis of CD161 expression on human AMs
Expression of CD161 on large, high cytoplasmic ratio cells found on the outside of lung issue while also co-expressing CD169 as highlighted by yellow arrows. Panels (i), (ii) and (iii) are magnified fields of sample 2 corresponding to their respectively labelled white bracket for every colour.

These results together provide evidence, albeit indirect, that human AMs potentially express CD161. Lack of quality biological tools as well as the difficulty in obtaining healthy human lung tissue will continue to hamper this kind of analysis for a significant amount of time.

CHAPTER 6

DISCUSSION

NKR-P1B, and its allelic variant NKR-P1D is a conserved member of the NK cell receptor family known to exhibit inhibitory function on NK-cells and to act as non-MHC-I recognition mechanism [102,115]. Here we report the expression of NKR-P1B on mouse AMs with functional consequences for AM metabolism and differentiation. Using NKR-P1B-deficient mice we uncovered an *Nkrp1b*$^{-/-}$ AM phenotype which results in the progressive collapse of the lung resident AM population and followed by a CCR2-driven reconstitution via peripheral blood monocytes. *Nkrp1b*$^{-/-}$ AMs displayed an inability to self-renew and a breakdown of surfactant processing, which appears to be rescued during *in vitro* culture, suggesting a critical role for NKR-P1B in helping AMs cope with the lipid rich alveolar environment. RNA sequencing, lipidomic analysis and lipid uptake experiments of NKR-P1B-deficient AMs shows a fundamental breakdown in lipid metabolism combined with an increase in lipid uptake. These dysregulated processes contribute to the accumulation of toxic lipid species that most likely lead to cell death via lipo-toxicity and foam cell formation in the lungs of *Nkrp1b*$^{-/-}$ mice. Cross-linking of the NKR-P1B receptor appeared to decrease lipid uptake indicating a direct role for NKR-P1B in mediating lipid uptake possibly through regulation of scavenger receptors or lipid metabolism proteins. Finally, the failure of Clr-b-deficient mice and known promiscuity of other NKR-P1 receptors[82,91], lead us to the hypothesis that NKR-P1B could be binding Clr-g in a unique receptor-ligand interaction that is restricted to the alveolar space. Collectively these findings demonstrate the role of NKR-P1B in delivering a new tissue-

specific signal which promotes proper tissue-resident AM lipid uptake, metabolism, and self-renewal.

6.1 AM Mediated Pulmonary Defense in the Context of NKR-P1B

AMs have a well-defined role in protecting the lungs from foreign pathogens, specifically bacterial pathogens such as *S. pneumoniae*, and to promote the resolution of inflammation following pathogenic insult. [154,195,196] Therefore, given that *Nkrp1b*$^{-/-}$ mice suffer from a collapse of AM population, it is no surprise that they also succumb to pneumococcal challenge. This principle can be extended to *Nkrp1b*$^{+/-}$ mice since the heterozygote condition of NKR-P1B deficiency is most vulnerable to pneumococcal infection at 12-weeks of age which corresponds to the observed delay in AM collapse by flow cytometry. The exact role that NKR-P1B deficiency may have on AM immune function is unclear. Our RNA-seq analysis result have provided insights into potential immune dysregulation as seen through the upregulation of GO pathways associated with a pro-inflammatory AM response this is unusual for AMs which tend to be more immuno-suppressive at steady-state. The observation that 12-week-old *Nkrp1b*$^{-/-}$ mice succumb to pneumococcal infection almost as readily as their 6-week-old counterparts despite there being nearly equal number of AMs is indicative of a possible immune dysfunction. The critical difference in this observation is, however, that the reconstituted population is derived from peripheral blood monocytes and has been shown to be transcriptionally different from tissue-resident AMs[249,278]. The lack of monocyte-derived AMs ability to protect the lung from bacterial infection implies an immune dysfunction in AM development at least from the perspective of a monocyte-derived population, the impact of which is yet to be determined. Our NK cell depletion data showed that the lack

of NKR-P1B on NK cells has no impact on outcomes in our model of *S. pneumoniae* infection. The role of NK cells in bacterial infection is not well understood and there are conflicting reports as to the detrimental or beneficial function of NK cells in this context [196,279–281]. The one common factor is that the contribution of NK cells, or lack of, is highly dependent on the dose, serotype, age of the organism and type of mice being used. Thus, in our model of acute lethal pneumonia, NK cells play a negligible part.

6.2 Distinct Role of NKR-P1B in Liver Monocyte-Derived, Tissue-Resident AMs

The AM phenotype produced by a lack of NKR-P1B signalling results in the slow progressive collapse of the tissue-resident AM population over the course of 4-6 weeks. This is contrasted against seminal reports using GM-CSF receptor-, PPARγ-, and TGF-β-deficient mice, in which AMs fail to develop properly and are not present in any significant numbers from birth, or they collapse very shortly (7-14 days) post-partum[153,184,232]. Similar findings have been reported in articles highlighting the role of VHL, mTORC, and BACH2[242–244] in AM metabolism. A study in Bhlhe40/Bhlhe41 double knockout mice did not find any particular disruption in AM numbers at steady-state, but did discover that these AMs are incapable of colonizing the alveolar niche in competitive mixed bone marrow chimera experiments and exhibit surfactant metabolism defects[245]. All the studies mentioned above reported a collapse of the AM population and the appearance of a residual foamy, lipid-laden AMs in the lungs because of disruptions to signalling in AMs either through the ablation of critical cytokine receptors or transcription factors. Most of these disruptions prove lethal to the mouse through pulmonary alveolar proteinosis as AMs are unable to clear surfactant leading to mortality through gas exchange interruption. Our study is the first to report a similar phenotype of

foamy AMs in the lungs, but one in which AMs appear to develop normally during the firsts two critical weeks post-partum before their decline in the following 4 weeks. More interestingly, this phenotype appears to be caused by the absence of a type II C-type lectin like receptor, NKR-P1B, as opposed to a critical cytokine receptor or a transcription factor. This indicates a potential new role for lectin like receptors in immune cell development and homeostasis. Given that previous reports that similar phenotypes tend to produce lethal consequences for the mice via PAP, it was surprising that the *Nkrp1b*$^{-/-}$ mice were completely healthy and viable. This led us to investigate the AM population kinetics in *Nkrp1b*$^{-/-}$ mice as they age. Experiments using the CCR2 and NKR-P1B double knockout mice showed that while the tissue-resident AMs collapse, they are replenished in a CCR2-dependent manner from the blood monocyte pool. This is consistent with previous reports that peripheral monocytes can replace tissue-resident AMs under infectious conditions or at stead- state conditions when the AMs were subjected to damage (such as γ-radiation) that impairs their self-renewal ability, allowing peripheral blood monocytes to outcompete resident AMs for the alveolar niche[127,152,282]. The data obtained from CCR2 and NKR-P1B double knockout mice aligns with the concept that the replenishment of AMs with peripheral blood monocytes via CCR2 in NKR-P1B-deficient mice is analogous to a bone marrow allograft. There is no reason to believe that a bone marrow transfer would result in alveolar niche repopulation kinetics dissimilar to what is observed in *Nkrp1b*$^{-/-}$ mice regardless of genotypic origin of the PBMCs. There exist non-CCR2 mediated pathways of monocyte egress and entry into tissues which are likely playing a role in the slight increase of AMs observed between the

12 and 21 week timepoint in *Nkrp1b*$^{-/-}$;*Ccr2*$^{-/-}$ mice, such as through CX_3CR1 and/or $S1PR_5$[283,284].

Our microscopy and histological data demonstrate that *Nkrp1b*$^{-/-}$ AMs tend to have a foamy, lipid-laden phenotype in accordance with previously cited reports of similar observations. These phenotypes are usually accompanied by mucous/protein accumulation, which is easily detected in the lungs through Periodic-acid Schiff staining [254,285]. The NKR-P1B-deficient AM phenotype is unique among these in that it does not result in PAP, nor any significant protein/mucous accumulation in the alveolar space at all. NKR-P1B signalling appears to be significantly pronounced in tissue-resident AMs which develop from fetal liver monocytes, whose population undergoes a catastrophic collapse. While blood monocytes are able to recolonize the alveolar niche and differentiate enough to prevent *Nkrp1b*$^{-/-}$ mice from succumbing to PAP, the contribution of NKR-P1B to PBMC derived AM differentiation and function is unclear. Under the guidance of tissue signalling[255], monocytes are able to differentiate into full-fledged AMs and repopulate the alveolar niche[286], turning into fully functional AMs with some subtle differences from liver monocyte-derived tissue-resident AMs[287]. These key differences in AM origin may be the functional determinant that allows the NKR-P1B deficient mouse to survive the collapse of tissue-resident AMs and allowing the subsequent replacement by monocytes, which are then able to carry out the necessary surfactant metabolism to prevent PAP related mortality. However, our data indicates that even the replacement monocytes do not appear to undergo full AM differentiation with subtle variation in CD11b, SIGLEC-F, and MHCII levels as well as very slightly aberrant scatter profiles and presence of some lipid-laden cells in the lung persisting at 12 weeks of age for NKR-

P1B-deficient mice. RNA-seq data combined with the inability of reconstituted AMs to adequately clear *S. pneumoniae*, despite their adequate numbers in the alveolar niche, points to a potential immune homeostatic role of NKR-P1B in AMs which could be investigated in further studies.

Lipid metabolism dysfunction tends to be followed by other metabolic dysregulation specifically in glucose turnover and mitochondrial activity, similar to observations reported in transition to glycolysis from oxidative phosphorylation in immune cell[288]. Emerging evidence has begun to link GM-CSF with mitochondrial functioning and glucose uptake in AMs as well[289]. While our data does show increased rates of glucose uptake more work needs to be performed to elucidate mitochondrial status due to the results presented here be only a superficial and surface exploration of NKR-P1B contribution to overall macrophage metabolism. How the loss of NKR-P1B effects non-lipid metabolic activity, specifically mitochondria, or if the observed increase in glucose uptake is a simple compound effect of ongoing lipid dysfunction remains an open question. Following through on this functional analysis we also assessed the AMs ability to phagocytize beads and cancer cells as well. Surprisingly, there was little to no difference in phagocytic capability in bead or cancer cell internalization. Phagocytic beads and cancer cells assess antibody-dependent phagocytosis and SIRPα-Cd47 interaction respectively, it is entirely possible that internalization pathways dependent on other cell receptors or other methods (such as macropinocytosis) may be affected if examined in the future.

6.3 Unique Requirements of NKR-P1B Signalling in AM Function

Flow Cytometry data also indicates that *Nkrp1b*$^{+/-}$ AMs express half as much NKR-P1B compared to their WT counterparts which is a dynamic unlike that seen in NK cells where the heterozygous condition results in roughly half of the NK cells having full expression and half having no expression[115]. This raises interesting possibilities of new receptor signalling expression dynamics unique to AMs reinforced by our observation that the foamy AM phenotype is delayed in the heterozygous condition, thus showing that even half as much NKR-P1B signalling is sufficient to extend the AMs lifespan before their lipid metabolism fails. Given the subtlety and long manifestation time of the NKR-P1B-deficient AM phenotype, it is possible that upon reconstitution the AMs undergo a constant cycle of cell death due to lipo-toxicity and continuous replacement which would account for the longevity of the NKR-P1B knockout mouse as well as the small aberrations found in AMs extracted from 12-week-old NKR-P1B mice. It is also entirely possible that tissue-resident AMs are required to promote proper maturation and differentiation into AMs of incoming PBMC derived monocytes. Cell tracing studies and bone marrow chimera experiments are needed to experimentally verify these hypotheses. The presence of increasing number of CD103^{+} DCs in the lungs of *Nkrp1b*$^{-/-}$ mice is inversely related to the number of AMs in the lungs of these mice which raises some interesting possibilities. These are the only other immune cell type which has direct access into the alveolar lumen and previous studies have shown that these DCs have a preference towards phagocytosis of apoptotic bodies[252] and are able to act on the behest of the alveolar epithelium under certain inflammatory conditions[290]. It is possible that what we are observing is the clearance of apoptotic/dying AMs by CD103^{+} DCs whose

numbers normalize once the alveolar spaces have been cleared and new AMs have reconstituted the niche.

6.4 Metabolic and Cell Cycle Dysfunction in *Nkrp1b*$^{-/-}$ AMs is Dependent on Confounding Factors Present in the Alveolar Environment

The ability at steady-state to self-renew with very little input from the peripheral blood monocyte population is a hallmark of AMs. NKR-P1B loss triggers aberrant AM metabolic programming which leads to their eventual decline and replacement by blood monocytes; thus, the loss of NKR-P1B mediated metabolic programming cripples the AMs ability to self-renew. However, our experiments have shown that this proliferative impairment is not permanent and AMs were able to survive in culture for up to a week without cytokine stimulation and divide upon addition of GM-CSF as demonstrated previously[243,291,292]. This data shows that the lipid-rich alveolar environment combined with dysregulation of tissue-specific AM metabolic programming resulting in NKR-P1B-deficient AMs inability to cope with their lipid burden is the main causative factor behind their loss of self-renewal. That AMs were able to proliferate at similar rates when extracted from *Nkrp1b*$^{-/-}$*Ccr2*$^{-/-}$ mice that were 2 weeks old (when lipid burden is low) and 6-weeks-old (when foamy cells are the predominant AM phenotype) is a testament to the *Nkrp1b*$^{-/-}$ AMs ability to resolve their lipid burden and resume cell cycle *in vitro*. However, transcriptomic data from 2-week-old *Nkrp1b*$^{-/-}$ reveals that even at the 2-week point there is a significant disruption to cell cycle genes. This is supported by our flow analysis of Ki67 which appears to be lower in *Nkrp1b*$^{-/-}$ AMs as well as by BrdU analysis, which shows characteristic hallmarks of S-phase arrest[293,294]. This implies a potentially more fundamental role for NKR-P1B in AM self-renewal, which is also

reinforced by the increased appearance of double nuclei in *Nkrp1b*$^{-/-}$ AMs after *in vitro* culture. The NKR-P1B-deficient, double-nucleated AMs do not resemble the prototypical giant cell found in granulomas[295] and granuloma formation is not associated with lung based, lipid storage diseases (ie. PAP)[296,297]. However, a recent report has indicated that persistent inflammation and DNA damage resulted in the formation of polyploid macrophages without cell-to-cell fusion[298]. Lack of NKR-P1B signalling resulting in accumulation of toxic lipid species may be the trigger that induces chronic stress on the AMs, some of which resort to a polyploid phenotype to preserve genomic stability. Further experimentation is necessary to validate this hypothesis.

Since we have established that the AM population collapses at around 6-weeks of age, we decided to perform RNA-Seq and lipidomics on AMs derived from WT and *Nkrp1b*$^{-/-}$ mice 2-week-old and 6-week-old, respectively. The results of these assays reveal an *Nkrp1b*$^{-/-}$ AM metabolic profile characterized by an increase in lipid storage and upregulation of certain lipid processing pathways with gene dysregulation such as increase in *Apoe, CD36*, and various forms of lipid processing enzymes followed by a downregulation of cholesterol efflux pumps (*Abca1, Abcg1*) could explain the increased rate of lipid accumulation and formation of lipid droplets in AMs. This phenotype is similar to other reports where RNA-seq on metabolically impaired AMs was performed[184,266]. One of the key differences between the NKR-P1B-deficient phenotype is that PPAR, GM-CSF receptor levels and secretion of GM-CSF into the alveolar space remained unchanged, indicating a potential downstream modulation of these critical AM signalling pathways by NKR-P1B. Another likely possibility is the involvement of other AM metabolic molecules such as Rara and Rarg and parts of the Ras pathway which

appear to be downregulated and are necessary for AM metabolic programing[299–303]. Lipidomic analysis performed on 6-week-old lipid-laden AMs revealed a dramatic increase in the PC, PG, LPC, and LPG pool, which is not entirely surprising since these are the main constituents of pulmonary surfactant[219,226], thus indicating potentially increased uptake or a slowdown in surfactant metabolism causing a backlog of unprocessed lipid. Combining the RNA-Seq and lipidomics along with known metabolism pathways allowed us to create a working model of AM lipo-toxicity due to loss of NKR-P1B. Upregulation of CD36 and LDLR leads to an increase in pulmonary surfactant uptake thus triggering an increase in metabolism enzymes responsible for converting PC/PG into DAG. This is compounded by lipid enzymatic dysregulation which results in excess DAG formation through draining of PA/LPA pools and excess PC/PG. This excess DAG and an increase in PNPLA2 activity leads to an accumulation of FA and a decrease in TGs. These metabolic changes in combination with a decrease in cholesterol efflux pump transcription rates and poor conversion of CE to FC leads to lethal intracellular lipid composition. TGs and CEs are known to be safe lipid storage molecules[264,304], while excess accumulation of free cholesterol, free fatty acids and DAG induces lipo-toxicity[265,305,306]. As such, the combined lipidomic and transcriptomic data paints a picture of NKR-P1B loss contributing to increased uptake of surfactant and a fundamental shift in lipid metabolism which contributes to the storage of toxic lipid species leading to the slow but inevitable collapse of the resident AM population.

AM metabolism revolves around the kinetics of both lipid uptake and lipid processing. RNA-seq analysis has demonstrated that *Nkrp1b*$^{-/-}$ deficiency may be causing dysregulation of lipid uptake, due to an increase in CD36[307], and thus contributing to the

collapse of AMs via lipo-toxicity. Flow cytometry experiments show that *Nkrp1b*$^{-/-}$ AMs not only take up surfactant faster, but that engaging the NKR-P1B receptor through antibody-mediated cross-linking exerts the opposite effect, that is, a statistically significant decrease in the uptake of surfactant components. We have thus demonstrated a direct impact of NKR-P1B signalling on the lipid uptake kinetics of AMs. While a previous report has shown that downregulating CD36 reduces DPPC uptake by AMs[257], our data suggests that signalling through NKR-P1B has a direct influence on the uptake of surfactant lipid components, perhaps by mediating the action of CD36, which contains a signalling domain and whose gene expression is enhanced by the binding of its ligand[308]. Likewise, we have conducted a qPCR screen to determine whether cross-linking of NKR-P1B has any influence on the transcription of certain key metabolic genes. Transcription levels of genes such as SERPINB6, FABP5 and APOE, normally upregulated in *Nkrp1b*$^{-/-}$ AMs were downregulated upon NKR-P1B engagement indicating a direct involvement of NKR-P1B signalling in the transcriptional control of these genes. The question remained however, as to whether *Nkrp1b*$^{-/-}$ AMs can process their *in vivo* lipid burden if they are rescued from this lipid rich environment. *In vitro* culture of foamy, lipid-laden AMs extracted from *Nkrp1b*$^{-/-}$ mice have shown that *Nkrp1b*$^{-/-}$ AMs lose ORO staining after 6 days in culture when compared to their freshly lavaged counterparts. This is indicative of a metabolic defect that is not severe enough to cause terminal lipo-toxicity assuming that supply of lipid is removed from the environment. It could also be indicative of a phenotype in which ablation of NKR-P1B causes an increase in lipid uptake to such an extent that AMs *in vivo* are unable to metabolize it within a sufficient timeframe, thus resulting in their overload and collapse.

Conversely, experiments attempting to recreate the lipid accumulation phenotype *in vitro* failed. This is highly likely due to the artificial nature of the system. The experiments did not involve an air-liquid interface culture and replicating the cytokine milieu of the alveolar space is difficult. Likewise, the surfactant used in the experiment is a simple phospholipid extract free of any cholesterol, minority lipid species and the surfactant proteins whose role in maintaining surfactant stability and uptake is critical[58,309]. A recent report has also found that cholesterol is the main driver of the AM foam cell formation, at least in the context of absent GM-CSF signalling[310]. However, some cell granularity was observed, especially at the 6-day timepoint, which could be indicative of lipid inclusions of lipid species which are not detectable by ORO staining. Further attempts to recreate the lipid-laden phenotype *in vivo* should consider not only the culture type and cytokine conditions but the composition of the lipid surfactant, specifically the addition of cholesterol, and more detailed methods of data gathering such as quantitative lipidomics.

6.5 NKR-P1B Loss in AMs Results in the Breakdown of Multiple Signalling Pathways Likely Mediated Through NKR-P1B Mediated SHP-1 Signalling

In this work, we have made attempts to rescue the AM population collapse and lipid-laden phenotype both *in vivo* and *in vitro* respectively with some limited success. Guided by our RNA-seq results which have shown potential AKT and P38-MAPK dysregulation, as well as the known roles[311,312] these two kinases play in AM and macrophage signalling, we chose those two points as good candidates for a pharmacological intervention. Outcomes proved to be mixed with AKT inhibition relieving lipid uptake in an *in vitro* setting but being detrimental *in vivo*. Conversely, P38-MAPK inhibition had no effect *in vitro* but did appear to boost Ki67 levels an *in vivo*

setting. However, none of these interventions manage to fully restore the WT condition or even improve the number of AMs in the lungs, which we see as the most positive outcome of any phenotype rescue attempt. A slightly more encouraging result was obtained using SSO[313] to inhibit CD36 as it is a major lipid transporter[257] and was found dysregulated in our NKR-P1B deficient phenotype. *In vivo* application of SSO appeared to alleviate AM numbers by a small extent but more data is needed to establish this with confidence. This is hampered mostly through the cost and amount of drug that needs to be applied to get the desired effect. Starting the experiment at an earlier time-point of 2-weeks of age may also help in providing more satisfactory data since the AMs collapse at 3-weeks-of age may have entered a stage where reversing it is improbable. Lastly, statins are well known to modify lipid uptake in cells by acting on the well-characterized HMG-CoA pathway[314] and a recent publication has noted potential for alleviating lipid-laden AMs as well[272]. Therefore, we decided to replicate and expand on these findings in our NKR-P1B deficient mice. While no increase in AMs was noted post statin treatment, we were able to notice a dramatic reduction in ORO positivity in the lungs of statin treated mice showing that there is potential for rescuing the lipid-laden AM phenotype in the context of NKR-P1B loss as well. It is highly likely that no single treatment would be able to fully restore NKR-P1B deficient AMs back to their normal state. Our phenotype rescue attempts solidified observations from our other data, that the loss of NKR-P1B may be a subtle but complex phenotype which appears to affect tissue-resident AM lipid metabolism, cell cycle and terminal differentiation in a multi-faceted fashion.

In an effort to further understand NKR-P1B signalling, we assessed lipid update dynamics of an NKR-P1B-expressing AMJ-C11 cell line we generated. The AMJ-P1B

cell line was not only able to uptake lipid, but also able to respond to antibody mediated NKR-P1B cross-linking by decreasing lipid uptake, similar to primary AMs. This result gave us the confidence to begin trials to determine the downstream signalling partner of NKR-P1B in the context of AMs. As mentioned previously, SHP-1 is the main downstream binding partner of NKR-P1B on NK cells and it is responsible for its inhibitory function. As such, this was the best target to determine whether the same dynamic holds true in AMs. Performing a pull-down assay using NKR-P1B as the pulling antibody on pervanadate treated, NKR-P1B expressing AMJ-C11 produced mixed results with SHP-1 being detected in the empty vector and isotype controls (albeit in lower amounts than NKR-P1B expressing cells) despite previously verifying for endogenous expression on NKR-P1B. It is also possible that we were observing some non-specific as well and therefore we tried the opposite approach of using SHP-1 as the pulling antibody. This experiment produced good isotype controls, but we still detected NKR-P1B in empty vector controls. It is possible that AMJ cells are also expressing an alternative splice-form of NKR-P1B which was not detected by our RT-PCR or perhaps the antibody is binding non-specifically. While we have some evidence that NKR-P1B does bind to SHP-1 upon stimulation in AMs, further experiments will be needed to verify this interaction.

6.6 Analysis of Human AMs Hints at Possible Expression of NKR-P1A

As discussed previously the only known human analog of NKR-P1B/D is NKR-P1A, whose expression has so far been confirmed on NK cells, subsets of T-cells and monocytes. In cooperation with Dr. Xiaolin Xu, we were able to obtain human samples and use them with commercially available NKR-P1A antibodies to conduct a novel

analysis attempting to characterize the expression patterns of NKR-P1A on human AMs. The cytometric data obtained from this analysis pointed to possible NKR-P1A expression on human AMs but we also encountering significant variability between samples which complicated the analysis. We therefore decided to focus on microscopy to help clarify the cytometric results. However, processing frozen sections for lungs comes with a multitude technical challenges and to conclusively categorize human AMs requires a significant number of different markers (most of which are exclusively mouse monoclonal antibodies)[315] which makes this analysis difficult. Using an approach that categorizes cells as macrophages based on CD169 expression as well as size, location and shape we can show, tentatively, NKR-P1A expression on these cells. These findings are encouraging in providing some translational value between the phenotype observed in NKR-P1B mice and human AMs, but more work is required to reach a definitive conclusion.

6.7 Consequences of Clr-g Being a Potentially New Interacting Partner for NKR-P1B

The most surprising aspect of this AM phenotype is that it is not recapitulated in Clr-b-deficient mice, the only known verified ligand for NKR-P1B. *Clr-b*$^{-/-}$ mice do not exhibit any AM deficiency as observed in the *Nkrp1b*$^{-/-}$ mice. This implies that there must be a novel, tissue-specific, NKR-P1B interaction. We have previously described how Clr-g is expressed in lung tissue[120] and recent crystallography studies have found that Clr-b most closely resembles Clr-g in terms of structure[101]. Previous studies analyzing the interactions between the NKRs and Clrs tended to rely on a HEK (human embryonic kidney) based expression system[102], which while effective, may be suboptimal for

determining unique, tissue-specific interactions since post-translational modification and glycosylation has a well-documented and critical role to play in C-type lectin and lectin-like receptor binding[316–318]. As such we decided to analyze the ability of NKR-P1B tetramers to bind Clr-g when expressed in a cell line derived from mouse type-II pneumocytes. Strikingly, the NKR-P1B tetramers were able to bind to Clr-g expressing MLE-12 cells suggesting that unique post-translational modification might be taking place within type-II pneumocytes that allow for this previously undiscovered interaction to occur. We have also observed downregulation of Clr-g in the lung when the mice are exposed to pathogens, which has interesting implications for AM epithelial interactions through NKR-P1B and Clr-g. Due to the slow degeneration of NKR-P1B-deficient AMs combined with their inability to carry out basal AM specific metabolic programming, we speculate that the NKR-P1B:Clr-g interaction in the lungs is one of the key components that maintains AM lipid homeostasis and immunosuppressive state. During infection the epithelium removes the ligand thus providing instructions to the AMs to shift from surfactant metabolism and homeostasis into a more immune active phenotype. Further studies utilizing infection models and cytokine profiling of WT and NKR-P1B-deficient AMs could be used to elucidate the immunomodulatory role of the AM NKR-P1B:Clr-g interaction. In this report we have demonstrated the presence of a novel, lung specific receptor ligand interaction (NKR-P1B and Clr-g) which subtly controls key components of AM homeostasis maintenance and pulmonary surfactant clearance, thus providing another piece into the puzzle of tissue-specific determinants governing resident macrophage identity factors.

CHAPTER 7

Conclusions and Limitations

While the work presented here proposes some interesting new insights into the role of NKR-P1B in the regulation of AMs it is not without its limitations. One of the major caveats in this investigation is the lack of a conditional knockout mouse. Since the *Nkrp1b*$^{-/-}$ mouse is a systemic knockout, we did as much as we could to verify that other macrophage populations were not disrupted, as described previously in chapter 3. We have likewise verified the integrity of Clr-b expression in the NKR-P1B mouse which was done in our previous work described above. However, it is of course entirely plausible that a systemic disruption of NKR-P1B may be causing some unforeseen effects. As such a conditional NKR-P1B knockout under the control of the CD11c promoter which would disable it specifically in AMs, a technique used routinely for conditional AM disruptions. We have observed no expression of NKR-P1B on CD11c^{+} DCs, and thus this off-target effect would be negligible. Following on this theme the lack of tools to analyze Clr-g is a serious drawback in this investigation. In chapter 5 we showed through microscopy the shared binding of tetramer in lungs of WT and *Clr-b*$^{-/-}$ mice which we then verified in a reductionist *in vitro* assay by utilizing a type-II pneumocyte cell line transfected with Clr-g. While this evidence is quite strong, a Clr-g deficient mice would be ideal to show that this is the true nature of the relationship between NKR-P1B and Clr-g in the lung. Observation of a similar collapse in AM population with formation of foamy, lipid-laden cells in a Clr-g deficient mouse would provide the most direct evidence for the new relationship between this receptor-ligand pair outlined in this investigation.

In chapter 3 we have also presented counts of mitochondria in our AMs as determined by electron microscopy. It is important to note that mitochondrial counting is prone to several inaccuracies, the main being that distribution or polarization of the mitochondria themselves means that the number counted can vary greatly based on the particular cell slice. More visible mitochondria may be present in one slice compared to another which can make accurate determination difficult. However, considered alongside our metabolic data, especially our increased glucose uptake, we are confident that the NKR-P1B deficient AMs do possess differences in mitochondrial number or activity. Verification through direct metabolic measure, such as by utilizing the SeaHorse instrument, would be invaluable in demonstrating this in a more quantitative way.

In chapter 4 we present results which show that *Nkrp1b*$^{-/-}$ AMs are able to process their ORO positive lipid burden and survive in an *in vitro* setting, thus providing compelling evidence that constant exposure to the lipid rich alveolar environment is a main contributor to the appearance of the ORO positive phenotype and foam cell accumulation. However, we were not able to recreate this foam cell phenotype *in vitro* using WT AMs and incubating them in medium containing varying concentrations of Infasurf (bovine derived surfactant used to treat premature neonates). Several confounding factors and limitations are likely responsible for this failure. One is the lack of cytokine milieu present in the *in vitro* environment. As mentioned above, other research has shown that GM-CSF is one of the crucial secreted factors, along with TGF-β, to induce and maintain the unique AM metabolic phenotype. Lack of these secreted factors in the culture medium means that once removed from the alveoli, the AMs rapidly de-differentiate and lose their unique lipid uptake and metabolic properties altogether,

regardless of presence or absence of surfactant. Since AMs are located on the alveolar surface, the best *in vitro* replication of this environment would be an air-liquid interface culture method which was not done in our experiments. Creating a more representative artificial environment is likely to play a large role in this system. Secondly, all commercially available surfactant formulations contain exclusively purified phospholipids with no other lipid or protein species. Surfactant itself is a complex mixture of phospholipids, cholesterol and 4 different surfactant proteins. These extra components are likely to a play a role in AM metabolism as well since, as described above, surfactant protein D and cholesterol have been implicated in AM foam cell formation as well. Supplementing commercially available phospholipid-based surfactant with other surfactant components may yield better results and reveal the causative factor between lack of NKR-P1B signalling, dysfunctional AM metabolism and surfactant components. Extracting surfactant from mice is also possible, but the process is laborious, time consuming and demands an extremely high mouse number making such an endeavor vastly inefficient.

Likewise in chapter 4 we presented a model of what our available data suggest is occurring metabolically inside the AM during a lack of NKR-P1B signalling. This model was created through the synthesis of the RNA-seq and lipidomic data presented in this work. In particular the lipidomic data presented has no significances associated with it and this is due to the nature of the analysis conducted (a single timepoint) and of lipid species inside the cell which tend to exist as dynamic pools that are constantly in flux, increasing or decreasing, rapidly. As such, our experimental set-up is capturing a moment of these lipid species in time and is not necessarily representative of the totality of lipid

species present in the cells or their rate of fluctuation, thus making statistical analysis of this lipidomic experiment mathematically meaningless. As such the model that we have assembled based on this data would require further experimental validation using more dynamic experimental designs such as the conversion of one lipid species into another and quantifying this using radio-labelled lipids. It is also necessary to point out that the breakdown of surfactant lipids by AMs is a notoriously under-explored area of cell metabolism and the actual pathway and intermediary lipids involved in the breakdown of surfactant inside AMs are mostly unknown. This work attempted to present a workable hypothetical model of NKR-P1B mediated deficiency of AM metabolic breakdown based on the objective and significant data that was obtained from both transcriptomics and lipidomics and what is known about lipid breakdown and conversion as verified by experimental confirmation.

In chapter 5 we have a certain discrepancy between the *in-situ* hybridization and tetramer staining via confocal microscopy. Specifically, the results from the hybridization experiments indicate a more widespread expression of Clr-g mRNA while tetramer appears to be largely focused on type-II pneumocytes. As discussed in previous sections genetic similarity between the Clr family members is quite high so it is not necessarily surprising that we might be seeing some potential off-target effects using *in situ* hybridization. What is important is that those experiments clearly showed the staining restricted to the alveolar epithelium and not bronchial epithelium, vasculature or what appear to be immune cells present in the alveoli (ie. likely AMs based on physical characteristics). It is also likely that while Clr-g mRNA is present in type-I pneumocytes it is not being translated or being translated at a much lower rate than type-II

pneumocytes, possibly accounting for the discrepancy hybridization and confocal microscopy.

Chapter 4 looked at a multitude of pharmacological interventions that were attempted both *in vitro* and *in vivo* in an attempt to at least partially alleviate the AM lipid laded phenotype. The majority of these interventions produced, at best, only partial phenotype rescues with results differing from *in vivo* to *in vitro* applications. This mix of variable results highlights the multifaceted failure that the loss of NKR-P1B precipitates onto AM physiology. The accumulation of lipids, the failure of cell cycling, and deficiencies in development could be looked at as downstream effects of general lipid metabolic failure, but the results presented here appear to warrant a deeper exploration of the signalling capabilities of NKR-P1B. NKR-P1B signalling may be influencing a wide array of signalling pathway in subtle ways or it could be restricted to influencing merely one or two pathways but at a more proximate signalling point which could then produce downstream effects in subsequent differing signalling cascades. It is also possible that systemic delivery of these interventions is simply not producing the desired effects or is creating too many off target effects to really make a meaningful difference. Targeted delivery into the lungs could help alleviate this issue. Likewise, we have already described the slow nature of this phenotype, it takes a minimum of 3-4 weeks post-partum to detect a noticeable drop in AMs. It is entirely possible that the length of treatment for the interventions used here (ie. 2 weeks) is simply far too short to make a noticeable difference.

Lastly, in chapter 5 we have presented data attempting to elucidate the downstream binding partners of NKR-P1B. While we were able to demonstrate that

pulling down SHP-1 shows co-localization with NKR-P1B expressed on an alveolar macrophage cell line, using anti-NKR-P1B as the pulling antibody produced inconclusive results. This could be due to the low lever presence of endogenous NKR-P1B on the parental AMJ-C11 cells, despite RT-PCR analysis for NKR-P1B transcript coming back negative, or perhaps cross-reactivity with other surface proteins. In the future, a tagged version of NKR-P1B would be useful in confirming definitively the immediate downstream binding partner of NKR-P1B in the context of AMs. Likewise, a mass spectrometry screen performed on NKR-P1B pulled down from stimulated AMJ-P1B cells might prove informative.

REFERENCES

1. Janeway, C. A. Approaching the asymptote? Evolution and revolution in immunology. *Cold Spring Harb. Symp. Quant. Biol.* **54**, 1–13 (1989).

2. Takeuchi, O. & Akira, S. Pattern Recognition Receptors and Inflammation. *Cell* **140**, 805–820 (2010).

3. Amarante-Mendes, G. P. *et al.* Pattern recognition receptors and the host cell death molecular machinery. *Front. Immunol.* **9**, 1–19 (2018).

4. Jaeger, M., Stappers, M. H. T., Joosten, L. A. B., Gyssens, I. C. & Netea, M. G. Genetic variation in pattern recognition receptors: Functional consequences and susceptibility to infectious disease. *Future Microbiol.* **10**, 989–1008 (2015).

5. Brunette, R. L. *et al.* Extensive evolutionary and functional diversity among mammalian AIM2-like receptors. *J. Exp. Med.* **209**, 1969–1983 (2012).

6. Nakaya, Y., Lilue, J., Stavrou, S., Moran, E. A. & Ross, S. R. AIM2-like receptors positively and negatively regulate the interferon response induced by cytosolic DNA. *MBio* **8**, 1–17 (2017).

7. Takeda, K., Kaisho, T. & Akira, S. Toll-like receptors. *Annu. Rev. Immunol.* **21**, 335–376 (2003).

8. Medzhitov, R., Preston-Hurlburt, P. & Janeway, C. A. A human homologue of the Drosophila toll protein signals activation of adaptive immunity. *Nature* **388**, 394–397 (1997).

9. Poltorak, A. *et al.* Defective LPS signaling in C3H/HeJ and C57BL/10ScCr mice:

Mutations in Tlr4 gene. *Science (80-.).* **282**, 2085–2088 (1998).

10. Lemaitre, B., Nicolas, E., Michaut, L., Reichhart, J. M. & Hoffmann, J. A. The dorsoventral regulatory gene cassette spatzle/Toll/Cactus controls the potent antifungal response in Drosophila adults. *Cell* **86**, 973–983 (1996).

11. Akira, S. & Takeda, K. Toll-like receptor signalling. *Nat. Rev. Immunol.* **4**, 499–511 (2004).

12. Kato, H. *et al.* Length-dependent recognition of double-stranded ribonucleic acids by retinoic acid-inducible gene-I and melanoma differentiation-associated gene 5. *J. Exp. Med.* **205**, 1601–1610 (2008).

13. Franchi, L., Warner, N., Viani, K. & Nuñez, G. Function of Nod-likeFunction of Nod-like Receptors in Microbial Recognition and Host Defense. *Immunol. Rev.* **227**, 106–128 (2010).

14. Martinon, F., Mayor, A. & Tschopp, J. The inflammasomes: Guardians of the body. *Annu. Rev. Immunol.* **27**, 229–265 (2009).

15. Martinon, F., Pétrilli, V., Mayor, A., Tardivel, A. & Tschopp, J. Gout-associated uric acid crystals activate the NALP3 inflammasome. *Nature* **440**, 237–241 (2006).

16. Weis, W. I., Taylor, M. E. & Drickamer, K. The C-type lectin superfamily in the immune system. *Immunol. Rev.* **163**, 19–34 (1998).

17. Zelensky, A. N. & Gready, J. E. The C-type lectin-like domain superfamily. *FEBS J.* **272**, 6179–6217 (2005).

18. Brown, G. D., Willment, J. A. & Whitehead, L. C-type lectins in immunity and homeostasis. *Nat. Rev. Immunol.* **18**, 374–389 (2018).

19. Pyz, E., Marshall, A. S. J., Gordon, S. & Brown, G. D. C-type lectin-like receptors on myeloid cells. *Ann. Med.* **38**, 242–251 (2006).

20. Radaev, S. & Sun, P. D. Structure and function of natural killer cell surface receptors. *Annu. Rev. Biophys. Biomol. Struct.* **32**, 93–114 (2003).

21. Dambuza, I. M. & Brown, G. D. C-type lectins in immunity: Recent developments. *Curr. Opin. Immunol.* **32**, 21–27 (2015).

22. Kerrigan, A. M. & Brown, G. D. C-type lectins and phagocytosis. *Immunobiology* **214**, 562–575 (2009).

23. Burgdorf, S., Lukacs-Kornek, V. & Kurts, C. The Mannose Receptor Mediates Uptake of Soluble but Not of Cell-Associated Antigen for Cross-Presentation. *J. Immunol.* **176**, 6770–6776 (2006).

24. Huang, Y. W., Dryman, B. A., Li, W. & Meng, X. J. Porcine DC-SIGN: Molecular cloning, gene structure, tissue distribution and binding characteristics. *Dev. Comp. Immunol.* **33**, 464–480 (2009).

25. McGreal, E. P., Miller, J. L. & Gordon, S. Ligand recognition by antigen-presenting cell C-type lectin receptors. *Curr. Opin. Immunol.* **17**, 18–24 (2005).

26. Khoo, U. S., Chan, K. Y. K., Chan, V. S. F. & Lin, C. L. S. DC-SIGN and L-SIGN: The SIGNs for infection. *J. Mol. Med.* **86**, 861–874 (2008).

27. Manh, T. P. V. *et al.* Defining mononuclear phagocyte subset homology across

several distant warm-blooded vertebrates through comparative transcriptomics. *Front. Immunol.* **6**, 1–26 (2015).

28. Pyz, E. *et al.* Characterisation of murine MICL (CLEC12A) and evidence for an endogenous ligand. *Eur. J. Immunol.* **38**, 1157–1163 (2008).

29. Redelinghuys, P. *et al.* MICL controls inflammation in rheumatoid arthritis. *Ann. Rheum. Dis.* **75**, 1386–1391 (2016).

30. Kato, M., Khan, S., d'Aniello, E., McDonald, K. J. & Hart, D. N. J. The Novel Endocytic and Phagocytic C-Type Lectin Receptor DCL-1/CD302 on Macrophages Is Colocalized with F-Actin, Suggesting a Role in Cell Adhesion and Migration. *J. Immunol.* **179**, 6052–6063 (2007).

31. Hardison, S. E. & Brown, G. D. C-type lectin receptors orchestrate antifungal immunity. *Nat. Immunol.* **13**, 817–822 (2012).

32. Marakalala, M. J., Kerrigan, A. M. & Brown, G. D. Dectin-1: A role in antifungal defense and consequences of genetic polymorphisms in humans. *Mamm. Genome* **22**, 55–65 (2011).

33. McQueen, K. & Parham, P. Variable receptors controlling activation and inhibition of NK cells. *Curr. Opin. Immunol.* **14**, 615–621 (2002).

34. Pirillo, A., Norata, G. D. & Catapano, A. L. LOX-1, OxLDL, and atherosclerosis. *Mediators Inflamm.* **2013**, (2013).

35. Suzuki-Inoue, K., Inoue, O. & Ozaki, Y. Novel platelet activation receptor CLEC-2: From discovery to prospects. *J. Thromb. Haemost.* **9**, 44–55 (2011).

36. Mourão-Sá, D. *et al.* CLEC-2 signaling via Syk in myeloid cells can regulate inflammatory responses. *Eur. J. Immunol.* **41**, 3040–3053 (2011).

37. Sattler, S. *et al.* The Human C-Type Lectin-Like Receptor CLEC-1 is Upregulated by TGF-β and Primarily Localized in the Endoplasmic Membrane Compartment. *Scand. J. Immunol.* **75**, 282–292 (2012).

38. Chiffoleau, E. C-type lectin-like receptors as emerging orchestrators of sterile inflammation represent potential therapeutic targets. *Front. Immunol.* **9**, 1–9 (2018).

39. Thebault, P. *et al.* The C-Type Lectin-Like Receptor CLEC-1, Expressed by Myeloid Cells and Endothelial Cells, Is Up-Regulated by Immunoregulatory Mediators and Moderates T Cell Activation. *J. Immunol.* **183**, 3099–3108 (2009).

40. Robles, M. D. L. *et al.* Cell-surface C-type lectin-like receptor CLEC-1 dampens dendritic cell activation and downstream Th17 responses. *Blood Adv.* **1**, 557–568 (2017).

41. Cambier, J. C. New nomenclature for the Reth motif (or ARH1/TAM/ARAM/YXXL). *Immunol. Today* **16**, 110 (1995).

42. Burshtyn, D. N. *et al.* Recruitment of Tyrosine Phosphatase HCP (SHP-1) by the Killer Cell Inhibitory Receptor. *Immunity* **4**, 77–85 (1996).

43. Mócsai, A., Ruland, J. & Tybulewicz, V. L. J. The SYK tyrosine kinase: A crucial player in diverse biological functions. *Nat. Rev. Immunol.* **10**, 387–402 (2010).

44. Howell, K. W. *et al.* Toll-like receptor 4 mediates oxidized LDL-induced

macrophage differentiation to foam cells. *J. Surg. Res.* **171**, e27–e31 (2011).

45. Chávez-Sánchez, L. *et al.* The role of TLR2, TLR4 and CD36 in macrophage activation and foam cell formation in response to oxLDL in humans. *Hum. Immunol.* **75**, 322–329 (2014).

46. Higashimori, M. *et al.* ROLE OF TOLL-LIKE RECEPTOR 4 IN INTIMAL FOAM CELL ACCUMULATION IN APOLIPOPROTEIN E-DEFICIENT MICE. *Arter. Thromb Vasc Biol* **31**, 50–57 (2012).

47. Delneste, Y. *et al.* Involvement of LOX-1 in Dendritic Cell-Mediated Antigen Cross-Presentation Yves. *Int. J. Prev. Med.* **17**, 353–362 (2002).

48. Lobato-Pascual, A., Saether, P. C., Fossum, S., Dissen, E. & Daws, M. R. Mincle, the receptor for mycobacterial cord factor, forms a functional receptor complex with MCL and FcεRI-γ. *Eur. J. Immunol.* **43**, 3167–3174 (2013).

49. Ishikawa, E. *et al.* Direct recognition of the mycobacterial glycolipid, trehalose dimycolate, by C-type lectin Mincle. *J. Exp. Med.* **206**, 2879–2888 (2009).

50. Kostarnoy, A. V. *et al.* Receptor Mincle promotes skin allergies and is capable of recognizing cholesterol sulfate. *Proc. Natl. Acad. Sci. U. S. A.* **114**, E2758–E2765 (2017).

51. Das, B. K. *et al.* Characterization of a Protein Complex Containing Spliceosomal Proteins SAPs 49, 130, 145, and 155. *Mol. Cell. Biol.* **19**, 6796–6802 (1999).

52. Dzionek, A. *et al.* BDCA-2, a novel plasmacytoid dendritic cell-specific type II C-type lectin, mediates antigen capture and is a potent inhibitor of interferon α/β

induction. *J. Exp. Med.* **194**, 1823–1834 (2001).

53. Riboldi, E. *et al.* Human C-type lectin domain family 4, member C (CLEC4C/BDCA-2/CD303) is a receptor for asialo-galactosyl-oligosaccharides. *J. Biol. Chem.* **286**, 35329–35333 (2011).

54. Jégouzo, S. A. F. *et al.* A novel mechanism for binding of galactose-terminated glycans by the C-type carbohydrate recognition domain in blood dendritic cell antigen 2. *J. Biol. Chem.* **290**, 16759–16771 (2015).

55. Nakamura-Ishizu, A., Takubo, K., Kobayashi, H., Suzuki-Inoue, K. & Suda, T. CLEC-2 in megakaryocytes is critical for maintenance of hematopoietic stem cells in the bone marrow. *J. Exp. Med.* **212**, 2133–2146 (2015).

56. Wu, H. *et al.* Surfactant proteins A and D inhibit the growth of Gram-negative bacteria by increasing membrane permeability. *J. Clin. Invest.* **111**, 1589–1602 (2003).

57. Chavarha, M., Loney, R. W., Rananavare, S. B. & Hall, S. B. An anionic phospholipid enables the hydrophobic surfactant proteins to alter spontaneous curvature. *Biophys. J.* **104**, 594–603 (2013).

58. Cañadas, O., Olmeda, B., Alonso, A. & Pérez-Gil, J. Lipid–protein and protein–protein interactions in the pulmonary surfactant system and their role in lung homeostasis. *Int. J. Mol. Sci.* **21**, (2020).

59. Mi, Y. *et al.* Functional consequences of mannose and asialoglycoprotein receptor ablation. *J. Biol. Chem.* **291**, 18700–18717 (2016).

60. Mio, H. *et al.* Isolation and characterization of a cDNA for human, mouse, and rat full-length stem cell growth factor, a new member of C-type lectin superfamily. *Biochem. Biophys. Res. Commun.* **249**, 124–130 (1998).

61. Yue, R., Shen, B. & Morrison, S. J. Clec11a/osteolectin is an osteogenic growth factor that promotes the maintenance of the adult skeleton. *Elife* **5**, 27 (2016).

62. Kerrigan, A. M. & Brown, G. D. Syk-coupled C-type lectins in immunity. *Trends Immunol.* **32**, 151–156 (2011).

63. Sancho, D. & Sousa, C. R. Signaling by myeloid C-type lectin receptors in immunity and homeostasis David. *Annu Rev Immunol* **30**, 491–529 (2015).

64. Gringhuis, S. I., den Dunnen, J., Litjens, M., van der Vlist, M. & Geijtenbeek, T. B. H. Carbohydrate-specific signaling through the DC-SIGN signalosome tailors immunity to Mycobacterium tuberculosis, HIV-1 and Helicobacter pylori. *Nat. Immunol.* **10**, 1081–1088 (2009).

65. Gringhuis, S. I., Kaptein, T. M., Wevers, B. A., Mesman, A. W. & Geijtenbeek, T. B. H. Fucose-specific DC-SIGN signalling directs T helper cell type-2 responses via IKKε-and CYLD-dependent Bcl3 activation. *Nat. Commun.* **5**, (2014).

66. Gringhuis, S. I. *et al.* Dectin-1 directs T helper cell differentiation by controlling noncanonical NF-κB activation through Raf-1 and Syk. *Nat. Immunol.* **10**, 203–213 (2009).

67. del Fresno, C., Iborra, S., Saz-Leal, P., Martínez-López, M. & Sancho, D. Flexible signaling of Myeloid C-type lectin receptors in immunity and inflammation. *Front.*

Immunol. **9**, 1–13 (2018).

68. Lahoud, M. H. *et al.* The C-Type Lectin Clec12A Present on Mouse and Human Dendritic Cells Can Serve as a Target for Antigen Delivery and Enhancement of Antibody Responses. *J. Immunol.* **182**, 7587–7594 (2009).

69. Zhu, L. Le *et al.* C-type lectin receptors dectin-3 and dectin-2 form a heterodimeric pattern-recognition receptor for host defense against fungal infection. *Immunity* **39**, 324–334 (2013).

70. Li, K. *et al.* The uric acid crystal receptor Clec12A potentiates type I interferon responses. *Proc. Natl. Acad. Sci. U. S. A.* **116**, 18544–18549 (2019).

71. Troegeler, A. *et al.* C-type lectin receptor DCIR modulates immunity to tuberculosis by sustaining type I interferon signaling in dendritic cells. *Proc. Natl. Acad. Sci. U. S. A.* **114**, E540–E549 (2017).

72. Rahim, M. M. A. *et al.* Ly49Q Positively Regulates Type I IFN Production by Plasmacytoid Dendritic Cells in an Immunoreceptor Tyrosine–Based Inhibitory Motif–Dependent Manner. *J. Immunol.* **190**, 3994–4004 (2013).

73. Omatsu, Y. *et al.* Development of Murine Plasmacytoid Dendritic Cells Defined by Increased Expression of an Inhibitory NK Receptor, Ly49Q. *J. Immunol.* **174**, 6657–6662 (2005).

74. Iborra, S. *et al.* The DC receptor DNGR-1 mediates cross-priming of CTLs during vaccinia virus infection in mice. *J. Clin. Invest.* **122**, 1628–1643 (2012).

75. Iborra, S. *et al.* Optimal Generation of Tissue-Resident but Not Circulating

Memory T Cells during Viral Infection Requires Crosspriming by DNGR-1+ Dendritic Cells. *Immunity* **45**, 847–860 (2016).

76. Fischer, M. *et al.* Isoform localization of Dectin-1 regulates the signaling quality of anti-fungal immunity. *Eur. J. Immunol.* **47**, 848–859 (2017).

77. Iborra, S. *et al.* Leishmania Uses Mincle to Target an Inhibitory ITAM Signaling Pathway in Dendritic Cells that Dampens Adaptive Immunity to Infection. *Immunity* **45**, 788–801 (2016).

78. Rajaram, M. V. S. *et al.* M. tuberculosis-Initiated Human Mannose Receptor Signaling Regulates Macrophage Recognition and Vesicle Trafficking by FcRγ-Chain, Grb2, and SHP-1. *Cell Rep.* **21**, 126–140 (2017).

79. Yokoyama, W. M. & Seaman, W. E. The Ly-49 and NKR-P1 gene families encoding lectin-like receptors on natural killer cells: The NK gene complex. *Annu. Rev. Immunol.* **11**, 613–635 (1993).

80. Lanier, L. L. Up on the tightrope: Natural killer cell activation and inhibition. *Nat. Immunol.* **9**, 495–502 (2008).

81. Carlyle, J. R. *et al.* Evolution of the Ly49 and Nkrp1 recognition systems. *Semin. Immunol.* **20**, 321–330 (2008).

82. Kirkham, C. L. & Carlyle, J. R. Complexity and Diversity of the NKR-P1:Clr (Klrb1:Clec2) Recognition Systems. *Front. Immunol.* **5**, 214 (2014).

83. Hao, L., Klein, J. & Nei, M. Heterogeneous but conserved natural killer receptor gene complexes in four major orders of mammals. *Proc. Natl. Acad. Sci. U. S. A.*

103, 3192–3197 (2006).

84. Carrillo-Bustamante, P., Keşmir, C. & de Boer, R. J. The evolution of natural killer cell receptors. *Immunogenetics* **68**, 3–18 (2016).

85. Rahim, M. M. A. *et al.* Ly49 receptors: Innate and adaptive immune paradigms. *Front. Immunol.* **5**, 1–11 (2014).

86. Kim, S. *et al.* Licensing of natural killer cells by host major histocompatibility complex class I molecules. *Nature* **436**, 709–713 (2005).

87. Wight, A. *et al.* Critical role for the Ly49 family of class i MHC receptors in adaptive natural killer cell responses. *Proc. Natl. Acad. Sci. U. S. A.* **115**, 11579–11584 (2018).

88. Bauer, S. *et al.* Activation of NK cells and T cells by NKG2D, a receptor for stress- inducible MICA. *Science (80-.).* **285**, 727–729 (1999).

89. Petrie, E. J. *et al.* CD94-NKG2A recognition of human leukocyte antigen (HLA)-E bound to an HLA class I leader sequence. *J. Exp. Med.* **205**, 725–735 (2008).

90. Vieira, F., Kung, J. W. & Bhatti, F. Structure, Genetics and Function of The Pulmonary Associated Surfactant Proteins A and D: The Extra-Pulmonary Role of These C Type Lectins. *Ann anat* **211**, 184–201 (2017).

91. Rozbeský, D. *et al.* Nkrp1 family, from lectins to protein interacting molecules. *Molecules* **20**, 3463–3478 (2015).

92. Carlyle, J. R. *et al.* Mouse NKR-P1B, a novel NK1.1 antigen with inhibitory function. *J. Immunol.* **162**, 5917–23 (1999).

93. Chen, P. *et al.* Analysis of the mouse 129-strain Nkrp1-Clr gene cluster reveals conservation of genomic organization and functional receptor-ligand interactions despite significant allelic polymorphism. *Immunogenetics* **63**, 627–640 (2011).

94. Lanier, L. L., Chang, C. & Phillips, J. H. Human NKR-P1A. A disulfide-linked homodimer of the C-type lectin superfamily expressed by a subset of NK and T lymphocytes. *J. Immunol.* **153**, 2417–28 (1994).

95. Kamishikiryo, J., Fukuhara, H., Okabe, Y., Kuroki, K. & Maenaka, K. Molecular basis for LLT1 protein recognition by human CD161 protein (NKRP1A/KLRB1). *J. Biol. Chem.* **286**, 23823–23830 (2011).

96. Takahashi, T., Dejbakhsh-Jones, S. & Strober, S. Expression of CD161 (NKR-P1A) Defines Subsets of Human CD4 and CD8 T Cells with Different Functional Activities. *J. Immunol.* **176**, 211–216 (2006).

97. Yun, S. H. *et al.* Isolation of a human homolog of osteoclast inhibitory lectin that inhibits the formation and function of osteoclasts. *J. Bone Miner. Res.* **19**, 89–99 (2004).

98. Iizuka, K., Naidenko, O. V., Plougastel, B. F. M., Fremont, D. H. & Yokoyama, W. M. Genetically linked C-typed lectin-related ligands for the NKRP1 family of natural killer cell receptors. *Nat. Immunol.* **4**, 801–807 (2003).

99. Sovová, Ž. *et al.* Structural analysis of natural killer cell receptor protein 1 (NKR-P1) extracellular domains suggests a conserved long loop region involved in ligand specificity. *J. Mol. Model.* **17**, 1353–1370 (2011).

100. Germain, C. *et al.* Characterization of alternatively spliced transcript variants of CLEC2D gene. *J. Biol. Chem.* **285**, 36207–36215 (2010).

101. Balaji, G. R. *et al.* Recognition of host Clr-b by the inhibitory NKR-P1B receptor provides a basis for missing-self recognition. *Nat. Commun.* **9**, (2018).

102. Carlyle, J. R. *et al.* Missing self-recognition of Ocil/Clr-b by inhibitory NKR-P1 natural killer cell receptors. *Proc. Natl. Acad. Sci. U. S. A.* **101**, 3527–32 (2004).

103. Plougastel, B., Dubbelde, C. & Yokoyama, W. M. Cloning of Clr, a new family of lectin-like genes localized between mouse Nkrp1a and Cd69. *Immunogenetics* **53**, 209–214 (2001).

104. Kveberg, L. *et al.* Phylogenetic and functional conservation of the NKR-P1F and NKR-P1G receptors in rat and mouse. *Immunogenetics* **63**, 429–436 (2011).

105. Karlhofer, F. M. & Yokoyama, W. M. Stimulation of murine natural killer (NK) cells by a monoclonal antibody specific for the NK1.1 antigen. IL-2-activated NK cells possess additional specific stimulation pathways. *J. Immunol.* **146**, 3662–73 (1991).

106. Arase, N. *et al.* Association with FcRγ is essential for activation signal through NKR- P1 (CD161) in natural killer (NK) cells and NK1.1+ T cells. *J. Exp. Med.* **186**, 1957–1963 (1997).

107. Carlyle, J. R. *et al.* Molecular and Genetic Basis for Strain-Dependent NK1.1 Alloreactivity of Mouse NK Cells. *J. Immunol.* **176**, 7511–7524 (2006).

108. Campbell, K. S. & Giorda, R. The cytoplasmic domain of rat NKR-P1 receptor

interacts with the N-terminal domain of p56(ick) via cysteine residues. *Eur. J. Immunol.* **27**, 72–77 (1997).

109. Vivier, E., Nunès, J. A. & Vély, F. Natural killer cell signaling pathways. *Science (80-.).* **306**, 1517–1519 (2004).

110. Burshtyn, D. N., Yang, W., Yi, T. & Long, E. O. A novel phosphotyrosine motif with a critical amino acid at position -2 for the SH2 domain-mediated activation of the tyrosine phosphatase SHP-1. *J. Biol. Chem.* **272**, 13066–13072 (1997).

111. Ljutic, B. *et al.* Functional Requirements for Signaling through the Stimulatory and Inhibitory Mouse NKR-P1 (CD161) NK Cell Receptors. *J. Immunol.* **174**, 4789–4796 (2005).

112. Rosen, D. B. *et al.* Cutting Edge: Lectin-Like Transcript-1 Is a Ligand for the Inhibitory Human NKR-P1A Receptor. *J. Immunol.* **175**, 7796–7799 (2005).

113. Černý, J. *et al.* Association of human NK cell surface receptors NKR-P1 and CD94 with Src-family protein kinases. *Immunogenetics* **46**, 231–236 (1997).

114. Poggi, A. *et al.* Expression of human NKRP1A by CD34+ immature thymocytes: NKRP1A-mediated regulation of proliferation and cytolytic activity. *Eur. J. Immunol.* **26**, 1266–1272 (1996).

115. Rahim, M. M. a *et al.* The mouse NKR-P1B : Clr-b recognition system is a negative regulator of innate immune responses. **125**, 2217–2228 (2015).

116. Chen, P. *et al.* Genetic Investigation of MHC-Independent Missing-Self Recognition by Mouse NK Cells Using an In Vivo Bone Marrow Transplantation

Model. *J. Immunol.* (2015) doi:10.4049/jimmunol.1401523.

117. Mathew, S. O., Chaudhary, P., Powers, S. B., Vishwanatha, J. K. & Mathew, P. A. Overexpression of LLT1 (OCIL, CLEC2D) on prostate cancer cells inhibits NK cell-mediated killing through LLT1-NKRP1A (CD161) interaction. *Oncotarget* **7**, 68650–68661 (2016).

118. Tian, W. *et al.* C-type lectin OCILRP2/Clr-g and its ligand NKRP1f costimulate T cell proliferation and IL-2 production. *Cell. Immunol.* **234**, 39–53 (2005).

119. Leibelt, S. *et al.* Dedicated immunosensing of the mouse intestinal epithelium facilitated by a pair of genetically coupled lectin-like receptors. *Mucosal Immunol.* **8**, 232–242 (2015).

120. Zhang, Q. *et al.* Mouse Nkrp1-Clr Gene Cluster Sequence and Expression Analyses Reveal Conservation of Tissue-Specific MHC-Independent Immunosurveillance. *PLoS One* **7**, (2012).

121. Aguilar, O. A. *et al.* Modulation of Clr Ligand Expression and NKR-P1 Receptor Function during Murine Cytomegalovirus Infection. *J. Innate Immun.* **7**, 584–600 (2015).

122. Rutkowski, E. *et al.* Clr-a: A Novel Immune-Related C-Type Lectin-like Molecule Exclusively Expressed by Mouse Gut Epithelium. *J. Immunol.* **198**, 916–926 (2017).

123. Kartsogiannis, V. *et al.* Osteoclast inhibitory lectin, an immune cell product that is required for normal bone physiology in vivo. *J. Biol. Chem.* **283**, 30850–30860

(2008).

124. Pineda, B., Laporta, P., Cano, A. & García-Pérez, M. A. The Asn19Lys substitution in the osteoclast inhibitory lectin (OCIL) gene is associated with a reduction of bone mineral density in postmenopausal women. *Calcif. Tissue Int.* **82**, 348–353 (2008).

125. Epelman, S., Lavine, K. J. & Randolph, G. J. Origin and Functions of Tissue Macrophages. *Immunity* **41**, 21–35 (2014).

126. Guilliams, M., Thierry, G. R., Bonnardel, J. & Bajenoff, M. Establishment and Maintenance of the Macrophage Niche. *Immunity* **52**, 434–451 (2020).

127. Hashimoto, D. *et al.* Tissue-resident macrophages self-maintain locally throughout adult life with minimal contribution from circulating monocytes. *Immunity* **38**, 792–804 (2013).

128. Ginhoux, F. *et al.* Fate mapping analysis reveals that adult microglia derive from primitive macrophages. *Science (80-.).* **330**, 841–845 (2010).

129. Wang, Y. *et al.* IL-34 is a tissue-restricted ligand of CSF1R required for the development of Langerhans cells and microglia. *Nat. Immunol.* **13**, 753–760 (2012).

130. Li, F., Okreglicka, K. M., Pohlmeier, L. M., Schneider, C. & Kopf, M. Fetal monocytes possess increased metabolic capacity and replace primitive macrophages in tissue macrophage development. *EMBO J.* **39**, 1–16 (2020).

131. Epelman, S. *et al.* Embryonic and adult-derived resident cardiac macrophages are

maintained through distinct mechanisms at steady state and during inflammation. *Immunity* **40**, 91–104 (2015).

132. Hoeffel, G. *et al.* Adult Langerhans cells derive predominantly from embryonic fetal liver monocytes with a minor contribution of yolk sac-derived macrophages. *J. Exp. Med.* **209**, 1167–1181 (2012).

133. Morales-Nebreda, L., Misharin, A. V., Perlman, H. & Scott Budinger, G. R. The heterogeneity of lung macrophages in the susceptibility to disease. *Eur. Respir. Rev.* **24**, 505–509 (2015).

134. Ginhoux, F. & Jung, S. Monocytes and macrophages: developmental pathways and tissue homeostasis TL - 14. *Nat. Rev. Immunol.* **14 VN-r**, 392–404 (2014).

135. Haldar, M. *et al.* Heme-mediated SPI-C induction promotes monocyte differentiation into iron-recycling macrophages. *Cell* **156**, 1223–1234 (2015).

136. Reichard, J. F., Sartor, M. A. & Puga, A. BACH1 is a specific repressor of HMOX1 that is inactivated by arsenite. *J. Biol. Chem.* **283**, 22363–22370 (2008).

137. Luo, W., Xu, Q., Wang, Q., Wu, H. & Hua, J. Effect of modulation of PPAR-γ activity on Kupffer cells M1/M2 polarization in the development of non-alcoholic fatty liver disease. *Sci. Rep.* **7**, 1–13 (2017).

138. Helmy, K. Y. *et al.* CRIg: A macrophage complement receptor required for phagocytosis of circulating pathogens. *Cell* **124**, 915–927 (2006).

139. Cain, D. W. *et al.* Identification of a Tissue-Specific, C/EBPβ-Dependent Pathway of Differentiation for Murine Peritoneal Macrophages. *J. Immunol.* **191**, 4665–

4675 (2013).

140. Cassado, A. dos A. *et al.* Cellular renewal and improvement of local cell effector activity in peritoneal cavity in response to infectious stimuli. *PLoS One* **6**, 1–8 (2011).

141. Okabe, Y. & Medzhitov, R. Tissue-Specific Signals Control Reversible Program of Localization and Functional Polarization of Macrophages. *Cell* **157**, 832–844 (2014).

142. T'Jonck, W., Guilliams, M. & Bonnardel, J. Niche signals and transcription factors involved in tissue-resident macrophage development. *Cell. Immunol.* **330**, 43–53 (2018).

143. Daneman, R., Zhou, L., Kebede, A. A. & Barres, B. A. Pericytes are required for blood-brain barrier integrity during embryogenesis. *Nature* **468**, 562–566 (2010).

144. Chung, W. S., Welsh, C. A., Barres, B. A. & Stevens, B. Do Glia Drive Synaptic and Cognitive Impairment in Disease? *Nat Neurosci.* **176**, 139–148 (2015).

145. Nayak, D., Roth, T. L. & McGavern, D. B. Microglia development and function. *Annu. Rev. Immunol.* **32**, 367–402 (2014).

146. Charles, J. F. & Aliprantis, A. O. Osteoclasts: More than 'bone eaters'. *Trends Mol. Med.* **20**, 449–459 (2014).

147. Schlesinger, P. H., Blair, H. C., Teitelbaum, S. L. & Edwards, J. C. Characterization of the osteoclast ruffled border chloride channel and its role in bone resorption. *J. Biol. Chem.* **272**, 18636–18643 (1997).

148. Blair, H. C., Teitelbaum, S. L., Tan, H. L., Koziol, C. M. & Schlesinger, P. H. Passive chloride permeability charge coupled to H+-ATPase of avian osteoclast ruffled membrane. *Am. J. Physiol. - Cell Physiol.* **260**, (1991).

149. Pasparakis, M., Haase, I. & Nestle, F. O. Mechanisms regulating skin immunity and inflammation. *Nat. Rev. Immunol.* **14**, 289–301 (2014).

150. Guilliams, M. *et al.* Dendritic cells, monocytes and macrophages: A unified nomenclature based on ontogeny. *Nat. Rev. Immunol.* **14**, 571–578 (2014).

151. West, H. C. & Bennett, C. L. Redefining the role of langerhans cells as immune regulators within the skin. *Front. Immunol.* **8**, 1–8 (2018).

152. Guilliams, M. *et al.* Alveolar macrophages develop from fetal monocytes that differentiate into long-lived cells in the first week of life via GM-CSF. *J. Exp. Med.* **210**, 1977–92 (2013).

153. Shibata, Y. *et al.* GM-CSF regulates alveolar macrophage differentiation and innate immunity in the lung through PU.1. *Immunity* **15**, 557–567 (2001).

154. Ghoneim, H. E., Thomas, P. G. & McCullers, J. a. Depletion of alveolar macrophages during influenza infection facilitates bacterial superinfections. *J. Immunol.* **191**, 1250–9 (2013).

155. Fejer, G., Sharma, S. & Gyory, I. Immunobiology Self-renewing macrophages – A new line of enquiries in mononuclear phagocytes. *Immunobiology* **220**, 169–174 (2015).

156. Draijer, C., Penke, L. R. K. & Peters-Golden, M. Distinctive Effects of GM-CSF

and M-CSF on Proliferation and Polarization of Two Major Pulmonary Macrophage Populations. *J. Immunol.* **202**, 2700–2709 (2019).

157. Yona, S. *et al.* Fate mapping reveals origins and dynamics of monocytes and tissue macrophages under homeostasis. *Immunity* **38**, 79–91 (2013).

158. Schulz, C. *et al.* A lineage of myeloid cells independent of myb and hematopoietic stem cells. *Science (80-.).* **335**, 86–90 (2012).

159. Bain, C. C. *et al.* Resident and pro-inflammatory macrophages in the colon represent alternative context-dependent fates of the same Ly6C hi monocyte precursors. *Mucosal Immunol.* **6**, 498–510 (2013).

160. Priller, J. *et al.* Targeting gene-modified hematopoietic cells to the central nervous system: Use of green fluorescent protein uncovers microglial engraftment. *Nat. Med.* **7**, 1356–1361 (2001).

161. Simard, A. R. & Rivest, S. Bone marrow stem cells have the ability to populate the entire central nervous system into fully differentiated parenchymal microglia. *FASEB J.* **18**, 998–1000 (2004).

162. Murphy, J., Summer, R., Wilson, A. A., Kotton, D. N. & Fine, A. The prolonged life-span of alveolar macrophages. *Am. J. Respir. Cell Mol. Biol.* **38**, 380–385 (2008).

163. Reyfman, P. A. *et al.* Single-cell transcriptomic analysis of human lung provides insights into the pathobiology of pulmonary fibrosis. *Am. J. Respir. Crit. Care Med.* **199**, 1517–1536 (2019).

164. Kooguchi, K. *et al.* Role of alveolar macrophages in initiation and regulation of inflammation in Pseudomonas aeruginosa pneumonia. *Infect. Immun.* **66**, 3164–3169 (1998).

165. Barth, M. W., Hendrzak, J. A., Melnicoff, M. J. & Morahan, P. S. Review of the macrophage disappearance reaction. *J. Leukoc. Biol.* **57**, 361–7 (1995).

166. Shi, C. & Pamer, E. G. Monocyte recruitment during infection and inflammation. *Nat. Rev. Immunol.* **11**, 762–74 (2011).

167. Zasłona, Z. *et al.* Resident alveolar macrophages suppress, whereas recruited monocytes promote, allergic lung inflammation in murine models of asthma. *J. Immunol.* **193**, 4245–53 (2014).

168. Stanley, E. R. *et al.* Biology and action of colony-stimulating factor-1. *Mol. Reprod. Dev.* **46**, 4–10 (1997).

169. Rojo, R. *et al.* Deletion of a Csf1r enhancer selectively impacts CSF1R expression and development of tissue macrophage populations. *Nat. Commun.* **10**, 1–17 (2019).

170. Noguera, N. I. *et al.* PML/RARa inhibits PTEN expression in hematopoietic cells by competing with PU.1 transcriptional activity. *Oncotarget* **7**, 66386–66397 (2016).

171. Mueller, B. U. *et al.* Heterozygous PU.1 mutations are associated with acute myeloid leukemia [6]. *Blood* **101**, 2074 (2003).

172. Aziz, A., Soucie, E., Sarrazin, S. & Sieweke, M. H. MafB/c-Maf Deficiency

Enables Self-Renewal of Differentiated Functional Macrophages. *Science (80-.).* **326**, 867–872 (2009).

173. Soucie, E. L. *et al.* Lineage-specific enhancers activate self-renewal genes in macrophages and embryonic stem cells. *Science (80-.).* **351**, (2016).

174. Scott, C. L. *et al.* The Transcription Factor ZEB2 Is Required to Maintain the Tissue-Specific Identities of Macrophages. *Immunity* **49**, 312-325.e5 (2018).

175. Buechler, M. B. *et al.* A Stromal Niche Defined by Expression of the Transcription Factor WT1 Mediates Programming and Homeostasis of Cavity-Resident Macrophages. *Immunity* **51**, 119-130.e5 (2019).

176. Bonnardel, J. *et al.* Stellate Cells, Hepatocytes, and Endothelial Cells Imprint the Kupffer Cell Identity on Monocytes Colonizing the Liver Macrophage Niche. *Immunity* **51**, 638-654.e9 (2019).

177. Kohyama, M. *et al.* Role for Spi-C in the development of red pulp macrophages and splenic iron homeostasis. *Nature* **457**, 318–321 (2009).

178. Lu, Y. *et al.* Interleukin-33 Signaling Controls the Development of Iron-Recycling Macrophages. *Immunity* **52**, 782-793.e5 (2020).

179. Zöller, T. *et al.* Silencing of TGFβ signalling in microglia results in impaired homeostasis. *Nat. Commun.* **9**, 1–13 (2018).

180. Zhang, X., Gu, J., Yu, F. S., Zhou, L. & Mi, Q. S. TGF-β1-induced transcription factor networks in Langerhans cell development and maintenance. *Allergy* **71**, 758–764 (2016).

181. Borkowski, T. A., Letterio, J. J., Farr, A. G. & Udey, M. C. A role for endogenous transforming growth factor β1 in Langerhans cell biology: The skin of transforming growth factor β1 null mice is devoid of epidermal Langerhans cells. *J. Exp. Med.* **184**, 2417–2422 (1996).

182. Zhang, X. *et al.* Impaired epidermal Langerhans cell maturation in TGFβ-inducible early gene 1 (TIEG1) knockout mice. *Oncotarget* **8**, 112875–112882 (2017).

183. Chakarov, S., Ginhoux, F. & Ble, C. Review Determinants of Resident Tissue Macrophage Identity and Function. 957–970 (2020) doi:10.1016/j.immuni.2020.05.014.

184. Yu, X. *et al.* The Cytokine TGF-β Promotes the Development and Homeostasis of Alveolar Macrophages. *Immunity* **47**, 903-912.e4 (2017).

185. Hussell, T. & Bell, T. J. Alveolar macrophages: plasticity in a tissue-specific context. *Nat. Rev. Immunol.* **14**, 81–93 (2014).

186. Laza-Stanca, V. *et al.* Rhinovirus Replication in Human Macrophages Induces NF-κB-Dependent Tumor Necrosis Factor Alpha Production. *J. Virol.* **80**, 8248–8258 (2006).

187. Gordon, S. B., Irving, G. R. B., Lawson, R. A., Lee, M. E. & Read, R. C. Intracellular trafficking and killing of Streptococcus pneumoniae by human alveolar macrophages are influenced by opsonins. *Infect. Immun.* **68**, 2286–2293 (2000).

188. Chacón-Salinas, R. *et al.* Differential pattern of cytokine expression by macrophages infected in vitro with different Mycobacterium tuberculosis genotypes. *Clin. Exp. Immunol.* **140**, 443–449 (2005).

189. Jung, J. Y. *et al.* The intracellular environment of human macrophages that produce nitric oxide promotes growth of mycobacteria. *Infect. Immun.* **81**, 3198–3209 (2013).

190. Zhou, J. *et al.* Differential expression of chemokines and their receptors in adult and neonatal macrophages infected with human or avian influenza viruses. *J. Infect. Dis.* **194**, 61–70 (2006).

191. Nicol, M. Q. & Dutia, B. M. The role of macrophages in influenza A virus infection. *Future Virol.* **9**, 847–862 (2014).

192. Schneider, C. *et al.* Alveolar Macrophages Are Essential for Protection from Respiratory Failure and Associated Morbidity following Influenza Virus Infection. *PLoS Pathog.* **10**, (2014).

193. Guillon, A. *et al.* Pneumonia recovery reprograms the alveolar macrophage pool. *JCI Insight* **5**, (2020).

194. Yao, Y. *et al.* Induction of Autonomous Memory Alveolar Macrophages Requires T Cell Help and Is Critical to Article Induction of Autonomous Memory Alveolar Macrophages Requires T Cell Help. *Cell* **175**, 1634-1650.e17 (2018).

195. Dockrell, D. H. *et al.* Alveolar Macrophage Apoptosis Contributes to Pneumococcal Clearance in a Resolving Model of Pulmonary Infection. *J.*

Immunol. **171**, 5380–5388 (2003).

196. Knapp, S. *et al.* Alveolar macrophages have a protective antiinflammatory role during murine pneumococcal pneumonia. *Am. J. Respir. Crit. Care Med.* **167**, 171–179 (2003).

197. Neupane, A. S. *et al.* Patrolling Alveolar Macrophages Conceal Bacteria from the Immune System to Maintain Homeostasis. *Cell* **183**, 110-125.e11 (2020).

198. Fadok, V. A. *et al.* Macrophages that have ingested apoptotic cells in vitro inhibit proinflammatory cytokine production through autocrine/paracrine mechanisms involving TGF-β, PGE2, and PAF. *J. Clin. Invest.* **101**, 890–898 (1998).

199. Kadioglu, A. & Andrew, P. W. Susceptibility and resistance to pneumococcal disease in mice. *Briefings Funct. Genomics Proteomics* **4**, 241–247 (2005).

200. Jang, Y. *et al.* Cutting Edge: Check Your Mice—A Point Mutation in the Ncr1 Locus Identified in CD45.1 Congenic Mice with Consequences in Mouse Susceptibility to Infection . *J. Immunol.* **200**, 1982–1987 (2018).

201. Weiser, J. N., Ferreira, D. M. & Paton, J. C. *Streptococcus pneumoniae: transmission, colonization and invasion*. vol. 16 (2018).

202. Peteranderl, C., Herold, S. & Schmoldt, C. Human Influenza Virus Infections. *Semin. Respir. Crit. Care Med.* **37**, (2016).

203. Small, C.-L. *et al.* Influenza infection leads to increased susceptibility to subsequent bacterial superinfection by impairing NK cell responses in the lung. *J. Immunol.* **184**, 2048–56 (2010).

204. Mestas, J. & Hughes, C. C. W. Of Mice and Not Men: Differences between Mouse and Human Immunology. *J. Immunol.* **172**, 2731–2738 (2004).

205. Williams, S. H. *et al.* New York City house mice (Mus musculus) as potential reservoirs for pathogenic bacteria and antimicrobial resistance determinants. *MBio* **9**, (2018).

206. Tao, L. & Reese, T. A. Making Mouse Models That Reflect Human Immune Responses. *Trends Immunol.* **38**, 181–193 (2017).

207. Baz, M. *et al.* Synergistic PA and HA mutations confer mouse adaptation of a contemporary A/H3N2 influenza virus. *Sci. Rep.* **9**, 1–14 (2019).

208. Wyde, P. R., Couch, R. B., Mackler, B. F., Cate, T. R. & Levy, B. M. Effects of low and high passage influenza virus infection in normal and nude mice. *Infect. Immun.* **15**, 221–229 (1977).

209. Hraiech, S., Papazian, L., Rolain, J. M. & Bregeon, F. Animal models of polymicrobial pneumonia. *Drug Des. Devel. Ther.* **9**, 3279–3292 (2015).

210. Southam, D. S., Dolovich, M., O'Byrne, P. M. & Inman, M. D. Distribution of intranasal instillations in mice: Effects of volume, time, body position, and anesthesia. *Am. J. Physiol. - Lung Cell. Mol. Physiol.* **282**, 833–839 (2002).

211. Mizgerd, J. P. & Skerrett, S. J. Animal models of human pneumonia. *Am. J. Physiol. - Lung Cell. Mol. Physiol.* **294**, (2008).

212. Careau, E. & Bissonnette, E. Y. Adoptive transfer of alveolar macrophages abrogates bronchial hyperresponsiveness. *Am. J. Respir. Cell Mol. Biol.* **31**, 22–27

(2004).

213. Morimoto, K. *et al.* Alveolar macrophages that phagocytose apoptotic neutrophils produce hepatocyte growth factor during bacterial pneumonia in mice. *Am. J. Respir. Cell Mol. Biol.* **24**, 608–615 (2001).

214. Bourdonnay, E. *et al.* Transcellular delivery of vesicular SOCS proteins from macrophages to epithelial cells blunts inflammatory signaling. *J. Exp. Med.* **212**, 729–742 (2015).

215. Speth, J. M. *et al.* Alveolar epithelial cell-derived prostaglandin E2 serves as a request signal for macrophage secretion of suppressor of cytokine signaling 3 during innate inflammation. *J Immunol* **196**, 5112–5120 (2016).

216. Mihrshahi, R., Barclay, A. N. & Brown, M. H. Essential Roles for Dok2 and RasGAP in CD200 Receptor-Mediated Regulation of Human Myeloid Cells. *J. Immunol.* **183**, 4879–4886 (2009).

217. Morris, D. G., Huang, X., Kaminski, N. & Wang, Y. Loss of integrin a v b 6-mediated TGF- b activation causes Mmp12-dependent emphysema. *Nature* **12450**, 169–173 (2003).

218. Yamashita, C. M., Veldhuizen, R. A. & Gill, S. E. Alveolar macrophages and pulmonary surfactant—more than just friendly neighbours. *OA Biol.* 1–6 (2013) doi:http://dx.doi.org/10.1016/j.jns.2007.09.033.

219. Kingma, P. & Jobe, A. H. *The Surfactant System*. *Kendig's Disorders of the Respiratory Tract in Children* (Elsevier Inc., 2019). doi:10.1016/B978-0-323-

44887-1.00005-5.

220. Chakraborty, M. & Kotecha, S. Pulmonary surfactant in newborn infants and children. *Breathe* **9**, 476–488 (2013).

221. Sano, H. *et al.* Pulmonary surfactant protein A modulates the cellular response to smooth and rough lipopolysaccharides by interaction with CD14. *J. Immunol.* **163**, 387–95 (1999).

222. Chavarha, M., Loney, R. W., Kumar, K., Rananavare, S. B. & Hall, S. B. Differential Effects of the Hydrophobic Surfactant Proteins on the Formation of Inverse Bicontinuous Cubic Phases. *Langmuir* **28**, 16596–16604 (2012).

223. Botas, C. *et al.* Altered surfactant homeostasis and alveolar type II cell morphology in mice lacking surfactant protein D. *Proc. Natl. Acad. Sci. U. S. A.* **95**, 11869–74 (1998).

224. Jacobs, H. C., Ikegami, I., Jobe, A. H., D.D., B. & Jones, S. Reutilization of surfacant phosphatidylcholine in adult rabbits. *Biochim. Biophys. Acta* **837**, 77–84 (1985).

225. Kumar, A., Abdelmalak, B., Inoue, Y. & Culver, D. A. Pulmonary alveolar proteinosis in adults: pathophysiology and clinical approach. *Lancet Respir. Med.* **6**, 554–565 (2018).

226. Lopez-rodriguez, E., Gay-jordi, G. & Mucci, A. Lung surfactant metabolism : early in life , early in disease and target in cell therapy. *Cell Tissue Res* **367**, 721–735 (2017).

227. Yayo, Y. *et al.* Specific Localization of Lysosomal Aminopeptidases in Type II Alveolar Epithelial Cells of the Rat Lung. *Arch Histol. Cytol.* **64**, 89–97 (2001).

228. Perez-Gil, J. & Weaver, T. E. Pulmonary surfactant pathophysiology: Current models and open questions. *Physiology* **25**, 132–141 (2010).

229. Out, R. *et al.* Macrophage ABCG1 deletion disrupts lipid homeostasis in alveolar macrophages and moderately influences atherosclerotic lesion development in LDL receptor-deficient mice. *Arterioscler. Thromb. Vasc. Biol.* **26**, 2295–2300 (2006).

230. Wang, N., Silver, D. L., Thiele, C. & Tall, A. R. ATP-binding Cassette Transporter A1 (ABCA1) Functions as a Cholesterol Efflux Regulatory Protein. *J. Biol. Chem.* **276**, 23742–23747 (2001).

231. Venkateswaran, A. *et al.* Control of cellular cholesterol efflux by the nuclear oxysterol receptor LXRα. *Proc. Natl. Acad. Sci. U. S. A.* **97**, 12097–12102 (2000).

232. Schneider, C. *et al.* Induction of the nuclear receptor PPAR-γ by the cytokine GM-CSF is critical for the differentiation of fetal monocytes into alveolar macrophages. *Nat. Immunol.* **15**, 1026–1037 (2014).

233. Baker, A. D. *et al.* Targeted PPARγ deficiency in alveolar macrophages disrupts surfactant catabolism. *J. Lipid Res.* **51**, 1325–1331 (2010).

234. Griese, M. *et al.* Respiratory disease in Niemann-Pick type C2 is caused by pulmonary alveolar proteinosis. *Clin. Genet.* **77**, 119–130 (2010).

235. Yao, X. *et al.* Apolipoprotein E negatively regulates house dust mite-induced

asthma via a low-density lipoprotein receptor-mediated pathway. *Am. J. Respir. Crit. Care Med.* **182**, 1228–1238 (2010).

236. Snelgrove, R. J. *et al.* A critical function for CD200 in lung immune homeostasis and the severity of influenza infection. *Nat. Immunol.* **9**, 1074–1083 (2008).

237. Hu, J. F., Zhang, W., Zuo, W., Tan, H. Q. & Bai, W. Inhibition of the PD-1/PD-L1 signaling pathway enhances innate immune response of alveolar macrophages to mycobacterium tuberculosis in mice. *Pulm. Pharmacol. Ther.* **60**, 101842 (2020).

238. Shinohara, M. *et al.* CD47 regulation of epithelial cell spreading and migration, and its signal transduction. *Cancer Sci.* **97**, 889–895 (2006).

239. Bissonnette, E. Y., Lauzon-Joset, J. F., Debley, J. S. & Ziegler, S. F. Cross-Talk Between Alveolar Macrophages and Lung Epithelial Cells is Essential to Maintain Lung Homeostasis. *Front. Immunol.* **11**, 1–12 (2020).

240. Garbi, N. & Lambrecht, B. N. Location, function, and ontogeny of pulmonary macrophages during the steady state. *Pflugers Arch. Eur. J. Physiol.* **469**, 561–572 (2017).

241. Whitsett, J. A., Wert, S. E. & Weaver, T. E. Diseases of pulmonary surfactant homeostasis. *Annu. Rev. Pathol. Mech. Dis.* **10**, 371–393 (2015).

242. Nakamura, A. *et al.* Transcription repressor Bach2 is required for pulmonary surfactant homeostasis and alveolar macrophage function. *J. Exp. Med.* **210**, 2191–2204 (2013).

243. Deng, W. *et al.* Essential Role of mTORC1 in Self-Renewal of Murine Alveolar

Macrophages. *J. Immunol.* 1501845 (2016) doi:10.4049/jimmunol.1501845.

244. Izquierdo, H. M. *et al.* Von Hippel-Lindau Protein Is Required for Optimal Renewal , and Function Report Von Hippel-Lindau Protein Is Required for Optimal Alveolar Macrophage Terminal Differentiation , Self-Renewal , and Function. *Cell Rep.* **24**, 1738–1746 (2018).

245. Rauschmeier, R. *et al.* Bhlhe40 and Bhlhe41 transcription factors regulate alveolar macrophage self-renewal and identity. *EMBO J.* **38**, 1–20 (2019).

246. Kartsogiannis, V. *et al.* Osteoclast inhibitory lectin, an immune cell product that is required for normal bone physiology in vivo. *J. Biol. Chem.* **283**, 30850–30860 (2008).

247. Mahmoud, A. B. *et al.* Influenza Virus Targets Class I MHC-Educated NK Cells for Immunoevasion. *PLoS Pathog.* **12**, 1–22 (2016).

248. Abou-Samra, E. *et al.* NKR-P1B expression in gut-associated innate lymphoid cells is required for the control of gastrointestinal tract infections. *Cell. Mol. Immunol.* **16**, 868–877 (2019).

249. Misharin, A. V *et al.* Monocyte-derived alveolar macrophages drive lung fibrosis and persist in the lung over the life span. *JEM* **214**, 2387–2404 (2017).

250. Aegerter, H. *et al.* Influenza-induced monocyte-derived alveolar macrophages confer prolonged antibacterial protection. *Nat. Immunol.* **21**, 145–157 (2020).

251. Opalek, J. M., Ali, N. A., Lobb, J. M., Hunter, M. G. & Marsh, C. B. Alveolar macrophages lack CCR2 expression and do not migrate to CCL2. *J. Inflamm.* **4**, 1–

10 (2007).

252. Desch, A. N. *et al.* CD103+ pulmonary dendritic cells preferentially acquire and present apoptotic cell-associated antigen. *J. Exp. Med.* **208**, 1789–1797 (2011).

253. Jakubzick, C. *et al.* Minimal differentiation of classical monocytes as they survey steady state tissues and transport antigen to lymph nodes Claudia. *Immunity* **39**, 599–610 (2013).

254. Shah, P. L., Hansell, D., Lawson, P. R., Reid, K. B. M. & Morgan, C. V. Pulmonary alveolar proteinosis : clinical aspects and current concepts on pathogenesis. 67–77 (2000).

255. Guth, A. M. *et al.* Lung environment determines unique phenotype of alveolar macrophages. *Am. J. Physiol. - Lung Cell. Mol. Physiol.* **296**, 936–946 (2009).

256. Kraus, N. A. *et al.* Quantitative assessment of adipocyte differentiation in cell culture. *Adipocyte* **5**, 351–358 (2016).

257. Dodd, C. E., Pyle, C. J., Glowinski, R., Rajaram, M. V. S. & Schlesinger, L. S. CD36-Mediated Uptake of Surfactant Lipids by Human Macrophages Promotes Intracellular Growth of Mycobacterium tuberculosis . *J. Immunol.* **197**, 4727–4735 (2016).

258. Rahaman, S. O., Zhou, G. & Silverstein, R. L. Vav protein guanine nucleotide exchange factor regulates CD36 protein-mediated macrophage foam cell formation via calcium and dynamin-dependent processes. *J. Biol. Chem.* **286**, 36011–36019 (2011).

259. Kültürsay, N., Uygur, Ö. & Yalaz, M. The use of surfactant in the neonatal period-the known, those still under research and those need to be further investigated. *Turk Pediatr. Ars.* **49**, 1–12 (2014).

260. Hentschel, R., Bohlin, K., van Kaam, A., Fuchs, H. & Danhaive, O. Surfactant replacement therapy: from biological basis to current clinical practice. *Pediatr. Res.* **88**, 176–183 (2020).

261. Moya, F. & Maturana, A. Animal-Derived Surfactants Versus Past and Current Synthetic Surfactants: Current Status. *Clin. Perinatol.* **34**, 145–177 (2007).

262. Choi, S. *et al.* AIBP augments cholesterol efflux from alveolar macrophages to surfactant and reduces acute lung inflammation Graphical abstract Find the latest version : AIBP augments cholesterol efflux from alveolar macrophages to surfactant and reduces acute lung infla. *JCI Insight* **3**, (2018).

263. Costet, P. *et al.* Retinoic Acid Receptor-Mediated Induction of ABCA1 in Macrophages. *Mol. Cell. Biol.* **23**, 7756–7766 (2003).

264. Borradaile, N. M. *et al.* Disruption of endoplasmic reticulum structure and integrity in lipotoxic cell death. *J. Lipid Res.* **47**, 2726–2737 (2006).

265. Bosma, M., Kersten, S., Hesselink, M. K. C. & Schrauwen, P. Re-evaluating lipotoxic triggers in skeletal muscle: Relating intramyocellular lipid metabolism to insulin sensitivity. *Prog. Lipid Res.* **51**, 36–49 (2012).

266. Dong, Y. *et al.* CD44 Loss Disrupts Lung Lipid Surfactant Homeostasis and Exacerbates Oxidized Lipid-Induced Lung Inflammation. *Front. Immunol.* **11**, 1–

18 (2020).

267. He, W. *et al.* Alveolar macrophages are critical for broadly-reactive antibody-mediated protection against influenza A virus in mice. *Nat. Commun.* **8**, 1–13 (2017).

268. Tay, M. Z., Wiehe, K. & Pollara, J. Antibody dependent cellular phagocytosis in antiviral immune responses. *Front. Immunol.* **10**, 1–18 (2019).

269. McDonald, C. F. & Atkins, R. C. Defective cytostatic activity of pulmonary alveolar macrophages in primary lung cancer. *Chest* **98**, 881–885 (1990).

270. Lecoultre, M., Dutoit, V. & Walker, P. R. Phagocytic function of tumor-associated macrophages as a key determinant of tumor progression control: A review. *J. Immunother. Cancer* **8**, 1–11 (2020).

271. Russ, A. *et al.* Blocking 'don't eat me' signal of CD47-SIRPα in hematological malignancies, an in-depth review Atlantis. *Blood Rev.* **176**, 139–148 (2019).

272. Mccarthy, C. *et al.* Statin as a novel pharmacotherapy of pulmonary alveolar proteinosis. *Nat. Commun.* **3127**, 1–9 (2018).

273. Westphalen, K. *et al.* Sessile alveolar macrophages communicate with alveolar epithelium to modulate immunity. *Nature* **506**, 503–506 (2014).

274. Svedberg, F. R. *et al.* The lung environment controls alveolar macrophage metabolism and responsiveness in type 2 inflammation. *Nat. Immunol.* **20**, 571–580 (2019).

275. McQuattie-Pimentel, A. C. *et al.* The lung microenvironment shapes a

dysfunctional response of alveolar macrophages in aging. *J. Clin. Invest.* **131**, (2021).

276. Svedberg, F. R. *et al.* macrophage metabolism and responsiveness in type 2 inflammation. *Nat. Immunol.* **20**, (2019).

277. Guillon, A. *et al.* Pneumonia recovery reprograms the alveolar macrophage pool. *JCI Insight* **5**, (2020).

278. Gangwar, R. S. *et al.* Differential contribution of bone marrow-derived infiltrating monocytes and resident macrophages to persistent lung inflammation in chronic air pollution exposure. *Sci. Rep.* **10**, 1–15 (2020).

279. Kerr, A. R. *et al.* Identification of a detrimental role for NK cells in pneumococcal pneumonia and sepsis in immunocompromised hosts. *Microbes Infect.* **7**, 845–852 (2005).

280. Elhaik-Goldman, S. *et al.* The natural cytotoxicity receptor 1 contribution to early clearance of Streptococcus pneumoniae and to natural killer-macrophage cross talk. *PLoS One* **6**, (2011).

281. Ivin, M. *et al.* Natural killer cell-intrinsic type I IFN signaling controls Klebsiella pneumoniae growth during lung infection. *PLoS Pathog.* **13**, 1–29 (2017).

282. Machiels, B. *et al.* A gammaherpesvirus provides protection against allergic asthma by inducing the replacement of resident alveolar macrophages with regulatory monocytes. *Nat. Immunol.* **18**, 1310–1320 (2017).

283. Geissmann, F., Jung, S. & Littman, D. R. Blood monocytes consist of two

principal subsets with distinct migratory properties. *Immunity* **19**, 71–82 (2003).

284. Teh, Y. C., Ding, J. L., Ng, L. G. & Chong, S. Z. Capturing the fantastic voyage of monocytes through time and space. *Front. Immunol.* **10**, 1–9 (2019).

285. Juvet, S. C., Hwang, D., Waddell, T. K. & Downey, G. P. Rare lung disease II: pulmonary alveolar proteinosis. *Can. Respir. J.* **15**, 203–10 (2008).

286. van de Laar, L. *et al.* Yolk Sac Macrophages, Fetal Liver, and Adult Monocytes Can Colonize an Empty Niche and Develop into Functional Tissue-Resident Macrophages. *Immunity* **44**, 755–768 (2016).

287. Gibbings, S. L. *et al.* Transcriptome analysis highlights the conserved difference between embryonic and postnatal-derived alveolar macrophages. *Blood* **126**, 1357–1366 (2015).

288. Viola, A., Munari, F., Sánchez-Rodríguez, R., Scolaro, T. & Castegna, A. The metabolic signature of macrophage responses. *Front. Immunol.* **10**, 1–16 (2019).

289. Wessendarp, M. *et al.* Role of GM-CSF in regulating metabolism and mitochondrial functions critical to macrophage proliferation. *BioRxiv* (2021).

290. Unkel, B. *et al.* Alveolar epithelial cells orchestrate DC function in murine viral pneumonia. *J. Clin. Invest.* **122**, 3652–3664 (2012).

291. Lin, H. S., Lokeshwar, B. L. & Hsu, S. Both granulocyte-macrophage CSF and macrophage CSF control the proliferation and survival of the same subset of alveolar Why The JI ? Submit online . • Rapid Reviews ! 30 days * from submission to initial decision • No Triage ! Every submission reviewed b. *J.*

Immunol. (2020).

292. Nakata, K. *et al.* Augmented proliferation of human alveolar macrophages after allogeneic bone marrow transplantation. *Blood* **93**, 667–673 (1999).

293. Zhao, P., Fu, J. L., Yao, B. Y., Jia, Y. R. & Zhou, Z. C. S phase cell percentage normalized BrdU incorporation rate, a new parameter for determining S arrest. *Biomed. Environ. Sci.* **27**, 215–219 (2014).

294. Xu, X. *et al.* Inhibition of DNA Replication and Induction of S Phase Cell Cycle Arrest by G-rich Oligonucleotides. *J. Biol. Chem.* **276**, 43221–43230 (2001).

295. Gasser, A. & Möst, J. Generation of multinucleated giant cells in vitro by culture of human monocytes with Mycobacterium bovis BCG in combination with cytokine- containing supernatants. *Infect. Immun.* **67**, 395–402 (1999).

296. Sato, K. *et al.* Diffuse progressive pulmonary interstitial and intra-alveolar cholesterol granulomas in childhood. *Eur. Respir. J.* **9**, 2419–2422 (1996).

297. Griese, M. Pulmonary alveolar proteinosis: A comprehensive clinical perspective. *Pediatrics* **140**, (2017).

298. Herrtwich, L. *et al.* DNA Damage Signaling Instructs Polyploid Macrophage Fate in Granulomas. *Cell* **167**, 1264-1280.e18 (2016).

299. Krautwald, S., Büscher, D., Kummer, V., Buder, S. & Baccarini, M. Involvement of the protein tyrosine phosphatase SHP-1 in Ras-mediated activation of the mitogen-activated protein kinase pathway. *Mol. Cell. Biol.* **16**, 5955–5963 (1996).

300. Guidez, F., Li, A. C., Horvai, A., Welch, J. S. & Glass, C. K. Differential

Utilization of Ras Signaling Pathways by Macrophage Colony-Stimulating Factor (CSF) and Granulocyte-Macrophage CSF Receptors during Macrophage Differentiation. *Mol. Cell. Biol.* **18**, 3851–3861 (1998).

301. Kurotaki, D., Sasaki, H. & Tamura, T. Transcriptional control of monocyte and macrophage development. *Int. Immunol.* **29**, 97–107 (2017).

302. Chen, C. *et al.* Potentiation of IL-4 Signaling by Retinoic Acid in Intestinal Epithelial Cells and Macrophages—Mechanisms and Targets. *Front. Immunol.* **11**, (2020).

303. Roszer, T., Menéndez-Gutiérrez, M. P., Cedenilla, M. & Ricote, M. Retinoid X receptors in macrophage biology. *Trends Endocrinol. Metab.* **24**, 460–468 (2013).

304. Cohena, P. & Spiegelmanb, B. M. Cell biology of fat storage. *Mol. Biol. Cell* **27**, 2523–2527 (2016).

305. Pol, A., Gross, S. P. & Parton, R. G. Biogenesis of the multifunctional lipid droplet: Lipids, proteins, and sites. *J. Cell Biol.* **204**, 635–646 (2014).

306. Yuan, Y., Li, P. & Ye, J. Lipid homeostasis and the formation of macrophage-derived foam cells in atherosclerosis. *Protein Cell* **3**, 173–181 (2012).

307. Huang, S. C. C. *et al.* Cell-intrinsic lysosomal lipolysis is essential for alternative activation of macrophages. *Nat. Immunol.* **15**, 846–855 (2014).

308. Silverstein, R. L., Li, W., Park, Y. M. & Rahaman, S. O. MECHANISMS OF CELL SIGNALING BY THE SCAVENGER RECEPTOR CD36: IMPLICATIONS IN ATHEROSCLEROSIS AND THROMBOSIS. *Trans. Am.*

Clin. Climatol. Assoc. **121**, 206–220 (2010).

309. Veldhuizen, E. J. A. & Haagsman, H. P. Role of pulmonary surfactant components in surface film formation and dynamics. *Biochim. Biophys. Acta - Biomembr.* **1467**, 255–270 (2000).

310. Sallese, A. *et al.* Targeting cholesterol homeostasis in lung diseases. *Sci. Rep.* **7**, 1–14 (2017).

311. Bozinovski, S., Jones, J. E., Vlahos, R., Hamilton, J. A. & Anderson, G. P. Granulocyte/macrophage-colony-stimulating factor (GM-CSF) regulates lung innate immunity to lipopolysaccharide through Akt/Erk activation of NFκB and AP-1 in vivo. *J. Biol. Chem.* **277**, 42808–42814 (2002).

312. Smith, S. J. *et al.* Inhibitory effect of p38 mitogen-activated protein kinase inhibitors on cytokine release from human macrophages. *Br. J. Pharmacol.* **149**, 393–404 (2006).

313. Dhungana, H. *et al.* Sulfosuccinimidyl oleate sodium is neuroprotective and alleviates stroke-induced neuroinflammation. *J. Neuroinflammation* **14**, 1–13 (2017).

314. Schonewille, M. *et al.* Statins increase hepatic cholesterol synthesis and stimulate fecal cholesterol elimination in mice. *J. Lipid Res.* **57**, 1455–1464 (2016).

315. Shimizu, T. *et al.* Isolation and immunophenotyping of mononuclear cells from human lung tissue. *Intern. Med.* **46**, 163–169 (2007).

316. Ryan, E. J. *et al.* Dendritic Cell-Associated Lectin-1: A Novel Dendritic Cell-

Associated, C-Type Lectin-Like Molecule Enhances T Cell Secretion of IL-4. *J. Immunol.* **169**, 5638–5648 (2002).

317. Bloem, K. *et al.* Ligand Binding and Signaling of Dendritic Cell Immunoreceptor (DCIR) Is Modulated by the Glycosylation of the Carbohydrate Recognition Domain. *PLoS One* **8**, (2013).

318. Polanska, U. M., Duchesne, L., Harries, J. C., Fernig, D. G. & Kinnunen, T. K. N-glycosylation regulates fibroblast growth factor receptor/EGL-15 activity in Caenorhabditis elegans in vivo. *J. Biol. Chem.* **284**, 33030–33039 (2009).

APPENDIX

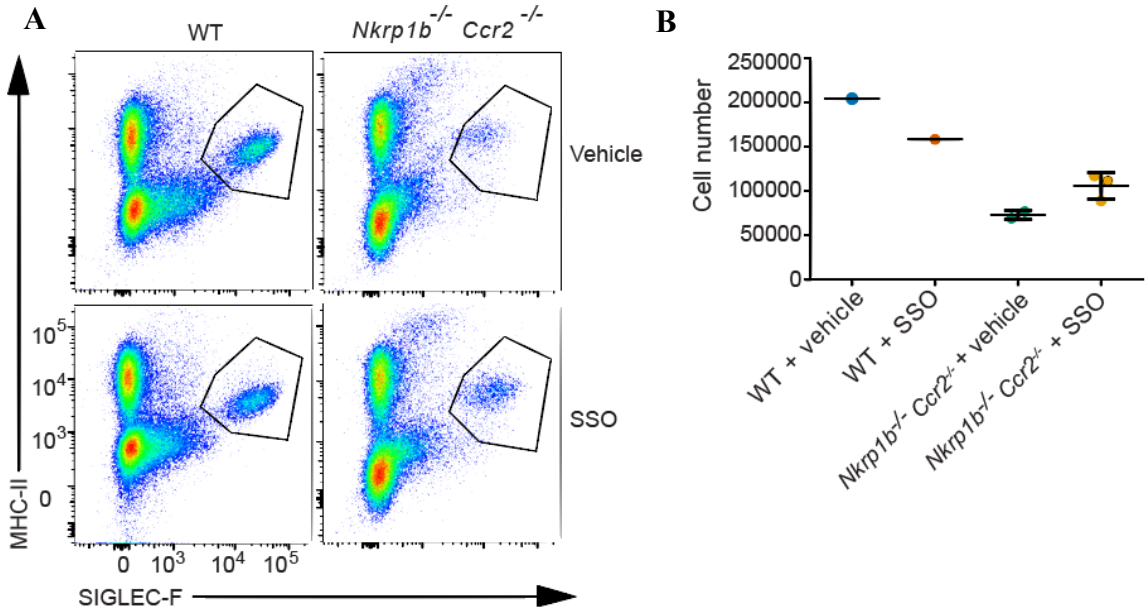

Fig A1: SSO administration *in vivo* appears to partially rescue AM numbers in *Nkrp1b*$^{-/-}$ mice.
(A) Flow cytometry dot plots of AM numbers found in the lungs of WT and *Nkrp1b*$^{-/-}$ mice at 5 weeks of age after 2 weeks of treatment with vehicle or SSO. Images are representative of 2 different experiments.
(B) Quantifications of AMs obtained by flow cytometric analysis from WT and *Nkrp1b*$^{-/-}$ mice at 5 weeks of age after 2 weeks of treatment with vehicle or SSO. Error bars represent SEM. N = 1-3. Statistics not performed due to low sample number

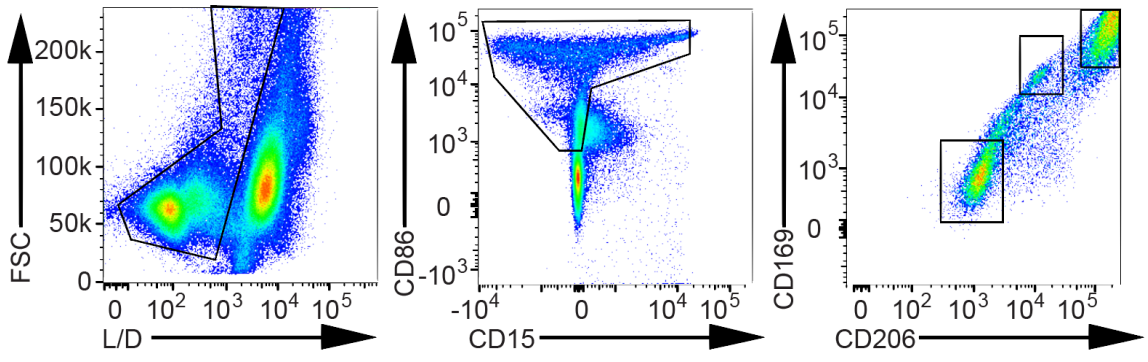

Fig A2: Gating strategy used for human AM isolation.
Humans AMs were defined as CD86^{+}CD15$^{+/-}$CD169^{+}CD206^{+}. Interstitial AMs were defined as CD86^{+}CD15$^{+/-}$CD169^{mid}CD206^{mid} and monocytes were defined CD86^{+}CD15$^{+/-}$CD169^{lo}CD206^{lo}